Investigating the effects of surfactants on nanobubble stability in plant xylem using mathematical models

A thesis submitted to the School of Engineering, Mathematics and Physics at the University of East Anglia in partial fulfilment of the requirements for the degree of Doctor of Philosophy

Jared Connor Carpenter

January 2026

Abstract

Water transport in vascular plants occurs under negative pressures, placing xylem sap in a metastable state that is susceptible to cavitation and embolism. Recent experimental observations have revealed the widespread presence of long-lived, surfactant-coated nanobubbles in xylem sap, challenging the traditional view that gas bubbles inevitably lead to hydraulic failure. The mechanisms by which such nanobubbles persist under physiologically relevant conditions, however, remain poorly understood.

In this thesis, a mathematical framework is developed to investigate the dynamics and stability of surfactant-covered nanobubbles in plant xylem. Starting from the Navier–Stokes equations, the Stokes flow regime appropriate for xylem conditions is derived using dimensional analysis, and classical bubble dynamics are reviewed through the Rayleigh–Plesset equation. Linear stability theory and Floquet theory are employed to analyse both steady and time-periodic bubble behaviour.

Axisymmetric models are formulated to describe deformable bubbles with surfactant-coated interfaces, incorporating interfacial stress balances, gas compressibility, and surfactant transport along the bubble surface. Exact expressions for growth rates are obtained for bubbles with constant base-state radius, both in the presence and absence of surfactants, while time-periodically varying bubbles are analysed using a combination of analytical and numerical techniques. Numerical optimisation methods, including genetic algorithms and simulated annealing, are used to explore the high-dimensional parameter space associated with these models.

The analysis is extended to non-axisymmetric perturbations, allowing fully three-dimensional surface deformations to be considered. In addition, inertial effects are incorporated by relaxing the Stokes flow assumption and considering a simplified inertial regime. Across all models investigated, numerical results consistently indicate that surfactant-covered nanobubbles are dynamically stable over a wide range of physiologically relevant parameters. No growing modes are observed for either axisymmetric or non-axisymmetric perturbations, even under periodic forcing of the bubble radius. The inclusion of inertia does not destabilise steady bubbles within the regimes considered.

These findings suggest that surfactants play a stabilising role in nanobubble dynamics and provide a plausible theoretical explanation for the persistence of nanobubbles observed experimentally in plant xylem. The results support the view that surfactant-covered nanobubbles need not inevitably lead to embolism and contribute to a mathematical understanding of water transport under tension in vascular plants.

Access Condition and Agreement

Each deposit in UEA Digital Repository is protected by copyright and other intellectual property rights, and duplication or sale of all or part of any of the Data Collections is not permitted, except that material may be duplicated by you for your research use or for educational purposes in electronic or print form. You must obtain permission from the copyright holder, usually the author, for any other use. Exceptions only apply where a deposit may be explicitly provided under a stated licence, such as a Creative Commons licence or Open Government licence.

Electronic or print copies may not be offered, whether for sale or otherwise to anyone, unless explicitly stated under a Creative Commons or Open Government license. Unauthorised reproduction, editing or reformatting for resale purposes is explicitly prohibited (except where approved by the copyright holder themselves) and UEA reserves the right to take immediate ‘take down’ action on behalf of the copyright and/or rights holder if this Access condition of the UEA Digital Repository is breached. Any material in this database has been supplied on the understanding that it is copyright material and that no quotation from the material may be published without proper acknowledgement.

Contents

List of Figures

List of Tables

Acknowledgements

First and foremost, I would like to express my sincere gratitude to my supervisory team. My primary supervisor, Professor Richard Morris, my secondary supervisor, Professor Mark Blyth, and Dr Hugh Woolfenden, a postdoctoral member of the team, have provided outstanding guidance, support, and encouragement throughout my PhD. Your mentorship has been invaluable, both academically and personally, and I could not have asked for better people to work with.

I would also like to thank the UK Research and Innovation Biotechnology and Biological Sciences Research Council (BBSRC) for funding my studentship [grant number BB/T008717/1] and enabling me to study within the Norwich Research Park Doctoral Training Partnership (NRPDTP).

My thanks also go to the University of East Anglia's Department of Engineering, Mathematics and Physics (EMP, formerly the School of Mathematics) and the John Innes Centre (JIC) for their support and resources during my research. I am grateful to my fellow PhD researchers in EMP and the Morris lab at JIC, who have made me feel so welcome and helped create such an enjoyable and collaborative working environment.

A special thanks goes to my family, especially my mum, whose unwavering support and belief in me have made this journey possible. I would not be where I am today without her. I am also deeply grateful to Amanda Leggett, my specialist autism mentor, who has supported me on this journey since I started as an undergraduate in 2017; your guidance has helped me more than you will ever know.

To my Showhouse family — James, Charlotte (and Dan), Jasmine, and Daniel — thank you for creating such a positive and supportive home environment. Likewise, thank you to UEA Showchoir for the fun, friendship, and much-needed breaks from research that have enriched my PhD experience.

Finally, I would like to acknowledge the music that has accompanied much of my research journey: Taylor Swift, ABBA and David Bowie. Your soundtracks have provided motivation and joy throughout this project.

Dedications

In loving memory of Lee Clarke.

1

Introduction

1.1 Long-distance transport in plants

The long-distance transport of water and minerals in plants is essential to support their growth and metabolism. Xylem transports water and other nutrients from root to shoot, while phloem transports energy-rich solutes made during photosynthesis from shoot to root (Jensen et al., 2016). Xylem and phloem are found in all vascular plants, including seedless plants, as well as angiosperms and gymnosperms. Xylem tissue consists of various specialised water-conducting elements known as tracheary elements. These consist of cells known as *tracheids*, which are single-celled, and *vessel elements* (Jensen et al., 2016).

Coniferous trees, along with most gymnosperms and seedless plants, such as the Douglas-fir tree (Domec et al., 2008), lack a continuous system of xylem vessels and instead depend on tracheids, which are non-living conducting cells that serve to transport water and to support the trunk (White, 2012). Figure 1.1.1 illustrates the structure and function of wood.

Tracheids, which range in length from 2 to 6 mm, can also disrupt long-distance transport in annual plant species, for example, at the root-shoot junction or in the nodes of the stem. This poses internal resistance to xylem volume flow and, as a consequence, permits intensive xylem–phloem solute transfer (White, 2012).

The geometry of xylem and the width of its vessels are central to understanding

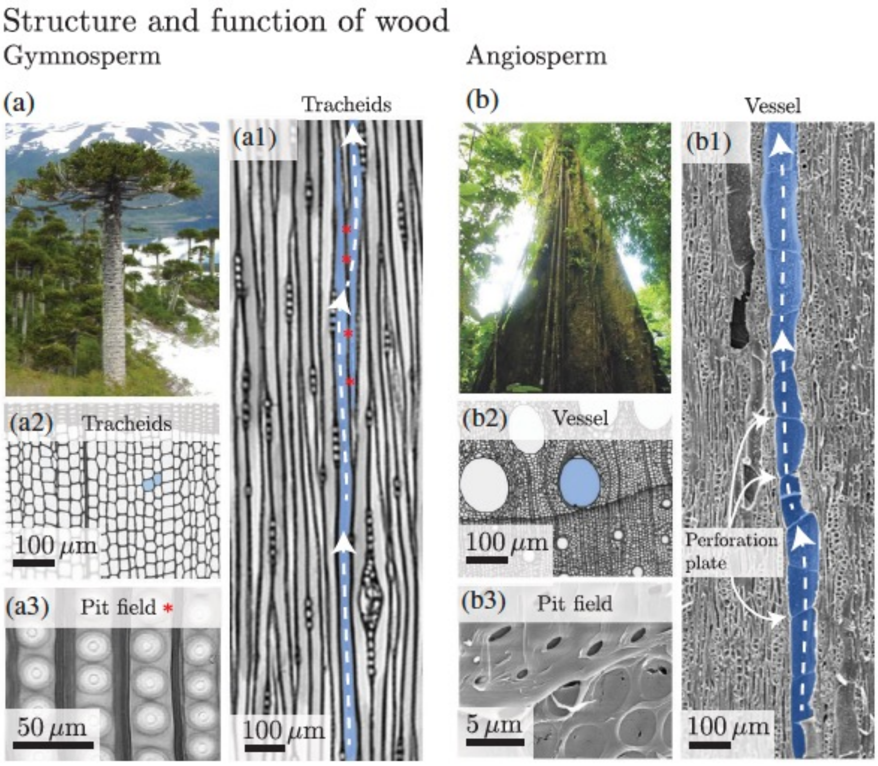

Figure 1.1.1: Wood structure in (a) gymnosperms and (b) angiosperms, taken from Jensen et al. (2016).

plant water transport. Xylem vessels are typically tubular, with widths varying significantly among different plant species and in response to environmental conditions. Angiosperms feature wider vessels (20 to 500 µm), while gymnosperms have narrower tracheids (10 to 80 µm). The balance between vessel width and the risk of cavitation is a key aspect of plant physiology, influencing how plants adapt to their environments.

Plants are amazing lifeforms that are able to drive a vascular system, which sustains growth and development, without a central heart. The basic mechanics of this flow have been difficult to determine due to the sensitive nature of the conduits. We seek to further develop the understanding of the behaviour of nanobubbles in xylem. The theory and mathematics of plant signalling and variation potentials is discussed in Blyth & Morris (2019). The mathematics of fluid transport in plants, which provides good background knowledge, can be found in Blyth & Morris (2018). In this thesis, we will focus on the mathematics of bubble dynamics.

1.2 Negative pressure in xylem

Large amounts of water are needed in order for plants to live and grow. In fact, ninety percent of trees with an average height of 21 m transport a maximum of between 10 and 200 litres of water each day (Wullschleger et al., 1998). The transportation of this water occurs through the xylem. This water needs to travel upwards.

Our theoretical understanding of this transport came around the turn of the 20th century with a very influential theory published by Dixon & Joly (1894). The theory was that the driving force of the flow in xylem comes from suction generated in the leaves via evaporation of water into the atmosphere, i.e. transpiration. Water is lost from plants primarily through transpiration, which occurs via stomata — microscopic pores located in the epidermis of leaves and young stems. Each stoma is bordered by a pair of guard cells that regulate its opening and closing in response to environmental and physiological signals, such as light, humidity, and internal water status (see, for example, Wilson et al., 2025).

When the stomata are open, water evaporates from the moist cell walls within the leaf into the intercellular air spaces and diffuses out to the atmosphere. This evaporation lowers the water potential within the leaf, generating a tension that is transmitted through the continuous water column in the xylem. As a result, water is drawn upward from the roots by capillary forces to replace that lost on the surface of the leaf, maintaining the transpiration stream (see, for example, Venturas et al., 2017).

Transpiration is driven by photosynthesis. Photorespiration is a wasteful pathway that occurs when in the second stage of photosynthesis — the Calvin cycle — the enzyme rubisco acts on oxygen instead of carbon dioxide. This can cause a significant loss in vital crop yields (Cavanagh et al., 2022). In terms of photosynthesis, plants are divided into three categories: C_3, C_4 and Crassulacean acid metabolism (CAM) (see, for example, Wang et al., 2008). The majority of plants are C_3 and have no special features to combat photorespiration. However, C_4 and CAM plants have evolved mechanisms to combat photorespiration.

A result that may seem surprising is that the pressures inside the xylem are even lower than that of a vacuum, that is, they are negative. In fact, the maximum negative pressures recorded in plants are around −100 bar (or −10 MPa) (see, for example, Kanduč et al., 2020).

The idea of negative pressure may seem counter-intuitive from a physics point of view if one considers equilibrium thermodynamics. In fact, negative pressures only occur in non-equilibrium or metastable states.

One example of negative pressures being observed experimentally can be found in Briggs (1953), in which mercury in Pyrex© glass was able to sustain negative pressures of 425 bar (42.5 MPa) at 28°C. Experiments have also been carried out by Pallares et al. (2014) to record measurements of sound velocity in water that is both super-cooled and at a negative pressure. A more recent, and also exciting, use of negative pressure is the use of lower body negative pressure (LBNP) to move upper-body blood, and other fluids, towards the legs during spaceflight. This is to help offset the effects, including decreased visual acuity, that long-duration spaceflights have on passengers (Arbeille et al., 2021).

A more popular conception of water transport in plants is that it is analogous to that of a mechanical vacuum pump. That is, a pressure gradient-driven flow. However, if this were the case, water transport would be limited to less than 10 m (Jensen et al., 2016). This can be verified mathematically by considering the hydrostatic pressure head. This can be calculated using the equation, first derived by Bernoulli (1738), for an incompressible fluid with constant density where the flow is steady and there is no viscosity

$$p + \frac{1}{2}\rho v^2 + \rho g h = B\,,$$

where p is pressure, ρ is density, v is velocity, h is elevation, g is gravitational acceleration and B is the *Bernoulli constant.* We can apply Bernoulli's equation at two different points within a xylem vessel, which we model as a perfect cylinder, and equate the resulting expressions under the assumption that the flow is irrotational. In steady flow, streamlines and particle paths coincide, which justifies the application of Bernoulli's equation along a streamline. This set-up is illustrated in Figure 1.2.1.

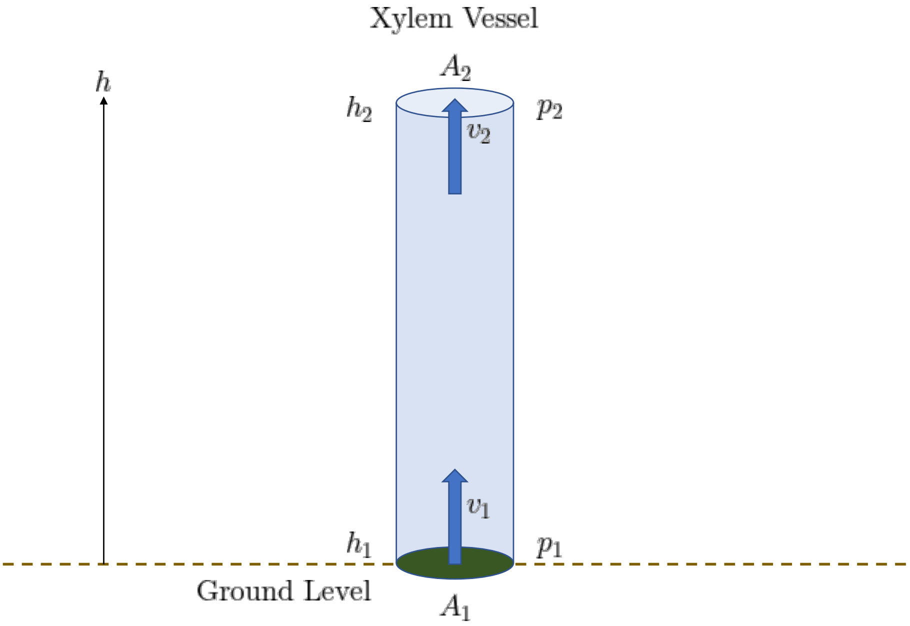

Figure 1.2.1: A simple schematic representation of a xylem vessel.

From this set-up we get,

$$p_1 + \frac{1}{2}v_1^2 + \rho g h_1 = p_2 + \frac{1}{2}v_2^2 + \rho g h_2\,, \tag{1.2.1}$$

and the continuity condition (by continuity of mass),

$$\rho A_1 v_1 = \rho A_2 v_2 \,.$$

As in our case $A_1 = A_2$, we get $v_1 = v_2$. So (1.2.1) can be simplified to

$$p_1 - p_2 = \rho g (h_2 - h_1)\,.$$

Suppose that at ground level the xylem is at atmospheric pressure $p_1 = 100$ kPa. Under the commonly invoked "vacuum pump" picture, the lowest attainable pressure is assumed to be zero, corresponding to a perfect vacuum. Taking $p_2 = 0$ then yields the maximum height to which water could be transported by a pressure gradient alone,

$$h_2 = \frac{p_1}{\rho g}\,.$$

Good approximate values of the variables for the flow of water in xylem are $\rho = 1000$ kgm^{-3} and $g = 10$ ms^{-2}. This would give us a head of

$$h_2 = \frac{10^5}{10^3 \cdot 10}\,\mathrm{m} \; = 10\,\mathrm{m}\,.$$

This obviously could not work as many trees grow to heights much taller — for example the aforementioned Douglas-fir conifer can grow to heights between 100–127 m (Domec et al., 2008). Thus, water transport in plants cannot be explained by a simple pressure-gradient mechanism limited by atmospheric pressure. Instead, pressures within the xylem must fall below atmospheric pressure, placing the water under tension rather than compression.

Also, as discussed in Prendin et al. (2018), Norwegian spruce trees prioritise hydraulic efficiency, to allow growths of greater height, over embolism safety. This implies that the pressure at the top of the xylem would have to be below zero.

Vascular plants are the only organism that transports water utilising the cohesion between water molecules which acts to pull water through a hydraulic system as opposed to it being pushed via positive pressure (Yang et al., 2020). However, many vascular plants show positive pressure (above atmospheric pressure) in the xylem on a daily or seasonal pattern, or during early development stages. What is interesting is that the mechanisms of this positive pressure are also largely unknown but a discussion of which can be found in Schenk et al. (2021a).

The pulling caused by cohesion slightly increases the distance between water molecules, thus creating negative pressure. As discussed in many papers, this pull force is generated by the evaporation of water from nanocapillaries in the cell walls of leaves and the negative pressure is generated by the weight of the water column and hydraulic resistance in xylem. This is known as the *cohesion–tension theory*; see, for example: Schenk et al. (2021a); Kanduč et al. (2020); Yang et al. (2020); Jensen et al. (2016); Domec et al. (2008).

The mechanism of cohesion-tension operates under negative pressures. The three contributing forces to the pressure gradient are gravitational (generally the smallest contributor), soil water potential (the most significant factor) and friction. If, for example, we consider water at 20°C it will boil at an absolute pressure of 2.3 kPa. So, relative to an atmospheric pressure of 101.3 kPa water should boil at -99 kPa (Venturas et al., 2017).

Figure 1.2.2 shows the relationship between xylem sap pressure and tree height for drying soil. The black line illustrates the case for fully hydrated soil and closed stomata — the hanging water column balances gravitational force. The red line shows that as long as there is no flow, as the soil dries the starting point of the pressure gradient is more negative but the slope is unchanged. The blue lines show the effects of the stomata opening, that is the slope of the pressure gradient within the plant increases due to friction and transpiration (E) is proportional to the plant's hydraulic conductance and its soil to leaf pressure drop. Plants are able to vary E by adjusting their stomatal aperture. The dashed blue line is the pressure drop for low E and the solid blue is line is for high E. The red dash-dot

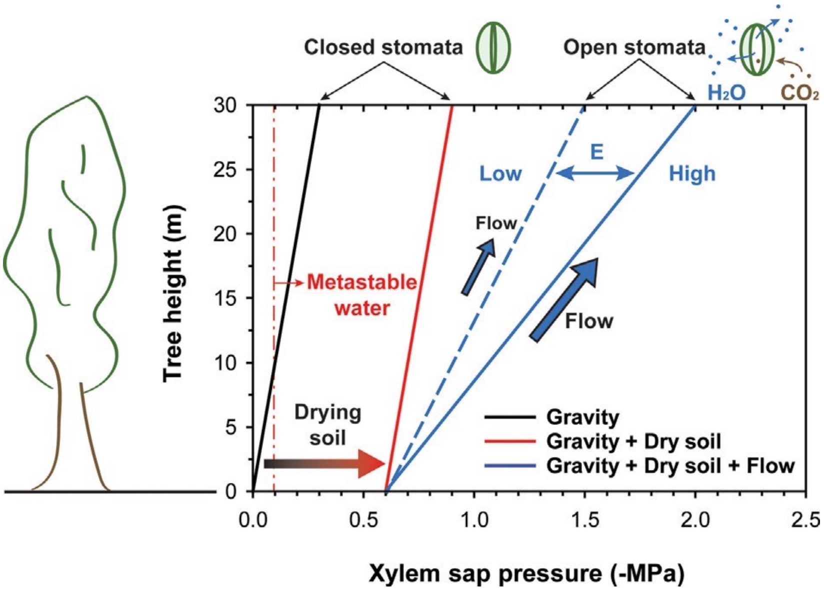

Figure 1.2.2: Pressure gradients in a tree, taken from Venturas et al. (2017).

line represents the boiling point of water −99 kPa (Venturas et al., 2017).

Under these negative pressures, in order for the cohesion tension mechanism to work, the boiling of water in the xylem must be avoided. Hence, the water must enter a metastable liquid phase.

Light stress also has an impact on transpiration as plants have evolved to combat physiological damage through a variety of techniques including opening and closing stomata (Shi et al., 2022).

Phloem transport is just as important as it transports vital sugars, a product of photosynthesis, to where they are needed. In contrast to the xylem, phloem tubes (or sieve elements) are living cells. The main transport mechanism in the phloem (other possible mechanisms have been proposed over the years.) is the so-called *Münch mechanism*. In 1930, Ernst Münch hypothesised that gradients of hydrostatic pressure are generated osmotically between phloem source (high pressure due to loading) and sink organs (low pressure due to unloading) (Knoblauch & Peters, 2010). A schematic representation of both cohesion–tension (a) and Münch mechanisms (b) can be seen in Figure 1.2.3.

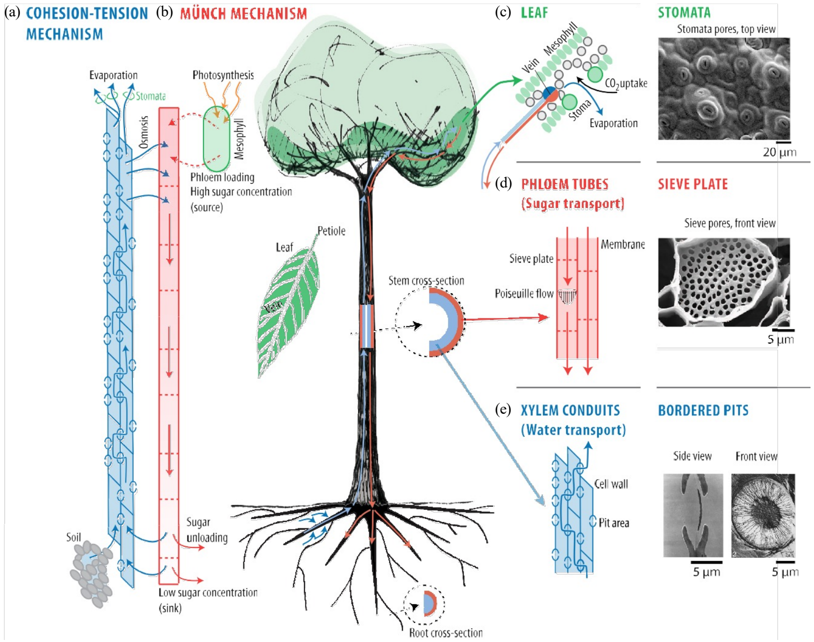

Figure 1.2.3: Schematic representation of vascular transport in plants, taken from Jensen et al. (2016).

1.3 Nanobubbles and embolisms

The fact that water transport in plants relies on negative pressure causes challenges. This negative pressure can lead to cavitation (the formation of vapour bubbles when liquids are under tension — i.e. negative pressure) and thence embolisms, which can cause hydraulic failure (see, for example, Wason et al., 2021; Schenk et al., 2015; Brodersen & McElrone, 2013). The process of gas formation in xylem is often referred to as *air seeding* in the literature — see for example: Ingram et al. (2021); Wason et al. (2021); Yang et al. (2020); Schenk et al. (2015); Domec et al. (2008).

An *embolism* in a plant refers to the formation of air-filled voids or emboli within the water-conducting xylem conduits, which interrupts the continuous column of water under tension and severely reduces the plant's ability to transport water from roots to leaves. Extensive embolism formation impedes sap flow, reduces photosynthesis and growth, and can lead to branch or whole-plant death if a critical fraction of conduits becomes blocked (see, for example, Lens et al., 2013).

Water is transported via necrotic cells known as *xylem conduits* which provide a low-resistance route. Because the xylem conduits are of finite length, the water is forced to move to neighbouring conduits via *pit borders*: narrow cavities. These pit borders are not complete openings in the cell wall; a modified, nanoporous primary cell wall — called the *pit membrane* — is retained. This is shown in Figure 1.3.1.

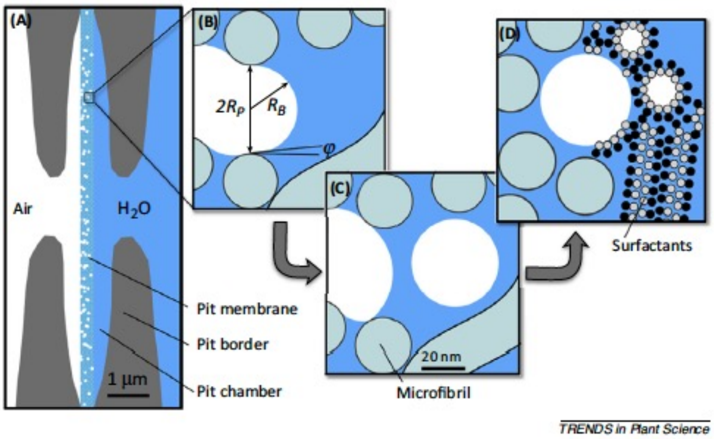

Figure 1.3.1: Proposed model of nanobubble formation in an angiosperm pit membrane, taken from Schenk et al. (2015).

An important question is: how do nanobubbles form in the pit membrane? This can be answered in three stages. Firstly, Figure 1.3.1(C) shows how a nanobubble is snapped off due to the movement of a meniscus (the curve in the upper surface of the water — caused by surface tension) through a nanoporous constriction. This happens when the radius of the constriction is less than half of the radii of the pore on either side — see Figure 1.3.1(B) (Schenk et al., 2015).

Secondly, as a gas meniscus moves into a liquid-filled pore, it is stabilised as local pressure increases. This contributes to bubble 'snap-off' at the pore restriction. Due to the low compressibility of water — a discussion of density and compressibility of water can be found in Gaiduk et al. (2015) — the pressure release of bubble entry into water under negative pressure is substantial — about 2 MPa of negative pressure (Schenk et al., 2015).

Finally, bubbles are formed under a principle of surface-area minimisation (this is a fascinating area of mathematics in its own right and more can be read about it in e.g. Morgan (1994)) and under negative pressure, a liquid will favour bubble formation over rupture of hydrogen bonds between water molecules — this is due to thermodynamics (Schenk et al., 2015).

What is of particular interest is the fact that stable nanobubbles have been discovered in plant xylem — that is, bubbles that do not form an embolism (see, for example, Ingram et al., 2021; Schenk et al., 2015). Although this has proven to be difficult to recreate in a laboratory setting, the effect of nanobubble creation (i.e. 'snapping off') has been demonstrated artificially in experiments by Duan et al. (2012) where nanobubbles snap-off under negative pressure at a silica nanochannel entrance — see Figure 1.3.2.

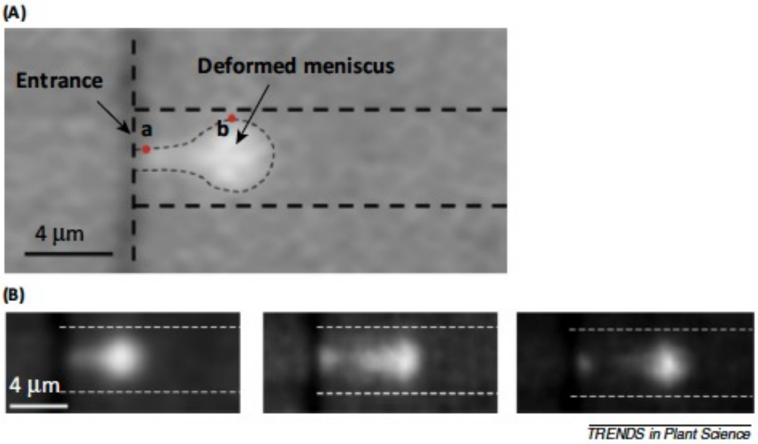

Figure 1.3.2: Top view microscope images of deformed menisci and nanobubbles (nanochannels are 4 μm wide and 58 nm in height), taken from Schenk et al. (2015).

It was Blake (1949) who first recognised that gas bubbles under a certain radius, known as the *Blake threshold*, are stable. The mathematics of this Blake threshold will be discussed in Section 4.6.2. What recent studies have shown, for example Ingram et al. (2021); Yang et al. (2020); Schenk et al. (2017), is that dynamic surface tension increases the stability of nanobubbles and thus reduces the risk of an embolism forming. Dynamic surface tension can be brought on by *surfactants*.

1.4 An introduction to surfactants

Surfactants are molecules that preferentially adsorb to fluid interfaces and lower the surface tension, between two liquids, between a gas and a liquid, or between a liquid and a solid (Manikantan & Squires, 2020). The word "surfactant" is a contraction of the term *surface-active agent* (Rosen & Kunjappu, 2012). Many surfactants are *amphiphilic*, meaning they have both *hydrophilic* (the head) and *hydrophobic* (the tail) parts — see Figure 1.4.1(a). In the case of nanobubbles in xylem, these amphiphilic surfactants adsorb to the gas-water interface with their hydrophobic tails directed out of the water phase, thus coating the bubble surface in hydrophobic tails, resulting in the reduction of surface tension (See Figure 1.4.1(b,c)).

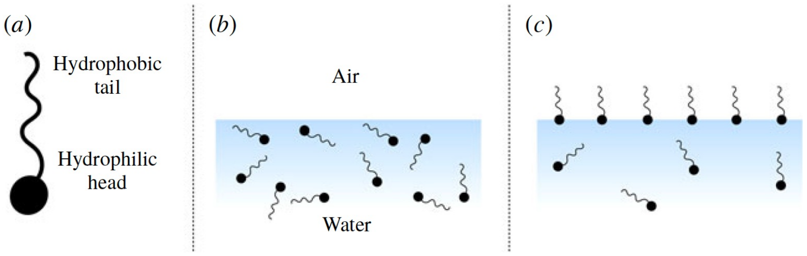

Figure 1.4.1: Diagrams showing a surfactant (a) and how surfactants are adsorbed to an air–water interface, taken from Manikantan & Squires (2020).

Soluble surfactants in plants can be of various origins. They can be produced endogenously by the plant or absorbed from the environment. Endogenous surfactants include certain proteins, saponins, and lipids secreted by plant cells (Zheng et al., 2020), particularly in response to stress or injury. Exogenous surfactants might enter the plant system through the uptake of agrochemicals or through root interactions with soil microbes that produce biosurfactants.

1.5 Surfactant-covered nanobubbles

The focus of this thesis is on nanobubbles that form in the xylem. Nanobubbles are bubbles that experimentally have an average radius of 50 nm and a lifetime of over 2 weeks (Ohgaki et al., 2010). These nanobubbles have the potential to form embolisms which are detrimental to the plant (see, for example, Wason et al., 2021; Schenk et al., 2015; Brodersen & McElrone, 2013). However, these bubbles may also exist in a metastable state (see, for example, Vehmas & Makkonen, 2021). There is a lot of literature around the area of drought-induced embolisms, see for example, Isasa et al. (2023); Lens et al. (2022); Pritzkow et al. (2022).

What is also amazing about plants is that even if embolisms occur in the xylem, there are various repair mechanisms in place (see, for example, Brodersen & McElrone, 2013) to mitigate the damage. One of these, that operates under positive pressure — which we previously mentioned — is to refill the embolised xylem conduits with water (see, for example, Schenk et al., 2021a).

An exciting and recent development in this area is the detection of airborne sounds emitted by stressed plants. Khait et al. (2023) recorded ultrasonic sounds emitted by tomato and tobacco plants inside an acoustic chamber — see Figure 1.5.1. Using machine learning models, you can identify the condition of the plant, including dehydration level and injury, based solely on these emitted sounds. Plants under drought conditions experience cavitation, where nanobubbles form then expand and collapse which then cause vibrations. These vibrations have been recorded by connecting a recording device directly to the plant.

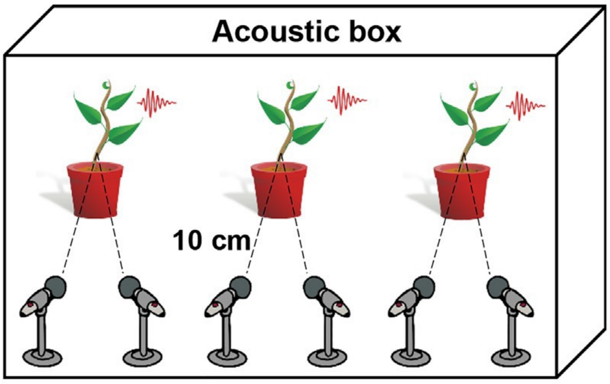

Figure 1.5.1: Acoustic box setup. The three plants are placed inside a $50 \times 100 \times 150\,\mathrm{cm}^3$ acoustic box with two directional microphones oriented at each plant. Taken from Khait et al. (2023).

The existence of gas nanobubbles was first hypothesised after observations of gas flow in wood (Ingram et al., 2023). This hypothesis led to studies of nanobubble concentrations in xylem sap using nanoparticle tracking analysis (NTA). NTA can be used to qualitatively assess whether nanoparticles are spherical, which was the case for all flowering plant species whose xylem sap was analysed using NTA. In the samples, which included trees, shrubs and a liana species, nanoparticles ranging between 20 and 300 nm in radius were found in their sap using data from Schenk et al. (2017) and Guan et al. (2022), as illustrated in Figure 1.5.2.

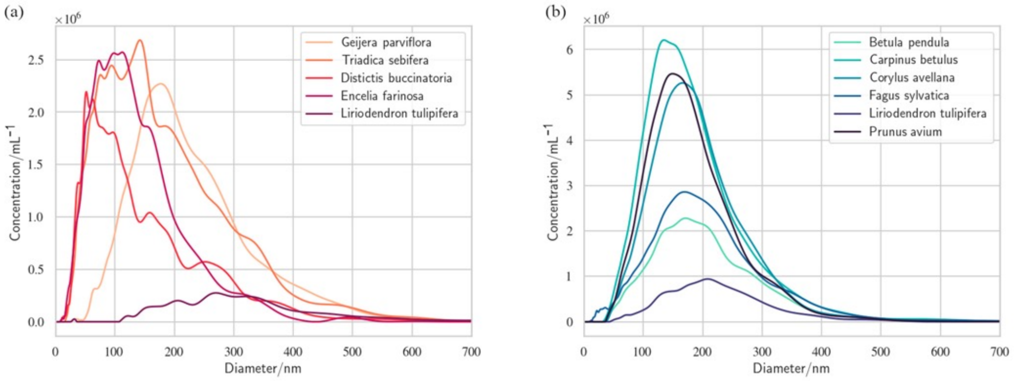

Figure 1.5.2: Size distributions and concentrations of nanoparticles observed in eleven flowering plant species. Data taken from (a) (Schenk et al., 2017) and (b) (Guan et al., 2022). The data in (a) were collected in moving samples while the data in (b) were from stationary samples. Figure taken from Ingram et al. (2023).

NTA, however, does not distinguish between nanobubbles and other nanoparticles. To assess whether the nanoparticles in xylem sap were indeed nanobubbles, freeze-fracture electron microscopy was used to investigate the sap from two plant species: *Geijera parviflora* and *Corylus avellana*. The results of this are shown in Figure 1.5.3.

Nanobubbles in xylem sap are coated in surfactants. Analysis by Schenk et al. (2017) found evidence for both polar lipids (amphiphilic lipids with a hydrophilic head and a hydrophobic tail) and proteins. Polar lipids extracted from xylem sap of thirteen flowering plant species were analysed by Guan et al. (2022) and Schenk et al. (2021b) using mass spectrometry and included both phospholipids and galactolipids, with a high proportion of phosphatidic acid, a phospholipid with a

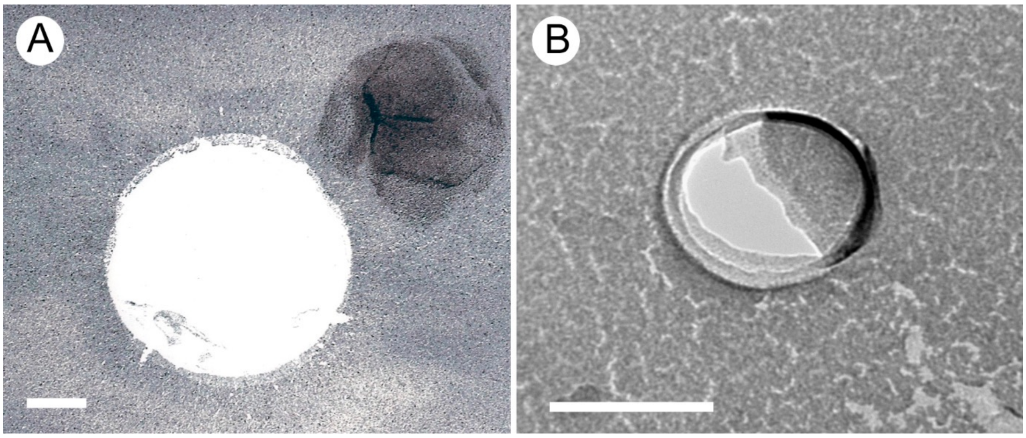

Figure 1.5.3: Freeze-fracture EM images of surfactant-coated nanobubbles in *Geijera parviflora* (A) and *Corylus avellana* (B). The gas bubble cores are visible as the white Pt/C free areas, while the dark areas represent the surfactant coat. Scale bars = 100 nm. Figure taken from Ingram et al. (2023).

negatively charged headgroup. The concentrations and chemical composition of these polar lipids is shown in Figure 1.5.4.

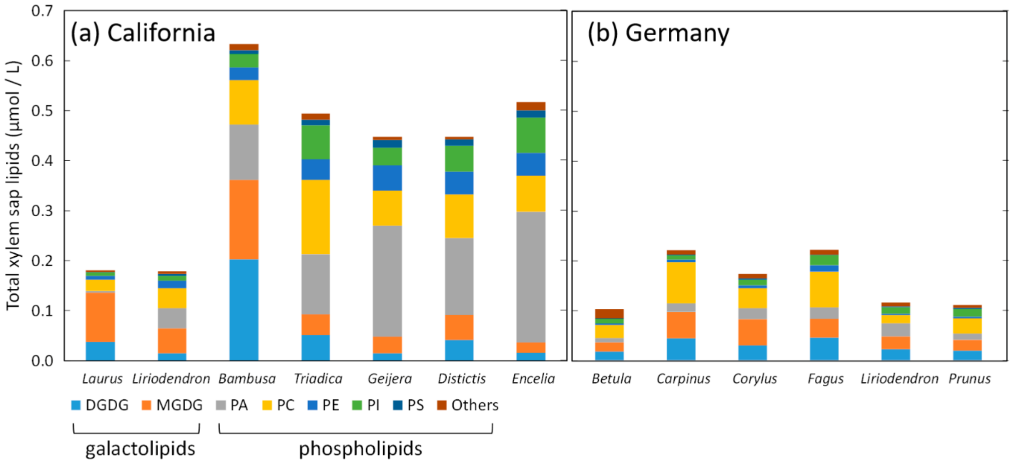

Figure 1.5.4: Data from (a) California (Schenk et al., 2021b), and (b) Germany (Guan et al., 2022). DGDG, digalactosyldiacylglycerol; MGDG, monogalactosyldiacylglycerol; PA, phosphatidic acid; PC, phosphatidylcholine; PE, phosphatidylethanolamine; PI, phosphatidylinositol; PS, phosphatidylserine. Figure modified from Schenk et al. (2021b). See Figure 1.5.2 for the full species names. Figure taken from Ingram et al. (2023).

Lipid surfactants have also been measured in tropical plants. In a study by Huang et al. (2024), the lipid composition of xylem sap for angiosperm species from a tropical savanna (seven species) and a seasonal rainforest (five species) was quantified using mass spectrometry. Lipids were found in xylem sap in all species studied, including galactolipids, phospholipids and triacylglycerols, with a total lipid concentration ranging from 0.09 to 0.26 nmol/L. The list of species studied can be found in Figure 1.5.5. The lipid concentrations from these tropical angiosperm species can be found in Figure 1.5.6.

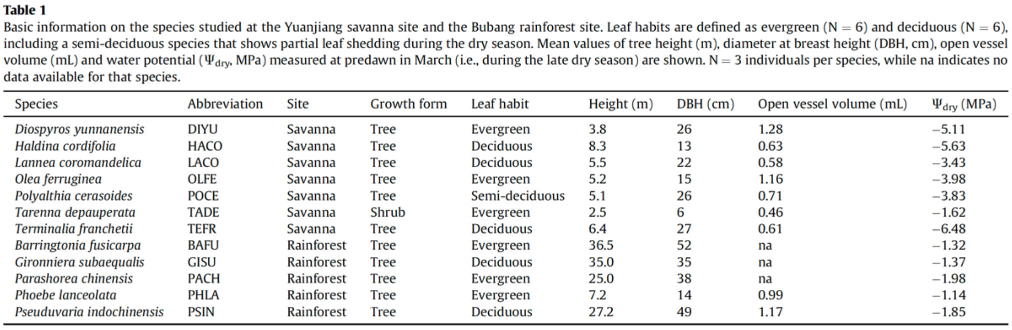

Table 1

Basic information on the species studied at the Yuanjiang savanna site and the Bubang rainforest site. Leaf habits are defined as evergreen (N = 6) and deciduous (N = 6), including a semi-deciduous species that shows partial leaf shedding during the dry season. Mean values of tree height (m), diameter at breast height (DBH, cm), open vessel volume (mL) and water potential (Ψ_{dry}, MPa) measured at predawn in March (i.e., during the late dry season) are shown. N = 3 individuals per species, while na indicates no data available for that species.

Species	Abbreviation	Site	Growth form	Leaf habit	Height (m)	DBH (cm)	Open vessel volume (mL)	Ψ_{dry} (MPa)
Diospyros yunnanensis	DIYU	Savanna	Tree	Evergreen	3.8	26	1.28	−5.11
Haldina cordifolia	HACO	Savanna	Tree	Deciduous	8.3	13	0.63	−5.63
Lannea coromandelica	LACO	Savanna	Tree	Deciduous	5.5	22	0.58	−3.43
Olea ferruginea	OLFE	Savanna	Tree	Evergreen	5.2	15	1.16	−3.98
Polyalthia cerasoides	POCE	Savanna	Tree	Semi-deciduous	5.1	26	0.71	−3.83
Tarenna depauperata	TADE	Savanna	Shrub	Evergreen	2.5	6	0.46	−1.62
Terminalia franchetii	TEFR	Savanna	Tree	Deciduous	6.4	27	0.61	−6.48
Barringtonia fusicarpa	BAFU	Rainforest	Tree	Evergreen	36.5	52	na	−1.32
Gironniera subaequalis	GISU	Rainforest	Tree	Deciduous	35.0	35	na	−1.37
Parashorea chinensis	PACH	Rainforest	Tree	Evergreen	25.0	38	na	−1.98
Phoebe lanceolata	PHLA	Rainforest	Tree	Evergreen	7.2	14	0.99	−1.14
Pseuduvaria indochinensis	PSIN	Rainforest	Tree	Deciduous	27.2	49	1.17	−1.85

Figure 1.5.5: Table taken from Huang et al. (2024).

While surfactants in xylem sap are often considered stabilising agents for nanobubbles, molecular dynamics simulations indicate that they can also trigger bubble destabilisation under certain conditions (Xiao et al., 2017). Specifically, for nanobubbles attached to or near solid surfaces, surfactant adsorption can induce contact-line depinning, where the triple-phase boundary (gas, liquid, solid) becomes mobile, weakening the forces that maintain bubble shape and facilitating collapse. For bubbles suspended in the bulk liquid, surfactant molecules at the gas–liquid interface can reduce surface tension, generating interfacial instabilities that cause the bubble to shrink or rupture. These two mechanisms demonstrate that surfactants can paradoxically promote nanobubble collapse rather than persistence, depending on local environment and concentration, a phenomenon directly observed in the simulations of Xiao et al. (2017).

In the context of xylem sap, these findings suggest that the interplay between surface-active compounds and bubble geometry is likely to be crucial in determining the stability of gas-filled cavities under tension. While previous studies have largely treated surfactants as purely stabilising agents, the results

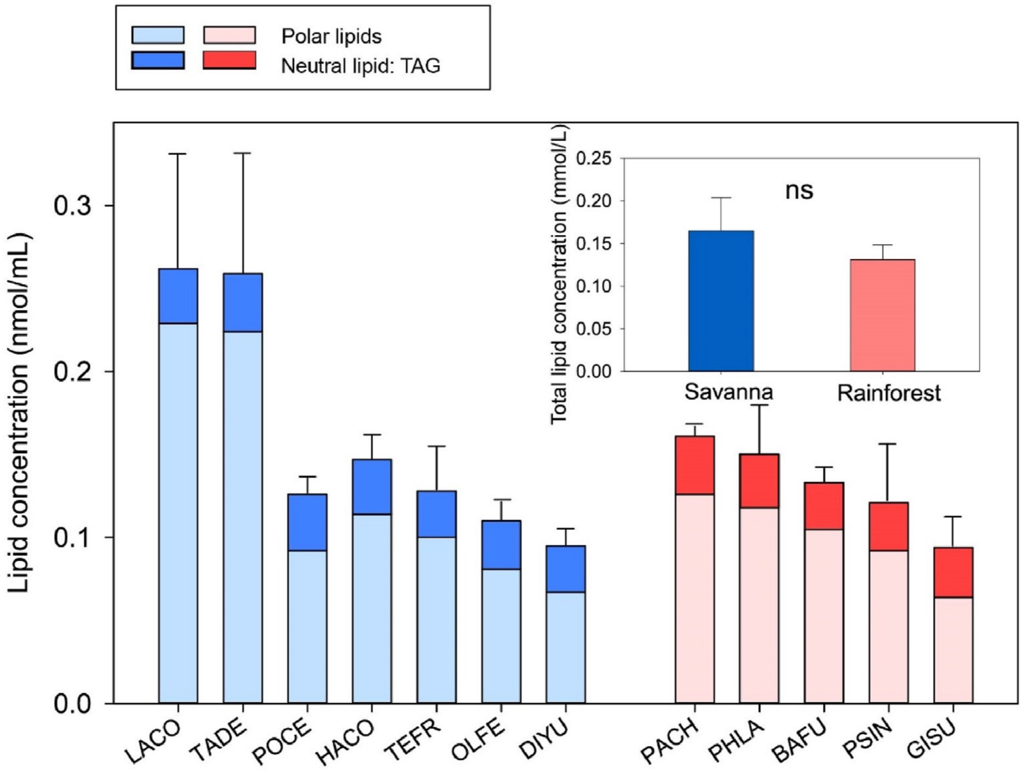

Figure 1.5.6: Lipid concentrations in xylem sap from 12 tropical angiosperm species collected during the dry season of 2022 (March). Shown are polar lipids and neutral lipids (TAG = triacylglycerol). Inset: mean values of the total lipid concentration for tropical savanna and rainforest species, respectively. NS indicates no significant difference between the two biomes ($p = 0.05$). Error bars are standard errors. Abbreviations for each species are listed in Figure 1.5.5. For each species, three specimens were studied. Figure taken from Huang et al. (2024).

in the paper by Xiao et al. (2017) highlight that adsorption dynamics and local flow conditions can reverse this effect. This motivates the present work, where I will investigate the linear stability of spherical and near-spherical gas bubbles in a viscous, surfactant-laden environment under conditions representative of xylem sap. By explicitly incorporating interfacial surfactant concentration and its coupling to bubble shape perturbations, the analysis aims to quantify the conditions under which surfactants enhance or undermine bubble persistence, thereby bridging molecular-level observations with mathematical predictions of bubble stability in plants.

Surfactants have also been shown to exert a destabilising influence in a range of other physical settings. For example, Frenkel & Halpern (2002) investigated a two-fluid shear flow with an insoluble surfactant on a flat interface and demonstrated that the presence of surfactants can destabilise the flow.

1.6 Structure of this thesis

This thesis develops a mathematical framework for understanding the dynamics and stability of surfactant-covered nanobubbles under the extreme physical conditions present in the xylem. Motivated by experimental evidence for stable, surfactant-coated nanobubbles and their proposed role in embolism formation and prevention, the work combines fluid mechanics, interfacial physics, and stability theory to investigate the mechanisms by which such bubbles may persist under negative pressure.

Chapter 2 introduces the mathematical background required for the analysis. Beginning with the Navier–Stokes equations, we derive the Stokes flow regime appropriate for xylem conditions and review classical bubble dynamics through the Rayleigh–Plesset equation. Methods from linear stability theory are then introduced, culminating in an overview of Floquet theory, which provides the principal framework for analysing periodically forced systems arising from a time-dependent bubble radius and pressure fluctuations.

In Chapter 3, we introduce numerical optimisation techniques that are used to explore the high-dimensional parameter space associated with surfactant-covered bubble models. In particular, global optimisation methods, including genetic algorithms and simulated annealing, are discussed and implemented to identify parameter regimes that promote bubble stability under physiologically relevant conditions.

Chapter 4 considers the axisymmetric bubble problem. A detailed mathematical model is developed for a deformable bubble immersed in a viscous fluid, incorporating interfacial stress balances, surfactant transport along the bubble surface and both constant and time-dependent bubble radii. Stability equations are derived for spherical and weakly deformed bubbles, allowing the influence of surfactants and gas compressibility on bubble stability to be quantified.

The analysis is extended in Chapter 5 to non-axisymmetric perturbations. Here, fully three-dimensional surface deformations are considered, and evolution equations for the perturbation amplitudes are derived. The resulting coupled stability system captures the interaction between hydrodynamics, surfactant redistribution, and interfacial elasticity, enabling a comprehensive assessment of the modes most likely to destabilise surfactant-coated nanobubbles in xylem sap.

Chapter 6 extends the modelling framework by relaxing the Stokes flow assumption and incorporating inertial effects through the full Navier–Stokes equations. Although inertial forces are expected to be small under typical xylem conditions, their inclusion allows the robustness of the stability results obtained in earlier chapters to be assessed. By deriving the modified kinematic and dynamic boundary conditions, this chapter examines whether inertia can destabilise surfactant-covered nanobubbles or introduce new instability mechanisms.

2

Mathematical background

Synopsis

In this chapter we will show how to get from the full Navier–Stokes equations to the Stokes equations. We will then see how, using the Navier–Stokes equations, we can derive an ordinary differential equation that governs how the radius of a bubble behaves over time. Finally, we will discuss how we can use methods from linear algebra to determine the stability of dynamical systems and how Floquet theory can generalise this.

2.1 Stokes flow

The Navier–Stokes equations are fundamental to the study of fluid mechanics. These equations govern the motion of viscous fluids by accounting for the balance of momentum under the influence of pressure, viscous stresses and external forces. The context we are interested in is bubbles immersed in a fluid. In which case these equations describe the interaction between the bubble interface and the surrounding flow, which is affected by surface tension, viscosity and pressure gradients, and in some cases, fluid compressibility.

Consider a position vector $\boldsymbol{x}$. For compressible Newtonian fluids with a velocity field $\boldsymbol{u}(\boldsymbol{x}, t)$ and a pressure field $p(\boldsymbol{x}, t)$, the equations of motion must include variations in density, $\rho(\boldsymbol{x}, t)$, a dynamic variable. The full set of compressible

Navier–Stokes equations is

$$\rho\left(\frac{\partial \boldsymbol{u}}{\partial t}+\boldsymbol{u}\cdot\nabla\boldsymbol{u}\right)=-\nabla p+\nabla\cdot\boldsymbol{\tau}+\boldsymbol{f}\,, \tag{2.1.1a}$$

$$\frac{\partial \rho}{\partial t}+\nabla\cdot(\rho\boldsymbol{u})=0\,, \tag{2.1.1b}$$

$$\boldsymbol{\tau}=\mu\left(\nabla\boldsymbol{u}+\nabla\boldsymbol{u}^{\mathsf{T}}\right)+\left(\lambda-\frac{2}{3}\mu\right)(\nabla\cdot\boldsymbol{u})\,\boldsymbol{I}\,, \tag{2.1.1c}$$

where $\boldsymbol{\tau}$ is the viscous stress tensor, μ and λ are the shear and bulk viscosities, respectively, and $\boldsymbol{f}$ represents external body forces, for example, gravity.

Equation (2.1.1c) represents the constitutive relation for a *Newtonian fluid*, which is defined as a fluid where the local viscous stress is linearly proportional to the local rate of strain. In this context, the shear viscosity (also known as *dynamic viscosity*), μ, acts as the constant of proportionality. It measures a fluid's resistance to shear deformation under an applied shear stress (e.g. Esmaeilnezhad et al., 2017). Bulk viscosity, λ, also known as volume or second viscosity, is a measure of a fluid's resistance to volumetric changes, such as compression or expansion (e.g. Ding & Ye, 2006).

The dynamic (shear) viscosity μ and density ρ can be combined to define the *kinematic viscosity* ν via

$$\nu=\frac{\mu}{\rho}\,, \tag{2.1.2}$$

which characterises the diffusion of momentum in the fluid independently of its density. Equation (2.1.1a) encapsulates momentum conservation, whereas equation (2.1.1b) represents mass conservation. A detailed explanation and derivation of these equations can be found in the book *An introduction to fluid dynamics* by Batchelor (1967). For the purposes of our work, we will take $\boldsymbol{f}=\boldsymbol{0}$ from this point onward, i.e. we study fluids in the absence of external forces.

We will discuss the implications of a compressible fluid later on. But for now, we will only consider an incompressible fluid, which means that

$$\frac{\mathrm{D}\rho}{\mathrm{D}t} = 0\,, \tag{2.1.3}$$

where

$$\frac{\mathrm{D}}{\mathrm{D}t} = \frac{\partial}{\partial t} + \boldsymbol{u}\cdot\nabla\,, \tag{2.1.4}$$

is the material derivative, in which case the Navier–Stokes equations (2.1.1) reduce to

$$\rho\left(\frac{\partial \boldsymbol{u}}{\partial t} + \boldsymbol{u}\cdot\nabla\boldsymbol{u}\right) = -\nabla p + \mu\nabla^2\boldsymbol{u}\,, \tag{2.1.5a}$$

$$\nabla\cdot\boldsymbol{u} = 0\,. \tag{2.1.5b}$$

We take (2.1.5) as the starting point for a model of a nanobubble. Due to the spherical geometry of a bubble, it is natural to reformulate the equations in spherical polar coordinates (r, θ, ϕ), corresponding to the radial distance, polar angle and azimuthal angle, respectively (see Figure 2.1.1). In this coordinate system, the position vector is

$$\boldsymbol{x} = r\hat{\boldsymbol{r}}\,, \tag{2.1.6}$$

where $\hat{\boldsymbol{r}}$ denotes the outward radial unit vector. The full spherical basis consists of

$$\hat{\boldsymbol{r}} = \sin\theta\cos\phi\,\hat{\mathbf{i}} + \sin\theta\sin\phi\,\hat{\mathbf{j}} + \cos\theta\,\hat{\mathbf{k}}\,, \tag{2.1.7a}$$

$$\hat{\boldsymbol{\theta}} = \cos\theta\cos\phi\,\hat{\mathbf{i}} + \cos\theta\sin\phi\,\hat{\mathbf{j}} - \sin\theta\,\hat{\mathbf{k}}\,, \tag{2.1.7b}$$

$$\hat{\boldsymbol{\phi}} = -\sin\phi\,\hat{\mathbf{i}} + \cos\phi\,\hat{\mathbf{j}}\,, \tag{2.1.7c}$$

where $\hat{\mathbf{i}}, \hat{\mathbf{j}}, \hat{\mathbf{k}}$ are the Cartesian unit vectors along the $x-, y-$ and $z-$axes, respectively. These unit vectors given in (2.1.7) form an orthonormal set at each point in space.

In terms of this basis, the fluid velocity field can be written as

$$\boldsymbol{u}(r,\theta,\phi,t) = u_r(r,\theta,\phi,t)\hat{\boldsymbol{r}} + u_\theta(r,\theta,\phi,t)\hat{\boldsymbol{\theta}} + u_\phi(r,\theta,\phi,t)\hat{\boldsymbol{\phi}}\,, \tag{2.1.8}$$

which provides the natural decomposition of the Navier–Stokes equations in spherical coordinates for describing bubble dynamics.

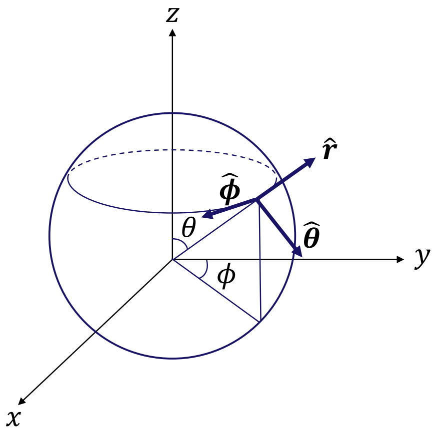

Figure 2.1.1: Diagram representing spherical polar coordinates.

We consider a nanobubble within the xylem of a plant, whose undisturbed radius is denoted by $r = a(t)$, where $a(t)$ is a periodic function of time with period T. The periodic variation of $a(t)$ may arise from pressure fluctuations in the xylem sap, which occur due to diurnal changes in transpiration and water transport (Ingram et al., 2023). Furthermore, periodicity can result from the intrinsic dynamics of the bubble, driven by the balance between surface tension, the surrounding fluid, and the gas pressure inside the bubble (Ingram et al., 2021).

To facilitate analysis, we decompose $a(t)$ into a time-averaged radius and a dimensionless oscillatory component:

$$a(t) = \overline{a}a^*(t)\,, \tag{2.1.9}$$

where

$$\overline{a} = \frac{1}{T}\int_0^T a(t)\mathrm{d}t\,, \tag{2.1.10}$$

is the mean radius over one period and $a^*(t)$ is the dimensionless radius capturing the temporal variation about the mean. This decomposition separates the characteristic length scale of the nanobubble from its oscillatory dynamics, which is particularly useful for nondimensionalisation.

To incorporate interfacial forces, we consider the surface tension of the bubble, denoted by σ. Surface tension is a physical property of a fluid interface that arises from the cohesive forces between molecules. Molecules at the surface experience an imbalance of intermolecular forces compared to those in the bulk, which creates a contractive effect that tends to minimise the surface area. In the context of bubbles, surface tension is responsible for maintaining the bubble's shape and stabilising the interface (Brennen, 1995). When the surface of the bubble is clean (that is, free of surfactants or contaminants), the surface tension takes a constant value $\sigma = \sigma_c$.

Given the physical parameters that we have, we will now perform a dimensional analysis of (2.1.5). We introduce the following characteristic scales:

- $\dfrac{\sigma_c}{\mu}$: velocity scale
- $\overline{a}$: length scale
- P: pressure scale
- $\dfrac{\overline{a}\mu}{\sigma_c}$: time scale.

Now we define dimensionless variables:

$$\boldsymbol{u}^* = \frac{\mu}{\sigma_c}\boldsymbol{u}\,, \qquad \boldsymbol{x}^* = \frac{1}{\overline{a}}\boldsymbol{x}\,, \qquad t^* = \frac{\sigma_c}{\overline{a}\mu}t\,, \qquad p^* = \frac{p}{P}\,, \tag{2.1.11}$$

and the derivatives become

$$\nabla = \frac{1}{\overline{a}}\nabla^*\,, \qquad \frac{\partial}{\partial t} = \frac{\sigma_c}{\overline{a}\mu}\frac{\partial}{\partial t^*}\,. \tag{2.1.12}$$

If we substitute the dimensionless variables (2.1.11) into (2.1.5a) we get

$$La\left(\frac{\partial \boldsymbol{u}^*}{\partial t} + \boldsymbol{u}^* \cdot \nabla \boldsymbol{u}^*\right) = -\frac{\overline{a}P}{\sigma_c}\nabla^* p^* + {\nabla^*}^2 \boldsymbol{u}^*\,, \tag{2.1.13}$$

where La is the Laplace number and is given by

$$La = \frac{\rho \sigma_c \overline{a}}{\mu^2} \,. \tag{2.1.14}$$

The Laplace number is a dimensionless quantity that characterises the relative importance of surface tension forces compared to viscous forces in a flow. It is particularly prevalent in the field of free surfaces, droplets and bubbles. See, for example, Martínez-Calvo et al. (2020). The Laplace number (La) is sometimes called the Suratman number (Su) in engineering literature. The name's appearance in the literature can be traced indirectly through Ryley (1962), who cites a 1955 paper by Van Der Leeden et al. (1955) — although that 1955 paper does not itself coin the term 'Suratman number'. For the sake of brevity, we will drop the * notation in (2.1.13) moving forward.

Based on whether La is large or small we choose a suitable pressure scale P. For small La we want to balance the pressure and viscous terms and make

$$\frac{\overline{a} P}{\sigma_c} = 1 \,, \tag{2.1.15}$$

and so we choose

$$P = \frac{\sigma_c}{\overline{a}} \,. \tag{2.1.16}$$

Making the substitution of (2.1.16) into (2.1.13) gives the non-dimensional Navier–Stokes equations in the form

$$La \left(\frac{\partial \boldsymbol{u}}{\partial t} + \boldsymbol{u} \cdot \nabla \boldsymbol{u} \right) = -\nabla p + \nabla^2 \boldsymbol{u} \,, \tag{2.1.17a}$$

$$\nabla \cdot \boldsymbol{u} = 0 \,. \tag{2.1.17b}$$

We observe that if we take the limit of $La \to 0$, (2.1.17) simplifies further. This limit may be realised when the characteristic bubble radius $\overline{a}$ is sufficiently small.

Representative physical parameter values for nanobubbles in plant xylem are summarised in Table 2.1. These values can then be used to estimate the corresponding Laplace number.

Parameter value	Approximate value in plant xylem
ρ	$1000\,\mathrm{kg\,m^{-3}}$
σ_c	$(19 \text{ to } 74) \times 10^{-3}\,N\,\mathrm{m}^{-1}$
$\overline{a}$	$50 \times 10^{-9}\,\mathrm{m}$
μ	$10^{-3}\,\mathrm{Pa\,s}$

Table 2.1: Table showing typical physical parameter values in the plant xylem. These values are taken from the literature, for example Rand (1983); Roth (1996); Ellerby & Ennos (1998); Losso et al. (2017); Yang et al. (2020).

Substituting the parameter values from Table 2.1 into (2.1.14) yields Laplace numbers in the approximate range $0.95 \lesssim La \lesssim 3.7$.

Smaller Laplace numbers, on the order of $La \sim 10^{-1}$, are possible for sufficiently small nanobubbles present in the xylem. In this regime, viscous forces dominate and the Stokes flow approximation is well justified. At the same time, the estimated range indicates that scenarios with $La \sim O(1)$ are also physically relevant, in which inertial and viscous effects are of comparable magnitude. Consequently, it is appropriate to consider both limits in the analysis, as will be done in this thesis.

For the case where $La \sim 10^{-1}$ in the xylem, we can reasonably take the limit $La \to 0$ in (2.1.17a) and we retrieve the Stokes equations of fluid flow

$$\nabla p = \nabla^2 \boldsymbol{u}\,, \tag{2.1.18a}$$

$$\nabla \cdot \boldsymbol{u} = 0\,, \tag{2.1.18b}$$

or, in dimensional form

$$\nabla p = \mu \nabla^2 \boldsymbol{u}\,, \tag{2.1.19a}$$

$$\nabla \cdot \boldsymbol{u} = 0\,. \tag{2.1.19b}$$

This is a classical result and can be found in many standard texts (see, for example, Batchelor, 1967). The Stokes equations form the basis of much of the analysis presented in this thesis, beginning in Chapter 4. However, in Chapter 6, the full Navier–Stokes equations will be used.

2.2 Newtonian stress tensor

At the interface between the gas inside the bubble (typically air) and the surrounding liquid, the dynamics are governed by a balance of forces. In particular, Newton's second law requires that the net force acting on an infinitesimal interfacial element be balanced by the surface forces acting upon it. This balance gives rise to the interfacial stress condition, which relates the stresses in the two fluids to the effects of surface tension.

Specifically, the stress balance across the interface is given by

$$\left(\boldsymbol{T}^{(2)} - \boldsymbol{T}^{(1)}\right) \cdot \hat{\boldsymbol{n}} = 2\kappa_m n\sigma\hat{\boldsymbol{n}} - \nabla_{\mathrm{s}}\sigma\,, \tag{2.2.1}$$

where $\boldsymbol{T}^{(1)}$ is the Newtonian stress tensor of the gas inside the bubble and $\boldsymbol{T}^{(2)}$ is the stress tensor of the water in the xylem, $\hat{\boldsymbol{n}}$ is the unit normal vector to the bubble surface, κ_m is the mean curvature of the bubble surface, σ is a measure of surface tension and ∇_{s} is the surface gradient operator given by (e.g. Stone & Leal, 1990)

$$\nabla_{\mathrm{s}} = (\boldsymbol{I} - \hat{\boldsymbol{n}}\hat{\boldsymbol{n}}) \cdot \nabla\,, \tag{2.2.2}$$

which projects the gradient onto the tangent plane of the interface. The stress tensors are defined as follows

$$\boldsymbol{T}^{(1,2)} \cdot \hat{\boldsymbol{n}} = (-p^{(1,2)}\boldsymbol{I}_n + 2\mu_{(1,2)}\boldsymbol{e}^{(1,2)}) \cdot \hat{\boldsymbol{n}}\,, \tag{2.2.3}$$

where μ_1 is the dynamic viscosity of the gas inside the bubble, μ_2 is the viscosity of the water and $\boldsymbol{I}_n$ is the identity matrix. The rate-of-strain tensor is defined in spherical polar coordinates as (e.g. Batchelor, 1967)

$$\boldsymbol{e} = \begin{pmatrix} e_{rr} & e_{r\theta} & e_{r\phi} \\ e_{\theta r} & e_{\theta\theta} & e_{\theta\phi} \\ e_{\phi r} & e_{\phi\theta} & e_{\phi\phi} \end{pmatrix} .$$

We nondimensionalise (2.2.1) $\boldsymbol{e}$, $\boldsymbol{T}^{(1,2)}$, p_G and κ_m as

$$\boldsymbol{e} = \left(\frac{\sigma_c}{\bar{a}\mu_2}\right)\boldsymbol{e}^* , \qquad \boldsymbol{T}^{(1,2)} = \left(\frac{\sigma_c}{\bar{a}}\right)\boldsymbol{T}^{(1,2)^*} \qquad \kappa_m = \frac{1}{\bar{a}}\kappa_m^* ,$$
$$\sigma = \sigma_c\sigma^* \qquad \text{and} \qquad \nabla_{\mathrm{s}} = \frac{1}{\bar{a}}\nabla_{\mathrm{s}}^* , \tag{2.2.4}$$

where $\boldsymbol{e}^*$, $\boldsymbol{T}^{(1,2)^*}$, κ_m^* and σ^* are non-dimensional quantities. The non-dimensional stress tensor of the gas is hence given by

$$\boldsymbol{T}^{(1)^*} = -p^{(1)^*}\boldsymbol{I} + 2\frac{\mu_1}{\mu_2}\boldsymbol{e}^* , \tag{2.2.5a}$$

and for the water in the xylem we have

$$\boldsymbol{T}^{(2)^*} = -p^{(2)^*}\boldsymbol{I} + 2\boldsymbol{e}^* . \tag{2.2.5b}$$

Substituting (2.2.4) and (2.2.5) into (2.2.1) gives us

$$\left[-p^{(2)^*}\boldsymbol{I} + p^{(1)^*}\boldsymbol{I} + 2\left(1 - \frac{\mu_1}{\mu_2}\right)\boldsymbol{e}^*\right] \cdot \hat{\boldsymbol{n}} = 2\kappa_m^*\sigma^*\hat{\boldsymbol{n}} - \nabla_{\mathrm{s}}^*\sigma^* . \tag{2.2.6}$$

By noting that the viscosity of the water is much greater than the viscosity of the gas in the bubble we have

$$\frac{\mu_1}{\mu_2} \ll 1 . \tag{2.2.7}$$

Also, we let $p^{(1)^*} = p_G$, where p_G denotes the pressure of the gas inside the bubble, and $p^{(2)^*} = p$, which is to be evaluated at the bubble surface, and

$$\boldsymbol{T}^* = -p\boldsymbol{I} + 2\boldsymbol{e}^* . \tag{2.2.8}$$

Therefore, (2.2.6) becomes

$$\boldsymbol{T} \cdot \hat{\boldsymbol{n}} + p_G \hat{\boldsymbol{n}} = 2\kappa_m \sigma \hat{\boldsymbol{n}} - \nabla_{\mathrm{s}} \sigma \,, \tag{2.2.9}$$

where we have dropped the * notation for the sake of brevity but all terms are non-dimensional.

2.3 Rayleigh–Plesset equation

Having established the Navier–Stokes equations, we now derive an equation governing the dynamics of an unperturbed bubble. In this idealised model, the bubble is assumed to remain perfectly spherical, with its interface described by $r = a(t)$. We will work in spherical polar coordinates as shown in Figure 2.1.1. We therefore begin with the Navier–Stokes equations (2.1.17), which are given by

$$La \left(\frac{\partial \boldsymbol{u}}{\partial t} + (\boldsymbol{u} \cdot \nabla) \boldsymbol{u} \right) = -\nabla p + \nabla^2 \boldsymbol{u} \,, \tag{2.3.1a}$$

$$\nabla \cdot \boldsymbol{u} = 0 \,, \tag{2.3.1b}$$

where we recall that La is the Laplace number. A general velocity field, in spherical polar coordinates, is in the form $\boldsymbol{u} = (u_r, u_\theta, u_\phi)$. For an unperturbed spherical bubble, by symmetry, it is reasonable to assume that the velocity field is of the form

$$\boldsymbol{u} = F(r,t) \hat{\boldsymbol{r}} \,,$$

where $F(r,t)$ is a function to be determined and $\hat{\boldsymbol{r}}$ is the unit vector in the radial direction. As a consequence, equation (2.3.1a) becomes

$$r\text{-direction}: \quad La \left(\frac{\partial F}{\partial t} + F \frac{\partial F}{\partial r} \right) = -\frac{\partial p}{\partial r} + \left[\frac{1}{r^2} \frac{\partial}{\partial r} \left(r^2 \frac{\partial F}{\partial r} \right) - \frac{2F}{r^2} \right] \,, \tag{2.3.2a}$$

$$\theta\text{-direction}: \quad 0 = -\frac{1}{r} \frac{\partial p}{\partial \theta} \,, \tag{2.3.2b}$$

$$\phi\text{-direction} \quad 0 = -\frac{1}{r \sin\theta} \frac{\partial p}{\partial \phi} \,, \tag{2.3.2c}$$

and equation (2.3.1b) becomes

$$\frac{1}{r^2}\frac{\partial}{\partial r}\left(r^2 F\right) = 0\,. \tag{2.3.3}$$

From equation (2.3.2b) and (2.3.2c) we can immediately deduce that the pressure p is a function of r and t only, that is $p = p(r,t)$.

In order for equation (2.3.3) to hold, the function F must be of the form

$$F(r,t) = \frac{A(t)}{r^2}\,, \tag{2.3.4}$$

where $A(t)$ is an arbitrary function to be determined. Substituting (2.3.4) into (2.3.2a) yields

$$La\left(\frac{1}{r^2}\frac{\mathrm{d}A}{\mathrm{d}t} - \frac{2A^2}{r^5}\right) = -\frac{\mathrm{d}p}{\mathrm{d}r}\,,$$

which we now integrate with respect to r to obtain

$$La\int_r^\infty \left(\frac{1}{r'^2}\frac{\mathrm{d}A}{\mathrm{d}t} - \frac{2A^2}{r'^5}\right)\mathrm{d}r' = -\int_r^\infty \frac{\mathrm{d}p}{\mathrm{d}r'}\,\mathrm{d}r'\,. \tag{2.3.5}$$

Solving equation (2.3.5) for p gives us

$$p = p_\infty + La\left(\frac{1}{r}\frac{\mathrm{d}A}{\mathrm{d}t} - \frac{A^2}{2r^4}\right)\,, \tag{2.3.6}$$

where p_∞ is the far-field pressure. To proceed, we require both dynamic and kinematic boundary conditions. The dynamic condition expresses the balance of forces prevailing at the interface between the gas in the bubble and the fluid outside. At the interface, Newton's second law applies. That is, the net force on an infinitesimal patch must be balanced by the surface forces.

The balance of normal and tangential forces at the bubble surface is expressed by the dynamic stress condition (2.2.9):

$$\boldsymbol{T}\cdot\hat{\boldsymbol{n}} + p_G\hat{\boldsymbol{n}} = 2\kappa_m\sigma\hat{\boldsymbol{n}} - \nabla_{\mathrm{s}}\sigma\,, \tag{2.3.7}$$

where $\boldsymbol{T}$ is a Newtonian stress tensor,

$$\boldsymbol{T} = -p\boldsymbol{I} + 2\boldsymbol{e}\,, \tag{2.3.8}$$

and $\boldsymbol{e}$ is the rate-of-strain tensor defined in spherical polar coordinates as

$$\boldsymbol{e} = \begin{pmatrix} e_{rr} & e_{r\theta} & e_{r\phi} \\ e_{\theta r} & e_{\theta\theta} & e_{\theta\phi} \\ e_{\phi r} & e_{\phi\theta} & e_{\phi\phi} \end{pmatrix},$$

where, in our case,

$$e_{rr} = \frac{\partial F}{\partial r}\,, \quad e_{\theta\theta} = e_{\phi\phi} = \frac{F}{r}\,, \quad e_{r\theta} = e_{r\phi} = e_{\theta r} = e_{\theta\phi} = e_{\phi r} = e_{\phi\theta} = 0\,.$$

The mean curvature of a smooth surface with normal vector $\hat{\boldsymbol{n}}$ can be calculated using the following equation, a detailed description of which can be found in Peters (2001),

$$\kappa_m = \frac{\nabla \cdot \hat{\boldsymbol{n}}}{2}\,,$$

where in the case of a spherical bubble $\hat{\boldsymbol{n}} = \hat{\boldsymbol{r}}$ and

$$\kappa_m = \frac{1}{2}\nabla \cdot \hat{\boldsymbol{r}} = \frac{1}{2}\left[\frac{1}{r^2}\frac{\partial}{\partial r}(r^2 \cdot 1)\right]_{r=a(t)} = \frac{1}{a} \tag{2.3.9}$$

at the bubble surface $r = a(t)$. The bubble surface has two mutually orthogonal tangential vectors, $\hat{\boldsymbol{t}}_1 = \hat{\boldsymbol{\theta}}$ and $\hat{\boldsymbol{t}}_2 = \hat{\boldsymbol{\phi}}$, which are both perpendicular to the normal vector $\hat{\boldsymbol{n}}$. By taking the dot product of (2.3.7) with $\hat{\boldsymbol{n}}$, $\hat{\boldsymbol{t}}_1$ and $\hat{\boldsymbol{t}}_2$, respectively, we obtain three component equations

$$2(\boldsymbol{e} \cdot \hat{\boldsymbol{n}}) \cdot \hat{\boldsymbol{n}} - p + p_G = \frac{2\sigma}{a}\,, \tag{2.3.10a}$$

$$2(\boldsymbol{e} \cdot \hat{\boldsymbol{n}}) \cdot \hat{\boldsymbol{t}}_1 = -\nabla_{\mathrm{s}}\sigma \cdot \hat{\boldsymbol{t}}_1\,, \tag{2.3.10b}$$

and

$$2(\boldsymbol{e} \cdot \hat{\boldsymbol{n}}) \cdot \hat{\boldsymbol{t}}_2 = -\nabla_{\mathrm{s}}\sigma \cdot \hat{\boldsymbol{t}}_2\,, \tag{2.3.10c}$$

where

$$\boldsymbol{e}\cdot\hat{\boldsymbol{n}} = \begin{pmatrix} \dfrac{\partial F}{\partial r} & 0 & 0 \\ 0 & \dfrac{F}{r} & 0 \\ 0 & 0 & \dfrac{F}{r} \end{pmatrix} \begin{pmatrix} 1 \\ 0 \\ 0 \end{pmatrix} = \begin{pmatrix} \dfrac{\partial F}{\partial r} \\ 0 \\ 0 \end{pmatrix} . \tag{2.3.11}$$

We will now simplify the problem by assuming that the surface tension does not vary on the surface of a bubble, thus $\nabla_{\mathrm{s}}\sigma = 0$. In physical terms, this means that we are ignoring the effects of surfactants. From this assumption, we can see that equations (2.3.10b) and (2.3.10c) are consistent. Equation (2.3.10a), using (2.3.11), becomes

$$p_G - p(a) + 2\frac{\partial F}{\partial r} = \frac{2\sigma}{a} , \tag{2.3.12}$$

noting that

$$\frac{\partial F}{\partial r} = -\frac{2A(t)}{r^3} ,$$

equation (2.3.12) can be rearranged to give

$$p(a) = p_G - \frac{4A}{a^3} - \frac{2\sigma}{a} . \tag{2.3.13}$$

The kinematic condition applies to any surface that is moving. Our surface shape is defined as $r - a = 0$ and it states that a particle sitting on the surface must move along with the fluid.

This requires the material derivative of the surface function to vanish at the bubble surface. This means

$$\frac{\mathrm{D}}{\mathrm{D}t}(r-a) = 0 ,$$

which leads to

$$-\frac{\partial a}{\partial t} + \left(\frac{A}{a^2}\hat{\boldsymbol{r}}\right)\cdot\left(\hat{\boldsymbol{r}}\frac{\partial}{\partial r}\right)(r-a) = -\frac{\mathrm{d}a}{\mathrm{d}t} + \frac{A}{a^2} = 0 . \tag{2.3.14}$$

From equation (2.3.14) we know that the function A is given by

$$A(t) = a^2\frac{\mathrm{d}a}{\mathrm{d}t} . \tag{2.3.15}$$

Substituting (2.3.15) into equations (2.3.6) and (2.3.13) we get

$$p(a) = p_\infty + La\left(a\frac{\mathrm{d}^2 a}{\mathrm{d}t^2} + \frac{3}{2}\left(\frac{\mathrm{d}a}{\mathrm{d}t}\right)^2\right) \tag{2.3.16}$$

and

$$p(a) = p_G - \frac{4}{a}\frac{\mathrm{d}a}{\mathrm{d}t} - \frac{2\sigma}{a}\,. \tag{2.3.17}$$

Equating equations (2.3.16) and (2.3.17), which eliminates p, and rearranging yields the following result

$$La\left(a\frac{\mathrm{d}^2 a}{\mathrm{d}t^2} + \frac{3}{2}\left(\frac{\mathrm{d}a}{\mathrm{d}t}\right)^2\right) + \frac{4}{a}\frac{\mathrm{d}a}{\mathrm{d}t} = \left(p_G(t) - p_\infty(t) - \frac{2\sigma}{a}\right)\,. \tag{2.3.18}$$

Equation (2.3.18) is called the Rayleigh–Plesset equation and it models the radius, a, of a bubble over time given specific physical parameters.

This agrees with the result derived by Plesset & Prosperetti (1977) by generalising the following equation for a bubble boundary $a(t)$, which was first derived by Rayleigh (1917), to include the effects of surface tension, liquid viscosity and non-constant p_∞

$$La\left(a\frac{\mathrm{d}^2 a}{\mathrm{d}t^2} + \frac{3}{2}\left(\frac{\mathrm{d}a}{\mathrm{d}t}\right)^2\right) = p(a) - p_\infty\,,$$

where again La is the Laplace number, p_∞ is the pressure in the liquid at a long distance from the bubble (i.e. a far-field condition) and $p(a)$ is the pressure of the liquid at the bubble surface.

2.4 Stability analysis

When we derive a bubble stability problem we will need to analyse the stability of systems of ordinary differential equations. Firstly, we will go over how the theory of eigenvalues and eigenvectors can be used to this end. The linear algebra used in this section is widely known and more details can be found in the literature, see for example Strang (2014).

Consider a system of ordinary differential equations with constant coefficients

$$\frac{\mathrm{d}\boldsymbol{x}}{\mathrm{d}t} = \boldsymbol{A}\boldsymbol{x}(t)\,, \tag{2.4.1}$$

where $\boldsymbol{x}(t) \in \mathbb{R}^n$ is a vector of n unknowns and $\boldsymbol{A} \in \mathbb{R}^{n\times n}$ is a constant matrix. Suppose we have the initial condition $\boldsymbol{x}(0) = \boldsymbol{x}_0$ then the solution to (2.4.1) is given by

$$\boldsymbol{x}(t) = e^{\boldsymbol{A}t}\boldsymbol{x}_0\,, \tag{2.4.2}$$

where the exponential matrix is given by

$$e^{At} = \boldsymbol{I}_n + \boldsymbol{A}t + \frac{1}{2!}(\boldsymbol{A}t)^2 + \frac{1}{3!}(\boldsymbol{A}t)^3 + ... + \frac{1}{k!}(\boldsymbol{A}t)^k + ...\,, \tag{2.4.3}$$

where the infinite series here can be shown to converge for all real numbers t. The Jordan Normal Form Theorem states that every square matrix $\boldsymbol{A} \in \mathbb{C}^{n\times n}$ is similar to a matrix in Jordan normal form. That is $\exists \boldsymbol{P} \in \mathbb{C}^{n\times n}$, which is invertible, such that

$$\boldsymbol{A} = \boldsymbol{P}\boldsymbol{J}\boldsymbol{P}^{-1}\,, \tag{2.4.4}$$

where $\boldsymbol{J}$ is a block-diagonal matrix of Jordan blocks and $\boldsymbol{P}$ is made up of eigenvectors and generalised eigenvectors of $\boldsymbol{A}$. Each Jordan block corresponds to one eigenvalue of $\boldsymbol{A}$, say λ_i, and has the form

$$\boldsymbol{J}_k(\lambda_i) = \begin{bmatrix} \lambda_i & 1 & 0 & ... & 0 \\ 0 & \lambda_i & 1 & ... & 0 \\ \vdots & \ddots & \ddots & \ddots & \vdots \\ 0 & ... & 0 & \lambda_i & 1 \\ 0 & ... & 0 & 0 & \lambda_i \end{bmatrix}_{k\times k} . \tag{2.4.5}$$

If all blocks are 1×1 (so that $J = \mathrm{diag}(\lambda_1, \lambda_2, ..., \lambda_n)$), then $\boldsymbol{A}$ is diagonalisable. Using (2.4.4) we can write (2.4.2) as

$$\boldsymbol{x}(t) = e^{\boldsymbol{P}\boldsymbol{J}\boldsymbol{P}^{-1}t}\boldsymbol{x}_0 = \boldsymbol{P}e^{\boldsymbol{J}t}\boldsymbol{P}^{-1}\boldsymbol{x}_0\,, \tag{2.4.6}$$

where each Jordan block has the exponential

$$e^{\boldsymbol{J}_k(\lambda_i)} = e^{\lambda_i t} \begin{bmatrix} 1 & t & \frac{t^2}{2!} & \dots & \frac{t^{k-1}}{(k-1)!} \\ 0 & 1 & t & \dots & \frac{t^{k-2}}{(k-2)!} \\ \vdots & \ddots & \ddots & \ddots & \vdots \\ 0 & 0 & \dots & 1 & t \\ 0 & 0 & \dots & 0 & 1 \end{bmatrix}_{k\times k} . \tag{2.4.7}$$

If $\boldsymbol{A}$ is not diagonalisable, that is we have at least one Jordan block of size at least 2, then this introduces t, t^2, ... polynomial terms that cause polynomial growth when eigenvalues have zero real part.

If $\boldsymbol{A}$ is diagonalisable and admits a full set of linearly independent eigenvectors $\{\boldsymbol{v}_1, ..., \boldsymbol{v}_n\}$ with corresponding eigenvalues $\{\lambda_1, ..., \lambda_n\}$ then the general solution to (2.4.1) can be expressed as

$$\boldsymbol{x}(t) = \sum_{i=1}^{n} c_i \boldsymbol{v}_i e^{\lambda_i t} , \tag{2.4.8}$$

where the constants c_i are determined by the initial condition $\boldsymbol{x}(0) = \boldsymbol{x}_0$ and λ_i are, in general, complex.

The eigenvalues λ_i of the matrix $\boldsymbol{A}$ play a fundamental role in determining the stability properties of the system (2.4.1), as summarized in Table 2.2. For the solutions of (2.4.1) to remain bounded, all eigenmodes must be stable. If any eigenmode is unstable, the corresponding solution grows without bound, and the system is considered unstable.

Eigenvalue behaviour	Maximum Jordan block size	Stability of mode
$\text{Re}(\lambda_i) < 0$	any size	Stable
$\text{Re}(\lambda_i) = 0$	size 1	Marginally stable
$\text{Re}(\lambda_i) = 0$	size ≥ 2	Unstable
$\text{Re}(\lambda_i) > 0$	any size	Unstable

Table 2.2: Table summarising how different values of $\text{Re}(\lambda_i)$, where Re denotes the real part, affects the stability of a system of ordinary differential equations.

2.5 Floquet theory

Floquet theory is a powerful mathematical framework used to analyse the stability and behaviour of solutions to linear differential equations with periodic coefficients. Named after the French mathematician Gaston Floquet, who introduced it in 1883 (Floquet, 1883), the theory provides insight into the dynamics of systems governed by linear time-periodic differential equations, which frequently arise in physics, engineering, and applied mathematics. The information in this section comes from Iooss & Joseph (1980) and Glendinning (1994). We wish to analyse a system where the coefficient matrix $\boldsymbol{A}$ is a periodic function, with period T, of time such that

$$\frac{\mathrm{d}\boldsymbol{x}}{\mathrm{d}t} = \boldsymbol{A}(t)\boldsymbol{x}\,, \qquad \boldsymbol{A}(t+T) = \boldsymbol{A}(t)\,, \tag{2.5.1}$$

for $t \in \mathbb{R}$. First, we consider the simplest case, i.e. $x \in \mathbb{R}$. Then

$$\frac{\mathrm{d}x}{\mathrm{d}t} = A(t)x\,, \qquad A(t) = A(t+T)\,, \tag{2.5.2}$$

which can be integrated immediately to obtain

$$x(t) = x_0 \exp\left\{\int_0^t A(t')\,\mathrm{d}t'\right\}\,. \tag{2.5.3}$$

Hence we say that

$$\phi(t) = \exp\left\{\int_0^t A(t')\,\mathrm{d}t'\right\} \tag{2.5.4}$$

is a fundamental solution for the problem with $x(t) = \phi(t)x_0$. Since we have

$$\int_0^{t+T} A(t')\,\mathrm{d}t' = \int_0^T A(t')\,\mathrm{d}t' + \int_T^{t+T} A(t')\mathrm{d}t'\,, \tag{2.5.5}$$

and using the periodicity of $A(t')$, $A(t') = A(t'+T)$,

$$\int_T^{t+T} A(t')\,\mathrm{d}t' = \int_0^t A(t')\,\mathrm{d}t'\,, \tag{2.5.6}$$

we have

$$\begin{aligned}\phi(t+T) &= \left(\exp\left\{\int_0^T A(t')\,\mathrm{d}t'\right\}\right)\left(\exp\left\{\int_T^{t+T} A(t')\,\mathrm{d}t'\right\}\right)\\ &= \phi(T)\phi(t)\,,\end{aligned} \tag{2.5.7}$$

and in particular, by induction on n,

$$\phi(nT) = \phi(T)^n\,. \tag{2.5.8}$$

The quantity $\phi(T)$, that is, the value of the solution after one period, is called the *Floquet multiplier*. It is convenient to write

$$\phi(T) = e^{sT}\,, \tag{2.5.9}$$

where s is called the *Floquet exponent* and may in general be complex. It is important to note that s is not uniquely defined, since the logarithm is multivalued. In particular,

$$s = \frac{1}{T}\log\phi(T) + \frac{2k\pi\mathrm{i}}{T}\,, \tag{2.5.10}$$

for any integer k. In the context of a system linearised around a *periodic orbit*, the origin of this linear system corresponds to the orbit itself. To determine its stability, we examine the growth or decay of perturbations by factoring out an exponential term from the solution. To this end, we define

$$v(t) = \phi(t)e^{-st}\,. \tag{2.5.11}$$

We then compute

$$v(t+T) = \phi(t+T)e^{-s(t+T)} = \phi(t)e^{-st}\,, \tag{2.5.12}$$

since $\phi(t+T)e^{-sT} = \phi(t)$. Hence, $v(t+T) = v(t)$ and therefore $v(t)$ is periodic and bounded. Putting this all together, we have

$$x(t) = \phi(t)x_0 = v(t)e^{st}x_0 \,. \tag{2.5.13}$$

Therefore, if $\mathrm{Re}(s) < 0$ solutions tend to zero, whilst if $\mathrm{Re}(s) > 0$ solutions are unbounded as $t \to \infty$.

We now generalise the idea of Floquet exponents to $\mathbb{R}^n$. To do this we go through the same process as before but we consider the equation

$$\frac{\mathrm{d}\boldsymbol{x}}{\mathrm{d}t} = \boldsymbol{A}(t)\boldsymbol{x} \,, \qquad \boldsymbol{x} \in \mathbb{R}^n \,, \qquad \boldsymbol{A}(t) = \boldsymbol{A}(t+T) \,. \tag{2.5.14}$$

Let $\boldsymbol{\Phi}(t)$ be the *fundamental matrix* of (2.5.14). A fundamental matrix is an $n \times n$ matrix whose columns consist of n linearly independent solution vectors of the system; it essentially maps any initial condition $\boldsymbol{x}(0)$ to its state at time t via the relation $\boldsymbol{x}(t) = \boldsymbol{\Phi}(t)\boldsymbol{x}(0)$. For our purposes, we define $\boldsymbol{\Phi}(t)$ such that it satisfies $\boldsymbol{\Phi}(0) = \boldsymbol{I}_n$, where $\boldsymbol{I}_n$ is the $n \times n$ identity matrix. The Floquet multipliers are then the eigenvalues of the matrix $\boldsymbol{\Phi}(T)$.

Since $\boldsymbol{\Phi}(t)$ is a fundamental matrix, we have that

$$\frac{\mathrm{d}}{\mathrm{d}t}\boldsymbol{\Phi}(t) = \boldsymbol{A}(t)\boldsymbol{\Phi}(t) \,. \tag{2.5.15}$$

Upon substituting $t+T$ into (2.5.15) we get

$$\frac{\mathrm{d}}{\mathrm{d}t}\boldsymbol{\Phi}(t+T) = \boldsymbol{A}(t+T)\boldsymbol{\Phi}(t+T) = \boldsymbol{A}(t)\boldsymbol{\Phi}(t+T) \,, \tag{2.5.16}$$

as $\boldsymbol{A}(t)$ is periodic. Therefore, we know that $\boldsymbol{\Phi}(t+T)$ is also a fundamental matrix of (2.5.14) and

$$\boldsymbol{\Phi}(t+T) = \boldsymbol{\Phi}(t)\boldsymbol{C} \,, \tag{2.5.17}$$

where $\boldsymbol{C}$ is a constant matrix. By setting $t = 0$ and using the condition $\boldsymbol{\Phi}(0) = I_n$

we determine that $\boldsymbol{C} = \boldsymbol{\Phi}(T)$ which means (2.5.17) becomes

$$\boldsymbol{\Phi}(t+T) = \boldsymbol{\Phi}(t)\boldsymbol{\Phi}(T)\,, \tag{2.5.18}$$

and, in particular, by induction on m,

$$\boldsymbol{\Phi}(mT) = \boldsymbol{\Phi}(T)^m\,. \tag{2.5.19}$$

Now let λ_k be the eigenvalues of $\boldsymbol{\Phi}(T)$ and $\boldsymbol{e}_k$ the corresponding eigenvectors. Here we will assume that the eigenvalues are all distinct. If not, we will need a more general approach like that set up in (2.4.4). The (λ_k) are called the Floquet multipliers and if $\lambda_k = e^{s_k T}$ then s_k is a Floquet exponent. As in the one-dimensional case, s_k is defined only up to multiples of $2\pi\mathrm{i}/T$.

Now we let

$$\boldsymbol{x}_0 = \sum_{k=1}^{n} a_k \boldsymbol{e}_k\,, \tag{2.5.20}$$

for constant a_k and recall that $\boldsymbol{x}(t) = \boldsymbol{\Phi}(t)\boldsymbol{x}_0$ for the particular choice of fundamental matrix made above. Hence, using (2.5.18)

$$\begin{aligned}\boldsymbol{x}(t+T) = \boldsymbol{\Phi}(t+T)\boldsymbol{x}_0 &= \boldsymbol{\Phi}(t)\boldsymbol{\Phi}(T)\left(\sum_{k=1}^{n} a_k \boldsymbol{e}_k\right)\\ &= \boldsymbol{\Phi}(t)\left(\sum_{k=1}^{n} e^{s_k T} a_k \boldsymbol{e}_k\right)\,.\end{aligned} \tag{2.5.21}$$

Let $\boldsymbol{x}_k(t) = \boldsymbol{\Phi}(t)a_k\boldsymbol{e}_k$, $1 \le k \le n$, so $\boldsymbol{x}_k(t+T) = e^{s_k T}\boldsymbol{x}_k(t)$. By analogy with the one-dimensional case, we define $\boldsymbol{v}_k = e^{-s_k t}\boldsymbol{x}_k(t)$. Then

$$\boldsymbol{v}_k(t+T) = e^{-s_k(t+T)}\boldsymbol{x}_k(t+T) = e^{-s_k t}\boldsymbol{x}_k(t) = \boldsymbol{v}_k(t)\,, \tag{2.5.22}$$

so every component of $\boldsymbol{v}_k(t)$ is periodic with period T. Furthermore,

$$\boldsymbol{x}(t) = \sum_{k=1}^{n} \boldsymbol{x}_k(t) = \sum_{k=1}^{n} e^{s_k t}\boldsymbol{v}_k(t)\,, \tag{2.5.23}$$

from which we can conclude, as in the one-dimensional case, that if all $\mathrm{Re}(s_k) < 0$

then (2.5.23) is asymptotically stable. However, if any $\mathrm{Re}(s_k) > 0$ then some solutions diverge to infinity.

3

Optimisers

3.1 Introduction to optimisers

Optimisation plays an important role in science and engineering, underpinning efforts to identify the most efficient, cost-effective or accurate solutions to complex problems. The goal of an optimiser is to find the best solution, whether a maximum or a minimum, from a set of feasible solutions. Optimisation problems can be classified into:

- Local Optimisation: finds the best solution in a nearby region of the solution space.
- Global Optimisation: aims to find the absolute best solution across the entire solution space, often in the presence of many local optima.

Whether in design, such as a wind farm layout (Yang & Cho, 2019); control, such as adaptive control of a DC–DC converter (Alqudah et al., 2014); machine learning, such as for microstructures (Shang et al., 2023); or physics-based modelling, such as in computational fluid dynamics (Owoyele et al., 2021), the ability to find optimal parameters or configurations is often critical to system performance. However, many real-world optimisation problems are non-convex, high-dimensional, and riddled with multiple local optima, posing significant challenges to conventional gradient-based or deterministic methods. This has led to the development and application of global optimisation algorithms, which are capable of exploring the solution space more thoroughly and avoiding premature convergence to suboptimal solutions.

3.2 An overview of global optimisers

Among the diverse family of global optimisation methods, Genetic Algorithms (GA) and Simulated Annealing (SA) stand out as two of the most prominent and widely applied approaches. Inspired by natural processes, biological evolution in the case of GA and the physical annealing process in SA, both algorithms use stochastic exploration mechanisms to navigate complex landscapes. Unlike local methods (e.g., gradient descent or Newton-Raphson), global optimisers do not rely on gradient information, which makes them suitable for noisy or non-differentiable functions. Their performance is often measured in terms of robustness (ability to avoid local minima), exploration–exploitation balance, and convergence speed.

Global optimisation techniques include metaheuristic algorithms such as Genetic Algorithms, Simulated Annealing, Particle Swarm Optimisation, Differential Evolution, and others. These algorithms use randomness in the search process to avoid premature convergence and to increase the likelihood of discovering the global optimum.

3.3 Genetic Algorithms

3.3.1 Origins and theory

Genetic Algorithms were first proposed by John Holland and colleagues in the 1970s at the University of Michigan, inspired by the principles of natural selection and evolutionary biology (Holland, 1975). GAs mimic the process of natural evolution, in which populations of organisms evolve over generations through mechanisms such as selection, crossover, and mutation.

3.3.2 How GA works

The basic workflow of a Genetic Algorithm involves the following steps:

1. Initialisation: a population of candidate solutions (chromosomes) is generated, either randomly or using a seeding strategy.
2. Evaluation: each candidate is assessed using a fitness function, which quantifies its quality with respect to the optimisation objective.
3. Selection: individuals with higher fitness are more likely to be selected for reproduction. Common strategies include roulette wheel, tournament, and rank-based selection.
4. Crossover (Recombination): pairs of selected individuals exchange segments of their structure to produce offspring, inheriting traits from both parents.
5. Mutation: with a small probability, parts of a chromosome are altered to introduce variability.
6. Replacement: the new generation replaces the old one and the cycle repeats.

Over successive generations, the population is expected to converge toward an optimal solution. Genetic Algorithms are widely used in engineering design, neural network optimisation, robot path planning, and multi-objective optimisation. Zigunov et al. (2022) use GA to optimise active flow control in cold and hot supersonic jets to minimise noise. Katoch et al. (2021) wrote a comprehensive review of the development and future of GAs discussing operators, variants, applications, strengths, and limitations.

3.4 Simulated annealing

Simulated Annealing was introduced by Scott Kirkpatrick, C. Daniel Gelatt, and Mario Vecchi (Kirkpatrick et al., 1983) as a probabilistic technique for approximating the global optimum of a function. The method is inspired by the physical process of annealing in metallurgy, where a material is heated and then slowly cooled to reduce defects and achieve a stable crystalline structure.

The underlying theory draws on statistical mechanics, specifically the

Metropolis–Hastings algorithm, a Markov Chain Monte Carlo (MCMC) method, which defines the probability of accepting a higher-energy state (i.e., a worse solution) to escape local minima (Metropolis et al., 1953).

In SA, it is adapted to control the acceptance of new solutions based on the change in the objective function (or "energy") ΔE, and a temperature parameter T:

$$P(\text{accept}) = \begin{cases} 1\,, & \text{if} \quad \Delta E \leq 0 \quad \text{(better solution)} \\ \exp\left(-\dfrac{\Delta E}{T}\right)\,, & \text{if} \quad \Delta E > 0 \quad \text{(worse solution)} \end{cases}\,, \tag{3.4.1}$$

where

- $\Delta E = E_{\text{new}} - E_{\text{current}}$
- T is the current temperature
- P is the probability of accepting a solution called the *Metropolis criterion.*

Equation (3.4.1) is inspired by the Boltzmann distribution from thermodynamics, which models the probability of a system being in a state with energy E

$$P(E) \propto \exp\left(-\frac{E}{kT}\right)\,. \tag{3.4.2}$$

In optimisation, the Boltzmann constant k is set to 1 for simplicity where the objective function is analogous to the energy of a physical system and the degree of randomness allowed is analogous to temperature.

The consequence of (3.4.1) is that better solutions are always accepted and worse solutions are accepted with a probability that depends on how much worse they are and the current temperature. The benefit of accepting worse solutions is that it promotes broader *exploration* of the solution space and helps prevent the algorithm from becoming trapped in local minima. As the temperature, T, decreases (cooling), the algorithm narrows its search as it hones in on one area — this is called *exploitation.*

3.4.1 How SA works

Simulated Annealing proceeds as follows:

1. Initialisation: start with an initial solution and an initial temperature T_0.
2. Neighbour Generation: generate a small perturbation of the current solution (a neighbour).
3. Evaluation: compute the change in objective function ΔE.
4. Acceptance Criterion: if $\Delta E < 0$, accept the new solution. If $\Delta E > 0$, accept it with probability $\exp(-\Delta E/T)$.
5. Cooling Schedule: gradually reduce the temperature, typically using exponential or logarithmic decay.
6. Termination: stop when the temperature is sufficiently low or a set number of iterations is reached.

3.4.2 Implementation considerations

When implementing SA you should consider the following key factors:

- Initial temperature, T_0: this affects exploration range.
- Cooling schedule: determines the rate of temperature decay.
- Neighbourhood function: defines how new solutions are generated.
- Stopping criteria: this can be based on temperature, iteration count or convergence.

Chikasue & Furukawa (2015) use SA as a numerical scheme to relax vorticity fields by preserving specified invariants in an incompressible neutral flow (without a magnetic field) and its magnetohydrodynamics (MHD). Suman & Kumar (2006) provide a comprehensive review of SA-based optimisation algorithms.

3.5 Finding the best pub in Norwich analogy

Here we compare how GA and SA would use exploration and exploitation for the problem of finding the best pub in the city of Norwich. It is said that the fine city of Norwich once had a pub for every day of the year.

Genetic Algorithm

- Exploration:

  Consider a group of friends all exploring the city.

  - Each person in the group tries pubs in different districts of Norwich.
  - They meet up, share their experiences (crossover) and sometimes one person tries a completely unexpected place (mutation).
  - This keeps the group from getting stuck in one area too soon.

- Exploitation:

  As time passes, the group starts revisiting the districts with their most highly rated pubs and trying similar ones nearby.

Simulated Annealing

- Exploration:

  Now consider that you are exploring. At first you're adventurous; you'll try almost any pub, even if the last one was bad. This is like high temperature: you're willing to take big risks and large detours.

- Exploitation:

  Over time, you get tired and more picky. In which case, you stick close to the best area you've found so far, occasionally taking a short walk to test a new spot nearby. This is like low temperature, which means low risk taking.

The key difference between the GA and SA approaches is that GA explores using a population and diversity from crossover and mutation (i.e. multiple people search in parallel) whereas SA explores with one search path, controlled by temperature. This slowly transitions from wide exploration to narrow exploitation. A key similarity is that you end up a bit drunk by the end of the process!

3.6 Applying GA and SA to a model

Consider the classic predator-prey model given by the Lotka-Volterra system (Lotka, 1925; Volterra, 1926). The variable x is the population density of prey (e.g., the number of rabbits per square mile) and the variable y is the population density of some predator (e.g. the number of foxes per square mile).

$$\frac{\mathrm{d}x}{\mathrm{d}t} = \alpha x - \beta x y\,, \tag{3.6.1a}$$

$$\frac{\mathrm{d}y}{\mathrm{d}t} = -\gamma y + \delta x y\,, \tag{3.6.1b}$$

where t is time and the unknown parameters are $\theta = [\alpha, \beta, \gamma, \delta]$. The prey parameters, α and β, describe the maximum growth and death rate of prey per capita and the effect of the presence of predators on the death rate of the prey, respectively. The predator parameters, γ and δ, describe the maximum death and growth of predators per capita and the effect of the presence of prey on the predator growth rate, respectively.

The system (3.6.1) is to be integrated forward in time starting from the initial condition $(x_{\mathrm{sim}}(0), y_{\mathrm{sim}}(0)) = (x_{\mathrm{sim},0}, y_{\mathrm{sim},0})$ to obtain the simulated solution $(x_{\mathrm{sim}}(t), y_{\mathrm{sim}}(t))$. If we have given observational data $x_{\mathrm{data}}(t_i)$ and $y_{\mathrm{data}}(t_i)$ for the set of time points $\{t_0, t_1, ..., t_N\}$, $t_0 = 0$, we can use GA and SA to estimate the values of θ such that the solution to (3.6.1), $x_{\mathrm{sim}}(t_i;\theta)$ and $y_{\mathrm{sim}}(t_i;\theta)$ provides the best fit to the given data. To do this, we set the objective function, $E(\theta)$ such that

$$E(\theta) = \sum_{i=0}^{N} \left((x_{\mathrm{sim}}(t_i;\theta) - x_{\mathrm{data}}(t_i))^2 + (y_{\mathrm{sim}}(t_i;\theta) - y_{\mathrm{data}}(t_i))^2 \right) . \tag{3.6.2}$$

Following the procedures of GA and SA, the objective function $E(\theta)$ will be minimised and the values of α, β, γ and δ which give this minimum will be returned. You can also set parameter constraints to the algorithms. For example, you may want to impose that $\alpha + \gamma \geq 10$. This would mean that GA and SA would minimise $E(\theta)$ for all parameters θ such that $\alpha + \gamma \geq 10$.

This example serves as a simple but representative demonstration of how global optimisation algorithms can be applied to nonlinear dynamical systems through the construction and minimisation of an objective function. Although the Lotka–Volterra model is used here in a data-fitting context, the key idea is more general: GA and SA provide a systematic way to explore parameter space and identify parameter values that optimise a chosen quantity, even in the presence of nonlinear coupling and constraints.

In Chapter 4, this framework is adapted to the nanobubble stability problem, where the objective is not to fit data but to determine the maximum growth rate of coupled perturbations in the bubble radius and surfactant concentration, subject to physical parameter constraints. This example therefore illustrates the flexibility of global optimisation methods and motivates their use in a more complex setting where the quantity of interest arises directly from the governing equations rather than external observations.

4

Stability analysis for an axisymmetric bubble

Synopsis

The aim of this chapter is to derive a stability equation for a nanobubble in xylem. We use an idealised model which assumes that the bubble is a sphere, centred at the origin, in an infinite domain. Due to the geometry of the problem, we work in spherical polar coordinates (r, θ, ϕ), corresponding to the radial distance, polar angle and azimuthal angle, respectively.

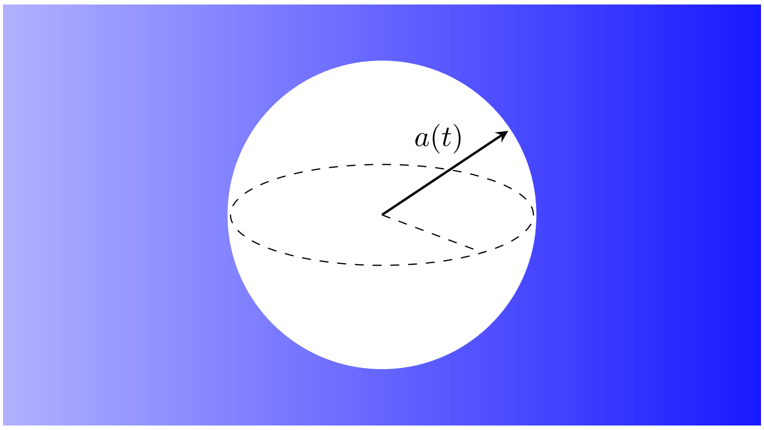

Figure 4.0.1: Schematic of a bubble of instantaneous radius $r = a(t)$ in an unbounded ambient viscous fluid.

4.1 Introduction

In this section, we assume that the Laplace number, La, is sufficiently small such that the effects of inertia are negligible in comparison to the effects of viscosity in the Navier–Stokes equation. As such, we will model the bubble using the non-dimensional Stokes equation. Given that the undisturbed radius of the bubble is $r = a(t)$ for some $a(t)$, the domain we are solving over is $r \in [a(t), \infty)$.

The equations of motion of the ambient fluid are given by (2.1.18)

$$\nabla p = \nabla^2 \boldsymbol{u}\,, \tag{4.1.1a}$$

$$\nabla \cdot \boldsymbol{u} = 0\,, \tag{4.1.1b}$$

where $\boldsymbol{u}$ is the velocity field and p is the pressure in the fluid. Using a well-known vector calculus identity, equation (4.1.1a) can be written as

$$\begin{aligned} \nabla p &= \nabla(\nabla \cdot \boldsymbol{u}) - \nabla \times (\nabla \times \boldsymbol{u}) && (4.1.2)\\ &= -\nabla \times (\nabla \times \boldsymbol{u})\,, && (4.1.3) \end{aligned}$$

where (4.1.1b) is substituted into (4.1.2) to obtain (4.1.3). The continuity equation (4.1.1b) allows us to introduce a Stokes stream function, $\psi(r, \theta, t)$, assuming that the flow is axisymmetric such that

$$\boldsymbol{u} = u_r(r, \theta, t)\hat{\boldsymbol{r}} + u_\theta(r, \theta, t)\hat{\boldsymbol{\theta}} + 0\hat{\boldsymbol{\phi}}\,, \tag{4.1.4}$$

where

$$u_r = \frac{1}{r^2 \sin\theta}\frac{\partial \psi}{\partial \theta}\,, \tag{4.1.5a}$$

$$u_\theta = -\frac{1}{r \sin\theta}\frac{\partial \psi}{\partial r}\,. \tag{4.1.5b}$$

Introducing a stream function reduces the axisymmetric vector problem to a scalar problem for the single variable $\psi(r, \theta, t)$. The relations in (4.1.5) can be written succinctly as

$$\boldsymbol{u} = \nabla \times \left(\frac{\psi}{r \sin\theta} \hat{\boldsymbol{\phi}} \right) , \tag{4.1.6}$$

using the definition of the curl for a vector field in spherical coordinates, $\boldsymbol{A} = A_r \hat{\boldsymbol{r}} + A_\theta \hat{\boldsymbol{\theta}} + A_\phi \hat{\boldsymbol{\phi}}$,

$$\begin{aligned} \nabla \times \boldsymbol{A} = & \frac{1}{r \sin\theta} \left(\frac{\partial}{\partial \theta} (A_\phi \sin\theta) - \frac{\partial A_\theta}{\partial \phi} \right) \hat{\boldsymbol{r}} + \frac{1}{r} \left(\frac{1}{\sin\theta} \frac{\partial A_r}{\partial \phi} - \frac{\partial}{\partial r} (r A_\phi) \right) \hat{\boldsymbol{\theta}} \\ & + \frac{1}{r} \left(\frac{\partial}{\partial r} (r A_\theta) - \frac{\partial A_r}{\partial \theta} \right) \hat{\boldsymbol{\phi}} . \end{aligned} \tag{4.1.7}$$

We now substitute the velocity field (4.1.6) into the Stokes equation (4.1.3) which gives us

$$\nabla p = -\nabla \times \nabla \times \nabla \times \left(\frac{\psi}{r \sin\theta} \hat{\boldsymbol{\phi}} \right) . \tag{4.1.8}$$

We can eliminate the pressure term, p, by taking the curl of equation (4.1.8), as $\nabla \times \nabla p = \boldsymbol{0}$, and obtain

$$\boldsymbol{0} = -\nabla \times \nabla \times \nabla \times \nabla \times \left(\frac{\psi}{r \sin\theta} \hat{\boldsymbol{\phi}} \right) . \tag{4.1.9}$$

It can be shown that

$$\nabla \times \nabla \times \left(\frac{\psi}{r \sin\theta} \hat{\boldsymbol{\phi}} \right) = \left(\frac{-D^2 \psi}{r \sin\theta} \hat{\boldsymbol{\phi}} \right) , \tag{4.1.10}$$

where

$$D^2 \equiv \frac{\partial^2}{\partial r^2} + \frac{1}{r^2} \frac{\partial^2}{\partial \theta^2} - \frac{\cos\theta}{r^2 \sin\theta} \frac{\partial}{\partial \theta} . \tag{4.1.11}$$

Thus, using the relation (4.1.10) on (4.1.9), we obtain the following equation governing the stream function ψ

$$D^4 \psi = D^2 (D^2 \psi) = 0 . \tag{4.1.12}$$

Once the solution to (4.1.12) is obtained it can then be substituted into (4.1.5) to give us the velocity profile, $\boldsymbol{u}$.

4.2 Formulating a Stokes stream function

The stream function formulation is a classical device in low Reynolds number hydrodynamics, going back to Stokes' nineteenth-century analysis and developed in detail in texts such as Happel & Brenner (1983). Its utility lies in reducing the vectorial Stokes system to a scalar one, particularly effective for axisymmetric flows.

To model how a gas-filled bubble behaves in the fluid we assume a basic-state flow driven by a source located at the centre of the bubble. Our aim is to assess the stability of the basic state by introducing infinitesimal axisymmetric perturbations of the form

$$\boldsymbol{u}(r,\theta,t) = \boldsymbol{u}_0(r,t) + \epsilon\boldsymbol{u}_1(r,\theta,t)\,, \tag{4.2.1}$$

where

$$\boldsymbol{u}_0(r,t) = u_r^{(0)}(r,t)\hat{\boldsymbol{r}} + u_\theta^{(0)}(r,t)\hat{\boldsymbol{\theta}}\,, \tag{4.2.2}$$

and

$$\boldsymbol{u}_1(r,\theta,t) = u_r^{(1)}(r,\theta,t)\hat{\boldsymbol{r}} + u_\theta^{(1)}(r,\theta,t)\hat{\boldsymbol{\theta}}\,, \tag{4.2.3}$$

where the subscripts 0 and 1 represent the basic and perturbed states respectively, which need to be determined, and ϵ is a small perturbation parameter. The Stokes stream function is perturbed as

$$\psi(r,\theta,t) = \psi_0(r,t) + \epsilon\psi_1(r,\theta,t)\,, \tag{4.2.4}$$

where $\epsilon \ll 1$. To obtain the basic state stream function, ψ_0, we consider a spherically symmetric potential $\Phi = \Phi(r)$ such that the basic state velocity is given by

$$\boldsymbol{u}_0 = \nabla\Phi\,. \tag{4.2.5}$$

By substituting (4.2.5) into (4.1.1b) we find Φ satisfies the Laplace equation such that

$$\nabla^2\Phi = \frac{1}{r^2}\frac{\mathrm{d}}{\mathrm{d}r}\left(r^2\frac{\mathrm{d}\Phi}{\mathrm{d}r}\right) = 0\,, \tag{4.2.6}$$

which yields the solution

$$\Phi(r) = -\frac{m}{r} + c\,, \tag{4.2.7}$$

where m and c are integration constants. This potential produces the radial velocity

$$\boldsymbol{u}_0 = \nabla\Phi = \frac{m}{r^2}\hat{\boldsymbol{r}} = u_{r,0}\hat{\boldsymbol{r}} \tag{4.2.8}$$

which corresponds to a source ($m > 0$) or a sink ($m < 0$) of strength m. By convention, $m = Q/4\pi$ where Q is the volume flux through the surface that encloses the source/sink.

In order to relate the flux Q to the radial velocity, we consider kinematic compatibility on the surface of the bubble, $r = a$. The kinematic boundary condition ensures that the bubble surface moves with the fluid, so that no fluid crosses it. A consequence of this is that the material derivative of the bubble surface must vanish at $r = a$, that is

$$\frac{\mathrm{D}}{\mathrm{D}t}(r-a) = 0\Big|_{r=a}\,. \tag{4.2.9}$$

From (4.2.9) we find that $u_{r,0}(r = a, t) = \dot{a}$, where the dot notation represents a derivative with respect to time, and hence $Q = 4\pi a^2\dot{a}$. Therefore, the velocity components of $\boldsymbol{u}_0$ are

$$u_r^{(0)} = \frac{a^2\dot{a}}{r^2} \qquad \text{and} \qquad u_\theta^{(0)} = 0\,. \tag{4.2.10}$$

Using the definition of the stream function, (4.1.5), and the calculated values of the velocity components of $\boldsymbol{u}_0$ (4.2.10), we get the following two partial differential equations (PDEs) for ψ_0

$$\frac{1}{r^2\sin\theta}\frac{\partial\psi_0}{\partial\theta} = \frac{a^2\dot{a}}{r^2}\,, \tag{4.2.11a}$$

and

$$-\frac{1}{r\sin\theta}\frac{\partial\psi_0}{\partial r}=0\,. \tag{4.2.11b}$$

From (4.2.11b) we can see that ψ_0 does not depend on r. Subsequently, solving (4.2.11a) gives us

$$\psi_0=-a^2\dot{a}\cos\theta+C(t)\,, \tag{4.2.12}$$

where we can take $C(t)=0$ as it is only a function of time and will not affect $u_{r,0}$ or $u_{\theta,0}$. This means that we can set our stream function to be

$$\psi=-a^2\dot{a}\cos\theta+\epsilon\psi_1(r,\theta,t)\,, \tag{4.2.13}$$

where ψ_1 is a function to be determined.

With the aim of simplifying the following calculations to find ψ_1, we now introduce the auxiliary variable

$$\xi=\cos\theta\in[-1,1]\,, \tag{4.2.14}$$

so that derivatives with respect to θ may be written compactly as

$$\frac{\partial}{\partial\theta}=-\sin\theta\frac{\partial}{\partial\xi}=-\sqrt{1-\xi^2}\frac{\partial}{\partial\xi}\,. \tag{4.2.15}$$

Using (4.2.15) we can write (4.1.11) as

$$D^2=\frac{\partial^2}{\partial r^2}+\frac{1-\xi^2}{r^2}\frac{\partial^2}{\partial\xi^2}\,, \tag{4.2.16}$$

and the velocity components (4.1.5a) and (4.1.5b) become

$$u_r=-\frac{1}{r^2}\frac{\partial\psi}{\partial\xi}\,, \tag{4.2.17a}$$

and

$$u_\xi=-\frac{1}{r\sqrt{1-\xi^2}}\frac{\partial\psi}{\partial r}\,. \tag{4.2.17b}$$

Returning to the stream function equation (4.1.12), we rewrite it in the form

$$D^2\psi = H\,, \tag{4.2.18}$$

where $H(r,\xi,t)$ satisfies

$$D^2 H = 0\,. \tag{4.2.19}$$

Thus, solving (4.2.19) allows us to subsequently determine ψ from (4.2.18).

Assuming an ansatz of the form $H(r,\xi,t) = A(r,t)B(\xi)$, substitution into (4.2.19) yields

$$\frac{\partial^2 A}{\partial r^2}B + \frac{1-\xi^2}{r^2}A\frac{\mathrm{d}^2 B}{\mathrm{d}\xi^2} = 0\,. \tag{4.2.20}$$

Proceeding via separation of variables, we obtain

$$\frac{r^2}{A}\frac{\partial^2 A}{\partial r^2} = -\frac{1-\xi^2}{B}\frac{\mathrm{d}^2 B}{\mathrm{d}\xi^2} = k, \tag{4.2.21}$$

for some separation constant k. This leads to the following ordinary differential equations for A and B:

$$r^2\frac{\partial^2 A}{\partial r^2} - kA = 0\,, \tag{4.2.22a}$$

$$(1-\xi^2)\frac{\mathrm{d}^2 B}{\mathrm{d}\xi^2} + kB = 0\,. \tag{4.2.22b}$$

Differentiating (4.2.22b) with respect to ξ gives

$$(1-\xi^2)\frac{\mathrm{d}^3 B}{\mathrm{d}\xi^3} - 2\xi\frac{\mathrm{d}^2 B}{\mathrm{d}\xi^2} + k\frac{\mathrm{d}B}{\mathrm{d}\xi} = 0\,. \tag{4.2.23}$$

Letting $k = \nu(1+\nu)$, where ν is a constant and $C = \dfrac{\mathrm{d}B}{\mathrm{d}\xi}$ we get

$$(1-\xi^2)\frac{\mathrm{d}^2 C}{\mathrm{d}\xi^2} - 2\xi\frac{\mathrm{d}C}{\mathrm{d}\xi} + \nu(1+\nu)C = 0\,, \tag{4.2.24}$$

which is precisely Legendre's equation of degree ν, with general solution

$$C(\xi) = a_1 P_\nu(\xi) + a_2 Q_\nu(\xi)\,, \tag{4.2.25}$$

where a_1 and a_2 are constants and P_ν and Q_ν are Legendre functions of the first and second kind, respectively.

For non-integer ν, the Legendre function $P_\nu(\xi)$ exhibits singular behaviour at $\xi = -1$, while $Q_\nu(\xi)$ is singular at both $\xi = \pm 1$. Since $\xi = \pm 1$ correspond to the poles of the spherical coordinate system, physical considerations require the solution to remain finite across the entire interval $\xi \in [-1, 1]$. This restricts admissible solutions to the case $\nu = n$, where n is a non-negative integer; in this case, $P_n(\xi)$ reduces to a polynomial that is regular at both poles. We therefore take $\nu = n$.

Integrating (4.2.25) with respect to ξ gives

$$B(\xi) = a_1 \mathscr{P}_n(\xi) + a_2 \mathscr{Q}_n(\xi) + \text{constant}\,, \tag{4.2.26}$$

where

$$\mathscr{P}_n(\xi) = \int_{-1}^{\xi} P_n(x)\,\mathrm{d}x\,, \qquad \mathscr{Q}_n(\xi) = \int_{-1}^{\xi} Q_n(x)\,\mathrm{d}x\,. \tag{4.2.27}$$

The Legendre functions of degree n are defined (see, for example, Abramowitz & Stegun, 1964) by Rodrigues' formula

$$P_n(\xi) = \frac{1}{2^n n!}\frac{\mathrm{d}^n(\xi^2-1)^n}{\mathrm{d}\xi^n}\,, \tag{4.2.28a}$$

$$Q_n(\xi) = \frac{1}{2}P_n(\xi)\ln\frac{1+\xi}{1-\xi} - W_{n-1}(\xi)\,, \tag{4.2.28b}$$

where

$$W_{n-1}(\xi) = \sum_{m=1}^{n}\frac{1}{m}P_{m-1}(\xi)P_{n-m}(\xi)\,, \tag{4.2.29}$$

$$W_{-1}(\xi) = 0\,. \tag{4.2.30}$$

Although $Q_n(\xi)$ has a logarithmic singularity at $\xi = \pm 1$, the integral defining $\mathscr{Q}_n(\xi)$ remains finite, so $\mathscr{Q}_n$ itself is well-defined. However, its derivative satisfies

$$\frac{\mathrm{d}\mathscr{Q}_n}{\mathrm{d}\xi} = Q_n(\xi)\,,$$

which diverges logarithmically at the poles. Since the velocity components are proportional to derivatives of the stream function (see (4.2.17)), any contribution from $\mathscr{Q}_n(\xi)$ would lead to unbounded velocities at $\xi = \pm 1$.

To ensure a physically admissible solution with finite velocity on the axis, we must therefore set $a_2 = 0$, retaining only the P_n contribution.

Finally, the remaining integration constant is arbitrary, as the stream function is only defined up to an additive constant. For convenience, we choose this constant such that

$$B(-1) = 0\,, \tag{4.2.31}$$

which sets a natural reference level for the stream function at the south pole ($\xi = -1$) without affecting the resulting velocity field.

This leaves us with the following solution for $B(\xi)$

$$B(\xi) = a_1 \mathscr{P}_n(\xi)\,. \tag{4.2.32}$$

Solving (4.2.22a) gives the following solution for A

$$A(r,t) = b_1(t) r^{-n} + b_2(t) r^{1+n}\,, \tag{4.2.33}$$

where $b_1(t)$ and $b_2(t)$ are arbitrary functions of t. This gives the following solution for H

$$H = (b_1(t) r^{-n} + b_2(t) r^{1+n}) \mathscr{P}_n(\xi)\,. \tag{4.2.34}$$

We now move on to present the solution to the original problem $D^4\psi = 0$, which is satisfied when $D^4\psi_1 = 0$, or

$$D^2\psi_1 = H\,. \tag{4.2.35}$$

We know that the complementary function of (4.2.35) is

$$\psi_{1,\mathrm{CF}} = \left(c_1(t) r^{-n} + c_2(t) r^{1+n}\right) \mathscr{P}_n(\xi) \tag{4.2.36}$$

where $c_1(t)$ and $c_2(t)$ are arbitrary functions of t. We find that the particular integral of (4.2.35) is

$$\psi_{1,\mathrm{PI}} = \frac{b_1(t)}{2-4n} r^{2-n} \mathscr{P}_n(\xi) + \frac{b_2(t)}{4n+6} r^{3+n} \mathscr{P}_n(\xi)\,. \tag{4.2.37}$$

Furthermore, we require that both u_r and u_ξ decay as $r \to \infty$. Referring to (4.2.17a) and (4.2.17b), we therefore demand that

$$\psi(r,\xi,t) \sim o(r^2) \qquad \text{as} \qquad r \to \infty\,. \tag{4.2.38}$$

Thus we need to take $b_2 = 0$ and $c_2 = 0$. Therefore, the general solution of (4.2.35) may be written as

$$\psi_1(r,\xi,t) = \sum_{n=0}^{\infty} \left(c_n(t) r^{-n} + d_n(t) r^{2-n} \right) \mathscr{P}_n(\xi)\,, \tag{4.2.39}$$

where $b_1(t) = (2-4n)d_n(t)$ and $c_n(t)$ and $d_n(t)$ are arbitrary functions of t that are to be determined.

4.3 Kinematic condition

To investigate the stability of a nanobubble to axisymmetric perturbations, we consider a small deformation of the bubble surface, which we write as

$$r = f(\xi,t)\,, \tag{4.3.1}$$

where

$$f(\xi,t) = a(t) + \epsilon \sum_{n=0}^{\infty} A_{1,n}(t) F_n(\xi)\,. \tag{4.3.2}$$

Here, $a(t)$ denotes the radius of the base-state bubble, ϵ is a small parameter with $\epsilon \ll 1$, and $A_{1,n}(t)$ is the amplitude of the first-order perturbation associated with the nth mode. The functions $F_n(\xi)$, where $\xi = \cos\theta$, describe the angular dependence of the perturbation which is to be determined below. In what follows, we analyse each mode separately.

Recall that the bubble radius can be decomposed as

$$a(t) = \overline{a}\, a^*(t)\,, \tag{4.3.3}$$

where $\overline{a}$ denotes the time-averaged bubble radius and $a^*(t)$ describes the dimensionless oscillatory variation. We take

$$a^*(t) = 1 + \Delta\cos(\omega t)\,, \tag{4.3.4}$$

where ω is the oscillation frequency and Δ is the oscillation amplitude, satisfying $0 \leq \Delta < 1$. The time-averaged bubble radius is defined by

$$\overline{a} = \frac{\omega}{2\pi}\int_0^{\frac{2\pi}{\omega}} a(t)\,\mathrm{d}t\,. \tag{4.3.5}$$

We non-dimensionalise (4.3.1) by defining

$$r = \overline{a}r^*\,, \quad t = \frac{\overline{a}\mu}{\sigma_c}t^*\,, \quad A_{1,n}(t) = \overline{a}A^*_{1,n}(t^*)\,, \quad f(\xi,t) = \overline{a}f^*(\xi,t^*)\,, \tag{4.3.6}$$

which gives us

$$r^* = f^*(\xi,t^*)\,, \tag{4.3.7}$$

where

$$f^*(\xi,t^*) = a^*(t^*) + \epsilon A^*_{1,n}(t^*)F_n(\xi)\,, \tag{4.3.8}$$

and

$$a^*(t^*) = 1 + \Delta\cos(Ca\,t^*)\,. \tag{4.3.9}$$

Taking the typical interfacial velocity scale to be $U \sim \overline{a}\omega$, the capillary number is given by

$$Ca = \frac{\mu\overline{a}\omega}{\sigma_c}\,. \tag{4.3.10}$$

This form arises by taking the characteristic velocity as the typical interface speed, $\overline{a}\omega$, rather than a steady flow velocity. The capillary number, Ca, quantifies the relative importance of viscous stresses to capillary forces under periodic forcing.

We will now drop the * notation.

We now seek a particular solution to (4.2.35) subject to the appropriate boundary conditions for the bubble problem. The kinematic condition encapsulates the requirement that the fluid velocity at the interface matches the motion of the interface itself. This is a standard starting point in free-boundary problems such as the stability of drops and bubbles, with precedent in classical works on interfacial dynamics by Prosperetti (1982) and others. Kinematic compatibility at the interface of the bubble $r = f(\xi, t)$ requires

$$\frac{\mathrm{D}}{\mathrm{D}t}(r - f) = 0\,, \tag{4.3.11}$$

at $r = f$. Expanding out (4.3.11) gives us

$$-\frac{\partial f}{\partial t} + u_r + \frac{u_\xi\sqrt{1-\xi^2}}{r}\frac{\partial f}{\partial \xi} = 0\bigg|_{r=f}\,. \tag{4.3.12}$$

At this stage, it is convenient to express the first-order stream function in separable form as

$$\psi_1(r, \xi, t) = G_n(r, t)\mathscr{P}_n(\xi)\,, \tag{4.3.13}$$

where

$$G_n(r, t) = c_n(t)r^{-n} + d_n(t)r^{2-n}\,, \tag{4.3.14}$$

The complete solution is obtained by summing over the modal index $n = 1, 2, \ldots.$ Substituting (4.2.17) into (4.3.12) and taking binomial expansions gives

$$\begin{aligned} &-\dot{a} - \epsilon\frac{\mathrm{d}A_{1,n}}{\mathrm{d}t}F_n(\xi) \\ &\quad - \frac{1}{a^2}\left(1 - \frac{2\epsilon}{a}A_{1,n}F_n(\xi)\right)\left(-a^2\dot{a} + \epsilon G_n(a,t)P_n(\xi)\right) + O(\epsilon^2) = 0\,. \end{aligned} \tag{4.3.15}$$

By linearising (4.3.15) with respect to ϵ we get the following amplitude evolution equation, which governs how $A_{1,n}$ behaves over time

$$\frac{\mathrm{d}A_{1,n}}{\mathrm{d}t} + \frac{2\dot{a}}{a}A_{1,n} = -\frac{1}{a^2}\frac{G_n(a,t)P_n(\xi)}{F_n(\xi)}\,. \tag{4.3.16}$$

The left-hand side of (4.3.16) depends only on t, whereas the right-hand side retains a dependence on ξ through the ratio $P_n(\xi)/F_n(\xi)$. For the equation to hold for all ξ, this ratio must be independent of ξ, which requires $F_n(\xi)$ to be proportional to $P_n(\xi)$.

This reflects the underlying structure of the governing equations: for axisymmetric disturbances, separation of variables leads to Legendre polynomials as the natural basis for the angular dependence. Consequently, all perturbation quantities inherit this ξ-dependence. We therefore take the angular dependence of all perturbation fields to be given by $P_n(\xi)$ and proceed by analysing each mode n separately.

4.4 Pressure term

In incompressible Stokes flow, the momentum equation can be simplified by introducing a stream function and taking its curl, which eliminates the pressure term and reduces the problem to a single equation for the velocity field. While this approach efficiently provides the velocity distribution, the pressure is still required to evaluate interfacial stresses.

Once the velocity field is determined from the stream function, the pressure can be recovered by returning to the original Stokes equation (4.1.8)

$$\nabla p = -\nabla \times \left(\frac{-D^2\psi}{r\sin\theta}\hat{\boldsymbol{\phi}} \right) . \tag{4.4.1}$$

In view of the angular structure established above, it is natural to seek the pressure in a consistent separated form. We therefore write

$$p = p_0 + \epsilon \sum_{n=0}^{\infty} p_{1,n}(r,t) P_n(\xi) \,, \tag{4.4.2}$$

where we recall that $P_n(\xi)$ is the Legendre polynomial of degree n. The orthogonality of the Legendre polynomials ensures that each mode evolves independently. Accordingly, we fix a particular mode n and suppress the subscript, writing $p_1(r,t)$ in place of $p_{1,n}(r,t)$ for notational convenience.

We now substitute (4.4.2) into (4.4.1) and linearise with respect to ϵ. At $O(1)$ we find

$$\nabla p_0 = 0\,. \tag{4.4.3}$$

Consequently, $p_0(t)$ is spatially uniform and depends only on t. At $O(\epsilon)$ we find

$$\frac{\partial p_1}{\partial r} P_n(\xi)\hat{\boldsymbol{r}} - \frac{\sin\theta}{r} p_1 P_n'(\xi)\hat{\boldsymbol{\theta}} = -\frac{1}{r^2}\frac{\partial(D^2\psi_1)}{\partial\xi}\hat{\boldsymbol{r}} - \frac{1}{r\sin\theta}\frac{\partial(D^2\psi_1)}{\partial r}\hat{\boldsymbol{\theta}}\,, \tag{4.4.4}$$

where the dash notation denotes a derivative with respect to ξ. From equation (4.2.18) we know that

$$D^2\psi_1 = (b_1(t)r^{-n} + b_2(t)r^{1+n})\mathscr{P}_n(\xi)\,, \tag{4.4.5}$$

where in an infinite domain we take $b_2 = 0$. Also, from (4.2.22b) we know that

$$\mathscr{P}_n(\xi) = -\frac{1-\xi^2}{n(n+1)}P_n'(\xi)\,, \tag{4.4.6}$$

where $P_n'(\xi) = \mathscr{P}_n''(\xi)$. Substituting (4.4.5) and (4.4.6) into (4.4.4) and taking the $\hat{\boldsymbol{r}}$ and $\hat{\boldsymbol{\theta}}$ components, respectively, gives us

$$\frac{\partial p_1}{\partial r} = -b_1(t)r^{-(2+n)}\,, \tag{4.4.7a}$$

and

$$p_1 = \frac{b_1(t)}{n+1}r^{-(1+n)}\,. \tag{4.4.7b}$$

The $\hat{\boldsymbol{\theta}}$-component (4.4.7b) determines p_1 directly, while the $\hat{\boldsymbol{r}}$-component (4.4.7a) provides its radial derivative. Integrating (4.4.7a) with respect to r recovers (4.4.7b), up to an arbitrary function of t, which may be absorbed into the base pressure since only ∇p appears in the governing equations.

Conversely, differentiating (4.4.7b) with respect to r recovers (4.4.7a), confirming that the two equations are consistent. In particular, the $\hat{\boldsymbol{\theta}}$-component does not introduce an additional constraint but is automatically satisfied once the radial component is enforced.

This consistency reflects the fact that the pressure is a scalar field whose gradient must be compatible across components. Using $b_1(t) = (2 - 4n)d_n(t)$, the perturbed pressure is therefore

$$p_1(r,t) = \frac{2(1-2n)}{n+1} d_n(t) r^{-(1+n)} \,. \tag{4.4.8}$$

In a finite domain, where we take $b_2 = (4n + 6)f_n$ in (4.4.5), the perturbed pressure is given by

$$p_1(r,t) = \frac{2(1-2n)}{n+1} d_n(t) r^{-(1+n)} - \frac{2(2n+3)}{n} f_n(t) r^n \,. \tag{4.4.9}$$

4.5 Dynamic condition

The motion and deformation of a bubble are governed by the balance of forces at its interface. At the surface, the stresses exerted by the surrounding Newtonian fluid — arising from both pressure and viscous effects — must be balanced by interfacial forces, including surface tension and any contributions from surfactants.

When surfactants are present on a bubble, the surface tension is no longer constant but depends on the local surfactant concentration at the interface. For a bubble that oscillates, its surface area changes and the surfactant distribution evolves: expansion dilutes the surfactant layer, leading to an increase in surface tension, while contraction compresses the layer, reducing the surface tension. This dynamic coupling between area change and surface concentration creates gradients in surface tension, known as Marangoni stresses, which oppose fluid motion along the interface. In this way, the surface equation of state — such as the Langmuir model (Manikantan & Squires, 2020) — provides the crucial link between interfacial thermodynamics and the hydrodynamics of bubble motion.

The Langmuir equation of state relates the surface tension, σ, to the surfactant concentration, Γ, via

$$\sigma = \sigma_c + \mathcal{R}\mathcal{T}\Gamma_\infty \ln\left(1 - \frac{\Gamma}{\Gamma_\infty}\right), \tag{4.5.1}$$

where $\mathcal{R}$ is the ideal gas constant, $\mathcal{T}$ is the absolute temperature, Γ_∞ is the maximum packing concentration of surfactant on the interface, and σ_c is the clean surface tension.

Consistent with the angular structure identified previously, all perturbation quantities are expanded in terms of Legendre polynomials $P_n(\cos\theta)$. Accordingly, we write

$$\sigma(\theta, t) = \sigma_0(t) + \epsilon \sum_{n=0}^{\infty} \sigma_{1,n}(t) P_n(\cos\theta), \tag{4.5.2}$$

and

$$\Gamma(\theta, t) = \Gamma_0(t) + \epsilon \sum_{n=0}^{\infty} \Gamma_{1,n}(t) P_n(\cos\theta). \tag{4.5.3}$$

Substituting these expansions into (4.5.1) and linearising with respect to ϵ gives

$$\sigma_0(t) = \sigma_c + \mathcal{R}\mathcal{T}\Gamma_\infty \ln\left(1 - \frac{\Gamma_0(t)}{\Gamma_\infty}\right), \tag{4.5.4}$$

and, for each mode n,

$$\sigma_{1,n}(t) = -\mathcal{R}\mathcal{T}\Gamma_\infty \frac{\Gamma_{1,n}(t)}{\Gamma_\infty - \Gamma_0(t)}. \tag{4.5.5}$$

Since the Legendre modes are orthogonal, each mode evolves independently. In what follows, we therefore consider a fixed mode n and suppress the subscript, writing $\sigma_1(t)$ in place of $\sigma_{1,n}(t)$ for notational simplicity.

We non-dimensionalise (4.5.4) and (4.5.5) with respect to σ_c, the surface tension value of a clean bubble surface. This gives us

$$\sigma(\theta, t) = \sigma_c \sigma^*(\theta, t), \quad \sigma_0(t) = \sigma_c \sigma_0^*(t) \quad \text{and} \quad \sigma_1(t) = \sigma_c \sigma_1^*(t), \tag{4.5.6}$$

where the non-dimensional surface tension values are given by

$$\sigma_0^*(t) = 1 + \beta_s \ln\left(1 - \frac{\Gamma_0(t)}{\Gamma_\infty}\right) , \tag{4.5.7a}$$

and

$$\sigma_1^*(t) = -\beta_s \frac{\Gamma_1(t)}{\Gamma_\infty - \Gamma_0(t)} . \tag{4.5.7b}$$

The parameter β_s, which is given by

$$\beta_s = \frac{\mathcal{R}\mathcal{T}\Gamma_\infty}{\sigma_c} , \tag{4.5.7c}$$

is a dimensionless measure of the effectiveness of the surfactant, comparing the maximum surface pressure contribution of a saturated monolayer to the surface tension of the clean interface. A larger β_s means that the surfactant has a stronger ability to lower surface tension relative to the baseline value.

At this stage, the surfactant concentration Γ is retained in dimensional form. A consistent non-dimensionalisation of Γ will be introduced later in Section 4.8, where it is incorporated into the full coupled bubble–surfactant system. For the sake of brevity, we now drop the * notation.

The balance of normal and tangential forces at the surface is expressed by the dynamic stress condition derived in Chapter 2 (2.2.9)

$$\boldsymbol{T} \cdot \hat{\boldsymbol{n}} + p_G \hat{\boldsymbol{n}} = 2\kappa_m \sigma \hat{\boldsymbol{n}} - \nabla_{\mathrm{s}} \sigma , \tag{4.5.8}$$

where $\boldsymbol{T}$ is a Newtonian stress tensor given by (2.2.8),

$$\boldsymbol{T} = -p\boldsymbol{I} + 2\boldsymbol{e} , \tag{4.5.9}$$

p_G is the pressure of the gas inside the bubble, κ_m is the mean curvature of the surface, $\hat{\boldsymbol{n}}$ is the unit normal vector to the surface, $\boldsymbol{e}$ is the rate-of-strain tensor and

$$\nabla_{\mathrm{s}} = (\boldsymbol{I} - \hat{\boldsymbol{n}}\hat{\boldsymbol{n}}) \cdot \nabla ,$$

is the surface gradient operator, which projects the gradient onto the tangent plane of the interface. The unit normal vector to the perturbed surface (4.3.1), defined by $r - f(\xi, t) = 0$, where

$$f(\xi, t) = a(t) + \epsilon A_{1,n}(t) P_n(\xi)\,, \tag{4.5.10}$$

is given by

$$\hat{\boldsymbol{n}} = \left.\frac{\nabla(r-f)}{|\nabla(r-f)|}\right|_{r=f}. \tag{4.5.11}$$

Computing the gradient in spherical coordinates, where $\xi = \cos\theta$, yields

$$\nabla(r-f) = \hat{\boldsymbol{r}} + \frac{\sin\theta}{r}\frac{\partial f}{\partial \xi}\hat{\boldsymbol{\theta}}, \tag{4.5.12}$$

so that, upon evaluating at $r = f(\xi, t)$,

$$\hat{\boldsymbol{n}} = \left(1 + \left(\frac{\sin\theta}{f}\frac{\partial f}{\partial \xi}\right)^2\right)^{-1/2} \left(\hat{\boldsymbol{r}} + \frac{\sin\theta}{f}\frac{\partial f}{\partial \xi}\hat{\boldsymbol{\theta}}\right). \tag{4.5.13}$$

Substituting (4.5.10) into (4.5.13) and expanding for small ϵ we obtain, to $O(\epsilon)$,

$$\hat{\boldsymbol{n}} = \hat{\boldsymbol{r}} + \epsilon\,\frac{\sin\theta}{a}\,A_{1,n}(t)\,\frac{\mathrm{d}}{\mathrm{d}\xi}P_n\hat{\boldsymbol{\theta}} + \boldsymbol{O}(\epsilon^2)\,. \tag{4.5.14}$$

The corresponding unit tangent vector, $\hat{\boldsymbol{t}}$ is given by

$$\hat{\boldsymbol{t}} = \left.\frac{\hat{\boldsymbol{\phi}} \times \hat{\boldsymbol{n}}}{|\hat{\boldsymbol{\phi}} \times \hat{\boldsymbol{n}}|}\right|_{r=f}, \tag{4.5.15}$$

which is calculated to be

$$\hat{\boldsymbol{t}} = -\epsilon\frac{\sin\theta}{a}\frac{\mathrm{d}}{\mathrm{d}\xi}P_n(\xi)A_{1,n}\hat{\boldsymbol{r}} + \hat{\boldsymbol{\theta}} + \boldsymbol{O}(\epsilon^2)\,. \tag{4.5.16}$$

The mean curvature term in (4.5.8) is given by

$$2\kappa_m = \nabla\cdot\hat{\boldsymbol{n}}\big|_{r=f} = \nabla^2 r - \nabla^2(a + \epsilon A_{1,n}P_n(\xi))\big|_{r=f} \tag{4.5.17}$$

To simplify (4.5.17), we use the standard identity for Legendre polynomials in spherical coordinates (see, for example, Jackson, 1999, p. 110):

$$\nabla^2 P_n(\xi) = -\frac{n(n+1)}{r^2} P_n(\xi)\,. \tag{4.5.18}$$

Substituting (4.5.18) into (4.5.17) and evaluating at the perturbed interface $r = f$, we obtain

$$2\kappa_m = \frac{2}{a} + \frac{\epsilon A_{1,n}}{a^2}(n-1)(n+2)P_n(\xi) + O(\epsilon^2)\,. \tag{4.5.19}$$

Therefore, we can express the perturbation of the mean curvature, κ_m as

$$\kappa_m = \kappa_m^{(0)} + \epsilon \kappa_m^{(1)} A_{1,n} P_n(\xi)\,, \tag{4.5.20}$$

where

$$\kappa_m^{(0)} = \frac{1}{a} \qquad \text{and} \qquad \kappa_m^{(1)} = \frac{(n-1)(n+2)}{2a^2}\,. \tag{4.5.21}$$

The form of $\boldsymbol{e}$ in the Newtonian stress tensor (4.5.9) is given by

$$\boldsymbol{e} = \begin{pmatrix} e_{rr} & e_{r\theta} & e_{r\phi} \\ e_{\theta r} & e_{\theta\theta} & e_{\theta\phi} \\ e_{\phi r} & e_{\phi\theta} & e_{\phi\phi} \end{pmatrix}, \tag{4.5.22}$$

where, in axisymmetric spherical polar coordinates,

$$e_{rr} = \frac{\partial u_r}{\partial r}\,, \qquad e_{\theta\theta} = \frac{1}{r}\frac{\partial u_\theta}{\partial \theta} + \frac{u_r}{r}\,, \qquad e_{\phi\phi} = \frac{u_r}{r} + \frac{u_\theta \cot\theta}{r}\,,$$

$$e_{r\theta} = e_{\theta r} = \frac{r}{2}\frac{\partial}{\partial r}\left(\frac{u_\theta}{r}\right) + \frac{1}{2r}\frac{\partial u_r}{\partial \theta} \qquad \text{and} \qquad e_{\theta\phi} = e_{\phi\theta} = e_{\phi r} = e_{r\phi} = 0\,, \tag{4.5.23}$$

as per Batchelor (1967), p. 601. In the following sections we calculate the normal and tangential components of (4.5.8) for different given forms of $p_G(r)$. In doing so, we will obtain a pair of simultaneous equations for $c_n(t)$ and $d_n(t)$, which are the unknowns of our expression for $\psi_1(r, \xi, t)$ (4.2.39), for each case.

4.5.1 Constant bubble pressure

In this section, we assume that the pressure inside the gas bubble, p_G, remains constant. We linearise the normal and tangential components of (4.5.8) with respect to ϵ, using the perturbation expansions introduced previously.

Taking the normal component at $O(1)$ yields the basic state pressure

$$p_0 = p_G - \frac{2}{a}\sigma_0 - 4\frac{\dot{a}}{a}\,. \tag{4.5.24}$$

At $O(\epsilon)$, the normal component evaluated at the interface $r = a$ gives

$$\begin{aligned} -p_1(a,t) + 12\frac{\dot{a}}{a^2}A_{1,n} + \frac{2}{a^2}\left(\frac{2}{a}G_n - \frac{\partial G_n}{\partial r}\right) \\ = \frac{2\sigma_1}{a} + \frac{A_{1,n}}{a^2}(n-1)(n+2)\sigma_0\,, \end{aligned} \tag{4.5.25}$$

where $p_1(a,t)$ denotes the perturbation pressure evaluated at the interface. Here, $G_n(r,t)$ represents the radial dependence of the perturbation stream function ψ_1, given by (4.3.14),

$$G_n = c_n(t)r^{-n} + d_n(t)r^{2-n}\,, \tag{4.5.26}$$

where $c_n(t)$ and $d_n(t)$ are to be determined. Similarly, taking the tangential component of (4.5.8) at $O(\epsilon)$ and evaluating at $r = a$ yields

$$\begin{aligned} 3n(n+1)\frac{\dot{a}}{a}A_{1,n} + \frac{1}{2a^2}\left(a^2\frac{\partial^2 G_n}{\partial r^2} - 2a\frac{\partial G_n}{\partial r} + n(n+1)G_n\right) \\ = \frac{n(n+1)}{2}\sigma_1\,. \end{aligned} \tag{4.5.27}$$

Equations (4.5.25) and (4.5.27) provide a closed system for determining the coefficients $c_n(t)$ and $d_n(t)$, which will be solved in Section 4.6.1.

4.5.2 Adiabatic gas equation

In this section, we assume that the gas inside the bubble undergoes an adiabatic process, meaning that no heat is exchanged with the surrounding fluid. Under this assumption, the internal gas pressure satisfies the adiabatic law

$$p_G(r)V^{\gamma} = \bar{k}\,, \tag{4.5.28}$$

where $\bar{k}$ is a constant, V is the volume of the bubble and γ is the adiabatic index of the gas. This modelling assumption is commonly adopted in studies of bubble dynamics (see, for example, Wang et al., 2021). Note that in the special case $\gamma = 1$, (4.5.28) reduces to Boyle's law. We non-dimensionalise (4.5.28) by setting

$$p_G = \frac{\sigma_c}{\bar{a}} p_G^* \qquad \text{and} \qquad V = \bar{a}^3 V^*\,, \tag{4.5.29}$$

where p_G^* and V^* are dimensionless quantities. The non-dimensional version of (4.5.28) is hence given by

$$p_G^* {V^*}^{\gamma} = \frac{1}{\sigma_c \bar{a}^{3\gamma-1}} \bar{k}\,. \tag{4.5.30}$$

We will now drop the * notation. The volume of the bubble can be calculated using the divergence theorem

$$\iiint_V \nabla \cdot \boldsymbol{r}\, \mathrm{d}V = \iint_S \boldsymbol{r} \cdot \hat{\boldsymbol{n}}\, \mathrm{d}S\,, \tag{4.5.31}$$

where S is the surface of the bubble. In spherical coordinates $\boldsymbol{r} = r\hat{\boldsymbol{r}}$ and

$$\nabla \cdot \boldsymbol{r} = \frac{1}{r^2} \frac{\partial \left(r^2 \cdot r\right)}{\partial r} = 3\,. \tag{4.5.32}$$

So, from (4.5.31) we get that

$$V = \frac{1}{3} \iint_S r \hat{\boldsymbol{r}} \cdot \hat{\boldsymbol{n}}\, \mathrm{d}S\,, \tag{4.5.33}$$

where, if $r = f = a + \epsilon A_{1,n} P_n(\xi)$,

$$\hat{\boldsymbol{r}} \cdot \hat{\boldsymbol{n}} = \hat{\boldsymbol{r}} \cdot \left(\hat{\boldsymbol{r}} + \frac{\epsilon \sin\theta}{a} A_{1,n} P_n'(\xi) \hat{\boldsymbol{\theta}} \right) = 1\,. \tag{4.5.34}$$

Therefore, the volume of the bubble is given by

$$V = \frac{1}{3}\iint_S f \,\mathrm{d}S\,, \qquad \text{where} \qquad \mathrm{d}S = f^2 \sin\theta \,\mathrm{d}\phi \,\mathrm{d}\theta\,, \tag{4.5.35}$$

and so

$$V = \frac{1}{3}\int_0^{\pi}\int_0^{2\pi} \left(a + \epsilon A_{1,n} P_n(\xi)\right)^3 \sin\theta \,\mathrm{d}\phi \,\mathrm{d}\theta + O(\epsilon^2)\,. \tag{4.5.36}$$

Using the substitution $\xi = \cos\theta$ we get

$$V = \frac{4\pi a^3}{3} + 2\pi\epsilon a^2 A_{1,n}\mathscr{P}_n(1) + O(\epsilon^2)\,. \tag{4.5.37}$$

So, returning to (4.5.30) we obtain

$$p_G = \frac{1}{\sigma_c \bar{a}^{3\gamma-1}}\left(\frac{k}{a^{3\gamma}} - \frac{3\epsilon k\gamma A_{1,n}}{2a^{3\gamma+1}}\mathscr{P}_n(1)\right) + O(\epsilon^2)\,, \tag{4.5.38}$$

where $k = \bar{k}/\left(\frac{4\pi}{3}\right)^{\gamma}$ and

$$\mathscr{P}_n(1) = \int_{-1}^{1} P_n(x)\,\mathrm{d}x = \int_{-1}^{1} P_0(x)P_n(x)\,\mathrm{d}x\,,$$

as $P_0(x) = 1$. However, we know

$$\int_{-1}^{1} P_m(x)P_n(x)\,\mathrm{d}x = \frac{2}{2n+1}\delta_{m,n}\,, \tag{4.5.39}$$

where $\delta_{m,n}$ denotes the Kronecker delta, equal to 1 if $m = n$ and to 0 otherwise — see, for example, Abramowitz & Stegun (1964) pp. 773–774 — so we have

$$\mathscr{P}_n(1) = 2\delta_{n,0}\,. \tag{4.5.40}$$

The linearised normal and tangential components of (4.5.8) for the adiabatic gas case, evaluated at $r = a$, are given by

$$-p_1(a,t) + 12\frac{\dot{a}}{a^2}A_{1,n} + \frac{2}{a^2}\left(\frac{2}{a}G_n - \frac{\partial G_n}{\partial r}\right) \\ = \frac{2\sigma_1}{a} + \frac{A_{1,n}}{a^2}\left((n+2)(n-1)\sigma_0 + \frac{\mathcal{B}}{a^{3\gamma-1}}\delta_{n,0}\right), \qquad (4.5.41)$$

and

$$3n(n+1)\frac{\dot{a}}{a}A_{1,n} + \frac{1}{2a^2}\left(a^2\frac{\partial^2 G_n}{\partial r^2} - 2a\frac{\partial G_n}{\partial r} + n(n+1)G_n\right) \\ = \frac{\sigma_1 n(n+1)}{2}, \qquad (4.5.42)$$

where the dimensionless group $\mathcal{B}$ is defined by

$$\mathcal{B} = \frac{3k\gamma}{\sigma_c \bar{a}^{3\gamma-1}}. \qquad (4.5.43)$$

Equations (4.5.41) and (4.5.42) can be solved simultaneously to determine $c_n(t)$ and $d_n(t)$, and hence the perturbed stream function (6.2.6) for an adiabatic gas. This is carried out in Section 4.6.2.

4.6 Linear stability analysis of a bubble with constant base-state radius

We simplify the problem by assuming that the leading-order bubble radius remains constant, which corresponds to setting $\Delta = 0$ in (4.3.9) and thus $a = 1$. Additionally, we neglect the effects of surfactants by taking $\beta_s = 0$ in (4.5.7), so that $\sigma_0 = 1$, $\sigma_1 = 0$, and

$$\nabla_s \sigma = 0. \qquad (4.6.1)$$

For this simplified case, the amplitude evolution equation (4.3.16) reduces to

$$\frac{\mathrm{d}A_{1,n}}{\mathrm{d}t} = -G_n(1,t), \qquad (4.6.2)$$

where G_n is defined by (4.3.14) as

$$G_n = c_n r^{-n} + d_n r^{2-n} \,. \tag{4.6.3}$$

If $A_{1,n}(t)$ remains bounded, then our system is stable.

4.6.1 Stability condition for constant bubble pressure

First, we will consider again the case where p_G is a constant. We can solve (4.5.25) and (4.5.27) simultaneously to calculate $c_n(t)$ and $d_n(t)$. Hence, we find

$$d_n(t) = \frac{n(n+1)(n+2)(n-1)}{2(2n^2+1)} A_{1,n} \,. \tag{4.6.4}$$

and

$$c_n(t) = -\frac{(n+1)^2(n+2)(n-1)^2}{2(n+2)(2n^2+1)} A_{1,n} \,. \tag{4.6.5}$$

Substituting (4.6.4) and (4.6.5) into (4.6.3) and thence into (4.6.2) gives us an amplitude evolution equation which determines the stability of our system, namely

$$\frac{\mathrm{d}A_{1,n}}{\mathrm{d}t} = M_n A_{1,n} \,, \tag{4.6.6}$$

where

$$M_n = -\frac{(2n+1)(n+1)(n-1)}{2(2n^2+1)} \,. \tag{4.6.7}$$

We can make the following remarks about (4.6.6):

1. The gas pressure makes no $O(\epsilon)$ contribution, therefore the restoring effect is purely due to surface tension.

2. The $n = 1$ mode (rigid translation) is neutral because the geometric factor $(n-1)$ vanishes in (4.6.7).

3. The $n = 0$ mode (volume change) is unstable as the value of M_n in (4.6.7) is positive.

4.6.2 Stability condition for adiabatic gas case

Now we consider the adiabatic gas case where

$$p_G = k - \mathcal{B}A_{1,n}\delta_{n,0}\,. \tag{4.6.8}$$

Solving (4.5.41) and (4.5.42) simultaneously gives the following expressions for $c_n(t)$ and $d_n(t)$

$$d_n(t) = \frac{n(n+1)}{2(2n^2+1)}\left((n+2)(n-1) + \mathcal{B}\delta_{n,0}\right)A_{1,n}\,, \tag{4.6.9}$$

and

$$c_n(t) = -\frac{(n+1)^2(n-1)}{2(n+2)(2n^2+1)}\left((n+2)(n-1)\sigma_0 + \mathcal{B}\delta_{n,0}\right)A_{1,n}\,, \tag{4.6.10}$$

If we substitute (4.6.9) and (4.6.10) into (4.6.2) we obtain the following stability equation:

$$\frac{\mathrm{d}A_{1,n}}{\mathrm{d}t} = M_n A_{1,n}\,, \tag{4.6.11}$$

where

$$M_n = -\frac{(2n+1)(n+1)}{2(n+2)(2n^2+1)}\left((n+2)(n-1) + \mathcal{B}\delta_{n,0}\right)\,. \tag{4.6.12}$$

Some important remarks follow immediately from (4.6.11):

1. For $n \geq 1$ we have $\delta_{n,0} = 0$, so the gas pressure makes no $O(\epsilon)$ contribution and the restoring effect is purely due to surface tension.
2. The $n = 1$ mode (rigid translation) is neutral because the geometric factor $(n-1)$ vanishes in (4.6.12).
3. The $n = 0$ mode (volume change) requires separate treatment because the gas pressure perturbation enters at leading order through $\delta_{n,0} = 1$.

For the spherically symmetric mode $n = 0$, the requirement that the solution to

(4.6.11) remains bounded imposes a constraint on the governing parameters. In particular, boundedness requires

$$-2 + \mathcal{B} > 0\,, \tag{4.6.13}$$

where $\mathcal{B}$ is defined in (4.5.43) as

$$\mathcal{B} = \frac{3k\gamma}{\sigma_c\,\bar{a}^{3\gamma-1}}\,. \tag{4.6.14}$$

This condition can be rewritten as

$$a^{3\gamma-1} < \frac{3k\gamma}{2\sigma_0}\,. \tag{4.6.15}$$

In the special case $n = 0$ and $\gamma = 1$, this reduces to

$$a^2 < \frac{3k}{2\sigma_0}\,. \tag{4.6.16}$$

This inequality corresponds to the classical *Blake threshold* (see, for example, Atchley, 1989). Notably, in the present formulation, this condition arises naturally from the requirement that the perturbation solution remains bounded, thereby providing an alternative route to the Blake threshold distinct from the standard derivation based on the Rayleigh–Plesset equation.

4.6.3 Comparison with Rayleigh–Plesset analysis

The Rayleigh–Plesset equation (2.3.18) is given by

$$La\left(a\frac{\mathrm{d}^2a}{\mathrm{d}t^2} + \frac{3}{2}\left(\frac{\mathrm{d}a}{\mathrm{d}t}\right)^2\right) + \frac{4}{a}\frac{\mathrm{d}a}{\mathrm{d}t} = \left(p_G(t) - p_\infty - \frac{2\sigma}{a}\right)\,, \tag{4.6.17}$$

where $a(t)$ denotes the radius of a spherical bubble and p_∞ is the (constant) far-field pressure. We assume Boyle's law for the gas pressure in the bubble, p_G given by the leading-order term of (4.5.38) with $\gamma = 1$

$$p_G = \frac{k}{\sigma_c\bar{a}^2a^3}\,. \tag{4.6.18}$$

The Rayleigh–Plesset equation is derived from the Navier–Stokes equations and therefore incorporates inertial effects. In contrast, the amplitude evolution equation (4.6.11) is obtained under the Stokes flow approximation, which corresponds to neglecting inertia and is equivalent to taking the limit of vanishing Laplace number, $La \to 0$. To compare the growth rates predicted by these two descriptions, we analyse the Rayleigh–Plesset equation in the limit of small La.

To this end, we first rescale time according to

$$t = La\tau \,, \tag{4.6.19}$$

which isolates the slow inertial dynamics. Substituting this scaling into (4.6.17) yields

$$a\frac{\mathrm{d}^2 a}{\mathrm{d}\tau^2} + \frac{3}{2}\left(\frac{\mathrm{d}a}{\mathrm{d}\tau}\right)^2 + \frac{4}{a}\frac{\mathrm{d}a}{\mathrm{d}\tau} = La\left(\frac{k}{\sigma_c \bar{a}^2 a^3} - p_\infty - \frac{2\sigma}{a}\right) . \tag{4.6.20}$$

We now consider a small perturbation about an equilibrium radius a_0, writing

$$a = a_0 + \delta a_1 e^{\lambda\tau} \,, \tag{4.6.21}$$

where a_0 and a_1 are constants, λ is the growth rate and $\delta \ll 1$. Upon substituting (4.6.21) into (4.6.20) and collecting terms at $O(\delta)$ gives

$$O(\delta) \,:\, a_0\lambda\left(\lambda + \frac{4}{a_0^2}\right) = \frac{La}{a_0^2}\left(2\sigma - \frac{3k}{\sigma_c \bar{a}^2 a_0^2}\right) . \tag{4.6.22}$$

Since we are interested in the small-La regime, we expand the growth rate as

$$\lambda = \lambda_0 + \lambda_1 La + O(La^2) \,, \tag{4.6.23}$$

and substitute (4.6.23) into (4.6.22). Comparing coefficients of like powers of La, the $O(1)$ terms yield

$$a_0\lambda_0\left(\lambda_0 + \frac{4}{a_0^2}\right) = 0 \,, \tag{4.6.24}$$

from which we obtain two possible leading-order growth rates,

$$\lambda_0 = 0 \qquad \text{or} \qquad \lambda_0 = -\frac{4}{a_0^2}\,. \tag{4.6.25}$$

At $O(La)$ we obtain the following.

$$2a_0\lambda_0\lambda_1 + \frac{4\lambda_1}{a_0} = \frac{2}{a_0^2}\left(\sigma - \frac{3k}{2\sigma_c\overline{a}^2a_0^2}\right)\,. \tag{4.6.26}$$

If $\lambda_0 = 0$, equation (4.6.26) yields

$$\lambda_1 = \frac{1}{2a_0}\left(\sigma - \frac{3k}{2\sigma_c\overline{a}^2a_0^2}\right)\,, \tag{4.6.27}$$

and hence

$$\lambda = \frac{La}{2a_0}\left(\sigma - \frac{3k}{2\sigma_c\overline{a}^2a_0^2}\right) + O(La^2)\,. \tag{4.6.28}$$

Substituting (4.6.28) into (4.6.21) and reverting to the original time variable $t = La\tau$, we find that the growth rate in physical time is

$$\lambda = \frac{1}{2a_0}\left(\sigma - \frac{3k}{2\sigma_c\overline{a}^2a_0^2}\right) + O(La)\,. \tag{4.6.29}$$

This expression coincides with the growth rate obtained from the amplitude evolution equation (4.6.12) for $n = 0$ and $\gamma = 1$, upon setting $a_0 = 1$ and $\sigma = 1$ in (4.6.29). Thus, the slow mode of the Rayleigh–Plesset equation recovers the Stokes-flow stability criterion in the limit $La \to 0$.

The second solution,

$$\lambda_0 = -\frac{4}{a_0^2}\,, \tag{4.6.30}$$

corresponds to a rapidly decaying mode. Substituting this value of λ_0 into (4.6.26) yields

$$\lambda_1 = -\frac{1}{2a_0}\left(\sigma - \frac{3k}{2\sigma_c\overline{a}^2a_0^2}\right)\,, \tag{4.6.31}$$

so that

$$\lambda = -\frac{4}{a_0^2} + O(La)\,. \tag{4.6.32}$$

This mode represents fast viscous relaxation arising from the viscous damping term in the Rayleigh–Plesset equation and is independent of the pressure balance at leading order. It decays on an $O(1)$ timescale in τ, or equivalently on an $O(La)$ timescale in time t and therefore does not influence the long-time stability of the bubble. In the Stokes-flow limit $La \to 0$, this viscous mode dominates the short-time dynamics, while the slow inertial mode determines the onset of instability.

In summary, the linear stability analysis of the Rayleigh–Plesset equation reveals two distinct dynamical behaviours. The slow mode, associated with $\lambda_0 = 0$, describes the long-time evolution of the bubble radius and yields a growth rate that, in the small-La limit, reduces to the same expression obtained under the Stokes flow approximation. This slow mode represents the quasistatic balance between pressure and surface tension that controls the onset of instability, such as the classical Blake threshold (4.6.16) in cavitation theory. The fast mode, associated with $\lambda_0 = -4/a_0^2$, represents rapid viscous relaxation and decays on a much shorter timescale, independent of the pressure balance. Such separation of modes — a slow inertial/balance mode and a fast viscous damping mode — is a common feature in reduced models of bubble dynamics and has been observed in the literature on Rayleigh–Plesset dynamics and bubble stability analyses (see, for example, Carreras-Casanova & Vanhille, 2025).

4.6.4 Interpretation of the $n = 1$ mode as rigid motion

Recall that the radius of the bubble given by (4.3.1) is

$$r = a(t) + \epsilon A_{1,n} P_n(\cos\theta)\,. \tag{4.6.33}$$

We now show that the $n = 1$ mode corresponds to a rigid translation of the bubble, rather than a deformation of its shape. We know that the radius of the bubble for $n = 1$ is given by

$$r = R\,, \tag{4.6.34}$$

where

$$R = a + \epsilon A_{1,1} P_1(\cos\theta) = a + \epsilon A_{1,1}(t)\cos\theta\,. \tag{4.6.35}$$

If we assume that the interface $r = R$ translates in the z-direction by $c = \chi\epsilon$ where $\chi = O(1)$ then it must have a new centre at $z = c$ and a radius d — see Figure 4.6.1. If $d = a$, the bubble has undergone a rigid translation without any change in shape.

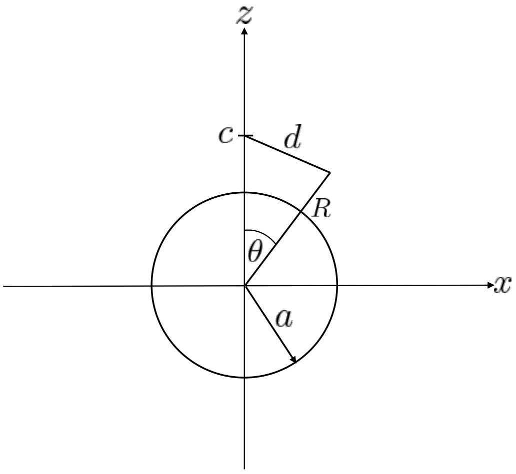

Figure 4.6.1: Diagram showing set-up for translating sphere in the $x - z$ plane.

Using the cosine rule, the distance d from the new centre to a point on the interface satisfies

$$d^2 = R^2 + c^2 - 2Rc\cos\theta\,. \tag{4.6.36}$$

Expanding R^2 gives

$$R^2 = a^2 + 2a\epsilon A_{1,1}\cos\theta + O(\epsilon^2)\,. \tag{4.6.37}$$

Substituting (4.6.37) into (4.6.36) and using $c = \epsilon\chi$, we obtain

$$d^2 = a^2 + 2\epsilon a\cos\theta(A_{1,1} - \chi) + O(\epsilon^2)\,,$$

Choosing $\chi = A_{1,1}$ we find that $d = a$, showing that the interface $r = R$ represents a rigid translation in the z-direction by a distance $\epsilon A_{1,1}$ without deforming its shape.

Since this mode represents rigid-body motion, we expect it not to evolve dynamically in the absence of external forcing. In particular, the normal velocity of the interface must vanish, which requires

$$\frac{\mathrm{d}A_{1,1}}{\mathrm{d}t} = 0\,. \tag{4.6.38}$$

This is consistent with equations (4.6.6) and (4.6.11), for $n = 1$, which show that (4.6.38) is satisfied for both the constant-pressure and adiabatic gas cases. That is, the bubble has the freedom to move from the origin without affecting its stability.

Having established this result analytically, we now illustrate the geometric interpretation of the perturbation. Figure 4.6.2 shows plots of the interface (4.6.33) for $n = 1, 2, 3$.

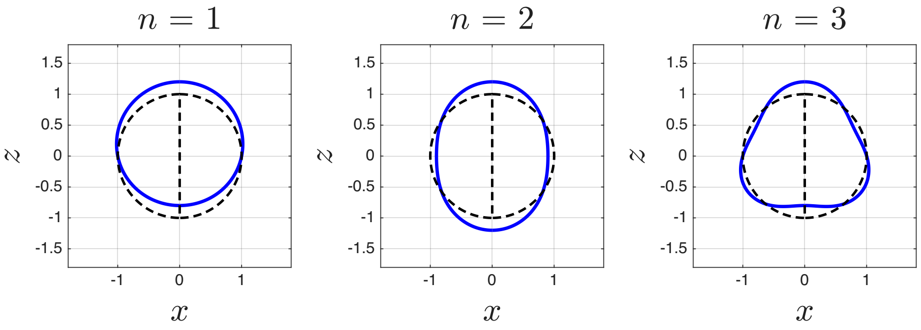

Figure 4.6.2: Plot of the perturbed bubble in the $x-y$ plane for $a(t) = 1$, $\epsilon = 0.2$ and $A_{1,1}(t) = 1$. The dashed circle shows the undisturbed initial bubble position and shape.

As predicted by the analysis above, the $n = 1$ mode corresponds to a rigid displacement of the bubble, while higher modes represent shape deformations.

4.6.5 Bubble dynamics in a finite geometry

In the previous sections, we analysed the stability of a gas bubble in an unbounded water domain. While this provides fundamental insight into the mechanisms governing bubble shape oscillations, it neglects an important geometric constraint present in biological systems. In particular, embolised gas bubbles in plant xylem vessels evolve within conduits of finite cross-section, bounded by rigid cell walls. The presence of these walls modifies the surrounding flow field and, consequently, the hydrodynamic stresses acting on the bubble interface. Motivated by this physical setting, we now extend our analysis to account for confinement effects by introducing a fixed, impermeable outer boundary.

We model the xylem conduit as a rigid spherical shell of radius $r = \beta a$, with $\beta > 1$, concentric with the bubble. The parameter β therefore quantifies the degree of confinement: large values of β recover the unbounded-domain limit, while smaller values correspond to stronger wall effects. This idealised geometry allows us to isolate the influence of finite domain size on the linear stability of the bubble without introducing additional geometric complexity.

To focus solely on confinement-induced hydrodynamic effects, we simplify the problem by assuming that the leading-order bubble radius remains constant in time. This corresponds to setting $\Delta = 0$ in (4.3.9), so that

$$a(t) = 1\,,$$

and the rigid spherical wall is located at

$$r = \beta\,.$$

Furthermore, we neglect the effects of interfacial surfactants by taking $\beta_s = 0$ in (4.5.7), which implies

$$\sigma_0 = 1\,, \qquad \sigma_1 = 0\,, \qquad \nabla_{\mathrm{s}}\sigma = 0\,.$$

Under these assumptions, the interface behaves as a clean surface with uniform surface tension.

The gas pressure inside the bubble is modelled by an adiabatic gas law of the form

$$p_G = k - \mathcal{B}A_{1,n}\delta_{n,0}\,,$$

where the Kronecker delta ensures that gas compressibility only affects the spherically symmetric mode $n = 0$.

The flow is described using a stream function,

$$\psi(r,\xi,t) = -a^2\dot{a}\,\xi + \epsilon\psi_1(r,\xi,t)\,, \tag{4.6.39}$$

which, for the present case $a = 1$, reduces to a purely perturbative contribution. For each spherical harmonic mode n, we write

$$\psi_1(r,\xi,t) = H_n(r,t)\mathscr{P}_n(\xi)\,,$$

where the general radial solution (4.3.14) in a finite domain is

$$H_n(r,t) = c_n(t)r^{-n} + d_n(t)r^{n+1} + e_n(t)r^{2-n} + f_n(t)r^{n+3}\,. \tag{4.6.40}$$

The four coefficients arise from the fourth-order radial operator governing Stokes flow.

At the rigid outer wall $r = \beta$, we impose no-slip and no-penetration conditions, which require the radial and polar velocities given by (4.2.17) to vanish such that

$$u_r = 0\,, \qquad u_\xi = 0 \qquad \text{on} \quad r = \beta\,,$$

which can be expressed equivalently in terms of the stream function as

$$\frac{\partial\psi}{\partial\xi} = 0\,, \qquad \frac{\partial\psi}{\partial r} = 0 \qquad \text{on} \quad r = \beta\,. \tag{4.6.41}$$

Substituting (4.6.39) and (4.6.40) into (4.6.41) yields the linear system

$$-nc_n\beta^{-(n+1)} + (n+1)d_n\beta^n + (2-n)e_n\beta^{1-n} + (n+3)f_n\beta^{n+2} = 0\,, \tag{4.6.42a}$$

$$c_n\beta^{-n} + d_n\beta^{n+1} + e_n\beta^{2-n} + f_n\beta^{n+3} = 0\,. \tag{4.6.42b}$$

Solving (4.6.42) simultaneously gives

$$c_n = \frac{2f_n\beta^{n+3} + (1-2n)e_n\beta^{2-n}}{(2n+1)\beta^{-n}}\,, \tag{4.6.43}$$

$$d_n = -\frac{2e_n\beta^{2-n} + (2n+3)f_n\beta^{n+3}}{(2n+1)\beta^{n+1}}\,, \tag{4.6.44}$$

which correctly eliminates two degrees of freedom.

The pressure perturbation associated with H_n is (4.4.9)

$$p_1 = \frac{2-4n}{n+1}d_n r^{-(n+1)} - \frac{4n+6}{n}f_n r^n\,,$$

which satisfies the Stokes equations in the bulk. At the bubble interface $r = 1$, the kinematic condition yields

$$\frac{\mathrm{d}A_{1,n}}{\mathrm{d}t} = -H_n(1,t)\,, \tag{4.6.45}$$

while the normal and tangential stress balances give

$$-p_1(a,t) + 2\left(2H_n - \frac{\mathrm{d}H_n}{\mathrm{d}r}\right) = \left((n-1)(n+2) + \mathcal{B}\delta_{n,0}\right)A_{1,n}\,. \tag{4.6.46}$$

and

$$\frac{\mathrm{d}^2H_n}{\mathrm{d}r^2} - 2\frac{\mathrm{d}H_n}{\mathrm{d}r} + n(n+1)H_n = 0\,, \tag{4.6.47}$$

Solving (4.6.46) and (4.6.47) simultaneously determines the remaining coefficients

e_n and f_n uniquely in terms of $A_{1,n}$, leading to the expressions quoted below.

$$c_n = \frac{n(n+1)\left[-\Lambda_1\beta^{2n+3} + (n-1)(n+1)\beta^{4n+2} + \Lambda_2\beta^{2n+1}\right] A_{1,n}\Pi}{(-\zeta_1\beta^{2n+3} - \zeta_2\beta^{4n+2} + \zeta_3\beta^{2n+1} - \zeta_4 - \zeta_5\beta^{2n-1})}\,, \tag{4.6.48}$$

$$d_n = \frac{n(n+1)\left[\Lambda_3\beta^{2n+3} - \Lambda_4\beta^{2n+1} + n(n+2)\right] A_{1,n}\Pi}{(-\zeta_1\beta^{2n+3} - \zeta_2\beta^{4n+2} + \zeta_3\beta^{2n+1} - \zeta_4 - \zeta_5\beta^{2n-1})}\,, \tag{4.6.49}$$

$$e_n = \frac{n(n+1)\left[-n(n+2)\beta^{4n+2} + \Lambda_4\beta^{2n+1} - \Lambda_3\beta^{2n-1}\right] A_{1,n}\Pi}{(-\zeta_1\beta^{2n+3} - \zeta_2\beta^{4n+2} + \zeta_3\beta^{2n+1} - \zeta_4 - \zeta_5\beta^{2n-1})}\,, \tag{4.6.50}$$

$$f_n = \frac{n(n+1)\left[-\Lambda_2\beta^{2n+1} - (n+1)(n-1) + \Lambda_1\beta^{2n-1}\right] A_{1,n}\Pi}{(-\zeta_1\beta^{2n+3} - \zeta_2\beta^{4n+2} + \zeta_3\beta^{2n+1} - \zeta_4 - \zeta_5\beta^{2n-1})}\,, \tag{4.6.51}$$

where

$$\Pi = (n+2)(n-1) + \mathcal{B}\delta_{n,0}\,, \tag{4.6.52}$$

$$\Lambda_1 = \frac{1}{2}(n-1)(n+1)(2n+1)\,, \tag{4.6.53}$$

$$\Lambda_2 = \frac{1}{2}n(n+2)(2n-1)\,, \tag{4.6.54}$$

$$\Lambda_3 = \frac{1}{2}n(n+2)(2n+1)\,, \tag{4.6.55}$$

$$\Lambda_4 = \frac{1}{2}(n+1)(n-1)(2n+3)\,, \tag{4.6.56}$$

$$\zeta_1 = n(n-1)(n+2)(n+1)(2n+1)^2\,, \tag{4.6.57}$$

$$\zeta_2 = 2n(n+2)(2n^2+1)\,, \tag{4.6.58}$$

$$\zeta_3 = 2n(n-1)(n+1)(n+2)(2n+3)(2n-1)\,, \tag{4.6.59}$$

$$\zeta_4 = 2(n-1)(n+1)(2n^2+4n+3)\,, \tag{4.6.60}$$

$$\zeta_5 = (2n+1)^2(n^4+2n^3-n^2-2n+3)\,. \tag{4.6.61}$$

$$\tag{4.6.62}$$

Substituting these results into (4.6.45) yields the linear amplitude evolution equation

$$\frac{\mathrm{d}A_{1,n}}{\mathrm{d}t} = \lambda_n(\beta)\,A_{1,n}\,, \tag{4.6.63}$$

where the growth rate $\lambda_n(\beta)$ is given explicitly by

$$\lambda_n(\beta) = \frac{n(n+1)(2n+1)\left[-\left(n+\frac{1}{2}\right)\beta^{2n+3} + \beta^{4n+2} - 1 + \left(n+\frac{1}{2}\right)\beta^{2n-1}\right]\Pi}{-\zeta_1\beta^{2n+3} - \zeta_2\beta^{4n+2} + \zeta_3\beta^{2n+1} - \zeta_4 - \zeta_5\beta^{2n-1}}\,. \tag{4.6.64}$$

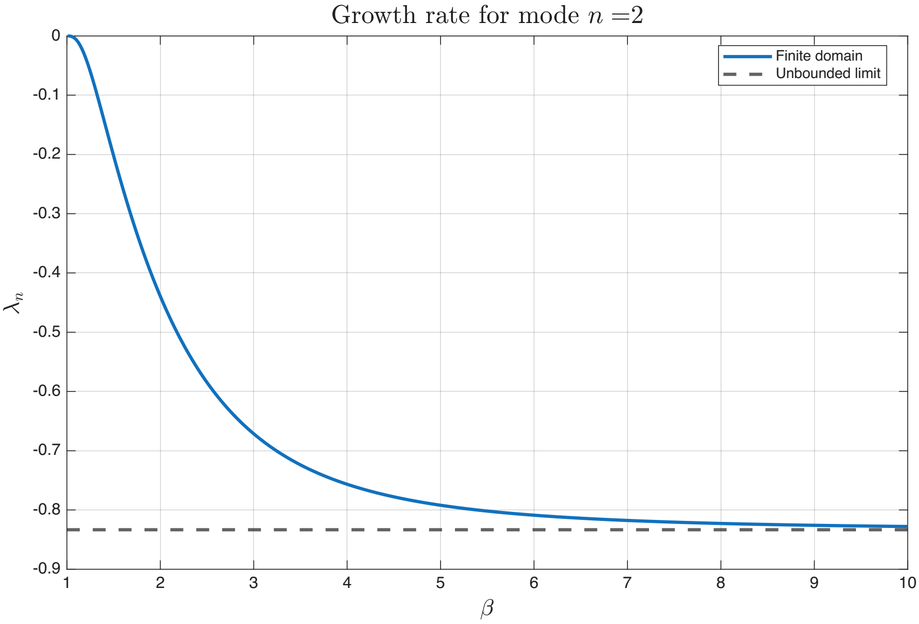

(a) Plot of equation (4.6.64) for $n = 2$.

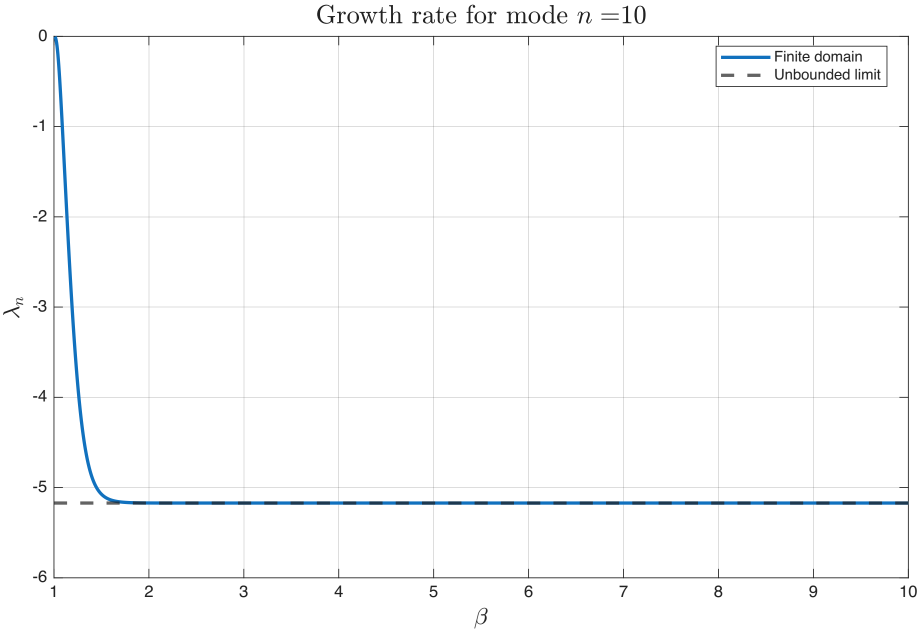

(b) Plot of equation (4.6.64) for $n = 10$.

Figure 4.6.3: Plots of how the growth rate λ_n varies as β increases from 1 for $n = 2$ and $n = 10$. The black dashed line is the limit given in (4.6.64).

The amplitude evolution equation (4.6.63) shows that the effect of confinement enters entirely through the dependence of the growth rate λ_n on the confinement parameter β. To assess the impact of the outer wall, we evaluate $\lambda_n(\beta)$ numerically for a range of mode numbers n and confinement ratios $\beta > 1$. The results for $n = 2$ and $n = 10$ are plotted in Figure 4.6.3.

Taking the limit as $\beta \to \infty$ in the expression for λ_n in (4.6.64) gives

$$\lambda_n \longrightarrow -\frac{(2n+1)(n+1)}{2(n+2)(2n^2+1)}\left((n+2)(n-1)+\mathcal{B}\delta_{n,0}\right) , \qquad \text{as} \quad \beta \to \infty \, . \tag{4.6.65}$$

For all modes n considered, the growth rate λ_n is found to be strictly negative for all $\beta > 1$, indicating that shape perturbations always decay in time. Moreover, for each such mode, λ_n is observed numerically to approach the limiting value (4.6.65) monotonically as β increases. While a general analytical proof of monotonicity for arbitrary n is not provided here, this behaviour has been consistently verified across all computed modes.

The limiting expression (4.6.65) exactly matches the growth rate obtained in the unbounded-domain analysis (4.6.12), providing a strong consistency check on the formulation and confirming that the classical infinite-domain result is recovered smoothly in the limit of weak confinement ($\beta \to \infty$).

Thus, within the present framework, the inclusion of a rigid outer boundary does not introduce any new instability mechanisms. Instead, confinement modifies the decay rate of perturbations without altering the qualitative stability of the bubble.

All numerical evidence indicates that, in the absence of surfactants and base-state radius oscillations, geometric confinement alone does not destabilise bubble modes. This suggests that additional physical effects — such as surfactant transport, elastic wall compliance, or unsteady radius dynamics — are required to produce sustained or growing shape perturbations in confined biological geometries such as xylem vessels.

4.7 Stability analysis of a bubble with a time-dependent base-state radius

We now remove the simplification that the radius of the bubble in the basic state is a constant, which means we take $\Delta \neq 0$ in (4.3.9) and hence

$$a(t) = 1 + \Delta \cos(Ca\, t)\,. \tag{4.7.1}$$

However, we will still assume that the effect of surfactants is neglected and as such we take $\beta_s = 0$ in (4.5.7) and therefore $\sigma_0 = 1$, $\sigma_1 = 0$ and

$$\nabla_{\mathrm{s}}\sigma = 0\,. \tag{4.7.2}$$

For this more complicated case, we need the full amplitude evolution equation (4.3.16)

$$\frac{\mathrm{d}A_{1,n}}{\mathrm{d}t} + \frac{2\dot{a}}{a}A_{1,n} = -\frac{1}{a^2}G_n(a,t)\,, \tag{4.7.3}$$

where G_n is defined by (4.3.14) as

$$G_n(r,t) = c_n(t)r^{-n} + d_n(t)r^{2-n}\,. \tag{4.7.4}$$

As before, if $A_n(t)$ remains bounded, then the bubble will be stable.

4.7.1 Constant bubble pressure

First, we will consider again the case where p_G is a constant. We can solve (4.5.25) and (4.5.27) simultaneously to calculate $c_n(t)$ and $d_n(t)$. Hence, we find

$$d_n(t) = \frac{n(n+1)(n+2)(n-1)a^{n-1}}{2(2n^2+1)}A_{1,n} + \frac{3n(n+1)(n-1)\dot{a}a^{n-1}}{2n^2+1}A_{1,n}\,, \tag{4.7.5}$$

and

$$\begin{aligned} c_n(t) = &-\frac{(n+1)^2(n-1)^2 a^{n+1}}{2(n+2)(2n^2+1)} A_{1,n} \\ &- \frac{3(n+1)(n^2-n+1)\dot{a}a^{n+1}}{(2n^2+1)} A_{1,n} \,. \end{aligned} \tag{4.7.6}$$

Substituting (4.7.5) and (4.7.6) into (4.7.4) and thence into (4.7.3) gives us an amplitude evolution equation which determines the stability of our system, namely

$$\frac{\mathrm{d}A_{1,n}}{\mathrm{d}t} = M_n(t) A_{1,n} \,. \tag{4.7.7}$$

where

$$M_n(t) = -\frac{(2n+1)(n-1)(n+1)}{2a(2n^2+1)} - \frac{(n-1)(4n+1)}{2n^2+1}\frac{\dot{a}}{a} \,. \tag{4.7.8}$$

4.7.2 Adiabatic gas case

Now we consider the adiabatic gas case where

$$p_G = \frac{k}{a^{3\gamma}} - \frac{\mathcal{B} A_{1,n}}{a^{3\gamma-1}} \delta_{n,0} \,, \tag{4.7.9}$$

where

$$\mathcal{B} = \frac{3k\gamma}{\sigma_0 \bar{a}^{3\gamma-1}} \,. \tag{4.7.10}$$

Solving (4.5.41) and (4.5.42) simultaneously gives the following expressions for $c_n(t)$ and $d_n(t)$

$$\begin{aligned} d_n(t) = &\frac{n(n+1)a^{n-1}}{2(2n^2+1)} \left((n+2)(n-1) + \frac{\mathcal{B}}{a^{3\gamma-1}} \delta_{n,0} \right) A_{1,n} \\ &+ \frac{3n(n+1)(n-1)\dot{a}a^{n-1}}{2n^2+1} A_{1,n} \,, \end{aligned} \tag{4.7.11}$$

and

$$\begin{aligned} c_n(t) = &- \frac{(n+1)^2(n-1)a^{n+1}}{2(n+2)(2n^2+1)} \left((n+2)(n-1) + \frac{\mathcal{B}}{a^{3\gamma-1}}\delta_{n,0} \right) A_{1,n} \\ &- \frac{3(n+1)(n^2-n+1)\dot{a}a^{n+1}}{(2n^2+1)} A_{1,n} \, . \end{aligned} \tag{4.7.12}$$

Substituting (4.7.5) and (4.7.6) into (4.7.4) and thence into (4.7.3) gives us an amplitude evolution equation which determines the stability of our system, namely

$$\frac{\mathrm{d}A_{1,n}}{\mathrm{d}t} = M_n(t)A_{1,n} \, . \tag{4.7.13}$$

where

$$\begin{aligned} M_n(t) = &- \frac{(2n+1)(n+1)}{2a(n+2)(2n^2+1)} \left((n-1)(n+2) + \frac{\mathcal{B}}{a^{3\gamma-1}}\delta_{n,0} \right) \\ &- \frac{(n-1)(4n+1)}{2n^2+1} \frac{\dot{a}}{a} \, . \end{aligned} \tag{4.7.14}$$

We can analyse the stability of (4.7.13) using Floquet theory as detailed in Chapter 2. First, we integrate (4.7.13) with respect to t to obtain

$$A_{1,n}(t) = A_0 \exp\left(\int_0^t M_n(s)\mathrm{d}s \right) \, , \tag{4.7.15}$$

where $A_{1,n}(0) = A_0$ and

$$\begin{aligned} \int_0^t M_n(s)\mathrm{d}s = &- \frac{(n-1)(4n+1)}{2n^2+1} \int_0^t \frac{\dot{a}}{a}\mathrm{d}s \\ &- \frac{(2n+1)(n+1)}{2(n+2)(2n^2+1)} \left((n-1)(n+2) \int_0^t \frac{1}{a}\,\mathrm{d}s + \mathcal{B}\delta_{n,0} \int_0^t \frac{1}{a^{3\gamma}}\mathrm{d}s \right) \, . \end{aligned} \tag{4.7.16}$$

Hence, we say that

$$\phi(t) = \exp\left\{ \int_0^t M_n(t')\mathrm{d}t' \right\} \tag{4.7.17}$$

is a fundamental solution for $A_{1,n}(t) = A_0\phi(t)$. We can evaluate the following integrals as

$$\int_0^t \frac{\dot{a}}{a}\mathrm{d}s = \log\left(\frac{a(t)}{a(0)} \right) \, , \tag{4.7.18}$$

where $a(0) = 1 + \Delta$ and

$$\int_0^t \frac{1}{a}\mathrm{d}s = \frac{2}{Ca\sqrt{1-\Delta^2}} \arctan\left(\sqrt{\frac{1-\Delta}{1+\Delta}} \tan\frac{Ca\,t}{2}\right) . \tag{4.7.19}$$

Therefore, for $n \geq 1$, the solution to (4.7.13) is

$$A_{1,n}(t) = A_0\left(\frac{a}{1+\Delta}\right)^{-\alpha} \exp\left(-\beta \arctan\left(\lambda \tan\frac{Ca\,t}{2}\right)\right) , \tag{4.7.20}$$

where

$$\alpha(n) = \frac{2(n-1)(4n+1)}{2n^2+1} , \tag{4.7.21}$$

$$\beta(n, \Delta, Ca) = \frac{(2n+1)(n+1)(n-1)}{Ca(2n^2+1)\sqrt{1-\Delta^2}} , \tag{4.7.22}$$

$$\lambda(\Delta) = \sqrt{\frac{1-\Delta}{1+\Delta}} , \tag{4.7.23}$$

and we define $\arctan(\lambda \tan Ca\,t/2)$ such that it is a continuous and increasing function of t

$$\arctan\left(\lambda \tan\frac{Ca\,t}{2}\right) = \mathrm{Arctan}\left(\lambda \tan\frac{Ca\,t}{2}\right) + (k-1)\pi \tag{4.7.24}$$

$$\text{for} \qquad \max\{0, (2k-3)\pi\} \leq Ca\,t < (2k-1)\pi , \qquad k = 1, 2, 3, \ldots ,$$

where we define

$$-\frac{\pi}{2} \leq \mathrm{Arctan}\left(\lambda \tan\frac{Ca\,t}{2}\right) < \frac{\pi}{2} ,$$

to be the principal arctan branch. The fundamental solution to (4.7.13) is

$$\phi(t) = \left(\frac{a}{1+\Delta}\right)^{-\alpha} \exp\left(-\beta \arctan\left(\lambda \tan\frac{Ca\,t}{2}\right)\right) , \tag{4.7.25}$$

where arctan is defined as in (4.7.24). As discussed in Section 2.5, the Floquet multiplier is given by

$$\exp\left(\frac{2\pi}{Ca}s\right) = \phi\left(\frac{2\pi}{Ca}\right) , \tag{4.7.26}$$

where

$$\phi\left(\frac{2\pi}{Ca}\right) = \exp(-\beta\pi) , \tag{4.7.27}$$

The Floquet exponent, s, is given by

$$s = \frac{Ca}{2\pi} \log \phi \left(\frac{2\pi}{Ca} \right) , \tag{4.7.28}$$

which is determined up to the constant $k\,Ca\mathrm{i}$ for any $k \in \mathbb{Z}$. From Floquet theory, we can write (4.7.20) as

$$A_{1,n}(t) = A_0 v(t) e^{st} , \tag{4.7.29}$$

where $v(t)$ is a periodic function. We can see that if $\mathrm{Re}(s) < 0$ solutions tend to zero, whilst if $\mathrm{Re}(s) > 0$ solutions are unbounded as $t \to \infty$. In this case, we know what s is exactly

$$s = -\frac{Ca\beta}{2} = -\frac{(2n+1)(n+1)(n-1)}{2(2n^2+1)\sqrt{1-\Delta^2}} , \tag{4.7.30}$$

where we recall that $0 < \Delta < 1$. The average curvature, κ_m of a bubble with radius $a = 1 + \Delta \cos(Ca\, t)$ is given by

$$\kappa_m = \frac{Ca}{2\pi} \int_0^{\frac{2\pi}{Ca}} \frac{1}{1 + \Delta \cos(Ca\, t)} \,\mathrm{d}t = \frac{1}{\sqrt{1-\Delta^2}} . \tag{4.7.31}$$

Therefore, we can write the growth rate s as

$$s = -\frac{(2n+1)(n+1)(n-1)}{2(2n^2+1)} \kappa_m , \tag{4.7.32}$$

and thus is proportional to the average curvature of the oscillating bubble.

Important remarks follow immediately from (4.7.30):

1. For $n \geq 1$ we have $\delta_{n,0} = 0$, so the gas pressure makes no $O(\epsilon)$ contribution and the restoring effect is purely due to surface tension.
2. The $n = 1$ mode (rigid translation) is neutral because the geometric factor $(n-1)$ vanishes in (4.7.30).
3. The $n = 0$ mode (volume change) requires separate treatment because the gas pressure perturbation enters at leading order through $\delta_{n,0} = 1$.

4. For $n > 1$ we have that $s \in \mathbb{R}$ and $s < 0$, which means that the solution to (4.7.13) tends to 0 as $t \to \infty$ and the bubble remains stable.

5. If we take $\Delta = 0$, i.e. $a = 1$, in (4.7.30) we obtain the growth rate for the steady bubble problem as shown in (4.6.12).

4.8 Surfactant transport equation

To extend our analysis of the spherical bubble problem, we now consider the presence of an insoluble surfactant with surface concentration Γ, which is confined to the interface and does not dissolve into the surrounding liquid. The surfactant is convected along the interface by the surface velocity and also undergoes surface diffusion. Its presence modifies the surface tension, σ, of the bubble, thereby influencing the interfacial dynamics.

The evolution of the surfactant concentration along the interface is described by the surface convection-diffusion equation

$$\frac{\partial \Gamma}{\partial t} + \nabla_{\mathrm{s}} \cdot (\Gamma \boldsymbol{u}_{\mathrm{s}}) + 2\Gamma \kappa_m u_n = D_{\mathrm{s}} \nabla_{\mathrm{s}}^2 \Gamma \,, \tag{4.8.1}$$

where $u_n = \boldsymbol{u} \cdot \hat{\boldsymbol{n}}$ is the normal velocity of the interface, $\boldsymbol{u}_s = (\boldsymbol{I} - \hat{\boldsymbol{n}}\hat{\boldsymbol{n}}) \cdot \boldsymbol{u}$ is the tangential (surface) velocity, $\nabla_{\mathrm{s}} = (\boldsymbol{I} - \hat{\boldsymbol{n}}\hat{\boldsymbol{n}}) \cdot \nabla$ is the surface gradient operator, D_{s} is the surfactant diffusivity, and $\nabla_{\mathrm{s}}^2 = \nabla_{\mathrm{s}} \cdot \nabla_{\mathrm{s}}$ is the surface Laplacian operator Blyth & Pozrikidis (2004); Stone & Leal (1990). The term $2\Gamma\kappa_m u_n$ accounts for interfacial stretching due to the normal motion of the bubble, with κ_m the mean curvature.

To simplify the analysis, we non-dimensionalise (4.8.1) using characteristic scales for length, velocity, time, and concentration:

$$\Gamma = \Gamma_\infty \Gamma^* \,, \qquad \boldsymbol{u}_{\mathrm{s}} = \frac{\sigma_c}{\mu} \boldsymbol{u}_{\mathrm{s}}^* \,, \qquad u_n = \frac{\sigma_c}{\mu} u_n^* \,, \qquad t = \frac{\bar{a}\mu}{\sigma_c} t^* \,, \tag{4.8.2a}$$

$$\kappa_m = \frac{1}{\bar{a}} \kappa_m^* \,, \qquad \nabla_{\mathrm{s}} = \frac{1}{\bar{a}} \nabla_{\mathrm{s}}^* \,, \tag{4.8.2b}$$

where the * denotes a dimensionless variable and Γ_∞ is the maximum packing concentration of surfactants, σ_c is the surface tension of a clean bubble, μ is the dynamic viscosity of water and $\overline{a}$ is the mean base-state bubble radius.

Substituting (4.8.2) into (4.8.1) gives the dimensionless surfactant transport equation

$$\frac{\partial \Gamma}{\partial t} + \nabla_\mathrm{s} \cdot (\Gamma \boldsymbol{u}_\mathrm{s}) + 2\Gamma \kappa_m u_n = \frac{1}{Pe} \nabla_\mathrm{s}^2 \Gamma \,, \tag{4.8.3}$$

where we have dropped the * notation for simplicity. Here,

$$Pe = \frac{\overline{a}\sigma_c}{\mu D_\mathrm{s}} \,, \tag{4.8.4}$$

is the *Péclet number*, which measures the relative importance of convective transport along the interface to surface diffusion.

4.8.1 Surface geometry and differential operators

To evaluate the terms appearing in the surfactant transport equation (4.8.1), we first define the geometry of the axisymmetric, two-dimensional bubble surface. The surface is given by

$$f(\theta, t) = a(t) + \epsilon A_{1,n} P_n(\cos\theta) \,, \tag{4.8.5}$$

where

$$a(t) = 1 + \Delta \cos(Ca\, t) \,, \tag{4.8.6}$$

as illustrated in Figure 4.8.1. Here, $a(t)$ is the mean bubble radius, $\epsilon A_{1,n}$ is the amplitude of the perturbation, and $P_n(\cos\theta)$ is the Legendre polynomial of degree n.

The outward unit normal vector to the surface, defined in (4.5.11), can be written as

$$\hat{\boldsymbol{n}} = \frac{1}{M}\left(\hat{\boldsymbol{r}} - \frac{f_\theta}{f} \hat{\boldsymbol{\theta}} \right) , \qquad M^2(\theta, t) = 1 + \frac{f_\theta^2}{f^2} \,, \tag{4.8.7}$$

where the interface is given by $r = f(\theta, t)$, $f_\theta = \partial f / \partial \theta$, and $M(\theta, t)$ is a

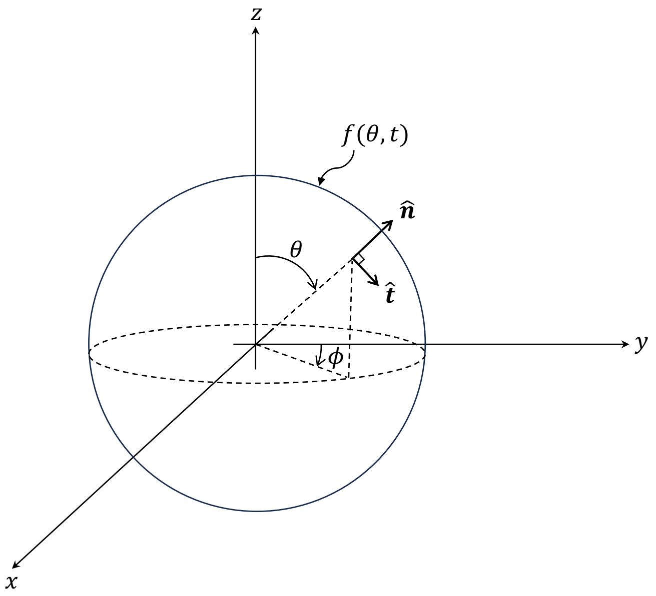

Figure 4.8.1: Schematic of the axisymmetric bubble surface described by $r = f(\theta, t)$.

normalisation factor that ensures that $\hat{\boldsymbol{n}}$ has unit length.

The corresponding unit tangent vector in the meridional plane, defined in (4.5.15), is given by

$$\hat{\boldsymbol{t}} = \hat{\boldsymbol{\phi}} \times \hat{\boldsymbol{n}} = \frac{1}{M}\left(\frac{f_\theta}{f}\hat{\boldsymbol{r}} + \hat{\boldsymbol{\theta}}\right). \tag{4.8.8}$$

Next, we express the surface gradient and Laplacian operators in the general formalism of a two-dimensional surface embedded in three-dimensional space, following Aris (2012); Stone & Leal (1990). This framework is required because the interface is a curved, time-dependent surface, and standard Cartesian differential operators must be reformulated in terms of local surface coordinates.

Let the surface be parametrised by curvilinear coordinates $(\nu^{(1)}, \nu^{(2)})$ as

$$\boldsymbol{x}_{\mathrm{s}} = \boldsymbol{x}_{\mathrm{s}}(\nu^{(1)}, \nu^{(2)}, t). \tag{4.8.9}$$

The associated covariant base vectors, which are tangent to the surface, are defined by

$$\boldsymbol{d}_\alpha = \frac{\partial \boldsymbol{x}_{\mathrm{s}}}{\partial \nu^\alpha}, \qquad \alpha = 1, 2. \tag{4.8.10}$$

These vectors form a local basis for the tangent plane at each point on the surface, allowing surface fields to be expressed intrinsically. For example, the surface velocity can be written as

$$\boldsymbol{u}_{\mathrm{s}} = u^{\alpha} \boldsymbol{d}_{\alpha} \,, \tag{4.8.11}$$

where u^{α} are the contravariant components.

The surface metric tensor is defined by

$$d_{\alpha\beta} = \boldsymbol{d}_{\alpha} \cdot \boldsymbol{d}_{\beta} \,, \tag{4.8.12}$$

which encodes the local geometric properties of the surface. Its inverse (or contravariant metric) $d^{\alpha\beta}$ satisfies

$$d^{\alpha\beta} d_{\beta\gamma} = \delta^{\alpha}_{\gamma} \,, \tag{4.8.13}$$

where δ^{α}_{γ} is the Kronecker delta. The determinant of the metric tensor is denoted by $d = \det(d_{\alpha\beta})$, and the element of arc length on the surface is

$$\mathrm{d}s^2 = d_{\alpha\beta} \, \mathrm{d}\nu^{\alpha} \mathrm{d}\nu^{\beta} \,. \tag{4.8.14}$$

Throughout, we adopt the Einstein summation convention, whereby repeated indices imply summation over $\alpha = 1, 2$. This notation allows tensorial expressions to be written compactly without explicit summation symbols.

With this formalism, the surface divergence and Laplacian operators appearing in (4.8.1) can be written as

$$\nabla_{\mathrm{s}} \cdot (\Gamma \boldsymbol{u}_{\mathrm{s}}) = \frac{1}{d^{1/2}} \frac{\partial}{\partial \nu^{\alpha}} \left(\Gamma d^{1/2} u^{\alpha} \right) \,, \tag{4.8.15}$$

and

$$\nabla^2_{\mathrm{s}} \Gamma = \frac{1}{d^{1/2}} \frac{\partial}{\partial \nu^{\alpha}} \left(d^{1/2} d^{\alpha\beta} \frac{\partial \Gamma}{\partial \nu^{\beta}} \right) \,. \tag{4.8.16}$$

This formulation allows us to rigorously evaluate all terms in the surfactant

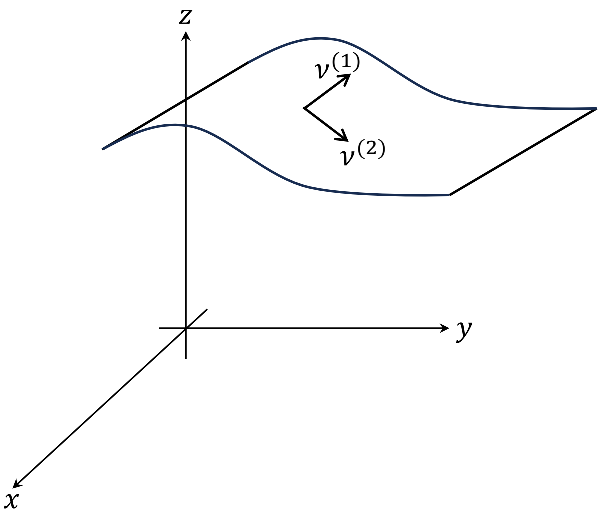

Figure 4.8.2: Schematic of a two-dimensional surface embedded in three-dimensional space, parameterised by $(\nu^{(1)}, \nu^{(2)})$.

transport equation (4.8.1) for arbitrary axisymmetric deformations of the bubble surface.

4.8.2 Spherical surface

We now consider the simplest case of a spherical bubble with constant radius in a fluid with axisymmetric motion. For a bubble with constant radius, we take $\Delta = 0$ in (4.3.9), which sets $r = 1$. Using spherical polar coordinates, we set

$$\nu^{(1)} = \theta \,, \quad \nu^{(2)} = \phi \,,$$

and Cartesian coordinates $y^i = (x, y, z)$ as

$$x = r \sin\theta \cos\phi \big|_{r=1} = \sin\theta\cos\phi \,, \tag{4.8.17}$$

$$y = r \sin\theta \sin\phi \big|_{r=1} = \sin\theta\sin\phi \,, \tag{4.8.18}$$

$$z = r \cos\theta \big|_{r=1} = \cos\theta \,. \tag{4.8.19}$$

The surface is then represented as

$$\boldsymbol{x}_s = x\,\hat{\mathbf{i}} + y\,\hat{\mathbf{j}} + z\,\hat{\mathbf{k}} \,, \tag{4.8.20}$$

with the surface velocity decomposed in the tangent basis as

$$\boldsymbol{u}_{\mathrm{s}} = u^{(1)}\boldsymbol{d}_1 + u^{(2)}\boldsymbol{d}_2\,, \tag{4.8.21}$$

where the covariant surface vectors are

$$\boldsymbol{d}_1 = \frac{\partial \boldsymbol{x}_s}{\partial \theta} = \cos\theta\cos\phi\,\hat{\mathbf{i}} + \cos\theta\sin\phi\,\hat{\mathbf{j}} - \sin\theta\,\hat{\mathbf{k}} = \hat{\boldsymbol{\theta}}\,, \tag{4.8.22}$$

$$\boldsymbol{d}_2 = \frac{\partial \boldsymbol{x}_s}{\partial \phi} = -\sin\theta\sin\phi\,\hat{\mathbf{i}} + \sin\theta\cos\phi\,\hat{\mathbf{j}} = \sin\theta\,\hat{\boldsymbol{\phi}}\,. \tag{4.8.23}$$

Thus, the surface velocity can be expressed as

$$\boldsymbol{u}_s = u^{(1)}\hat{\boldsymbol{\theta}} + \sin\theta\, u^{(2)}\hat{\boldsymbol{\phi}}\,. \tag{4.8.24}$$

For an axisymmetric fluid, the azimuthal component of velocity vanishes, $u_\phi = 0$, so the tangential velocity at the bubble surface is obtained by projecting the fluid velocity onto the tangent plane:

$$\begin{aligned} \boldsymbol{P}\cdot\boldsymbol{u}|_{r=1} &= (\boldsymbol{I} - \hat{\boldsymbol{r}}\hat{\boldsymbol{r}})\cdot(u_r\hat{\boldsymbol{r}} + u_\theta\hat{\boldsymbol{\theta}})|_{r=1} \\ &= u_\theta\hat{\boldsymbol{\theta}}\,, \end{aligned} \tag{4.8.25}$$

where $\boldsymbol{P} = \boldsymbol{I} - \hat{\boldsymbol{n}}\hat{\boldsymbol{n}}$ is the projection operator which removes the normal component of a vector and, for a sphere, the normal vector is $\hat{\boldsymbol{n}} = \hat{\boldsymbol{r}}$.

Comparing (4.8.24) and (4.8.25) gives

$$u^{(1)} = u_\theta\big|_{r=1}\,, \qquad u^{(2)} = 0\,, \tag{4.8.26}$$

with

$$u_\theta = -\frac{1}{r\sin\theta}\frac{\partial\psi}{\partial r}\bigg|_{r=1}\,, \tag{4.8.27}$$

where $\psi(r,\theta,t)$ is the stream function defined in (4.2.13).

To compute the surface divergence and Laplacian, we first evaluate the entries of the surface metric tensor:

$$\frac{\partial y^i}{\partial \nu^\alpha} = \begin{pmatrix} x_\theta & y_\theta & z_\theta \\ x_\phi & y_\phi & z_\phi \end{pmatrix}, \tag{4.8.28}$$

with

$$\begin{aligned} x_\theta &= \cos\theta\cos\phi\,, & x_\phi &= -\sin\theta\sin\phi\,, \\ y_\theta &= \cos\theta\sin\phi\,, & y_\phi &= \sin\theta\cos\phi\,, \\ z_\theta &= -\sin\theta\,, & z_\phi &= 0\,. \end{aligned}$$

The metric tensor entries are

$$d_{11} = x_\theta^2 + y_\theta^2 + z_\theta^2 = 1\,, \tag{4.8.29}$$

$$d_{22} = x_\phi^2 + y_\phi^2 + z_\phi^2 = \sin^2\theta\,, \tag{4.8.30}$$

$$d_{12} = d_{21} = x_\theta x_\phi + y_\theta y_\phi + z_\theta z_\phi = 0\,, \tag{4.8.31}$$

so that

$$d_{\alpha\beta} = \begin{pmatrix} 1 & 0 \\ 0 & \sin^2\theta \end{pmatrix}, \qquad d = \det(d_{\alpha\beta}) = \sin^2\theta\,. \tag{4.8.32}$$

We can calculate the entries of the conjugate of the surface metric tensor using results given by Aris (2012)

$$d^{11} = \frac{d_{22}}{d} = 1\,, \tag{4.8.33}$$

$$d^{12} = d^{21} = -\frac{d_{12}}{d} = 0\,, \tag{4.8.34}$$

and

$$d^{22} = \frac{d_{11}}{d} = \frac{1}{\sin^2\theta}\,. \tag{4.8.35}$$

Using these results, the surface divergence (4.8.15) becomes

$$\nabla_{\mathrm{s}} \cdot (\Gamma \boldsymbol{u}_{\mathrm{s}}) = \frac{1}{\sin\theta}\left[\frac{\partial}{\partial\theta}(\Gamma\sin\theta u^{(1)}) + \frac{\partial}{\partial\phi}(\Gamma\sin\theta u^{(2)})\right]. \tag{4.8.36}$$

Substituting (4.8.26) gives

$$\nabla_{\mathrm{s}} \cdot (\Gamma \boldsymbol{u}_{\mathrm{s}}) = \frac{1}{\sin\theta}\frac{\partial}{\partial\theta}(\Gamma \sin\theta u_\theta)\,. \tag{4.8.37}$$

The surface Laplacian (4.8.16) reduces to

$$\nabla_{\mathrm{s}}^2 \Gamma = \frac{1}{\sin\theta}\frac{\partial}{\partial\theta}\left(\sin\theta\frac{\partial\Gamma}{\partial\theta}\right)\,, \tag{4.8.38}$$

since $\Gamma = \Gamma(\theta, t)$ is axisymmetric.

Finally, the surfactant transport equation (4.8.1) on the spherical bubble becomes

$$\frac{\partial\Gamma}{\partial t} + \frac{1}{\sin\theta}\frac{\partial}{\partial\theta}(\Gamma\sin\theta u_\theta) + 2\Gamma\kappa_m u_n = \frac{1}{Pe\,\sin\theta}\frac{\partial}{\partial\theta}\left(\sin\theta\frac{\partial\Gamma}{\partial\theta}\right)\,. \tag{4.8.39}$$

For an insoluble surfactant with no normal motion ($u_n = 0$), this reduces to the classical form as given in, for example, Palaparthi et al. (2006):

$$\frac{\partial\Gamma}{\partial t} + \frac{1}{\sin\theta}\frac{\partial}{\partial\theta}(\Gamma\sin\theta u_\theta) = \frac{1}{Pe\,\sin\theta}\frac{\partial}{\partial\theta}\left(\sin\theta\frac{\partial\Gamma}{\partial\theta}\right)\,. \tag{4.8.40}$$

4.8.3 Axisymmetric deformed bubble surface

We now extend our analysis to a bubble with an axisymmetric deformation. The radius of the bubble is perturbed as (4.8.5)

$$r = f(\theta, t) = a(t) + \epsilon A_{1,n} P_n(\cos\theta)\,. \tag{4.8.41}$$

As before, we use spherical polar coordinates and set the surface coordinates as

$$\nu^{(1)} = \theta\,, \quad \nu^{(2)} = \phi\,,$$

with the Cartesian representation

$$x = f \sin\theta \cos\phi \,, \tag{4.8.42}$$

$$y = f \sin\theta \sin\phi \,, \tag{4.8.43}$$

$$z = f \cos\theta \,. \tag{4.8.44}$$

The surface vector is

$$\boldsymbol{x}_s = x\,\hat{\mathbf{i}} + y\,\hat{\mathbf{j}} + z\,\hat{\mathbf{k}} \,. \tag{4.8.45}$$

The covariant tangent vectors on the deformed surface are

$$\boldsymbol{d}_1 = \frac{\partial \boldsymbol{x}_s}{\partial \theta} = f_\theta \hat{\boldsymbol{r}} + f \hat{\boldsymbol{\theta}} \,, \tag{4.8.46}$$

$$\boldsymbol{d}_2 = \frac{\partial \boldsymbol{x}_s}{\partial \phi} = f \sin\theta \, \hat{\boldsymbol{\phi}} \,, \tag{4.8.47}$$

where $f_\theta = \partial f / \partial \theta$. The surface velocity is expressed in this basis as

$$\boldsymbol{u}_s = u^{(1)} \boldsymbol{d}_1 + u^{(2)} \boldsymbol{d}_2 = f_\theta u^{(1)} \hat{\boldsymbol{r}} + f u^{(1)} \hat{\boldsymbol{\theta}} + f \sin\theta \, u^{(2)} \hat{\boldsymbol{\phi}} \,. \tag{4.8.48}$$

The tangential velocity is obtained by projecting the fluid velocity onto the deformed surface using the projection operator $\boldsymbol{P} = \boldsymbol{I} - \hat{\boldsymbol{n}}\hat{\boldsymbol{n}}$, where the normal vector is

$$\hat{\boldsymbol{n}} = \frac{1}{M} \left(\hat{\boldsymbol{r}} - \frac{f_\theta}{f} \hat{\boldsymbol{\theta}} \right) \,. \tag{4.8.49}$$

Evaluating $\boldsymbol{P} \cdot \boldsymbol{u}$ gives

$$\boldsymbol{P} \cdot \boldsymbol{u}\big|_{r=f} = \frac{1}{M^2} \left(\frac{f_\theta^2}{f^2} u_r + \frac{f_\theta}{f} u_\theta \right) \hat{\boldsymbol{r}} + \frac{1}{M^2} \left(u_\theta + \frac{f_\theta}{f} u_r \right) \hat{\boldsymbol{\theta}} \,, \tag{4.8.50}$$

where

$$M(\theta, t)^2 = 1 + \frac{f_\theta^2}{f^2} \,. \tag{4.8.51}$$

Comparing (4.8.48) and (4.8.50), the surface velocity components are

$$u^{(1)} = \frac{1}{M^2} \left(\frac{f_\theta}{f^2} u_r + \frac{1}{f} u_\theta \right) \,, \qquad u^{(2)} = 0 \,, \tag{4.8.52}$$

with

$$u_r = \frac{1}{r^2 \sin\theta} \frac{\partial \psi}{\partial \theta}\bigg|_{r=f}, \qquad u_\theta = -\frac{1}{r \sin\theta} \frac{\partial \psi}{\partial r}\bigg|_{r=f}. \tag{4.8.53}$$

The covariant metric tensor is computed from the tangent vectors:

$$d_{11} = \boldsymbol{d}_1 \cdot \boldsymbol{d}_1 = f^2 + f_\theta^2\,, \tag{4.8.54}$$

$$d_{22} = \boldsymbol{d}_2 \cdot \boldsymbol{d}_2 = f^2 \sin^2\theta\,, \tag{4.8.55}$$

$$d_{12} = d_{21} = \boldsymbol{d}_1 \cdot \boldsymbol{d}_2 = 0\,, \tag{4.8.56}$$

so that

$$\boldsymbol{d}_{\alpha\beta} = \begin{pmatrix} f^2 + f_\theta^2 & 0 \\ 0 & f^2 \sin^2\theta \end{pmatrix}, \qquad d = \det(\boldsymbol{d}_{\alpha\beta}) = f^2 \sin^2\theta (f^2 + f_\theta^2)\,. \tag{4.8.57}$$

The conjugate (inverse) metric tensor is

$$d^{11} = \frac{1}{f^2 + f_\theta^2}, \quad d^{22} = \frac{1}{f^2 \sin^2\theta}, \quad d^{12} = d^{21} = 0\,. \tag{4.8.58}$$

Using the metric, the surface divergence (4.8.15) reduces to

$$\nabla_{\mathrm{s}} \cdot (\Gamma \boldsymbol{u}_s) = \frac{1}{M f^2 \sin\theta} \left[\frac{\partial}{\partial \theta} \left(\Gamma M f^2 \sin\theta u^{(1)} \right) + \frac{\partial}{\partial \phi} \left(\Gamma M f^2 \sin\theta u^{(2)} \right) \right], \tag{4.8.59}$$

which, using (4.8.52), becomes

$$\nabla_{\mathrm{s}} \cdot (\Gamma \boldsymbol{u}_s) = \frac{1}{M f^2 \sin\theta} \frac{\partial}{\partial \theta} \left(\frac{\Gamma \sin\theta f_\theta}{M} u_r + \frac{\Gamma \sin\theta f}{M} u_\theta \right). \tag{4.8.60}$$

Similarly, the surface Laplacian (4.8.16) simplifies under axisymmetry, where $\Gamma = \Gamma(\theta, t)$, to

$$\nabla_{\mathrm{s}}^2 \Gamma = \frac{1}{M f^2 \sin\theta} \frac{\partial}{\partial \theta} \left(\frac{\sin\theta}{M} \frac{\partial \Gamma}{\partial \theta} \right). \tag{4.8.61}$$

Finally, the surfactant transport equation (4.8.1) on the deformed bubble surface is

$$\frac{\partial \Gamma}{\partial t} + \frac{1}{M f^2 \sin\theta} \frac{\partial}{\partial \theta}\left(\frac{\Gamma \sin\theta f_\theta}{M} u_r + \frac{\Gamma \sin\theta f}{M} u_\theta\right) + 2\Gamma \kappa_m u_n$$
$$= \frac{1}{Pe\, M f^2 \sin\theta} \frac{\partial}{\partial \theta}\left(\frac{\sin\theta}{M} \frac{\partial \Gamma}{\partial \theta}\right). \tag{4.8.62}$$

If we linearise the surfactant transport equation (4.8.62) with respect to ϵ such that

$$\Gamma(\theta, t) = \Gamma_0(t) + \epsilon \Gamma_{1,n}(t) P_n(\cos\theta), \tag{4.8.63}$$

we get, by considering terms of $O(1)$,

$$\frac{\mathrm{d}\Gamma_0}{\mathrm{d}t} + 2\frac{\dot{a}}{a}\Gamma_0(t) = 0, \tag{4.8.64}$$

which can be integrated to give

$$\Gamma_0(t) = \frac{c}{a(t)^2}, \tag{4.8.65}$$

where c is a constant of integration and $a(t)$ is given by

$$a(t) = 1 + \Delta \cos(Ca\, t). \tag{4.8.66}$$

If we say that

$$\Gamma_0\left(\frac{\pi}{2Ca}\right) = \Gamma_R, \tag{4.8.67}$$

where Γ_R is some given reference, dimensionless, value of surfactant concentration, we can write the leading-order surfactant concentration as

$$\Gamma_0 = \frac{\Gamma_R}{a^2}. \tag{4.8.68}$$

If we consider terms of $O(\epsilon)$ in (4.8.62) we get

$$\begin{aligned}\frac{\mathrm{d}\Gamma_{1,n}}{\mathrm{d}t} &+ 2\frac{\dot{a}}{a}\Gamma_{1,n}(t) + n(n+1)\frac{1}{Pe}\frac{\Gamma_{1,n}(t)}{a^2} \\ &= -\frac{3n(n-1)(2n-1)\dot{a}\Gamma_0(t)}{a^2(2n^2+1)}A_{1,n}(t) \\ &+ \frac{(n+1)\Gamma_0(t)}{2a^2(2n^2+1)}\left((n+2)(n-1)\sigma_0 + \frac{\mathcal{B}}{a^{3\gamma-1}}\delta_{n,0}\right)A_{1,n}(t) \\ &+ \frac{(n+1)(2n^2-n+2)\Gamma_0(t)}{2a(2n^2+1)}\sigma_1 \,. \qquad (4.8.69)\end{aligned}$$

To close the system, we require a constitutive relation expressing the surface tension σ in terms of the surfactant concentration Γ. We adopt the non-dimensional Langmuir equation of state (4.5.1), which relates these quantities as

$$\sigma = 1 + \beta_s \ln\left(1 - \Gamma(\theta, t)\right) , \qquad (4.8.70)$$

where the parameter β_s is defined by

$$\beta_s = \frac{\mathcal{R}\mathcal{T}\Gamma_\infty}{\sigma_c} , \qquad (4.8.71)$$

with $\mathcal{R}$ the ideal gas constant, $\mathcal{T}$ the absolute temperature, Γ_∞ the maximum packing concentration, and σ_c the clean surface tension in the absence of surfactants.

Substituting the perturbation expansion for Γ (4.8.63) into (4.8.70) and linearising with respect to ϵ, we obtain expressions for the leading- and first-order surface tension components:

$$\sigma_0(t) = 1 + \beta_s \ln\left(1 - \Gamma_0(t)\right) , \qquad (4.8.72a)$$

and

$$\sigma_1(t) = -\beta_s \frac{\Gamma_{1,n}(t)}{1 - \Gamma_0(t)} \,. \qquad (4.8.72b)$$

4.9 Stability system for a bubble in an axisymmetric geometry

In this section we set up stability systems for the bubble using coupled amplitude evolution equation and surfactant transport equation.

4.9.1 Stability system for a constant base-state bubble radius

In this section we consider the simplified problem by assuming that the leading-order bubble radius remains constant, which corresponds to setting $\Delta = 0$ in (4.8.6) and thus $a = 1$. We will assume that the gas in the bubble obeys the adiabatic law.

For this simplified case, the amplitude evolution equation (4.3.16) reduces to

$$\frac{\mathrm{d}A_{1,n}}{\mathrm{d}t} = -G_n(1,t)\,, \tag{4.9.1}$$

where G_n is defined by (4.3.14) as

$$G_n = c_n r^{-n} + d_n r^{2-n}\,. \tag{4.9.2}$$

Recall that the surfactant concentration is non-dimensionalised according to (4.8.2)

$$\Gamma = \Gamma_\infty \Gamma^*\,,$$

where Γ_∞ denotes the maximum (close-packed) surfactant concentration, and Γ^* is the corresponding dimensionless surface concentration. For notational simplicity, the superscript * is dropped in what follows. With this scaling, the physically admissible range of the dimensionless surfactant concentration is

$$0 \leq \Gamma \leq 1\,.$$

In the constant-radius base state considered here, the leading-order surfactant concentration (4.8.68) is uniform and given by

$$\Gamma_0 = \Gamma_R \,,$$

where Γ_R is a prescribed reference value. The leading-order surface tension (4.8.72a) is then

$$\sigma_0 = 1 + \beta_s \ln(1 - \Gamma_R)\,.$$

Since surface tension must remain non-negative for physical consistency, we require

$$1 + \beta_s \ln(1 - \Gamma_R) \geq 0\,. \tag{4.9.3}$$

Inequality (4.9.3) imposes a strict upper bound on the permissible values of Γ_R. Solving for Γ_R gives

$$\ln(1 - \Gamma_R) \geq -\frac{1}{\beta_s} \quad \Longrightarrow \quad 1 - \Gamma_R \geq e^{-1/\beta_s}\,,$$

and hence

$$0 \leq \Gamma_R \leq 1 - e^{-1/\beta_s}\,. \tag{4.9.4}$$

Therefore, although the nondimensionalisation allows Γ_R to take values up to unity, the requirement of non-negative surface tension restricts the admissible reference concentration to the smaller interval (4.9.4). This restriction becomes increasingly severe as the parameter β_s increases. In the limit of strong surfactant effects ($\beta_s \gg 1$), only relatively small values of Γ_R are permissible, whereas for weak surfactant effects ($\beta_s \ll 1$), the upper bound approaches $\Gamma_R \to 1$.

The first-order surface tension perturbation term is now given by

$$\sigma_1(t) = -\beta_s \frac{\Gamma_{1,n}(t)}{1 - \Gamma_R}\,. \tag{4.9.5}$$

Solving the components of the dynamic stress condition (4.5.41) and (4.5.42) simultaneously gives us

$$\begin{aligned} d_n(t) = {} & \frac{n(n+1)}{2(2n^2+1)}\left((n+2)(n-1)\sigma_0 + \mathcal{B}\delta_{n,0}\right) A_{1,n}(t) \\ & - \frac{n(n+1)(n-1)\beta_s}{2(2n^2+1)} \frac{\Gamma_{1,n}(t)}{1-\Gamma_R}\,, \end{aligned} \tag{4.9.6}$$

and

$$\begin{aligned} c_n(t) = {} & -\frac{(n+1)^2(n-1)}{2(n+2)(2n^2+1)}\left((n+2)(n-1)\sigma_0 + \mathcal{B}\delta_{n,0}\right) A_{1,n}(t) \\ & - \frac{(n+1)(n^2-n+1)\beta_s}{2(2n^2+1)} \frac{\Gamma_{1,n}(t)}{1-\Gamma_R}\,, \end{aligned} \tag{4.9.7}$$

Substituting (4.9.6) and (4.9.7) into (4.9.2) and thence into (4.9.1) yields the following amplitude evolution equation

$$\begin{aligned} \frac{\mathrm{d}A_{1,n}}{\mathrm{d}t} = {} & -\frac{(2n+1)(n+1)A_{1,n}}{2(n+2)(2n^2+1)}\left((n+2)(n-1)\sigma_0 + \mathcal{B}\delta_{n,0}\right) \\ & + \frac{(n+1)\beta_s}{2(2n^2+1)} \frac{\Gamma_{1,n}(t)}{1-\Gamma_R}\,. \end{aligned} \tag{4.9.8}$$

The linearised surfactant transport equation (4.8.69) becomes

$$\begin{aligned} & \frac{\mathrm{d}\Gamma_{1,n}}{\mathrm{d}t} + n(n+1)\frac{1}{Pe}\Gamma_{1,n}(t) \\ & \quad = \frac{(n+1)\Gamma_R}{2(2n^2+1)}\left((n+2)(n-1)\sigma_0 + \mathcal{B}\delta_{n,0}\right) A_{1,n}(t) \\ & \quad - \frac{(n+1)(2n^2-n+2)\beta_s\Gamma_R}{2(2n^2+1)} \frac{\Gamma_{1,n}(t)}{1-\Gamma_R}\,, \end{aligned} \tag{4.9.9}$$

where we recall that $\mathcal{B}$ is defined in (4.5.43) and is given by

$$\mathcal{B} = \frac{3k\gamma}{\sigma_c \bar{a}^{3\gamma-1}}\,. \tag{4.9.10}$$

We can write the linear system (4.9.8) and (4.9.9) as a matrix equation such that

$$\frac{\mathrm{d}}{\mathrm{d}t}\begin{pmatrix} A_{1,n}(t) \\ \Gamma_{1,n}(t) \end{pmatrix} = \begin{pmatrix} m_1 & m_2 \\ m_3 & m_4 \end{pmatrix}\begin{pmatrix} A_{1,n}(t) \\ \Gamma_{1,n}(t) \end{pmatrix}\,, \tag{4.9.11}$$

where the matrix entries $m_i, i = 1, ..., 4$ are given by

$$
\begin{aligned}
m_1 &= -\frac{2n+1}{n+2} L\Pi\,, \qquad m_2 = \frac{\beta_s}{1-\Gamma_R} L\,,\\
m_3 &= \Gamma_R L\Pi\,, \qquad m_4 = -\frac{\beta_s(2n^2-n+2)\Gamma_R}{1-\Gamma_R} L - \frac{n(n+1)}{Pe}\,,
\end{aligned}
\tag{4.9.12}
$$

and

$$
\Pi = (n+2)(n-1)\sigma_0 + \mathcal{B}\delta_{n,0}\,, \qquad L = \frac{n+1}{2(2n^2+1)}\,. \tag{4.9.13}
$$

The general solution to (4.9.11) is given by

$$
(A_{1,n}, \Gamma_{1,n})^T = c_1 e^{\lambda_1 t} \boldsymbol{v}_1 + c_2 e^{\lambda_2 t} \boldsymbol{v}_2\,, \tag{4.9.14}
$$

where c_1 and c_2 are constants to be determined and λ_1 and λ_2 are the eigenvalues of the matrix

$$
\boldsymbol{M} = \begin{pmatrix} m_1 & m_2 \\ m_3 & m_4 \end{pmatrix}\,, \tag{4.9.15}
$$

and $\boldsymbol{v}_1$ and $\boldsymbol{v}_2$ are the corresponding eigenvectors. The eigenvalues of (4.9.15) are given by

$$
\lambda_{1,2} = \lambda_{\pm} = \frac{m_1+m_4}{2} \pm \sqrt{\left(\frac{m_1+m_4}{2}\right)^2 - (m_1 m_4 - m_2 m_3)}\,. \tag{4.9.16}
$$

To calculate the eigenvectors we need to solve

$$
\boldsymbol{M}\boldsymbol{v}_1 = \lambda_1 \boldsymbol{v}_1 \qquad \text{and} \qquad \boldsymbol{M}\boldsymbol{v}_2 = \lambda_2 \boldsymbol{v}_2\,. \tag{4.9.17}
$$

This gives us

$$
\boldsymbol{v}_1 = \begin{pmatrix} 1 \\ (\lambda_1 - m_1)/m_2 \end{pmatrix} \qquad \text{and} \qquad \boldsymbol{v}_2 = \begin{pmatrix} 1 \\ (\lambda_2 - m_1)/m_2 \end{pmatrix}\,. \tag{4.9.18}
$$

4.9.2 Sign of the eigenvalues and modal stability

The eigenvalues governing the linear stability of the coupled amplitude-surfactant system are given by

$$\begin{aligned}\lambda_{1,2} = &-\frac{2n+1}{2(n+2)}L\Pi - \frac{\beta_s(2n^2-n+2)\Gamma_R}{2(1-\Gamma_R)}L - \frac{n(n+1)}{2Pe}\\ &\pm\Bigg[\left(-\frac{2n+1}{2(n+2)}L\Pi - \frac{\beta_s(2n^2-n+2)\Gamma_R}{2(1-\Gamma_R)}L - \frac{n(n+1)}{2Pe}\right)^2\\ &\quad - \frac{2\beta_s n(2n^2+1)\Gamma_R}{(n+2)(1-\Gamma_R)}L^2\Pi - \frac{n(n+1)(2n+1)}{(n+2)Pe}L\Pi\Bigg]^{1/2},\end{aligned} \tag{4.9.19}$$

where we recall that L and Π are defined as in (4.9.13) as

$$L = \frac{n+1}{2(2n^2+1)}, \qquad \Pi = (n+2)(n-1)\sigma_0 + \mathcal{B}\delta_{n,0}\,. \tag{4.9.20}$$

Since $L > 0$ for all $n \geq 0$, the sign of the eigenvalues is governed primarily by the sign of Π and the trace of the system matrix. We define the half-trace contribution

$$T = \frac{m_1+m_4}{2} = -\frac{2n+1}{2(n+2)}L\Pi - \frac{\beta_s(2n^2-n+2)\Gamma_R}{2(1-\Gamma_R)}L - \frac{n(n+1)}{2Pe}\,. \tag{4.9.21}$$

The second term in (4.9.21) is non-positive and the third term is strictly negative for $0 \leq \Gamma_R < 1$ and $n \geq 1$, respectively. The sign of the first term depends on Π, which we now examine case by case.

Case $n \geq 2$: shape modes

For non-axisymmetric modes $n \geq 2$ we have

$$(n+2)(n-1) > 0\,, \tag{4.9.22}$$

and since $\sigma_0 \geq 0$ by (4.9.3), it follows that

$$\Pi = (n+2)(n-1)\sigma_0 \geq 0\,. \tag{4.9.23}$$

Consequently, one term in (4.9.21) is non-positive and the other two are strictly negative, and hence

$$T < 0\,, \qquad \text{for} \qquad n \geq 2\,. \tag{4.9.24}$$

Next, consider the discriminant appearing in (4.9.19). Writing it as

$$D = T^2 + S\,, \tag{4.9.25}$$

where

$$S = -\frac{2\beta_s n(2n^2+1)\Gamma_R}{(n+2)(1-\Gamma_R)} L^2\Pi - \frac{n(n+1)(2n+1)}{(n+2)Pe} L\Pi\,. \tag{4.9.26}$$

As $\beta_s > 0$ and $0 \leq \Gamma_R < 1$, we observe that

$$S \leq 0\,, \qquad \text{for} \qquad n \geq 2\,, \tag{4.9.27}$$

and therefore

$$0 < D \leq T^2\,. \tag{4.9.28}$$

It follows immediately that

$$\lambda_{1,2} = T \pm \sqrt{D} \leq 0\,, \qquad n \geq 2\,. \tag{4.9.29}$$

Hence, all non-axisymmetric shape modes are linearly stable where here we define $\lambda_1 = T + \sqrt{D}$ and $\lambda_2 = T - \sqrt{D}$, so that λ_1 is the dominant eigenvalue.

Proposition 4.9.1 (Surfactant-enhanced stability)**.** *For all modes* $n \geq 2$ *and any physically admissible non-zero surfactant concentration* $0 < \Gamma_R < 1$ *with* $\beta_s > 0$*, consider the linearised amplitude–surfactant system* (4.9.11)*, whose eigenvalues are*

$$\lambda_{1,2} = T \pm \sqrt{D}\,, \tag{4.9.30}$$

with

$$T = -\frac{2n+1}{2(n+2)} L\Pi - \frac{\beta_s(2n^2-n+2)\Gamma_R}{2(1-\Gamma_R)} L - \frac{n(n+1)}{2Pe}\,. \tag{4.9.31}$$

Then the dominant eigenvalue, λ_1, satisfies

$$\lambda_2 < \lambda_1 < \lambda_{\text{clean}}\,, \tag{4.9.32}$$

where

$$\lambda_{\text{clean}} = -\frac{2n+1}{n+2}L\Pi - \frac{n(n+1)}{2Pe} \tag{4.9.33}$$

is the eigenvalue corresponding to the clean interface limit ($\beta_s = 0$).

Consequently, the presence of surfactant strictly enhances the linear stability of all non-axisymmetric modes, since both eigenvalues are more negative than the corresponding clean-interface value.

Proof. From the definitions above, we have

$$2T = \lambda_{\text{clean}} - \frac{\beta_s(2n^2 - n + 2)\Gamma_R}{1-\Gamma_R}L\,. \tag{4.9.34}$$

The second term is strictly negative for $0 < \Gamma_R < 1$, $\beta_s > 0$ and $n \geq 2$. Therefore

$$2T < \lambda_{\text{clean}} \quad\implies\quad T < \frac{\lambda_{\text{clean}}}{2}\,. \tag{4.9.35}$$

Next, consider the discriminant D in the eigenvalue formula:

$$\lambda_{1,2} = T \pm \sqrt{D}.$$

From the structure of (4.9.19), for $0 < \Gamma_R < 1$ and $\beta_s > 0$, we have $0 < \sqrt{D} < |T|$ for $n \geq 2$, so that

$$\lambda_1 = T + \sqrt{D} < T + |T| = 0\,. \tag{4.9.36}$$

Comparing with the clean-interface growth rate, we have

$$\lambda_1 < 2T < \lambda_{\text{clean}}\,. \tag{4.9.37}$$

Therefore, the dominant eigenvalue in the presence of surfactant is strictly smaller than the clean-interface growth rate, proving that surfactants enhance stability for all modes $n \geq 2$. ☐

Case $n = 1$: translational mode

For $n = 1$ we have

$$\Pi = 0\,, \qquad \text{and} \qquad L = \frac{1}{3}\,. \tag{4.9.38}$$

The eigenvalues (4.9.19) reduce to

$$\lambda_1 = 0\,, \qquad \lambda_2 = -\frac{\beta_s \Gamma_R}{1-\Gamma_R} - \frac{2}{Pe} < 0\,. \tag{4.9.39}$$

The zero eigenvalue corresponds to rigid translation of the bubble and reflects the translational invariance of the governing equations.

Case $n = 0$: radial mode

For $n = 0$ the quantity Π becomes

$$\Pi = -2\sigma_0 + \mathcal{B} \qquad \text{and} \qquad L = \frac{1}{2}\,, \tag{4.9.40}$$

where we recall that $\mathcal{B}$ is defined in (4.9.10) and is given by

$$\mathcal{B} = \frac{3k\gamma}{\sigma_c \overline{a}^{3\gamma-1}}\,, \tag{4.9.41}$$

and the eigenvalues (4.9.19) simplify to

$$\lambda_1 = \frac{1}{2}\left[1 + \beta_s \ln(1-\Gamma_R) - \frac{2\beta_s\Gamma_R}{1-\Gamma_R} - \frac{\mathcal{B}}{2}\right]\,, \qquad \lambda_2 = 0\,. \tag{4.9.42}$$

The neutral eigenvalue again reflects the invariance of the base state, while the sign of λ_1 determines the stability of the radially symmetric mode. This mode alone can become unstable, depending on the balance between surface tension and gas compressibility.

In summary, the linear stability analysis shows that the coupled amplitude–surfactant dynamics possess a fundamentally stabilising structure.

All non-axisymmetric shape modes $n \geq 2$ are linearly stable, with both eigenvalues non-positive and strictly more negative in the presence of surfactant than in the corresponding clean-interface limit.

The translational mode $n = 1$ remains neutrally stable due to invariance under rigid translations of the bubble centre, while the second eigenvalue is strictly damped by surfactant and diffusive effects.

Consequently, insoluble surfactant acts to suppress perturbations and enhances the decay of shape deformations. The radially symmetric mode $n = 0$ is the only mode capable of instability, with its stability governed by the competition between capillary, surfactant and compressibility effects.

4.9.3 Stability system for a bubble with a time-dependent base-state radius

We now turn to the stability of a bubble whose leading-order radius varies periodically in time. This regime arises when the forcing parameter Δ in (4.8.6) is non-zero, corresponding physically to an oscillatory base-state driven, for example, by an imposed acoustic field or time-dependent ambient conditions. In contrast to the constant-radius configuration analysed previously, the unperturbed bubble radius now undergoes prescribed temporal oscillations, introducing parametric forcing into the perturbation dynamics.

Specifically, we take

$$a(t) = 1 + \Delta \cos(Ca\, t)\,, \tag{4.9.43}$$

where Δ denotes the oscillation amplitude and Ca sets the forcing frequency. The period of (4.9.43) is

$$T = \frac{2\pi}{Ca}\,. \tag{4.9.44}$$

The time dependence of the base state fundamentally alters the structure of the linear stability problem: the coefficients governing the evolution of shape and surfactant perturbations are now explicitly time-periodic, and classical eigenvalue analysis must be replaced by a Floquet framework.

As in the constant-radius case, we consider perturbations of mode n. However, the temporal modulation of $a(t)$ couples directly into the amplitude equations through both kinematic effects and surfactant transport, giving rise to a non-autonomous linear system. The aim of this section is to derive the governing stability system for each mode n, which will later be analysed using Floquet theory to determine conditions for parametric growth or decay.

For this regime, the amplitude evolution equation is given by (4.3.16)

$$\frac{\mathrm{d}A_{1,n}}{\mathrm{d}t} + \frac{2\dot{a}}{a}A_{1,n} = -\frac{G_n(a,t)}{a^2}\,, \tag{4.9.45}$$

where G_n is defined by (4.3.14) as

$$G_n(a,t) = c_n(t)a^{-n} + d_n(t)a^{2-n}\,. \tag{4.9.46}$$

Solving the components of the dynamic stress condition (4.5.41) and (4.5.42) simultaneously gives us

$$\begin{aligned} d_n = {} & \frac{n(n+1)a^{n-1}}{2(2n^2+1)}\left((n+2)(n-1)\sigma_0 + \mathcal{B}\delta_{n,0}\right)A_{1,n} \\ & + \frac{3n(n+1)(n-1)\dot{a}a^{n-1}}{2n^2+1}A_{1,n} - \frac{n(n+1)(n-1)a^n}{2(2n^2+1)}\sigma_1\,, \end{aligned} \tag{4.9.47}$$

and

$$\begin{aligned} c_n(t) = {} & -\frac{(n+1)^2(n-1)a^{n+1}}{2(n+2)(2n^2+1)}\left((n+2)(n-1)\sigma_0 + \mathcal{B}\delta_{n,0}\right)A_{1,n} \\ & - \frac{3(n+1)(n^2-n+1)\dot{a}a^{n+1}}{2n^2+1}A_{1,n} + \frac{(n+1)(n^2-n+1)a^{n+2}}{2(2n^2+1)}\sigma_1\,, \end{aligned} \tag{4.9.48}$$

Substituting (4.9.47) and (4.9.48) into (4.9.46) and thence into (4.9.45) yields the following amplitude evolution equation

$$\begin{aligned}\frac{\mathrm{d}A_{1,n}}{\mathrm{d}t} &= -\frac{(n-1)(4n+1)}{2n^2+1}\frac{\dot{a}}{a}A_{1,n} \\ &\quad -\frac{(2n+1)(n+1)A_{1,n}}{2(n+2)(2n^2+1)}\left((n+2)(n-1)\sigma_0+\mathcal{B}\delta_{n,0}\right)-\frac{(n+1)}{2(2n^2+1)}\sigma_1\,.\end{aligned} \tag{4.9.49}$$

Equation (4.9.49) is a generalisation of (4.6.11) taking into account that $a(t)$ is a function of time and surface tension σ can vary on the surface of the bubble.

The leading-order and first-order values of surface tension are given by

$$\sigma_0 = 1+\beta_s\ln(1-\Gamma_0(t))\,, \tag{4.9.50}$$

and

$$\sigma_1 = -\beta_s\frac{\Gamma_{1,n}(t)}{1-\Gamma_0(t)}\,. \tag{4.9.51}$$

The leading-order surfactant concentration is now given by (4.8.68)

$$\Gamma_0 = \frac{\Gamma_R}{a^2}\,, \tag{4.9.52}$$

and the equation for the first-order perturbation is

$$\begin{aligned}&\frac{\mathrm{d}\Gamma_{1,n}}{\mathrm{d}t}+2\frac{\dot{a}}{a}\Gamma_{1,n}(t)+n(n+1)\frac{1}{Pe}\frac{\Gamma_{1,n}(t)}{a^2} \\ &\quad = -\frac{3n(n-1)(2n-1)\dot{a}\Gamma_R}{a^4(2n^2+1)}A_{1,n} \\ &\quad + \frac{(n+1)\Gamma_R}{2a^4(2n^2+1)}\left((n+2)(n-1)\sigma_0+\frac{\mathcal{B}}{a^{3\gamma-1}}\delta_{n,0}\right)A_{1,n} \\ &\quad - \frac{(n+1)(2n^2-n+2)\beta_s\Gamma_R}{2a(2n^2+1)(a^2-\Gamma_R)}\Gamma_{1,n}\,.\end{aligned} \tag{4.9.53}$$

We can then write the bubble stability system as

$$\frac{\mathrm{d}}{\mathrm{d}t}\begin{pmatrix}A_{1,n}(t)\\ \Gamma_{1,n}(t)\end{pmatrix} = \begin{pmatrix}m_1(t) & m_2(t)\\ m_3(t) & m_4(t)\end{pmatrix}\begin{pmatrix}A_{1,n}(t)\\ \Gamma_{1,n}(t)\end{pmatrix}\,, \tag{4.9.54}$$

where the matrix entries $m_i(t), i = 1, ..., 4$ are periodic functions of time given by

$$m_1(t) = -\frac{(n-1)(4n+1)}{2n^2+1}\frac{\dot{a}}{a} - \frac{2n+1}{a(n+2)}L\Pi(t)\,, \tag{4.9.55}$$

$$m_2(t) = \frac{a^2\beta_s}{a^2-\Gamma_R}L\,,$$

$$m_3(t) = -\frac{3(n-1)(2n-1)}{(2n^2+1)}\frac{\dot{a}}{a^4} + \frac{\Gamma_R}{a^4}L\Pi(t)\,,$$

$$m_4(t) = -\frac{(2n^2-n+2)\beta_s\Gamma_R}{a(a^2-\Gamma_R)}L - \frac{1}{Pe}\frac{n(n+1)}{a^2} - 2\frac{\dot{a}}{a}\,, \tag{4.9.56}$$

and

$$\Pi(t) = (n+2)(n-1)\sigma_0(t) + \frac{\mathcal{B}}{a^{3\gamma-1}}\delta_{n,0}\,, \qquad L = \frac{n+1}{2(2n^2+1)}\,. \tag{4.9.57}$$

As our stability system (4.9.54) is in the form

$$\frac{\mathrm{d}\boldsymbol{x}}{\mathrm{d}t} = \boldsymbol{A}(t)\boldsymbol{x}\,, \tag{4.9.58}$$

where the entries of $\boldsymbol{A}(t)$ are all periodic with period T, we can analyse its stability via Floquet theory. By (2.5.23), the solution to (4.9.54) is given by

$$\boldsymbol{x}(t) = (A_{1,n}(t), \Gamma_{1,n}(t))^{\mathsf{T}} = e^{s_1 t}\boldsymbol{v}_1(t) + e^{s_2 t}\boldsymbol{v}_2(t)\,, \tag{4.9.59}$$

where s_1, s_2 are the Floquet exponents and $\boldsymbol{v}_1(t), \boldsymbol{v}_2(t)$ are periodic with period T. Using the method outlined in Section 2.5 we need to integrate the system (4.9.54) over one time period with the initial condition $\boldsymbol{x}(0) = \boldsymbol{x}_0$. These will give the entries of the fundamental matrix $\boldsymbol{\Phi}(t)$. The eigenvalues of this matrix, $\lambda_{1,2}$ are related to the Floquet exponents via

$$s_{1,2} = \frac{1}{T}\log(\lambda_{1,2})\,, \tag{4.9.60}$$

which is determined up to a constant. We can see that if either $\mathrm{Re}(s_{1,2}) > 0$, the solutions of (4.9.54) are unstable, if both $\mathrm{Re}(s_{1,2}) < 0$, they are stable.

We now show that the Floquet exponents associated with (4.9.54) are independent of the capillary number Ca. We rewrite (4.9.54) as

$$\frac{\mathrm{d}A_{1,n}}{\mathrm{d}t} + \alpha_1 \frac{\dot{a}}{a} A_{1,n} = \frac{\alpha_2(t)}{a} A_{1,n} + m_2(t)\Gamma_{1,n}\,, \tag{4.9.61a}$$

$$\frac{\mathrm{d}\Gamma_{1,n}}{\mathrm{d}t} + 2\frac{\dot{a}}{a}\Gamma_{1,n} = m_3(t)A_{1,n} + \alpha_3(t)\Gamma_{1,n}\,, \tag{4.9.61b}$$

where

$$\alpha_1 = \frac{(n-1)(4n+1)}{2n^2+1}\,, \qquad \alpha_2(t) = -\frac{2n+1}{n+2} L\Pi(t)\,, \tag{4.9.62a}$$

and

$$\alpha_3(t) = -\frac{(2n^2-n+2)\beta_s\Gamma_R}{a^3} L - \frac{1}{Pe}\frac{n(n+1)}{a^2}\,. \tag{4.9.62b}$$

Multiplying the first equation of (4.9.61) by a^{α_1} and the second by a^2 gives

$$\frac{\mathrm{d}}{\mathrm{d}t}\left(a^{\alpha_1}A_{1,n}\right) = \frac{\alpha_2(t)}{a}\left(a^{\alpha_1}A_{1,n}\right) + m_2(t)a^{\alpha_1}\Gamma_{1,n}\,, \tag{4.9.63a}$$

$$\frac{\mathrm{d}}{\mathrm{d}t}\left(a^2\Gamma_{1,n}\right) = m_3(t)a^2A_{1,n} + \alpha_3(t)\left(a^2\Gamma_{1,n}\right)\,. \tag{4.9.63b}$$

Since the coefficients are periodic with period T, Floquet theory implies that solutions may be written in the form

$$A_{1,n}(t) = e^{st}u(t)\,, \tag{4.9.64a}$$

$$\Gamma_{1,n}(t) = e^{st}v(t)\,, \tag{4.9.64b}$$

where $u(t)$ and $v(t)$ are periodic functions with period T, and s is a Floquet exponent.

Substituting (4.9.64) into (4.9.63a), dividing through by $a^{\alpha_1}A_{1,n}$, and integrating over one period gives

$$\int_0^T \frac{\frac{\mathrm{d}}{\mathrm{d}t}\left(a^{\alpha_1}A_{1,n}\right)}{a^{\alpha_1}A_{1,n}}\,\mathrm{d}t = \int_0^T \frac{\alpha_2(t)}{a}\,\mathrm{d}t + \int_0^T m_2(t)\frac{\Gamma_{1,n}}{A_{1,n}}\,\mathrm{d}t\,. \tag{4.9.65}$$

Using

$$\frac{\Gamma_{1,n}}{A_{1,n}} = \frac{v(t)}{u(t)}\,, \tag{4.9.66}$$

together with the periodicity of $a(t)$, $u(t)$, and $v(t)$, we obtain

$$\log\left(\frac{A_{1,n}(T)}{A_{1,n}(0)}\right) = sT = \int_0^T \frac{\alpha_2(t)}{a}\,\mathrm{d}t + \int_0^T m_2(t)\frac{v(t)}{u(t)}\,\mathrm{d}t\,. \tag{4.9.67}$$

Hence,

$$s = \frac{1}{T}\int_0^T \frac{\alpha_2(t)}{a}\,\mathrm{d}t + \frac{1}{T}\int_0^T m_2(t)\frac{v(t)}{u(t)}\,\mathrm{d}t\,. \tag{4.9.68}$$

An analogous expression follows from (4.9.63b), namely

$$s = \frac{1}{T}\int_0^T m_3(t)\frac{u_2(t)}{v_2(t)}\,\mathrm{d}t + \frac{1}{T}\int_0^T \alpha_3(t)\,\mathrm{d}t\,. \tag{4.9.69}$$

Now observe that all coefficient functions depend on time only through the combination $Ca\,t$ as

$$a(t) = 1 + \Delta\cos(Ca\,t)\,. \tag{4.9.70}$$

Thus all integrals appearing in (4.9.68) and (4.9.69) are of the form

$$J = \frac{1}{T}\int_0^T f(Ca\,t)\,\mathrm{d}t\,, \qquad T = \frac{2\pi}{Ca}\,. \tag{4.9.71}$$

Introducing the change of variables

$$\tau = Ca\,t\,, \qquad \mathrm{d}t = \frac{\mathrm{d}\tau}{Ca}\,, \tag{4.9.72}$$

gives

$$J = \frac{1}{2\pi}\int_0^{2\pi} f(\tau)\,\mathrm{d}\tau\,, \tag{4.9.73}$$

which is independent of Ca. Therefore, the Floquet exponents are independent of the capillary number Ca.

For the surfactant transport equation (4.9.53), the relative importance of surface diffusion is quantified by the Péclet number

$$Pe = \frac{a\,\sigma}{\mu D_{\rm s}}\,,$$

which compares Marangoni-driven surface convection to surface diffusion. Using values of $\overline{a}$, μ and σ_c from Table 2.1 and the estimated value of $D_{\rm s}$ for a surface in water which can be found in (see, for example, Li & He, 2023, p.13) of 10^{-10} we estimate the Péclet number as

$$Pe \sim \frac{50\times 10^{-9}\times 50\times 10^{-3}}{10^{-10}\times 10^{-3}} \sim 10^{4}\,, \tag{4.9.74}$$

and hence

$$\frac{1}{Pe} \sim 10^{-4}\,. \tag{4.9.75}$$

Consequently, the prefactor Pe^{-1} multiplying the surface Laplacian in the nondimensional surfactant transport equation (4.9.53) is asymptotically small.

In this regime, surfactant redistribution is dominated by advection along the interface, while surface diffusion acts only as a weak regularising mechanism. To leading order, the diffusive contribution may therefore be neglected, yielding a convection-dominated transport equation. This approximation is consistent with previous theoretical studies of insoluble surfactants on bubbles and drops at large Péclet number, and it captures the physically relevant limit for nanobubbles in xylem, where persistent surfactant gradients and strong Marangoni stresses are expected to arise.

From Floquet theory, the growth rates s_1 and s_2 can be evaluated numerically for any prescribed set of parameters. However, care must be taken when interpreting these results, as the numerical procedure alone does not enforce physical admissibility. For example, when $n = 2$, $\Delta = 0.2$, $Ca = 1$, $\gamma = 1$ and $\Gamma_R = 0.25$, the real part of the Floquet exponent $\mathrm{Re}(s_1)$ appears to attain positive values, as shown in Figure 4.9.1.

Crucially, the parameter combinations corresponding to positive growth rates violate the surfactant constraint (4.9.3) which ensures that we do not have a negative value of surface tension, viz.

$$1 + \beta_s \ln(1 - \Gamma_R) \geq 0\,, \tag{4.9.76}$$

where we recall that β_s, given by (4.5.7c), is a dimensionless measure of the effectiveness of the surfactant and Γ_R is some given reference dimensionless value of surfactant concentration such that $\Gamma_R = \Gamma_0(\pi/(2Ca))$. Therefore, the positive growth rates are not physically realisable. When this constraint is enforced, the apparent region of instability is eliminated entirely. Consequently, although positive Floquet growth rates may arise mathematically for unconstrained parameter values, they do not correspond to physically viable states of the system. This highlights the importance of incorporating physical constraints when assessing stability and motivates the use of constrained global optimisation to determine whether instability is possible within the admissible parameter regime.

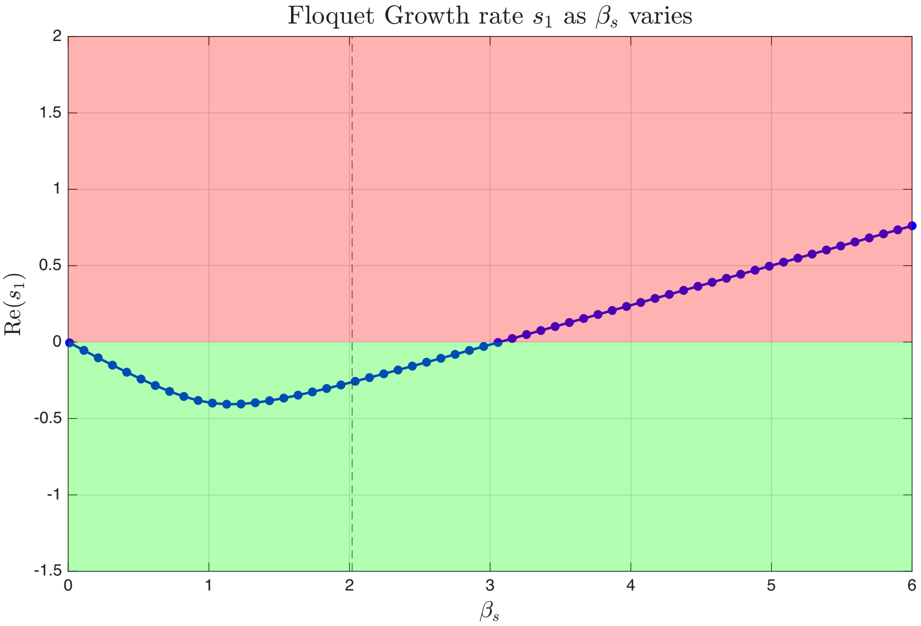

Figure 4.9.1: The green region represents stability and the red region represents instability. The dashed horizontal line indicates the maximum allowed value of β_s that satisfies (4.9.76) when $\Gamma_R = 0.25$.

4.9.4 Global optimisation of Floquet growth rates

The stability system (4.9.54) is linear with time-periodic coefficients and can therefore be analysed using Floquet theory. As discussed previously, the stability of the system is determined by the real parts of the Floquet exponents s_1 and s_2, which are obtained from the eigenvalues of the fundamental matrix over one forcing period. While these growth rates can be computed numerically for any fixed parameter set, establishing whether instability is possible requires a systematic exploration of a high-dimensional and constrained parameter space.

A direct parameter sweep is computationally expensive and risks missing isolated regions of instability. For this reason, we employ *global optimisation techniques*, as discussed in Chapter 3, which are designed to locate global extrema of objective functions defined over complex, non-convex landscapes. These methods are well suited to the present problem, where the dependence of the Floquet exponents on the parameters is highly nonlinear and involves numerical integration of the governing system over one period.

Objective function and constraints

Instability of the system corresponds to $\mathrm{Re}(s_i) > 0$ for at least one Floquet exponent. However, standard global optimisation algorithms are formulated as minimisation problems. To identify the largest possible growth rate, we therefore minimise the negative of the maximum Floquet exponent. Specifically, we define the objective function

$$J(\beta_s, \Gamma_R, \Delta) = \min(-\mathrm{Re}(s_1), -\mathrm{Re}(s_2)), \tag{4.9.77}$$

so that minimising J is equivalent to maximising $\max(s_1, s_2)$. If the optimal value of $\max(\mathrm{Re}(s_1), \mathrm{Re}(s_2))$ is negative, the system is linearly stable.

The optimisation is subject to the physical constraint (4.9.3) arising from surfactant coverage,

$$-\Gamma_R + (1 - e^{-1/\beta_s})(1-\Delta)^2 \leq 0\,, \tag{4.9.78}$$

which ensures that the surfactant concentration remains physically admissible.

The parameter space is explored over the ranges

$$\beta_s \in [\beta_{\text{min}}, 5]\,, \qquad \Gamma_R \in [0.1, \Gamma_{R,\text{max}}]\,, \qquad \Delta \in [\Delta_{\text{min}}, 0.99]\,, \tag{4.9.79}$$

where

$$\beta_{\text{min}} = 0.1\,, \qquad \Delta_{\text{min}} = 0.1\,, \qquad \Gamma_{R,\text{max}} = (1-\Delta_{\text{min}})^2(1 - e^{-1/\beta_{\text{min}}})\,. \tag{4.9.80}$$

Genetic Algorithm

Genetic Algorithms (GA), as discussed in Section 3.3, are population-based global optimisers inspired by evolutionary processes such as selection, crossover, and mutation. A population of candidate parameter sets is evolved over successive generations, with individuals producing larger Floquet growth rates preferentially retained. This approach is particularly effective at exploring large parameter spaces and avoiding premature convergence to local extrema.

In the present problem, each individual corresponds to a parameter triplet $(\beta_s, \Gamma_R, \Delta)$. The fitness function is taken to be $-J$, so that individuals yielding larger growth rates are favoured. Constraint violations are handled by rejecting infeasible individuals during the population update.

The results obtained using the Genetic Algorithm are summarised in Table 4.1. The Matlab code used for these calculations is in Appendix A1. For all mode numbers n considered, the optimal growth rates remain strictly negative, indicating stability. The optimiser consistently converges toward values of β_s, Γ_R and Δ close to their lower bounds, identifying these as the regions of parameter space most favourable for instability. The persistence of strictly negative Floquet growth rates even in this regime demonstrates that linear instability is precluded for all physically admissible parameter values.

n value	Optimal β_s	Optimal Γ_R	Optimal Δ	$\max(s_1, s_2)$	Stable
2	0.1	0.1	0.1	-0.013794	Yes
3	0.10006	0.1	0.10007	-0.019743	Yes
10	0.1	0.1002	0.1	-0.060314	Yes
50	0.1	0.1	0.1	-0.29066	Yes

Table 4.1: Table of results for Genetic Algorithm for $n = 2, 3, 10, 50$.

Simulated Annealing

Simulated Annealing (SA), as discussed in Section 3.4, is a stochastic optimisation method inspired by thermodynamic cooling processes. Unlike population-based approaches, SA evolves a single candidate solution, allowing occasional uphill moves with a probability that decreases as the algorithm progresses. This enables the method to escape local minima at early stages while converging toward a global optimum at later stages.

The same objective function, constraints, and parameter ranges used for the GA are employed for the SA optimisation. Candidate moves that violate the physical constraint are rejected. The results are presented in Table 4.2 and show close agreement with those obtained using the Genetic Algorithm, both in terms of the optimal parameter values and the resulting Floquet growth rates. The Matlab code for these calculations is in Appendix A2.

Discussion and conclusions

Both global optimisation methods consistently predict negative values of the maximum Floquet exponent across all tested values of n, providing evidence

n value	Optimal β_s	Optimal Γ_R	Optimal Δ	$\max(s_1, s_2)$	Stable
2	0.10031	0.1	0.10642	-0.013903	Yes
3	0.1004	0.1	0.1	-0.019801	Yes
10	0.10004	0.10008	0.10011	-0.060383	Yes
50	0.10046	0.10013	0.10004	-0.29242	Yes

Table 4.2: Table of results for Simulated Annealing for $n = 2, 3, 10, 50$.

that the system remains linearly stable within the physically admissible parameter regime. Moreover, the numerical values of the growth rates obtained using the Genetic Algorithm and Simulated Annealing are very similar across the parameter space, indicating that both optimisers converge to essentially the same extrema. This close quantitative agreement increases confidence that the true global maximum of the growth rate has been accurately identified, rather than an artefact of a particular optimisation strategy.

Although isolated regions of apparent instability may arise when physical constraints are ignored, as illustrated in Figure 4.9.1, enforcing the surfactant constraint eliminates these regions entirely. In all physically relevant cases, the optimised growth rates remain negative and of comparable magnitude for both methods.

Taken together, these results support the conclusion that surfactant-covered nanobubbles are dynamically stable under periodic forcing, with no evidence of linear instability for physically realistic parameter values.

5

Stability analysis for a non-axisymmetric bubble

Synopsis

> The aim of this section is to expand our investigation by removing the simplification we made in the previous section by allowing the system to vary in the azimuthal direction.

5.1 Stokes equation

We continue to work in spherical polar coordinates (r, θ, ϕ). To study the stability of the bubble surface, we introduce a small perturbation of the spherical state in the form

$$r = f(\theta, \phi, t) = a(t) + \epsilon \mathrm{Re} \left\{ \sum_{n=0}^{\infty} \sum_{m=-n}^{n} A_{1,m,n}(t) P_n^m(\cos\theta) e^{\mathrm{i}m\phi} \right\} , \qquad (5.1.1)$$

where

$$a(t) = 1 + \Delta \cos(Ca\, t) \, .$$

Here, Re denotes taking the real part, $\epsilon \ll 1$, P_n^m denotes the associated Legendre polynomial of degree n and order m, and $A_{1,m,n}(t)$ is the complex amplitude associated with the (m, n) spherical harmonic mode. The integer $n \geq 0$ represents the polar mode number, while m satisfies $0 \leq m \leq n$ and determines the azimuthal dependence of the perturbation. Since the physical bubble radius must be real-valued, we take the real part of the spherical harmonic expansion in (5.1.1).

In what follows, the governing equations will be analysed mode-by-mode, treating each pair (m, n) separately.

We can plot (5.1.1) by taking $\Delta = 0$, $\epsilon = 0.15$, $A_{1,m,n} = 1$ and

$$f = 1 + 0.15 P_n^m(\cos\theta)\cos(m\phi)\,, \tag{5.1.2}$$

and this is shown in Figures 5.1.1 and 5.1.2. We can see from Figure 5.1.2 that the mode $(n, m) = (1, 0)$ represents a rigid translation in the z-direction and the mode $(n, m) = (1, 1)$ represents a rigid translation in the $-x$-direction.

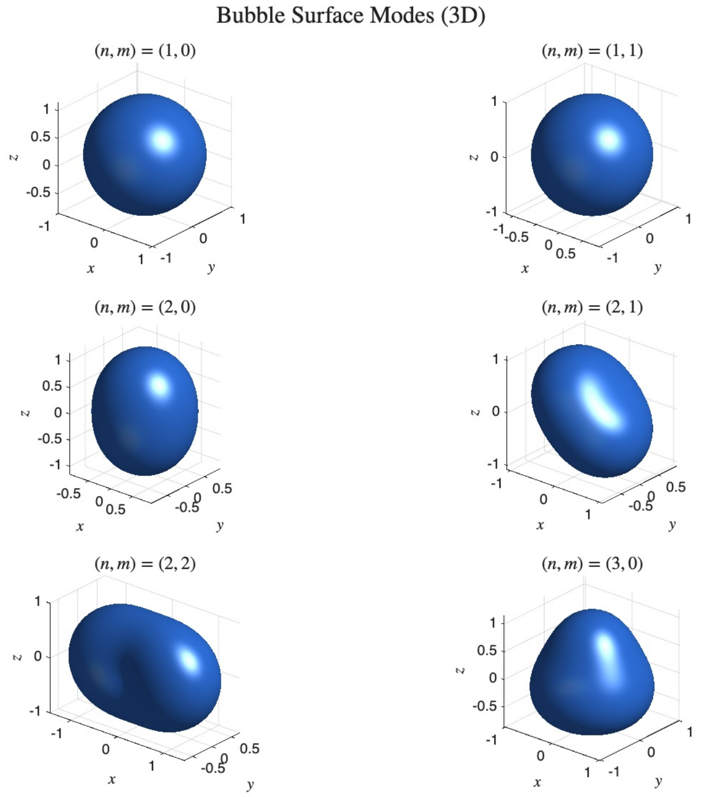

Figure 5.1.1: Plot of (5.1.2) for various modes (n, m).

All variables in this chapter are non-dimensional as in the previous chapter. We

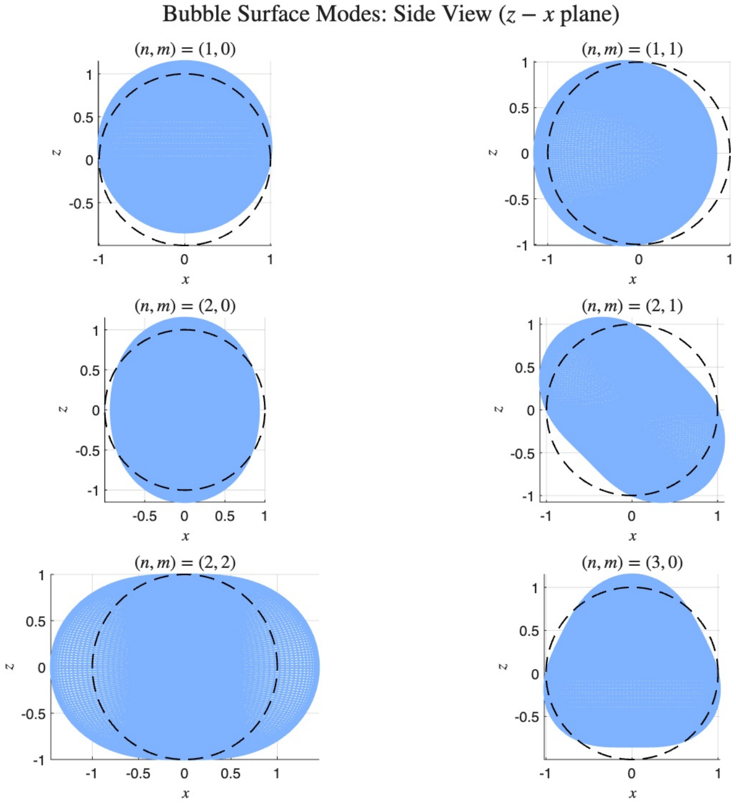

Figure 5.1.2: Plot of (5.1.2) in the $z - x$ plane for various modes (n, m). The dashed circle represents the unperturbed bubble at $r = 1$.

again assume that the Laplace number, La, is sufficiently small such that the effects of inertia are negligible in comparison to the effects of viscosity in the Navier–Stokes equation (2.1.18). As such, we will model the bubble using the non-dimensional Stokes equation

$$\nabla^2 \boldsymbol{u} = \nabla p \,, \tag{5.1.3a}$$

$$\nabla \cdot \boldsymbol{u} = 0 \,, \tag{5.1.3b}$$

where $\boldsymbol{u}$ is the velocity field given by $\boldsymbol{u} = u_r \hat{\boldsymbol{r}} + u_\theta \hat{\boldsymbol{\theta}} + u_\phi \hat{\boldsymbol{\phi}}$, p is the pressure. We perturb the flow by setting

$$\boldsymbol{u} = \boldsymbol{u}_0 + \epsilon \boldsymbol{u}_1 \,, \tag{5.1.4}$$

$$p = p_0 + \epsilon p_1 \,, \tag{5.1.5}$$

where the subscript 0 represents an unperturbed base state and the subscript 1 indicates a first-order perturbed state. We now substitute (5.1.4) and (5.1.5) into (5.1.3) which, after comparing coefficients of powers of ϵ gives us

$$\nabla^2 \boldsymbol{u}_0 = \nabla p_0 \,, \tag{5.1.6a}$$

$$\nabla \cdot \boldsymbol{u}_0 = 0 \,, \tag{5.1.6b}$$

and

$$\nabla^2 \boldsymbol{u}_1 = \nabla p_1 \,, \tag{5.1.7a}$$

$$\nabla \cdot \boldsymbol{u}_1 = 0 \,. \tag{5.1.7b}$$

We assume that the base state flow is purely radial and is hence irrotational and can be expressed as

$$\boldsymbol{u}_0 = \nabla \Phi \,, \tag{5.1.8}$$

where Φ is a velocity potential. Consequently, (5.1.6a) reduces to

$$\nabla p_0 = 0 \,, \tag{5.1.9}$$

as

$$\nabla^2 (\nabla \Phi) = \nabla (\nabla \cdot \nabla \Phi) - \nabla \times (\nabla \times \nabla \Phi) = 0 \,, \tag{5.1.10}$$

using (5.1.6b). Therefore, we conclude that $p_0(t)$ is a function of time only. As in the previous section, we find that the basic state velocity is

$$\boldsymbol{u}_0 = \frac{a^2 \dot{a}}{r^2} \hat{\boldsymbol{r}} \,. \tag{5.1.11}$$

Taking the divergence of (5.1.3), we find that the pressure perturbation satisfies Laplace's equation,

$$\nabla^2 p_1 = 0 \,. \tag{5.1.12}$$

Following the approach of, for example, Kim & Karrila (2005), we expand the solution in terms of solid spherical harmonics. Thus

$$p_1 = \sum_{n=-\infty}^{\infty} p_n \,, \tag{5.1.13}$$

where p_n denotes a solid spherical harmonic of order n. Harmonic functions in spherical coordinates consist of both regular harmonics, proportional to r^n, and decaying harmonics, proportional to r^{-n-1}, where in both cases the degree satisfies $n \geq 0$. Accordingly, for $n \geq 0$, the regular solid harmonics are written as

$$p_n = r^n \sum_{m=-n}^{n} a_{mn} P_n^m(\cos\theta) e^{\mathrm{i}m\phi} \,, \tag{5.1.14}$$

while the decaying solid harmonics are

$$p_{-n-1} = r^{-n-1} \sum_{m=-n}^{n} a_{mn} P_n^m(\cos\theta) e^{\mathrm{i}m\phi} \,. \tag{5.1.15}$$

Here, a_{mn} are constants. The notation p_{-n-1} refers only to the radial dependence r^{-n-1} and does not imply Legendre polynomials of negative degree.

Equation (5.1.7a) admits the general solution, known as the Lamb solution Lamb (1932),

$$\begin{aligned} \boldsymbol{u}_1 = & \sum_{\substack{n=-\infty \\ n\neq -1}}^{\infty} \left[\frac{(n+3) r^2 \nabla p_n}{2(n+1)(2n+3)} - \frac{n \boldsymbol{r} p_n}{(n+1)(2n+3)} \right] \\ & + \sum_{n=-\infty}^{\infty} \left[\nabla \Phi_n + \nabla \times (\boldsymbol{r} \chi_n) \right] \,, \end{aligned} \tag{5.1.16}$$

where $\boldsymbol{r} = r\hat{\boldsymbol{r}}$ is the position vector, and Φ_n and χ_n are solid harmonics. For $n \geq 0$, the regular harmonics are given by

$$\Phi_n = r^n \sum_{m=-n}^{n} b_{mn} P_n^m(\cos\theta) e^{\mathrm{i}m\phi} \,, \tag{5.1.17}$$

$$\chi_n = r^n \sum_{m=-n}^{n} c_{mn} P_n^m(\cos\theta) e^{\mathrm{i}m\phi} \,, \tag{5.1.18}$$

where b_{mn} and c_{mn} are constants, while the decaying harmonics are

$$\Phi_{-n-1} = r^{-n-1} \sum_{m=-n}^{n} b_{mn} P_n^m(\cos\theta) e^{\mathrm{i}m\phi} \,, \tag{5.1.19}$$

$$\chi_{-n-1} = r^{-n-1} \sum_{m=-n}^{n} c_{mn} P_n^m(\cos\theta) e^{\mathrm{i}m\phi} \,. \tag{5.1.20}$$

Because the net volumetric expansion or contraction of the bubble is already entirely accounted for by the purely radial base state (5.1.11), any physically admissible perturbation must be volume-preserving. This requirement eliminates the net mass-source mode ($n = 0$) from the perturbation field. Furthermore, since we are strictly concerned with the fluid behaviour exterior to the bubble, we discard the regular harmonics proportional to r^n, retaining only the decaying harmonics as $r \to \infty$. The velocity field therefore becomes

$$\begin{aligned} \boldsymbol{u}_1 = &\sum_{n=1}^{\infty} \left[-\frac{(n-2) r^2 \nabla p_{-n-1}}{2n(2n-1)} + \frac{(n+1) \boldsymbol{r} p_{-n-1}}{n(2n-1)} \right] \\ &+ \sum_{n=1}^{\infty} \left[\nabla \Phi_{-n-1} + \nabla \times (\boldsymbol{r} \chi_{-n-1}) \right] . \end{aligned} \tag{5.1.21}$$

Adding (5.1.11) and (5.1.21), and extracting the contribution from the nth mode, the velocity components become

$$u_r = \frac{a^2 \dot{a}}{r^2} + \epsilon \left[-\frac{n+1}{r} \Phi_{-n-1} + \frac{n+1}{2(2n-1)} r p_{-n-1} \right] , \tag{5.1.22a}$$

$$u_\theta = \epsilon \left[\frac{1}{r} \frac{\partial}{\partial \theta} \Phi_{-n-1} - \frac{n-2}{2n(2n-1)} r \frac{\partial}{\partial \theta} p_{-n-1} + \frac{1}{\sin\theta} \frac{\partial}{\partial \phi} \chi_{-n-1} \right] , \tag{5.1.22b}$$

$$u_\phi = \epsilon \left[\frac{1}{r \sin\theta} \frac{\partial}{\partial \phi} \Phi_{-n-1} - \frac{n-2}{2n(2n-1)} \frac{r}{\sin\theta} \frac{\partial}{\partial \phi} p_{-n-1} - \frac{\partial}{\partial \theta} \chi_{-n-1} \right] . \tag{5.1.22c}$$

5.2 Kinematic condition

We now wish to get a particular solution to (5.1.3) subject to appropriate boundary conditions for our bubble problem. Kinematic compatibility at the interface of the bubble $r = f(\theta, \phi, t)$ requires

$$\left(\frac{\partial}{\partial t} + \boldsymbol{u} \cdot \nabla\right)(r - f) = 0\,, \tag{5.2.1}$$

at $r = f$, which is given by (5.1.1). If we expand (5.2.1) we get

$$-\frac{\partial f}{\partial t} + u_r - \frac{u_\theta}{r}\frac{\partial f}{\partial \theta} - \frac{u_\phi}{r \sin\theta}\frac{\partial f}{\partial \phi}\bigg|_{r=f} = 0\,. \tag{5.2.2}$$

We now substitute (5.1.22a), (5.1.22b) and (5.1.22c) into (5.2.2) and collect coefficients of first-order epsilon terms to obtain the following amplitude evolution equation

$$\frac{\mathrm{d}A_{1,n}}{\mathrm{d}t} + \frac{2\dot{a}}{a}A_{1,n} = \frac{(n+1)a^{-n}}{2(2n-1)}a_{mn} - (n+1)a^{-n-2}b_{mn}\,. \tag{5.2.3}$$

5.3 Dynamic condition

As in the previous chapters, we have a condition that expresses the balance of normal and tangential forces prevailing on the bubble surface. This non-dimensional interfacial stress-balance equation (2.2.9) is governed by the following equation

$$\boldsymbol{T} \cdot \hat{\boldsymbol{n}} + p_G \hat{\boldsymbol{n}} = 2\kappa_m \sigma \hat{\boldsymbol{n}} - \nabla_{\mathrm{s}}\sigma\big|_{r=f}\,, \tag{5.3.1}$$

where $\boldsymbol{T}$ is a stress tensor given by

$$\boldsymbol{T} = \begin{pmatrix} -p & 0 & 0 \\ 0 & -p & 0 \\ 0 & 0 & -p \end{pmatrix} + 2\begin{pmatrix} e_{rr} & e_{r\theta} & e_{r\phi} \\ e_{\theta r} & e_{\theta\theta} & e_{\theta\phi} \\ e_{\phi r} & e_{\phi\theta} & e_{\phi\phi} \end{pmatrix}, \tag{5.3.2}$$

where

$$e_{rr} = \frac{\partial u_r}{\partial r}\,, \tag{5.3.3a}$$

$$e_{\theta\theta} = \frac{1}{r}\frac{\partial u_\theta}{\partial \theta} + \frac{u_r}{r}\,, \tag{5.3.3b}$$

$$e_{\phi\phi} = \frac{1}{r\sin\theta}\frac{\partial u_\phi}{\partial \phi} + \frac{u_r}{r} + \frac{u_\theta \cot\theta}{r}\,, \tag{5.3.3c}$$

$$e_{r\theta} = e_{\theta r} = \frac{r}{2}\frac{\partial}{\partial r}\left(\frac{u_\theta}{r}\right) + \frac{1}{2r}\frac{\partial u_r}{\partial \theta}\,, \tag{5.3.3d}$$

$$e_{\theta\phi} = e_{\phi\theta} = \frac{\sin\theta}{2r}\frac{\partial}{\partial \theta}\left(\frac{u_\phi}{r}\right) + \frac{1}{2r\sin\theta}\frac{\partial u_\theta}{\partial \phi}\,, \tag{5.3.3e}$$

and

$$e_{\phi r} = e_{r\phi} = \frac{1}{2r\sin\theta}\frac{\partial u_r}{\partial \phi} + \frac{r}{2}\frac{\partial}{\partial r}\left(\frac{u_\phi}{r}\right)\,, \tag{5.3.3f}$$

p_G is the pressure of the gas inside the bubble, κ_m is the mean curvature of the surface, $\hat{\boldsymbol{n}}$ is the normal unit vector to the surface, σ is a measure of surface tension which we perturb as

$$\sigma = \sigma_0 + \epsilon\sigma_1 P_n^m(\cos\theta)e^{im\phi}\,, \tag{5.3.4}$$

and the surface gradient operator is given by

$$\nabla_{\mathrm{s}} = (\boldsymbol{I} - \hat{\boldsymbol{n}}\hat{\boldsymbol{n}})\cdot\nabla\,. \tag{5.3.5}$$

The unit normal vector can be calculated as such

$$\hat{\boldsymbol{n}} = \left.\frac{\nabla(r-f)}{|\nabla(r-f)|}\right|_{r=f}\,, \tag{5.3.6}$$

where, for $\xi = \cos\theta$,

$$\begin{aligned}\nabla(r-f)|_{r=f} = \hat{\boldsymbol{r}} &- \epsilon\frac{\sin^2\theta}{a}A_{1,n}\frac{\mathrm{d}}{\mathrm{d}\xi}P_n^m(\xi)e^{\mathrm{i}m\phi}\hat{\boldsymbol{\theta}}\\ &- \epsilon\frac{\mathrm{i}m}{a\sin\theta}A_{1,n}P_n^m(\cos\theta)e^{\mathrm{i}m\phi}\hat{\boldsymbol{\phi}} + \boldsymbol{O}(\epsilon^2)\,,\end{aligned} \tag{5.3.7}$$

and

$$|\nabla(r-f)| = 1 + O(\epsilon^2)\,. \tag{5.3.8}$$

In this non-axisymmetric regime the normal vector $\hat{\boldsymbol{n}}$ will have two corresponding tangent vectors, namely $\hat{\boldsymbol{t}}_1$ and $\hat{\boldsymbol{t}}_2$ where

$$\hat{\boldsymbol{t}}_1 = \epsilon\frac{\sin^2\theta}{a}A_{1,n}\frac{\mathrm{d}}{\mathrm{d}\xi}P_n^m(\xi)e^{\mathrm{i}m\phi}\hat{\boldsymbol{r}} + \hat{\boldsymbol{\theta}} + \boldsymbol{O}(\epsilon^2)\,, \tag{5.3.9}$$

and

$$\hat{\boldsymbol{t}}_2 = -\epsilon \frac{\mathrm{i}m}{a \sin\theta} A_{1,n} P_n^m(\cos\theta) e^{\mathrm{i}m\phi} \hat{\boldsymbol{r}} - \hat{\boldsymbol{\phi}} + \boldsymbol{O}(\epsilon^2)\,. \tag{5.3.10}$$

For spherical harmonics $P_n^m(\cos\theta)e^{\mathrm{i}m\phi}$, the following equation holds (see, for example, Jackson, 1999)

$$r^2 \nabla^2 \left(P_n^m(\cos\theta) e^{\mathrm{i}m\phi} \right) = -n(n+1) P_n^m(\cos\theta) e^{\mathrm{i}m\phi}\,. \tag{5.3.11}$$

The mean curvature is given by

$$\begin{aligned} 2\kappa_m &= \nabla \cdot \hat{\boldsymbol{n}}\big|_{r=f} \\ &= \nabla^2 r - \nabla^2 (a + \epsilon A_{1,n} P_n^m(\cos\theta) e^{\mathrm{i}m\phi})\big|_{r=f} \\ &= \frac{2}{a} + \frac{\epsilon A_{1,n}}{a^2}(n-1)(n+2) P_n^m(\cos\theta) e^{\mathrm{i}m\phi} + O(\epsilon^2)\,, \end{aligned} \tag{5.3.12}$$

using (5.3.11). The Lamb solution (5.1.21) to the Stokes equations (5.1.3) has three unknown constants to be determined, namely a_{mn}, b_{mn} and c_{mn}. We will evaluate these by considering the normal and both tangential components of (5.3.1). Taking the dot product of (5.3.1) with $\hat{\boldsymbol{n}}$ gives

$$(\boldsymbol{T} \cdot \hat{\boldsymbol{n}}) \cdot \hat{\boldsymbol{n}} + p_G = 2\kappa_m \sigma\big|_{r=f}\,, \tag{5.3.13}$$

taking the dot product of (5.3.1) with $\hat{\boldsymbol{t}}_1$ gives

$$(\boldsymbol{T} \cdot \hat{\boldsymbol{n}}) \cdot \hat{\boldsymbol{t}}_1 = -\hat{\boldsymbol{t}}_1 \cdot \nabla\sigma\big|_{r=f}\,, \tag{5.3.14}$$

and taking the dot product of (5.3.1) with $\hat{\boldsymbol{t}}_2$ gives

$$(\boldsymbol{T} \cdot \hat{\boldsymbol{n}}) \cdot \hat{\boldsymbol{t}}_2 = -\hat{\boldsymbol{t}}_2 \cdot \nabla\sigma\big|_{r=f}\,. \tag{5.3.15}$$

Solving equations (5.3.13), (5.3.14) and (5.3.15) simultaneously will yield the values of a_{mn}, b_{mn} and c_{mn}. The results of which will be given in Section 5.5.

5.4 Adiabatic gas equation

In this section, we will work under the assumption that the gas in the bubble undergoes an adiabatic process. That is, a process in which a system does not gain or lose heat. This means p_G will be given by

$$p_G V^{\gamma} = \frac{\bar{k}}{\sigma_c \bar{a}^{3\gamma-1}}\,, \tag{5.4.1}$$

where $\bar{k}$ is a constant, V is the volume of the bubble and γ is the adiabatic index. Note that when $\gamma = 1$ we retrieve Boyle's law.

The volume of the bubble can be calculated using the divergence theorem

$$\iiint_V \nabla \cdot \boldsymbol{r}\,\mathrm{d}V = \iint_S \boldsymbol{r} \cdot \hat{\boldsymbol{n}}\,\mathrm{d}S\,, \tag{5.4.2}$$

where S is the surface of the bubble. In spherical coordinates $\boldsymbol{r} = r\hat{\boldsymbol{r}}$ and

$$\nabla \cdot \boldsymbol{r} = \frac{1}{r^2}\frac{\partial\left(r^2 \cdot r\right)}{\partial r} = 3\,. \tag{5.4.3}$$

So, from (5.4.2) we get that

$$V = \frac{1}{3}\iint_S r\hat{\boldsymbol{r}} \cdot \hat{\boldsymbol{n}}\,\mathrm{d}S\,, \tag{5.4.4}$$

where the bubble surface is given by $r = f = a + \epsilon A_{1,n} P_n^m(\cos\theta) e^{\mathrm{i}m\phi}$ which has the unit normal vector given by (5.3.6), namely

$$\hat{\boldsymbol{n}} = \hat{\boldsymbol{r}} - \frac{f_\theta}{f}\hat{\boldsymbol{\theta}} - \frac{f_\phi}{f\sin\theta}\hat{\boldsymbol{\phi}}\,, \tag{5.4.5}$$

where we define f_θ and f_ϕ to be

$$f_\theta = \frac{\partial f}{\partial \theta} \qquad \text{and} \qquad f_\phi = \frac{\partial f}{\partial \phi}\,. \tag{5.4.6}$$

In which case, we have

$$\hat{\boldsymbol{r}} \cdot \hat{\boldsymbol{n}} = 1\,. \tag{5.4.7}$$

Therefore,

$$V = \frac{1}{3}\iint_S f\,\mathrm{d}S\,, \qquad \mathrm{d}S = f^2 \sin\theta\,\mathrm{d}\phi\,\mathrm{d}\theta\,, \tag{5.4.8}$$

and so

$$\begin{aligned} V &= \frac{1}{3}\int_0^{\pi}\int_0^{2\pi}\left(a + \epsilon A_{1,m,n}P_n^m(\cos\theta)e^{\mathrm{i}m\phi}\right)^3 \sin\theta\,\mathrm{d}\phi\,\mathrm{d}\theta\,, \\ &= \frac{a^3}{3}\int_0^{\pi}\int_0^{2\pi}\left(1 + \frac{3\epsilon}{a}A_{1,m,n}P_n^m(\cos\theta)e^{\mathrm{i}m\phi}\right)\sin\theta\,\mathrm{d}\phi\,\mathrm{d}\theta + O(\epsilon^2)\,. \end{aligned} \tag{5.4.9}$$

To evaluate (5.4.9) we need to consider two cases: namely $m = 0$ and $m \neq 0$. For $m = 0$ we get

$$V = \frac{1}{3}\int_0^{\pi}\int_0^{2\pi}\left(a^3 + 3a^2\epsilon A_{1,m,n}P_n(\cos\theta)\right)\sin\theta\,\mathrm{d}\phi\,\mathrm{d}\theta + O(\epsilon^2)\,, \tag{5.4.10}$$

where

$$P_n^0(\cos\theta) = P_n(\cos\theta)\,. \tag{5.4.11}$$

In which case we obtain the same result as (4.5.37) namely

$$V = \frac{4\pi a^3}{3} + 4\pi\epsilon a^2 A_{1,n}\delta_{n,0} + O(\epsilon^2) \tag{5.4.12}$$

where $\delta_{n,0}$ is the Kronecker delta.

For $m \neq 0$, (5.4.9) becomes

$$V = \frac{2\pi a^3}{3}\int_0^{\pi}\sin\theta\,\mathrm{d}\theta = \frac{4\pi a^3}{3}\,. \tag{5.4.13}$$

So, combining the results (5.4.12) and (5.4.13), we get

$$V = \frac{4\pi a^3}{3} + 4\epsilon a^2 A_{1,m,n}(t)\delta_{n,0}\delta_{m,0}\,, \tag{5.4.14}$$

where

$$\delta_{n,0}\delta_{m,0} = \begin{cases} 1 & \text{if } m = n = 0 \\ 0 & \text{else} \end{cases}\,. \tag{5.4.15}$$

So, returning to (5.4.1) we obtain

$$p_G = \frac{k}{\sigma_c \bar{a}^{3\gamma-1} a^{3\gamma}} - \epsilon \frac{\mathcal{B}}{a^{3\gamma-1}} A_{1,m,n} \delta_{n,0} \delta_{m,0} + O(\epsilon^2) \,, \tag{5.4.16}$$

where $k = \bar{k} / \left(\frac{4\pi}{3}\right)^{\gamma}$ and $\mathcal{B}$ is defined as in the axisymmetric case (4.5.43) such that

$$\mathcal{B} = \frac{3k\gamma}{\sigma_c \bar{a}^{3\gamma-1}} \,. \tag{5.4.17}$$

5.5 Amplitude evolution equation

In this section, we want to find specific values of a_{mn}, b_{mn} and c_{mn} for (5.1.22). Returning to (5.3.13), (5.3.14) and (5.3.15) we can write these as:

$$-p + 2e_{rr} - 4e_{r\theta}\frac{f_\theta}{f} - 4e_{r\phi}\frac{f_\phi}{f\sin\theta} + p_G = 2\kappa_m \sigma \,, \tag{5.5.1a}$$

$$2(e_{rr} - e_{\theta\theta})\frac{f_\theta}{f} + 2e_{r\theta} - 2e_{\theta\phi}\frac{f_\phi}{f\sin\theta} = -\frac{1}{f}\frac{\partial\sigma}{\partial\theta} \,, \tag{5.5.1b}$$

$$2(e_{\phi\phi} - e_{rr})\frac{f_\phi}{f\sin\theta} - 2e_{\phi r} + 2e_{\phi\theta}\frac{f_\theta}{f} = \frac{1}{f\sin\theta}\frac{\partial\sigma}{\partial\phi} \,, \tag{5.5.1c}$$

all evaluated at $r = f$. We now substitute (5.3.3) into (5.5.1), linearise with respect to ϵ and compare coefficients of powers of ϵ. Considering terms of $O(1)$ in (5.5.1a), we get the same expression for the leading-order pressure as obtained in the axisymmetric case (4.5.24) where the gas in the bubble undergoes an adiabatic process

$$p_0 = \frac{k}{\sigma_c \bar{a}^{3\gamma-1} a^{3\gamma}} - \frac{2}{a}\sigma_0 - 4\frac{\dot{a}}{a} \,. \tag{5.5.2}$$

By considering all terms of $O(\epsilon)$ in (5.5.1) we obtain three simultaneous equations for the unknown variables a_{mn}, b_{mn} and c_{mn} to solve. Upon solving we get

$$\begin{aligned} a_{mn} = &-\frac{n(2n-1)a^{n-1}}{2n^2+1}\left[(n-1)(n+2)\sigma_0 + \frac{\mathcal{B}}{a^{3\gamma-1}}\delta_{n,0}\delta_{m,0}\right] A_{1,m,n} \\ &- \frac{6n(2n-1)(n-1)\dot{a}a^{n-1}}{2n^2+1} A_{1,m,n} + \frac{n(n-1)(2n-1)a^n}{(2n^2+1)}\sigma_1 \,, \end{aligned} \tag{5.5.3a}$$

$$\begin{aligned} b_{mn} = &-\frac{(n-1)(n+1)a^{n+1}}{2(2n^2+1)(n+2)}\left[(n-1)(n+2)\sigma_0 + \frac{\mathcal{B}}{a^{3\gamma-1}}\delta_{n,0}\delta_{m,0}\right]A_{1,m,n} \\ &- \frac{3(n^2-n+1)\dot{a}a^{n+1}}{2n^2+1}A_{1,m,n} + \frac{(n^2-n+1)a^{n+2}}{2(2n^2+1)}\sigma_1\,, \end{aligned} \tag{5.5.3b}$$

and

$$c_{mn} = 0\,, \tag{5.5.3c}$$

The vanishing of c_{mn} is particularly noteworthy. Since the coefficients c_{mn} multiply the toroidal contribution $\nabla \times (\boldsymbol{r}\chi_{-n-1})$ in the Lamb representation (5.1.21), the condition $c_{mn} = 0$ shows that no rotational or azimuthal component of the flow is generated at $O(\epsilon)$. Consequently, the perturbation dynamics are governed entirely by the irrotational and poloidal parts of the velocity field associated with a_{mn} and b_{mn}. In particular, despite allowing for fully three-dimensional perturbations with arbitrary azimuthal mode number m, the linearised dynamics do not excite any toroidal motion. Substituting (5.5.3) into (5.2.3) we obtain an amplitude evolution equation for the bubble

$$\begin{aligned} \frac{\mathrm{d}A_{1,m,n}}{\mathrm{d}t} = &-\frac{(n+1)(2n+1)}{2a(2n^2+1)(n+2)}\left[(n-1)(n+2)\sigma_0 + \frac{\mathcal{B}}{a^{3\gamma-1}}\delta_{n,0}\delta_{m,0}\right]A_{1,m,n} \\ &- \frac{(4n+1)(n-1)\dot{a}}{(2n^2+1)a}A_{1,m,n} - \frac{(n+1)}{2(2n^2+1)}\sigma_1\,, \end{aligned} \tag{5.5.4}$$

where we recall that the bubble has radius

$$r = a(t) + \epsilon A_{1,m,n}(t)P_n(\cos\theta)\,. \tag{5.5.5}$$

Therefore, if the solution of (5.5.4) grows in time, the bubble is unstable and if the solution decays in time it is stable. We note here that the amplitude evolution equation for the non-axisymmetric case (5.5.4) is the same as the one obtained for the axisymmetric case (4.9.8). Thus we need to consider the effects of surfactants to see if removing axisymmetry makes any difference to bubble stability.

5.6 Surfactant transport equation

We now allow the presence of an insoluble surfactant with surface concentration Γ, which is convected and diffuses along the bubble interface. The dimensionless surfactant transport equation is

$$\frac{\partial\Gamma}{\partial t} + \nabla_{\mathrm{s}} \cdot (\Gamma \boldsymbol{u}_{\mathrm{s}}) + 2\Gamma\kappa_m u_n = \frac{1}{Pe}\nabla_{\mathrm{s}}^2\Gamma\,, \tag{5.6.1}$$

where $\boldsymbol{u}_{\mathrm{s}} = (\boldsymbol{I} - \hat{\boldsymbol{n}}\hat{\boldsymbol{n}}) \cdot \boldsymbol{u}$ is the tangential surface velocity, $u_n = \boldsymbol{u} \cdot \hat{\boldsymbol{n}}$ is the normal velocity, κ_m is the mean curvature, and Pe is the Péclet number defined in (4.8.4) and given by

$$Pe = \frac{\bar{a}\sigma_c}{\mu D_{\mathrm{s}}}\,. \tag{5.6.2}$$

We need to calculate the terms $\nabla_{\mathrm{s}}\cdot(\Gamma\boldsymbol{u}_{\mathrm{s}})$, u_n and $\nabla_{\mathrm{s}}^2\Gamma$ in (5.6.1). The derivation of which closely follows the axisymmetric case in Section 4.8, the principal difference being the additional azimuthal dependence introduced through the ϕ-coordinate. For the perturbed interface

$$r = f(\theta,\phi,t) = a(t) + \epsilon A_{1,m,n}(t)P_n^m(\cos\theta)e^{\mathrm{i}m\phi}\,, \tag{5.6.3}$$

as shown in Figure 5.6.1, the outward unit normal vector is

$$\hat{\boldsymbol{n}} = \frac{1}{M}\left(\hat{\boldsymbol{r}} - \frac{f_\theta}{f}\hat{\boldsymbol{\theta}} - \frac{f_\phi}{f\sin\theta}\hat{\boldsymbol{\phi}}\right)\,, \tag{5.6.4}$$

where

$$M^2 = 1 + \frac{f_\theta^2}{f^2} + \frac{f_\phi^2}{f^2\sin^2\theta}\,, \tag{5.6.5}$$

and the two corresponding unit tangent vectors are

$$\hat{\boldsymbol{t}}_1 = \frac{1}{M}\left(\frac{f_\theta}{f}\hat{\boldsymbol{r}} + \hat{\boldsymbol{\theta}}\right)\,, \tag{5.6.6}$$

and

$$\hat{\boldsymbol{t}}_2 = \frac{1}{M}\left(\frac{f_\phi}{f\sin\theta}\hat{\boldsymbol{r}} + \hat{\boldsymbol{\phi}}\right)\,. \tag{5.6.7}$$

Consequently, the normal velocity is given by

$$u_n = \frac{1}{M}\left(u_r - \frac{f_\theta}{f}u_\theta - \frac{f_\phi}{f\sin\theta}u_\phi\right) . \tag{5.6.8}$$

Here we use the notation

$$f_\theta = \frac{\partial f}{\partial \theta} \qquad \text{and} \qquad f_\phi = \frac{\partial f}{\partial \phi} . \tag{5.6.9}$$

Using the surface metric associated with the parametrisation (θ, ϕ), the two-dimensional surface is given by

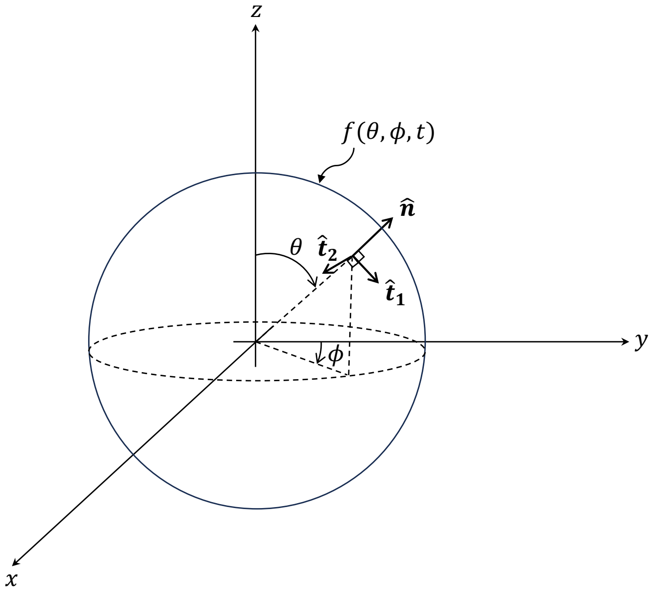

Figure 5.6.1: Diagram showing the surface of the bubble.

$$\boldsymbol{x}_\mathrm{s} = x\,\hat{\mathbf{i}} + y\,\hat{\mathbf{j}} + z\,\hat{\mathbf{k}} , \tag{5.6.10}$$

where (x, y, z) are constrained to lie on the surface such that

$$x = r\sin\theta\cos\phi|_{r=f} = f\sin\theta\cos\phi , \tag{5.6.11}$$

$$y = r\sin\theta\sin\phi|_{r=f} = f\sin\theta\sin\phi , \tag{5.6.12}$$

$$z = r\cos\theta|_{r=f} = f\cos\theta . \tag{5.6.13}$$

The surface velocity $\boldsymbol{u}_{\mathrm{s}}$ is given by

$$\boldsymbol{u}_{\mathrm{s}} = (f_\theta\, u^{(1)} + f_\phi\, u^{(2)})\hat{\boldsymbol{r}} + f\, u^{(1)}\hat{\boldsymbol{\theta}} + f\sin\theta\, u^{(2)}\hat{\boldsymbol{\phi}}\,, \tag{5.6.14}$$

where

$$u^{(1)} = \frac{(f^2 u_\theta + f_\theta f u_r)\sin^2\theta - f_\theta f_\phi \sin\theta u_\phi + f_\phi^2 u_\theta}{M^2 f^3 \sin^2\theta}\,, \tag{5.6.15a}$$

and

$$u^{(2)} = \frac{(f^2 + f_\theta^2)\sin\theta u_\phi + f_\phi(f u_r - f_\theta u_\theta)}{M^2 f^3 \sin^2\theta}\,, \tag{5.6.15b}$$

where u_r, u_θ and u_ϕ are given by (5.1.22a), (5.1.22b) and (5.1.22c) respectively and are to be evaluated at $r = f$.

The surface divergence and Laplacian operators associated with the surface parametrisation (θ, ϕ) may be written as

$$\nabla_{\mathrm{s}}\cdot(\Gamma\boldsymbol{u}_{\mathrm{s}}) = \frac{1}{Mf^2\sin\theta}\left[\frac{\partial}{\partial\theta}\left(\Gamma M f^2 \sin\theta\, u^{(1)}\right) + \frac{\partial}{\partial\phi}\left(\Gamma M f^2\sin\theta\, u^{(2)}\right)\right]\,, \tag{5.6.16}$$

and

$$\begin{aligned}\nabla_{\mathrm{s}}^2\Gamma = {}& \frac{1}{Mf^2\sin\theta}\frac{\partial}{\partial\theta}\left[\frac{f^2\sin^2\theta + f_\phi^2}{Mf^2\sin\theta}\frac{\partial\Gamma}{\partial\theta} - \frac{f_\theta f_\phi}{Mf^2\sin\theta}\frac{\partial\Gamma}{\partial\phi}\right] \\ &+ \frac{1}{Mf^2\sin\theta}\frac{\partial}{\partial\phi}\left[-\frac{f_\theta f_\phi}{Mf^2\sin\theta}\frac{\partial\Gamma}{\partial\theta} + \frac{f^2+f_\theta^2}{Mf^2\sin\theta}\frac{\partial\Gamma}{\partial\phi}\right]\,.\end{aligned} \tag{5.6.17}$$

We now substitute (5.6.16) and (5.6.17) into (5.6.1) and where $2\kappa_m$ and u_n are given by (5.3.12) and (5.6.8) respectively.

We linearise the surfactant transport equation (5.6.1) with respect to ϵ by writing

$$\Gamma(\theta,\phi,t) = \Gamma_0(t) + \epsilon\Gamma_{1,m,n}(t)P_n^m(\cos\theta)e^{\mathrm{i}m\phi}\,. \tag{5.6.18}$$

At $O(1)$ we recover

$$\frac{\mathrm{d}\Gamma_0}{\mathrm{d}t} + 2\frac{\dot{a}}{a}\Gamma_0 = 0\,, \tag{5.6.19}$$

with solution

$$\Gamma_0 = \frac{\Gamma_R}{a^2}\,, \tag{5.6.20}$$

where Γ_R is given as in (4.8.67). Proceeding to $O(\epsilon)$ yields

$$\begin{aligned}\frac{\mathrm{d}\Gamma_{1,m,n}}{\mathrm{d}t} &+ 2\frac{\dot{a}}{a}\Gamma_{1,m,n} + \frac{n(n+1)}{a^2}\frac{1}{Pe}\Gamma_{1,m,n} \\ &= -\frac{3n(n-1)(2n-1)\dot{a}\Gamma_0}{a^2(2n^2+1)}A_{1,m,n} \\ &\quad + \frac{(n+1)\Gamma_0}{2a^2(2n^2+1)}\left[(n+2)(n-1)\sigma_0 + \frac{\mathcal{B}}{a^{3\gamma-1}}\delta_{n0}\delta_{m0}\right]A_{1,m,n} \\ &\quad + \frac{(n+1)(2n^2-n+2)\Gamma_0}{2a(2n^2+1)}\sigma_1\,. \end{aligned} \tag{5.6.21}$$

The surface tension is related to the surfactant concentration through the Langmuir equation of state

$$\sigma = 1 + \beta_s \ln(1-\Gamma)\,, \tag{5.6.22}$$

which, upon linearisation, gives

$$\sigma_0 = 1 + \beta_s \ln(1-\Gamma_0)\,, \tag{5.6.23}$$

and

$$\sigma_1 = -\beta_s \frac{\Gamma_{1,m,n}}{1-\Gamma_0}\,. \tag{5.6.24}$$

We therefore recover the same leading-order surfactant transport structure (5.6.20) as in the axisymmetric problem (4.8.68), with the principal modification arising from the additional azimuthal dependence through the ϕ-coordinate. This introduces extra geometric contributions involving f_ϕ into the surface divergence and Laplacian operators, but the resulting linearised evolution equation for the surfactant perturbation (5.6.21) retains the same coupled amplitude–surfactant form obtained previously (4.8.69). Consequently, each spherical harmonic mode (m,n) evolves independently at linear order.

5.7 Stability system for a non-axisymmetric bubble

If we substitute (5.6.24) into (5.5.4) and (5.6.21) we obtain a linear system for the perturbed bubble radius and surfactant concentration

$$\frac{\mathrm{d}}{\mathrm{d}t}\begin{pmatrix} A_{1,n}(t) \\ \Gamma_{1,n}(t) \end{pmatrix} = \begin{pmatrix} m_1(t) & m_2(t) \\ m_3(t) & m_4(t) \end{pmatrix}\begin{pmatrix} A_{1,n}(t) \\ \Gamma_{1,n}(t) \end{pmatrix}, \tag{5.7.1}$$

where the matrix entries $m_i(t), i = 1, ..., 4$ are periodic functions of time given by

$$m_1(t) = -\frac{(n-1)(4n+1)}{2n^2+1}\frac{\dot{a}}{a} - \frac{2n+1}{a(n+2)}L\Pi(t)\,, \tag{5.7.2}$$

$$\begin{aligned} m_2(t) &= \frac{a^2\beta_s}{a^2-\Gamma_R}L\,, \\ m_3(t) &= -\frac{3n(n-1)(2n-1)\Gamma_R}{(2n^2+1)}\frac{\dot{a}}{a^4} + \frac{\Gamma_R}{a^4}L\Pi(t)\,, \\ m_4(t) &= -\frac{(2n^2-n+2)\beta_s\Gamma_R}{a(a^2-\Gamma_R)}L - \frac{n(n+1)\Gamma_R}{a^2}\frac{1}{Pe} - 2\frac{\dot{a}}{a}\,, \end{aligned} \tag{5.7.3}$$

and

$$\Pi(t) = (n+2)(n-1)\sigma_0(t) + \frac{\mathcal{B}}{a^{3\gamma-1}}\delta_{n,0}\,, \qquad L = \frac{n+1}{2(2n^2+1)}\,. \tag{5.7.4}$$

We observe that the system (5.7.1) is independent of the azimuthal mode number m and therefore exhibits no azimuthal dependence. Similar behaviour has been observed elsewhere in the literature. For example, Adou & Tuckerman (2016) used Floquet analysis for Faraday instability on a sphere in a non-axisymmetric regime and likewise obtained a stability problem independent of m. Comparing (5.7.1) with (4.9.54), we see that the axisymmetric and non-axisymmetric stability systems are identical.

Consequently, the corresponding Floquet multipliers and stability boundaries are also independent of m, with any coupling between azimuthal modes arising only through non-linear effects beyond the present linear analysis. This suggests that additional physical effects are required in order to generate instabilities. In Chapter 6, we therefore extend the analysis to include inertial effects.

6

Stability analysis for a bubble experiencing inertia

Synopsis

In this chapter, inertial effects are incorporated by extending the bubble model to the full incompressible Navier–Stokes equations. Using a stream-function formulation, a linear stability problem is derived for axisymmetric perturbations about a spherical base state.

Exact solutions are obtained for a steady bubble radius, leading to an implicit relation for the growth rate. Asymptotic and numerical analysis over a wide range of Laplace numbers provides evidence that inertia does not destabilise the bubble. In all cases considered, perturbations decay or remain neutrally stable.

6.1 The effect of inertia

All analysis up to this point has assumed that the effect of inertia was negligible in comparison to the effect of viscosity. We now relax this assumption and consider the full Navier–Stokes equations (2.1.17) for an incompressible fluid with velocity field $\boldsymbol{u}$

$$La\left(\frac{\partial \boldsymbol{u}}{\partial t} + (\boldsymbol{u}\cdot\nabla)\boldsymbol{u}\right) = -\nabla p + \nabla^2 \boldsymbol{u}\,, \tag{6.1.1a}$$

$$\nabla\cdot\boldsymbol{u} = 0\,, \tag{6.1.1b}$$

where La denotes the Laplace number and no external body forces are assumed.

To facilitate the use of a stream-function formulation, we take the curl of (6.1.1a),

$$La\left(\nabla\times\frac{\partial\boldsymbol{u}}{\partial t}+\nabla\times(\boldsymbol{u}\cdot\nabla)\boldsymbol{u}\right)=-\nabla\times\nabla p+\nabla\times\nabla^2\boldsymbol{u}\,. \tag{6.1.2}$$

Since $\nabla\times\nabla p=0$ and, for incompressible flow, $\nabla^2\boldsymbol{u}=-\nabla\times(\nabla\times\boldsymbol{u})$, this reduces to

$$La\left(\frac{\partial}{\partial t}(\nabla\times\boldsymbol{u})+\nabla\times(\boldsymbol{u}\cdot\nabla)\boldsymbol{u}\right)=-\nabla\times\nabla\times\nabla\times\boldsymbol{u}\,. \tag{6.1.3}$$

Using the vector identity

$$\nabla\times(\boldsymbol{u}\cdot\nabla)\boldsymbol{u}=\nabla\times\nabla\left(\frac{\boldsymbol{u}^2}{2}\right)-\nabla\times\boldsymbol{u}\times\nabla\times\boldsymbol{u} \tag{6.1.4}$$

$$=(\boldsymbol{u}\cdot\nabla)\nabla\times\boldsymbol{u}-((\nabla\times\boldsymbol{u})\cdot\nabla)\boldsymbol{u}\,, \tag{6.1.5}$$

equation (6.1.3) may be written in the vorticity form

$$La\left(\frac{\partial}{\partial t}(\nabla\times\boldsymbol{u})+(\boldsymbol{u}\cdot\nabla)\nabla\times\boldsymbol{u}\right)=La((\nabla\times\boldsymbol{u})\cdot\nabla)\boldsymbol{u}-\nabla\times\nabla\times\nabla\times\boldsymbol{u}\,, \tag{6.1.6}$$

We now assume axisymmetry, so that $\boldsymbol{u}=(u_r,u_\theta,0)$, and introduce a Stokes stream function $\psi(r,\theta,t)$ defined by

$$u_r=\frac{1}{r^2\sin\theta}\frac{\partial\psi}{\partial\theta}\,,\qquad u_\theta=-\frac{1}{r\sin\theta}\frac{\partial\psi}{\partial r}\,, \tag{6.1.7}$$

or equivalently,

$$\boldsymbol{u}=\nabla\times\left(\frac{\psi}{r\sin\theta}\hat{\boldsymbol{\phi}}\right)\,. \tag{6.1.8}$$

With this definition,

$$\nabla\times\boldsymbol{u}=\nabla\times\nabla\times\left(\frac{\psi}{r\sin\theta}\hat{\boldsymbol{\phi}}\right)=\left(\frac{-D^2\psi}{r\sin\theta}\hat{\boldsymbol{\phi}}\right)\,, \tag{6.1.9}$$

and

$$\nabla\times\nabla\times\nabla\times\nabla\times\left(\frac{\psi}{r\sin\theta}\hat{\boldsymbol{\phi}}\right)=\left(\frac{D^4\psi}{r\sin\theta}\hat{\boldsymbol{\phi}}\right)\,, \tag{6.1.10}$$

where the operator D^2 is defined by

$$D^2 \equiv \frac{\partial^2}{\partial r^2} + \frac{1}{r^2}\frac{\partial^2}{\partial \theta^2} - \frac{\cos\theta}{r^2 \sin\theta}\frac{\partial}{\partial \theta}\,. \tag{6.1.11}$$

The advective operator takes the form

$$\begin{align} \boldsymbol{u}\cdot\nabla &= \left(\frac{1}{r^2\sin\theta}\frac{\partial\psi}{\partial\theta}\hat{\boldsymbol{r}} - \frac{1}{r\sin\theta}\frac{\partial\psi}{\partial r}\hat{\boldsymbol{\theta}}\right)\cdot\left(\frac{\partial}{\partial r}\hat{\boldsymbol{r}} + \frac{1}{r}\frac{\partial}{\partial\theta}\hat{\boldsymbol{\theta}} + \frac{1}{r\sin\theta}\frac{\partial}{\partial\phi}\hat{\boldsymbol{\phi}}\right) \tag{6.1.12}\\ &= \frac{1}{r^2\sin\theta}\frac{\partial\psi}{\partial\theta}\frac{\partial}{\partial r} - \frac{1}{r^2\sin\theta}\frac{\partial\psi}{\partial r}\frac{\partial}{\partial\theta}\,, \tag{6.1.13} \end{align}$$

and so

$$\begin{align} (\boldsymbol{u}\cdot\nabla)(\nabla\times\boldsymbol{u}) &= \left(\frac{1}{r^2\sin\theta}\frac{\partial\psi}{\partial\theta}\frac{\partial}{\partial r} - \frac{1}{r^2\sin\theta}\frac{\partial\psi}{\partial r}\frac{\partial}{\partial\theta}\right)\left(\frac{-D^2\psi}{r\sin\theta}\hat{\boldsymbol{\phi}}\right)\\ &= -\frac{1}{r^3\sin^2\theta}\frac{\partial\psi}{\partial\theta}\frac{\partial}{\partial r}(D^2\psi)\hat{\boldsymbol{\phi}} + \frac{1}{r^4\sin^2\theta}\frac{\partial\psi}{\partial\theta}(D^2\psi)\hat{\boldsymbol{\phi}}\\ &+ \frac{1}{r^3\sin^2\theta}\frac{\partial\psi}{\partial r}\frac{\partial}{\partial\theta}(D^2\psi)\hat{\boldsymbol{\phi}} - \frac{\cos\theta}{r^3\sin^3\theta}\frac{\partial\psi}{\partial r}(D^2\psi)\hat{\boldsymbol{\phi}}\,, \tag{6.1.14} \end{align}$$

Next we calculate

$$(\nabla\times\boldsymbol{u})\cdot\nabla = \left(\frac{-D^2\psi}{r\sin\theta}\hat{\boldsymbol{\phi}}\right)\cdot\left(\frac{\partial}{\partial r}\hat{\boldsymbol{r}} + \frac{1}{r}\frac{\partial}{\partial\theta}\hat{\boldsymbol{\theta}} + \frac{1}{r\sin\theta}\frac{\partial}{\partial\phi}\hat{\boldsymbol{\phi}}\right) = \frac{-D^2\psi}{r^2\sin^2\theta}\frac{\partial}{\partial\phi}\,, \tag{6.1.15}$$

from which it follows that

$$\begin{align} ((\nabla\times\boldsymbol{u})\cdot\nabla)\boldsymbol{u} &= \frac{-D^2\psi}{r^2\sin^2\theta}\frac{\partial}{\partial\phi}\left(\frac{1}{r^2\sin\theta}\frac{\partial\psi}{\partial\theta}\hat{\boldsymbol{r}} - \frac{1}{r\sin\theta}\frac{\partial\psi}{\partial r}\hat{\boldsymbol{\theta}}\right) \tag{6.1.16}\\ &= -\frac{D^2\psi}{r^4\sin^2\theta}\frac{\partial\psi}{\partial\theta}\hat{\boldsymbol{\phi}} + D^2\psi\frac{\cos\theta}{r^3\sin^3\theta}\frac{\partial\psi}{\partial r}\hat{\boldsymbol{\phi}}\,, \tag{6.1.17} \end{align}$$

as

$$\frac{\partial\hat{\boldsymbol{r}}}{\partial\phi} = \sin\theta\hat{\boldsymbol{\phi}} \qquad \text{and} \qquad \frac{\partial\hat{\boldsymbol{\theta}}}{\partial\phi} = \cos\theta\hat{\boldsymbol{\phi}}\,. \tag{6.1.18}$$

Substituting (6.1.14) and (6.1.17) into (6.1.6) yields a single scalar evolution equation for the stream function. Introducing $\xi = \cos\theta$, this equation may be written as

$$La\left(\frac{\partial(D^2\psi)}{\partial t}+\frac{1}{r^2}\left[\frac{\partial\psi}{\partial r}\frac{\partial(D^2\psi)}{\partial\xi}-\frac{\partial(D^2\psi)}{\partial r}\frac{\partial\psi}{\partial\xi}\right]\right.$$
$$\left.+\frac{2}{r^2}\left[\frac{\xi}{1-\xi^2}\frac{\partial}{\partial r}+\frac{1}{r}\frac{\partial}{\partial\xi}\right]\psi D^2\psi\right)=D^4\psi\,. \tag{6.1.19}$$

By noting that the Jacobian determinant is given by

$$\frac{\partial(\psi,D^2\psi)}{\partial(r,\xi)}=\frac{\partial\psi}{\partial r}\frac{\partial(D^2\psi)}{\partial\xi}-\frac{\partial(D^2\psi)}{\partial r}\frac{\partial\psi}{\partial\xi}\,, \tag{6.1.20}$$

and defining the operator L as

$$L=\frac{\xi}{1-\xi^2}\frac{\partial}{\partial r}+\frac{1}{r}\frac{\partial}{\partial\xi}\,, \tag{6.1.21}$$

we can write (6.1.19) in the form

$$La\left[\frac{\partial(D^2\psi)}{\partial t}+\frac{1}{r^2}\left(\frac{\partial(\psi,D^2\psi)}{\partial(r,\xi)}+2D^2\psi L\psi\right)\right]=D^4\psi\,, \tag{6.1.22}$$

which agrees with the equivalent equation given in the paper by Riley (1966), for example.

6.2 Form of stream function in Navier–Stokes flow

As in Chapter 4, we introduce a perturbation to the stream function such that

$$\psi(r,\xi,t)=\psi_0(t)+\epsilon\psi_1(r,\xi,t)\,, \tag{6.2.1}$$

where $\epsilon \ll 1$ and we assume that ψ_0 is given as in (4.2.12)

$$\psi_0(t)=-a^2\dot{a}\xi\,, \tag{6.2.2}$$

corresponding to the spherically symmetric base flow induced by radial motion of the interface, while ψ_1 represents the perturbation to be determined.

Substituting (6.2.1) into the operators D^2 (6.1.11), L (6.1.21), and the Jacobian determinant (6.1.20), we obtain

$$D^2\psi = \epsilon\left(\frac{\partial^2\psi_1}{\partial r^2} + \frac{1-\xi^2}{r^2}\frac{\partial^2\psi_1}{\partial\xi^2}\right) = \epsilon D^2\psi_1\,, \tag{6.2.3}$$

$$L\psi = \epsilon\frac{\xi}{1-\xi^2}\frac{\partial\psi_1}{\partial r} + \frac{1}{r}\left(-a^2\dot{a} + \epsilon\frac{\partial\psi_1}{\partial\xi}\right)\,, \tag{6.2.4}$$

and

$$\frac{\partial(\psi, D^2\psi)}{\partial(r,\xi)} = \epsilon\frac{\partial\psi_1}{\partial r}\frac{\partial}{\partial\xi}(\epsilon D^2\psi_1) - \frac{\partial}{\partial r}(\epsilon D^2\psi_1)\left(-a^2\dot{a} + \epsilon\frac{\partial\psi_1}{\partial\xi}\right)\,. \tag{6.2.5}$$

Substituting these expressions into the stream-function equation (6.1.22), we find that the $O(1)$ terms vanish identically, confirming that the choice (6.2.2) is consistent with the governing equations. Retaining terms at $O(\epsilon)$ yields the linearised perturbation equation

$$La\left[\frac{\partial(D^2\psi_1)}{\partial t} + \frac{a^2\dot{a}}{r^2}\left(\frac{\partial(D^2\psi_1)}{\partial r} - \frac{2}{r}D^2\psi_1\right)\right] = D^4\psi_1\,. \tag{6.2.6}$$

We now decompose ψ_1 such that

$$\psi_1(r,\xi,t) = \sum_{n=0}^{\infty} g_n(r,t)\mathscr{P}_n(\xi)\,, \tag{6.2.7}$$

where we recall that

$$\mathscr{P}_n(\xi) = \int_{-1}^{\xi} P_n(x)\,\mathrm{d}x\,. \tag{6.2.8}$$

and the form of $g_n(r,t)$ is to be determined.

Applying D^2 once more gives

$$D^2\psi_1 = \frac{\partial^2 g}{\partial r^2}\mathscr{P}_n(\xi) + \frac{1-\xi^2}{r^2}g\mathscr{P}_n''(\xi)\,, \tag{6.2.9}$$

but we know from (4.2.22b) that

$$\mathscr{P}_n''(\xi) = -\frac{n(n+1)}{1-\xi^2}\mathscr{P}_n(\xi)\,, \tag{6.2.10}$$

which means we can express (6.2.9) as

$$D^2\psi_1 = w_n\mathscr{P}_n(\xi)\,, \tag{6.2.11}$$

where

$$w_n(r,t) = \frac{\partial^2 g_n}{\partial r^2} - \frac{n(n+1)}{r^2}g_n\,. \tag{6.2.12}$$

In addition, by taking the operator D^2 of both sides of (6.2.11) we obtain

$$D^4\psi_1 = \left(\frac{\partial^2 w_n}{\partial r^2} - \frac{n(n+1)}{r^2}w_n\right)\mathscr{P}_n(\xi)\,. \tag{6.2.13}$$

Substituting these expressions into (6.2.6), we obtain a governing equation for $w_n(r,t)$,

$$La\left[\frac{\partial w_n}{\partial t} + \frac{a^2\dot{a}}{r^2}\left(\frac{\partial w_n}{\partial r} - \frac{2}{r}w_n\right)\right] = \frac{\partial^2 w_n}{\partial r^2} - \frac{n(n+1)}{r^2}w_n\,. \tag{6.2.14}$$

The first-order radial derivative term arises from advection by the underlying radial flow and complicates the structure of the equation. We therefore seek a transformation which removes the advective contribution and reduces (6.2.14) to a simpler diffusion-type equation. To this end, we introduce the factorisation

$$w_n(r,t) = \zeta(r,t)\chi(r,t)\,, \tag{6.2.15}$$

which, upon substitution into (6.2.14), yields

$$\begin{aligned} La\chi\frac{\partial\zeta}{\partial t} + La\zeta\frac{\partial\chi}{\partial t} = \chi\frac{\partial^2\zeta}{\partial r^2} + 2\frac{\partial\chi}{\partial r}\frac{\partial\zeta}{\partial r} + \zeta\frac{\partial^2\chi}{\partial r^2} - La\frac{a^2\dot{a}}{r^2}\left(\chi\frac{\partial\zeta}{\partial r} + \zeta\frac{\partial\chi}{\partial r}\right)& \\ + \left(La\frac{2a^2\dot{a}}{r^3} - \frac{n(n+1)}{r^2}\right)\chi\zeta\,.& \end{aligned} \tag{6.2.16}$$

To eliminate all $\partial_r\zeta$ terms, we require χ to satisfy

$$2\frac{\partial\chi}{\partial r} - La\frac{a^2\dot{a}}{r^2}\chi = 0\,, \tag{6.2.17}$$

which integrates to

$$\chi(r,t) = C(t)\exp\left(-La\frac{a^2\dot{a}}{2r}\right). \tag{6.2.18}$$

Without loss of generality, we set $C(t) = 1$. Dividing (6.2.16) by χ then gives

$$La\frac{\partial\zeta}{\partial t} = \frac{\partial^2\zeta}{\partial r^2} + V(r,t)\zeta\,, \tag{6.2.19}$$

where

$$V(r,t) = La^2\frac{a^2\ddot{a}}{2r} + La^2\frac{a\dot{a}^2}{r} - La^2\frac{a^4\dot{a}^2}{4r^4} + La\frac{a^2\dot{a}}{r^3} - \frac{n(n+1)}{r^2}\,. \tag{6.2.20}$$

An additional advantage of the transformation is that the resulting equation (6.2.19) contains no first-order radial derivatives. This simplifies the numerical treatment of the problem, since only second-order radial derivatives need to be discretised, avoiding the additional approximation associated with advective terms. Although we do not pursue a numerical solution of the transformed system in this thesis and instead focus on solving (6.2.14) in Section 6.8, the transformed formulation could, in principle, be used as the basis for a numerical implementation.

6.3 Stream function solution for steady base-state bubble radius

To facilitate analytical progress, we first consider the simplified case in which the leading-order bubble radius remains constant. This corresponds to setting $\Delta = 0$ in (4.3.9), so that the base-state radius satisfies $a = 1$. The more general case of a time-dependent base-state bubble radius will be examined in Section 6.8.

Under this assumption, the coefficient $\chi(r,t)$ reduces to unity and the governing equation (6.2.19) for w_n simplifies to

$$La\frac{\partial w_n}{\partial t} = \frac{\partial^2 w_n}{\partial r^2} - \frac{n(n+1)}{r^2}w_n\,. \tag{6.3.1}$$

Substituting the definition of w given in (6.2.12) into (6.3.1) yields an evolution equation for the stream-function amplitude $g_n(r,t)$,

$$La\frac{\partial}{\partial t}\left(\frac{\partial^2 g_n}{\partial r^2}-\frac{n(n+1)}{r^2}g_n\right)=\frac{\partial^2}{\partial r^2}\left(\frac{\partial^2 g_n}{\partial r^2}-\frac{n(n+1)}{r^2}g_n\right)\\ -\frac{n(n+1)}{r^2}\left(\frac{\partial^2 g_n}{\partial r^2}-\frac{n(n+1)}{r^2}g_n\right). \tag{6.3.2}$$

We seek separable solutions of the form

$$g_n(r,t)=e^{st}F(r)\,, \tag{6.3.3}$$

where s denotes the temporal growth rate. Substitution of (6.3.3) into (6.3.2) leads to the fourth-order ordinary differential equation

$$F'''' - \frac{1}{r^2}\left(2n(n+1)+sLa\,r^2\right)F''+\frac{4n(n+1)}{r^3}F'\\ +\frac{n(n+1)}{r^4}\left((n+3)(n-2)+sLa\,r^2\right)F=0\,. \tag{6.3.4}$$

As a consistency check, we consider the highly viscous limit $La \ll 1$, in which inertial effects are negligible. In this regime, (6.3.4) reduces to

$$F''''-\frac{2n(n+1)}{r^2}F''+\frac{4n(n+1)}{r^3}F'+\frac{n(n+1)(n+3)(n-2)}{r^4}F=0+O(\epsilon^2)\,. \tag{6.3.5}$$

The general solution of (6.3.5) is

$$F(r)=c_1r^{-n}+c_2r^{n+1}+c_3r^{n+3}+c_4r^{2-n}\,, \tag{6.3.6}$$

which coincides with the classical solution obtained from the Stokes equations, providing a useful validation of the formulation.

For finite La, the general solution of (6.3.4) may be written as

$$F(r)=c_1r^{-n}+c_2r^{n+1}+c_3\sqrt{r}J_{n+\frac{1}{2}}(\sqrt{-sLa}\,r)+c_4\sqrt{r}Y_{n+\frac{1}{2}}(\sqrt{-sLa}\,r)\,, \tag{6.3.7}$$

where J and Y are Bessel functions of the first and second kind respectively.

Introducing the notation

$$z = \sqrt{-sLa}\,,$$

and expressing the solution in terms of spherical Bessel functions, (6.3.7) may equivalently be written as

$$F(r) = c_1 r^{-n} + c_2 r^{n+1} + \sqrt{\frac{2z}{\pi}}\, q(r)\,, \tag{6.3.8}$$

where, for the same c_3 and c_4 as in (6.3.7),

$$q(r) = c_3 r j_n(zr) + c_4 r y_n(zr)\,. \tag{6.3.9}$$

Here, $j_n(z)$ and $y_n(z)$ are spherical Bessel functions which are related to Bessel functions via

$$j_n(z) = \sqrt{\frac{\pi}{2z}}\, J_{n+\frac{1}{2}}(z) \qquad \text{and} \qquad y_n(z) = \sqrt{\frac{\pi}{2z}}\, Y_{n+\frac{1}{2}}(z)\,. \tag{6.3.10}$$

Spherical Bessel functions can be expressed by Rayleigh's formulas (see, for example, Abramowitz & Stegun, 1964, p.439)

$$j_n(z) = (-z)^n \left(\frac{1}{z}\frac{\mathrm{d}}{\mathrm{d}z}\right)^n \left(\frac{\sin z}{z}\right)\,, \tag{6.3.11a}$$

and

$$y_n(z) = -(-z)^n \left(\frac{1}{z}\frac{\mathrm{d}}{\mathrm{d}z}\right)^n \left(\frac{\cos z}{z}\right)\,. \tag{6.3.11b}$$

The admissible form of $F(r)$ is determined by enforcing the far-field condition

$$u_r \sim 0 \qquad \text{and} \qquad u_\theta \sim 0 \qquad \text{as} \qquad r \to \infty\,, \tag{6.3.12}$$

where the velocity components are given by

$$u_r = -\frac{1}{r^2}\frac{\partial \psi}{\partial \xi} = \frac{1}{r^2}\left[-a^2 \dot{a} + \epsilon e^{st} F(r) P_n(\xi)\right]\,, \tag{6.3.13a}$$

and

$$u_\theta = -\frac{1}{r\sqrt{1-\xi^2}}\frac{\partial\psi}{\partial r} = -\frac{\epsilon}{r\sqrt{1-\xi^2}}e^{st}F'(r)\mathscr{P}_n(\xi)\,. \tag{6.3.13b}$$

To analyse the far-field behaviour, we employ the large-argument asymptotics of the spherical Bessel functions. For fixed order and $|z| \gg 1$, the corresponding ordinary Bessel functions satisfy (see, for example, Abramowitz & Stegun, 1964, p.364)

$$J_n(z) = \sqrt{\frac{2}{\pi z}}\left\{\cos\left(z - \frac{n\pi}{2} - \frac{\pi}{4}\right) + O(|z|^{-1})\right\}\,, \tag{6.3.14a}$$

and

$$Y_n(z) = \sqrt{\frac{2}{\pi z}}\left\{\sin\left(z - \frac{n\pi}{2} - \frac{\pi}{4}\right) + O(|z|^{-1})\right\}\,. \tag{6.3.14b}$$

Using the relations between ordinary and spherical Bessel functions (6.3.10), it follows that, for $|z| \gg 1$, the spherical Bessel functions behave as

$$j_n(z) \sim \frac{1}{z}\sin\left(z - \frac{n\pi}{2}\right)\,, \tag{6.3.15a}$$

and

$$y_n(z) \sim -\frac{1}{z}\cos\left(z - \frac{n\pi}{2}\right)\,. \tag{6.3.15b}$$

Consequently, the large-r behaviour of (6.3.9) is

$$zq \sim c_3\sin\left(zr - \frac{n\pi}{2}\right) - c_4\cos\left(zr - \frac{n\pi}{2}\right)\,. \tag{6.3.16}$$

Writing $z = z_r + \mathrm{i}z_i$ and expressing the trigonometric functions in exponential form yields

$$\begin{aligned} zq \sim{}& \frac{c_3}{2\mathrm{i}}\left(\exp\left(\mathrm{i}z_r r - z_i r - \mathrm{i}\frac{n\pi}{2}\right) - \exp\left(-\mathrm{i}z_r r + z_i r + \mathrm{i}\frac{n\pi}{2}\right)\right) \\ &- \frac{c_4}{2}\left(\exp\left(\mathrm{i}z_r r - z_i r - \mathrm{i}\frac{n\pi}{2}\right) + \exp\left(-\mathrm{i}z_r r + z_i r + \mathrm{i}\frac{n\pi}{2}\right)\right)\,, \end{aligned} \tag{6.3.17}$$

Differentiating (6.3.8) gives

$$F'(r) = -c_1 n r^{-n-1} + (n+1)c_2 r^n + \sqrt{\frac{2z}{\pi}}q'(r)\,, \tag{6.3.18}$$

where, for $r \gg 1$,

$$q'(r) \sim \frac{c_3 - \mathrm{i}c_4}{2} \exp\left(\mathrm{i}z_r r - z_i r - \mathrm{i}\frac{n\pi}{2}\right) + \frac{c_3 + \mathrm{i}c_4}{2} \exp\left(-\mathrm{i}z_r r + z_i r + \mathrm{i}\frac{n\pi}{2}\right) . \tag{6.3.19}$$

We now distinguish three cases according to the sign of z_i, corresponding to different far-field behaviours.

Case 1: $z_i = 0$

In this case s_1 is purely real, with $s_i = 0$ and $s_r = -s_R$ for $s_R > 0$, so that $z = \sqrt{s_R La}$. Substituting (6.3.8) and (6.3.18) into (6.3.13), we find that the algebraic term proportional to r^n must be eliminated, requiring $c_2 = 0$. With this restriction, the oscillatory contributions decay as r^{-1} and hence both u_r and u_θ vanish as $r \to \infty$.

However, in this case the far-field condition (6.3.12) yields only a single non-trivial constraint, namely the elimination of the algebraically growing mode, which requires $c_2 = 0$. The remaining contributions decay algebraically as $O(r^{-1})$ and therefore automatically satisfy the far-field condition. As a result, three constants, c_1, c_3, and c_4 remain undetermined. Consequently, the solution is underdetermined: the boundary conditions do not uniquely fix the far-field behaviour. This reflects the fact that purely oscillatory modes with $z_i = 0$ neither grow nor decay exponentially, and therefore cannot be uniquely selected by the far-field condition alone.

Case 2: $z_i = z_I$, where $z_I > 0$

Here

$$s_{\mathrm{case}\,2} = \frac{1}{La}\left(z_I^2 - z_r^2 - 2z_r z_I \mathrm{i}\right) . \tag{6.3.20}$$

As $r \to \infty$, the second exponential term in (6.3.19) grows like $e^{z_I r}$ and must therefore be eliminated to satisfy (6.3.12). This requires

$$c_4 = \mathrm{i}c_3 , \tag{6.3.21}$$

together with $c_2 = 0$. Under these conditions, all remaining contributions decay exponentially and the far-field condition is satisfied.

Case 3: $z_i = -z_I$, where $z_I > 0$

In this case,

$$s_{\mathrm{case}\,3} = \frac{1}{La}\left(z_I^2 + z_r^2 - 2z_r z_I \mathrm{i}\right) , \tag{6.3.22}$$

but now the first exponential term of (6.3.19) grows as $r \to \infty$. To prevent this unphysical growth, we require

$$c_4 = -\mathrm{i}c_3 \, , \tag{6.3.23}$$

again with $c_2 = 0$, ensuring that the solution decays in the far field.

Notice that

$$s_{\mathrm{case}\,3} = \overline{s}_{\mathrm{case}\,2} \, , \tag{6.3.24}$$

where the overbar denotes complex conjugation. The far-field condition (6.3.12) therefore uniquely selects exponentially decaying solutions when $z_i \neq 0$, corresponding to Cases 2 and 3. These two cases are complex conjugates of one another, yielding conjugate pairs of growth rates. In contrast, when $z_i = 0$ the solution remains underdetermined, as the far-field condition alone is insufficient to exclude purely oscillatory modes. This distinction plays a crucial role in determining which perturbations represent physically admissible eigenmodes of the system.

6.4 Kinematic boundary condition

The non-dimensional bubble surface is written as

$$r = f(\theta, t) = a(t) + \epsilon A_{1,n}(t) P_n(\cos\theta) \, , \tag{6.4.1}$$

where $A_{1,n}(t)$ denotes the amplitude of the nth shape perturbation mode. The base-state bubble radius is given by

$$a(t) = 1 + \Delta \cos(Ca\, t)\,, \tag{6.4.2}$$

where Δ is the oscillation amplitude and Ca is the capillary number.

Kinematic compatibility at the interface requires that the bubble surface moves with the fluid, that is

$$\frac{\mathrm{D}}{\mathrm{D}t}(r - f) = 0\,. \tag{6.4.3}$$

Using spherical coordinates with $\xi = \cos\theta$, this condition may be written as

$$\frac{\partial}{\partial t}(r - f) + u_r \frac{\partial}{\partial r}(r - f) - \frac{u_\theta \sin\theta}{r}\frac{\partial}{\partial \xi}(r - f) = 0\,, \tag{6.4.4}$$

evaluated at $r = f$.

The velocity components expressed in terms of the stream function are

$$u_r = -\frac{1}{r^2}\frac{\partial \psi}{\partial \xi}\,, \qquad u_\theta = -\frac{1}{r\sin\theta}\frac{\partial \psi}{\partial r}\,. \tag{6.4.5}$$

Substituting the perturbation expansion (6.2.1)

$$\psi(r, \xi, t) = -a^2 \dot{a}\, \xi + \epsilon \psi_1(r, \xi, t)\,,$$

and evaluating at $r = f$, we obtain,

$$u_r = \dot{a} - 2\epsilon \frac{\dot{a}}{a} A_{1,n} P_n(\xi) - \epsilon \frac{1}{a^2}\frac{\partial \psi_1}{\partial \xi} + O(\epsilon^2)\,, \tag{6.4.6}$$

$$u_\theta = -\frac{\epsilon}{a\sin\theta}\frac{\partial \psi_1}{\partial r} + O(\epsilon^2)\,. \tag{6.4.7}$$

Substituting these expressions into (6.4.4) and collecting terms of $O(\epsilon)$ yields

$$-\frac{\mathrm{d}A_{1,n}}{\mathrm{d}t} P_n(\xi) - \frac{2\dot{a}}{a} A_{1,n} P_n(\xi) - \frac{1}{a^2}\frac{\mathrm{d}\psi_1}{\mathrm{d}\xi} = 0\,. \tag{6.4.8}$$

Using the modal expansion

$$\psi_1(r, \xi, t) = \sum_{n=0}^{\infty} g_n(r, t)\, \mathscr{P}_n(\xi)\,, \tag{6.4.9}$$

together with the identity

$$\frac{\partial \mathscr{P}_n}{\partial \xi} = P_n(\xi)\,,$$

equation (6.4.8) reduces, mode by mode, to

$$\frac{\mathrm{d}A_{1,n}}{\mathrm{d}t} + \frac{2\dot{a}}{a} A_{1,n} = -\frac{1}{a^2} g_n(a, t)\,, \tag{6.4.10}$$

In the simplified case of a steady base-state radius ($\dot{a} = 0$, $a = 1$), we write

$$g_n(r, t) = e^{st} F(r)\,, \tag{6.4.11}$$

so that the kinematic condition becomes

$$\frac{\mathrm{d}A_{1,n}}{\mathrm{d}t} = -e^{st} F(1)\,. \tag{6.4.12}$$

Seeking solutions of the form

$$A_{1,n}(t) = \tilde{A}\, e^{st}\,, \tag{6.4.13}$$

where $\tilde{A}$ is a constant, we obtain the dispersion relation

$$s = -\frac{1}{\tilde{A}} F(1)\,. \tag{6.4.14}$$

This equation implicitly determines the growth rate s, since $F(1)$ depends on s through the hydrodynamic eigenfunctions.

6.5 Dynamic boundary condition

We now consider the balance of forces on the bubble surface. The stress balance equation (2.2.9) is

$$\boldsymbol{T}\cdot\hat{\boldsymbol{n}}+p_G\hat{\boldsymbol{n}}=2\kappa_m\sigma\hat{\boldsymbol{n}}-\nabla_{\mathrm{s}}\sigma\,, \tag{6.5.1}$$

where the Newtonian stress tensor is

$$\boldsymbol{T}=-p\boldsymbol{I}+2\boldsymbol{e}\,, \tag{6.5.2}$$

and the surface tension is expanded as

$$\sigma=\sigma_0+\epsilon\sigma_1P_n(\cos\theta)\,, \tag{6.5.3}$$

with σ_0 and σ_1 given by (4.8.72), namely

$$\sigma_0(t)=1+\beta_s\ln\left(1-\Gamma_0(t)\right)\,, \tag{6.5.4a}$$

and

$$\sigma_1(t)=-\beta_s\frac{\Gamma_1(t)}{1-\Gamma_0(t)}\,. \tag{6.5.4b}$$

The derivation of the linearised stress conditions follows the same procedure as in the Stokes-flow model presented in Chapter 4. In particular, the geometric quantities, strain-rate components, and projections onto the normal and tangential directions are unchanged, since these depend only on the interface parametrisation and not on the governing bulk equations. We therefore omit the intermediate algebra and state the resulting $O(\epsilon)$ stress balances directly.

Projecting (6.5.1) onto the normal and tangential directions at $r=a(t)$ gives

$$\begin{aligned}-p_1(a,t)+12\frac{\dot{a}}{a}A_{1,n}(t)+\frac{2}{a^2}\left(\frac{2g_n(a,t)}{a}-\frac{\partial g_n}{\partial r}\right)\\=\frac{2\sigma_1}{a}+\frac{1}{a^2}\left((n-1)(n+2)\sigma_0+\mathcal{B}\delta_{n,0}\right)A_{1,n}(t)\,,\end{aligned} \tag{6.5.5a}$$

and

$$3n(n+1)\frac{\dot{a}}{a}A_{1,n}(t)+\frac{1}{2a^2}\left(a^2\frac{\partial^2 g_n}{\partial r^2}-2a\frac{\partial g_n}{\partial r}+n(n+1)g_n(a,t)\right)$$
$$=\frac{n(n+1)}{2}\sigma_1\,, \tag{6.5.5b}$$

where $\mathcal{B}$ is defined as in (4.5.43)

$$\mathcal{B}=\frac{3k\gamma}{\sigma_c\bar{a}^{3\gamma-1}}\,. \tag{6.5.6}$$

These expressions are identical in form to those obtained in the Stokes-flow problem (see Chapter 4, equations (4.5.41) and (4.5.42)). The effect of inertia therefore enters only through the governing bulk equations used to determine the functions $g_n(r,t)$ and $p_1(r,t)$.

6.6 Pressure field and perturbations

We now solve for the pressure field, which we expand as

$$p=p_0+\epsilon p_1 P_n(\cos\theta)\,, \tag{6.6.1}$$

where p_0 is the base-state pressure and p_1 is the first-order perturbation. Returning to (6.1.1), the pressure gradient satisfies

$$\nabla p=-\nabla\times\nabla\times\boldsymbol{u}-La\frac{\partial\boldsymbol{u}}{\partial t}-La(\boldsymbol{u}\cdot\nabla)\boldsymbol{u}\,, \tag{6.6.2}$$

where the velocity is expressed in terms of the stream function as

$$\boldsymbol{u}=\nabla\times\left(\frac{\psi}{r\sin\theta}\hat{\boldsymbol{\phi}}\right)\,. \tag{6.6.3}$$

Substituting (6.6.3) into (6.1.9) gives

$$\nabla p = -\nabla \times \left(\frac{-D^2\psi}{r\sin\theta} \hat{\boldsymbol{\phi}} \right) - La \frac{\partial}{\partial t} \nabla \times \left(\frac{\psi}{r\sin\theta} \boldsymbol{\phi} \right) \\ - La \left(\nabla \times \left(\frac{\psi}{r\sin\theta} \boldsymbol{\phi} \right) \cdot \nabla \right) \left[\nabla \times \left(\frac{\psi}{r\sin\theta} \boldsymbol{\phi} \right) \right] , \tag{6.6.4}$$

where

$$\frac{D^2\psi}{r\sin\theta} = \frac{\epsilon}{r\sin\theta} \left(\frac{\partial^2 \psi_1}{\partial r^2} + \frac{1-\xi^2}{r^2} \frac{\partial^2 \psi_1}{\partial \xi^2} \right) . \tag{6.6.5}$$

Breaking down each term of (6.6.4) we have

$$\nabla \times \left(\frac{-D^2\psi}{r\sin\theta} \hat{\boldsymbol{\phi}} \right) = \frac{\epsilon}{r^2} \frac{\partial D^2 \psi_1}{\partial \xi} \hat{\boldsymbol{r}} + \frac{\epsilon}{r\sin\theta} \frac{\partial D^2 \psi_1}{\partial r} \hat{\boldsymbol{\theta}} , \tag{6.6.6}$$

$$\frac{\partial}{\partial t} \nabla \times \left(\frac{\psi}{r\sin\theta} \hat{\boldsymbol{\phi}} \right) = \left(\frac{\ddot{a}a^2}{r^2} + \frac{2\dot{a}^2 a}{r^2} - \frac{\epsilon}{r^2} \frac{\partial^2 \psi_1}{\partial \xi \, \partial t} \right) \hat{\boldsymbol{r}} - \frac{\epsilon}{r\sin\theta} \frac{\partial^2 \psi_1}{\partial r \, \partial t} \hat{\boldsymbol{\theta}} , \tag{6.6.7}$$

and

$$\left(\nabla \times \left(\frac{\psi}{r\sin\theta} \hat{\boldsymbol{\phi}} \right) \cdot \nabla \right) \left[\nabla \times \left(\frac{\psi}{r\sin\theta} \hat{\boldsymbol{\phi}} \right) \right] = -\frac{2\dot{a}^2 a^4}{r^5} \hat{\boldsymbol{r}} \\ + \epsilon \left(\frac{\dot{a}a^2}{r^4 \sin\theta} \frac{\partial^2 \psi_1}{\partial r \, \partial \theta} - \frac{4\dot{a}a^2}{r^5 \sin\theta} \frac{\partial \psi_1}{\partial \theta} \right) \hat{\boldsymbol{r}} + \epsilon \left(-\frac{\dot{a}a^2}{r^3 \sin\theta} \frac{\partial^2 \psi_1}{\partial r^2} + \frac{\dot{a}a^2}{r^4 \sin\theta} \frac{\partial \psi_1}{\partial r} \right) \hat{\boldsymbol{\theta}} \\ - \frac{\epsilon \dot{a}a^2}{r^4 \sin\theta} \frac{\partial \psi_1}{\partial r} \hat{\boldsymbol{\theta}} + O(\epsilon^2) . \tag{6.6.8}$$

Therefore, considering terms of $O(1)$ of (6.6.4), we obtain the base-state pressure gradient

$$\nabla p_0 = -La \left(\frac{\ddot{a}a^2}{r^2} + \frac{2\dot{a}^2 a}{r^2} - \frac{2\dot{a}^2 a^4}{r^5} \right) \hat{\boldsymbol{r}} , \tag{6.6.9}$$

which gives

$$\frac{\partial p_0}{\partial r} = -La \left(\frac{\ddot{a}a^2}{r^2} + \frac{2\dot{a}^2 a}{r^2} - \frac{2\dot{a}^2 a^4}{r^5} \right) . \tag{6.6.10}$$

Integrating (6.6.10) with respect to r gives us

$$p_0(r,t) = La \left(\frac{\ddot{a}a^2}{r} + \frac{2\dot{a}^2 a}{r} - \frac{\dot{a}^2 a^4}{2r^4} \right) + C(t) , \tag{6.6.11}$$

where $C(t)$ is an arbitrary function of time. Evaluating at $r = a$ and using the

Young-Laplace condition gives

$$p_0 = p_G - 4\frac{\dot{a}}{a} - \frac{2\sigma_0}{a}\,. \tag{6.6.12}$$

By evaluating (6.6.11) at $r = a$, we get

$$p_0 = C(t) + La\left(\ddot{a}a + \frac{3}{2}\dot{a}^2\right)\,. \tag{6.6.13}$$

By equating (6.6.12) and (6.6.13) we get

$$La\left(\ddot{a}a + \frac{3}{2}\dot{a}^2\right) + 4\frac{\dot{a}}{a} = p_G - C(t) - \frac{2\sigma_0}{a}\,, \tag{6.6.14}$$

which recovers the Rayleigh–Plesset equation (2.3.18), with the integration function $C(t)$ playing the role of the far-field pressure $p_\infty(t)$.

6.6.1 First-order pressure perturbation

The first-order pressure gradient is

$$\nabla p_1 = \epsilon\frac{\partial p_1}{\partial r}P_n(\xi)\hat{\boldsymbol{r}} - \frac{\epsilon\sin\theta}{r}p_1\frac{\mathrm{d}}{\mathrm{d}\xi}P_n(\xi)\hat{\boldsymbol{\theta}}\,. \tag{6.6.15}$$

Therefore, considering terms of $O(\epsilon)$ in the $\hat{\boldsymbol{\theta}}$-component of equation (6.6.4) we get

$$p_1 = \frac{\partial}{\partial r}\left(-\frac{1}{n(n+1)}\frac{\partial^2 g_n}{\partial r^2} + \frac{1}{r^2}g_n\right) + \frac{La}{n(n+1)}\frac{\partial^2 g_n}{\partial r\,\partial t} + \frac{\dot{a}a^2 La}{r^2 n(n+1)}\frac{\partial^2 g_n}{\partial r^2}\,. \tag{6.6.16}$$

Similarly, the $\hat{\boldsymbol{r}}$-component gives

$$\frac{\partial p_1}{\partial r} = -\frac{1}{r^2}\frac{\partial^2 g_n}{\partial r^2} + La\frac{\dot{a}a^2}{r^4}\frac{\partial g_n}{\partial r} + \frac{La}{r^2}\frac{\partial g_n}{\partial t} - La\frac{4\dot{a}a^2}{r^5}g_n + \frac{n(n+1)}{r^4}g_n\,. \tag{6.6.17}$$

Differentiating (6.6.16) with respect to r and using (6.3.2) to eliminate $\partial_r^4 g_n$ confirms the consistency of the solution.

In the simplified case of a steady base-state radius, where $\dot{a} = 0$ and $a = 1$,

$g_n(r,t)$ can be written as (6.3.3)

$$g_n(r,t) = e^{st}F(r)\,, \tag{6.6.18}$$

with $F(r)$ given by (6.3.8).

Substituting this form into (6.6.16), we can express the first-order pressure perturbation as

$$p_1(r,t) = e^{st}\tilde{p}_1(r)\,, \tag{6.6.19}$$

where the spatial component $\tilde{p}_1(r)$ is

$$\tilde{p}_1(r) = \frac{\partial}{\partial r}\left(-\frac{1}{n(n+1)}\frac{\mathrm{d}^2F}{\mathrm{d}r^2} + \frac{1}{r^2}F\right) + \frac{s\,La}{n(n+1)}\frac{\mathrm{d}F}{\mathrm{d}r}\,. \tag{6.6.20}$$

This provides the first-order pressure perturbation associated with a given mode n and growth rate s in the steady radius base-state case.

6.7 Uniform surface tension and fixed-radius base state

In this section, we will make the simplifying assumptions that $\Delta = 0$ in (6.4.2), so $a = 1$, and $\beta_s = 0$ in (6.5.4), so $\sigma_0 = 1, \sigma_1 = 0$, which means that there is no variation of surface tension on the bubble surface. The first-order stream function perturbation can be written as (6.2.7)

$$\psi_1(r,\xi,t) = \sum_{n=0}^{\infty} g_n(r,t)\mathscr{P}_n(\xi)\,, \tag{6.7.1}$$

where g_n can be expressed as

$$g_n(r,t) = e^{st}F(r)\,, \tag{6.7.2}$$

with $F(r)$ given by (6.3.8).

In this regime, the amplitude evolution equation is given by (6.4.14)

$$s = -\frac{1}{\tilde{A}} F(1) \,. \tag{6.7.3}$$

The dynamic stress conditions (6.5.5) evaluated at the interface $r = 1$ become

$$\begin{aligned} -\tilde{p}_1(1) + 2\left(2F - \frac{\mathrm{d}F}{\mathrm{d}r}\right) \\ = \left((n-1)(n+2)\sigma_0 + \mathcal{B}\mathscr{P}_n(1)\right)\tilde{A} \,, \end{aligned} \tag{6.7.4a}$$

and

$$\frac{\mathrm{d}^2 F}{\mathrm{d}r^2} - 2\frac{\mathrm{d}F}{\mathrm{d}r} + n(n+1)F = 0 \,. \tag{6.7.4b}$$

As discussed previously, the admissible far–field behaviour of the solution leads to three distinct cases. We now examine each in turn.

6.7.1 Growth rate equation for Case 1

In Case 1, the far–field condition permits oscillatory behaviour without exponential growth or decay. After enforcing the decay of algebraically growing terms, the general solution involves three undetermined constants, c_1, c_3, and c_4, while only the two interfacial conditions (6.7.4) are available.

Consequently, the system is underdetermined and no discrete eigenvalue s can be obtained. This case therefore does not yield an eigenvalue problem that can be solved analytically and, as such, will not be considered further in this section.

6.7.2 Growth rate equation for Case 2

Case 2 corresponds to choosing the half-plane of $z = \sqrt{-sLa}$, $z_i > 0$, in which the exponentially growing contribution is eliminated by imposing

$$c_4 = \mathrm{i}c_3 \,.$$

Solving the interfacial conditions (6.7.4) simultaneously under this constraint yields

$$c_1 = \frac{(n+1)\left[\left(n(n+2) - \frac{1}{2}z^2\right) R_n^{(1)}(z) - z\right] \Pi \tilde{A}}{2z\left(\Lambda_2 + \frac{1}{2}z^2\right) - 2z^2\left(\Lambda_1 - \frac{1}{4}z^2\right) R_n^{(1)}(z)}\,, \tag{6.7.5}$$

and

$$c_3 = -\frac{n(n+1)(n+2)\sqrt{\pi} z^{-3/2} \Pi \tilde{A}}{2\sqrt{2}\left[\left(\Lambda_2 + \frac{1}{2}z^2\right) h_{n-1}^{(1)}(z) - z\left(\Lambda_1 - \frac{1}{4}z^2\right) h_n^{(1)}(z)\right]}\,. \tag{6.7.6}$$

Here,

$$\Pi = (n-1)(n+2) + \mathcal{B}\delta_{n,0}\,, \qquad \Lambda_1 = \frac{1}{2}(n+2)(2n+1)\,, \tag{6.7.7}$$

$$\Lambda_2 = (n-1)(n+1)(n+2)\,, \tag{6.7.8}$$

and $h_n^{(1)} = j_n + \mathrm{i} y_n$ denotes the spherical Hankel function of the first kind. We also define the ratio

$$R_n^{(1)} = \frac{h_n^{(1)}}{h_{n-1}^{(1)}}\,. \tag{6.7.9}$$

Substituting (6.7.5) and (6.7.6) into the amplitude equation (6.7.3) yields the transcendental growth rate equation

$$z^2 = -\frac{La\,(n+1)\left(2z + z^2 R_n^{(1)}(z)\right)\Pi}{4z\left(\Lambda_2 + \frac{1}{2}z^2\right) - 4z^2\left(\Lambda_1 - \frac{1}{4}z^2\right) R_n^{(1)}(z)}\,. \tag{6.7.10}$$

6.7.3 Growth rate equation for Case 3

Case 3 corresponds to choosing the half-plane of $z = \sqrt{-sLa}$, $z_i < 0$, in which the exponentially growing contribution is eliminated by imposing

$$c_4 = -\mathrm{i}c_3\,.$$

Proceeding in the same manner as in Case 2, the solution of (6.7.4) yields

$$c_1 = \frac{(n+1)\left[\left(n(n+2) - \frac{1}{2}z^2\right) R_n^{(2)}(z) - z\right] \Pi \tilde{A}}{2z\left(\Lambda_2 + \frac{1}{2}z^2\right) - 2z^2\left(\Lambda_1 - \frac{1}{4}z^2\right) R_n^{(2)}(z)}\,, \tag{6.7.11}$$

and

$$c_3 = -\frac{n(n+1)(n+2)\sqrt{\pi}z^{-3/2}\Pi\tilde{A}}{2\sqrt{2}\left[\left(\Lambda_2 + \frac{1}{2}z^2\right)h_{n-1}^{(2)}(z) - z\left(\Lambda_1 - \frac{1}{4}z^2\right)h_n^{(2)}(z)\right]}\,. \tag{6.7.12}$$

Here $h_n^{(2)} = j_n - \mathrm{i}y_n$ is the spherical Hankel function of the second kind, and

$$R_n^{(2)} = \frac{h_n^{(2)}}{h_{n-1}^{(2)}}\,. \tag{6.7.13}$$

Substitution into (6.7.3) yields

$$z^2 = -\frac{La\,(n+1)\left(2z + z^2 R_n^{(2)}(z)\right)\Pi}{4z\left(\Lambda_2 + \frac{1}{2}z^2\right) - 4z^2\left(\Lambda_1 - \frac{1}{4}z^2\right)R_n^{(2)}(z)}\,. \tag{6.7.14}$$

To relate Cases 2 and 3, we use the analytic continuation properties of the spherical Hankel functions. Since

$$h_n^{(1)}(z) = j_n(z) + \mathrm{i}y_n(z)\,, \qquad h_n^{(2)}(z) = j_n(z) - \mathrm{i}y_n(z)\,,$$

and the spherical Bessel functions satisfy (see, for example, Abramowitz & Stegun, 1964, p.361)

$$\overline{j_n(\bar{z})} = j_n(z)\,, \qquad \overline{y_n(\bar{z})} = y_n(z)\,,$$

it follows that

$$\overline{h_n^{(1)}(\bar{z})} = h_n^{(2)}(z)\,.$$

Consequently,

$$\overline{R_n^{(1)}(\bar{z})} = \overline{\frac{h_n^{(1)}(\bar{z})}{h_{n-1}^{(1)}(\bar{z})}} = \frac{\overline{h_n^{(1)}(\bar{z})}}{\overline{h_{n-1}^{(1)}(\bar{z})}} = \frac{h_n^{(2)}(z)}{h_{n-1}^{(2)}(z)} = R_n^{(2)}(z)\,.$$

Now define

$$F^{(1)}(z) = -\frac{La\,(n+1)\left(2z + z^2 R_n^{(1)}(z)\right)\Pi}{4z\left(\Lambda_2 + \frac{1}{2}z^2\right) - 4z^2\left(\Lambda_1 - \frac{1}{4}z^2\right)R_n^{(1)}(z)}\,,$$

so that (6.7.10) may be written as

$$z^2 = F^{(1)}(z)\,.$$

Since Λ_1, Λ_2, Π, and La are real-valued,

$$\overline{F^{(1)}(\bar{z})} = -\frac{La\,(n+1)\left(2z + z^2 R_n^{(2)}(z)\right)\Pi}{4z\left(\Lambda_2 + \frac{1}{2}z^2\right) - 4z^2\left(\Lambda_1 - \frac{1}{4}z^2\right)R_n^{(2)}(z)} = F^{(2)}(z)\,,$$

where $F^{(2)}(z)$ denotes the right-hand side of (6.7.14). Taking the complex conjugate of

$$z^2 = F^{(1)}(z)$$

therefore gives

$$\bar{z}^{\,2} = F^{(2)}(\bar{z})\,.$$

Hence, if z satisfies the growth-rate equation for Case 2, then $\bar{z}$ satisfies the growth-rate equation for Case 3. Since

$$z^2 = -sLa\,,$$

with $La \in \mathbb{R}$, it follows that the corresponding growth rates satisfy

$$s^{(2)} = \overline{s^{(1)}}\,.$$

Therefore, the growth rates associated with Cases 2 and 3 form a complex-conjugate pair. This algebraic conjugacy is consistent with the earlier result that the far-field condition distinguishes Cases 2 and 3 via opposite exponential branches, thereby enforcing a conjugate pairing of admissible growth rates.

6.7.4 Asymptotic growth rates in the small- and large-La limits

Having established the eigenvalue problem and the complex-conjugate nature of Cases 2 and 3, we now examine the behaviour of the growth rate s in the asymptotic limits of small and large Laplace number, La. These limits correspond physically to the regimes where viscous effects dominate ($La \to 0$) or inertial effects dominate ($La \to \infty$). Studying these limits allows us to connect the full Navier–Stokes formulation with the well-known Stokes-flow results and to identify the effect of inertia on the stability of the bubble.

Since Cases 2 and 3 are complex conjugates, their growth rates have the same magnitude and real part in each asymptotic regime. Therefore, it is sufficient to analyse one case in detail, knowing that the other exhibits the same growth or decay rate but with the sign of the imaginary part reversed.

Small-La limit ($La \to 0$)

We begin with Case 2. To evaluate the small-La limit, we require the asymptotic behaviour of the spherical Bessel functions for small argument. These may be expressed as (see, for example, Abramowitz & Stegun, 1964, p. 437)

$$j_n(z) = \frac{z^n}{(2n+1)!!}\left\{1 - \frac{z^2}{2(2n+3)} + \cdots\right\}, \tag{6.7.15a}$$

and

$$y_n(z) = \frac{(2n-1)!!}{z^{n+1}}\left\{1 - \frac{z^2}{2(1-2n)} + \cdots\right\}, \tag{6.7.15b}$$

where $z = \sqrt{-sLa}$. Here, the double factorial notation $n!!$ denotes the product of all positive integers up to n with the same parity as n such that $n!! = n(n-2)(n-4)\cdots$.

For integer $n \geq 1$, it follows that as $z \to 0$,

$$j_n(z) \sim \frac{z^n}{(2n+1)!!}, \tag{6.7.16a}$$

and

$$y_n(z) \sim -\frac{(2n-1)!!}{z^{n+1}}. \tag{6.7.16b}$$

Since $z = \sqrt{-sLa}$, taking the limit $La \to 0$ is equivalent to taking $z \to 0$. Using

(6.7.16), the spherical Hankel function of the first kind satisfies

$$h_n^{(1)}(z) = j_n(z) + \mathrm{i}y_n(z) \sim -\mathrm{i}(2n-1)!!\, z^{-(n+1)}\,, \tag{6.7.17}$$

and therefore the ratio function of the first kind (6.7.9) behaves as

$$R_n^{(1)}(z) \sim \frac{-\mathrm{i}(2n-1)!!\, z^{-(n+1)}}{-\mathrm{i}(2n-3)!!\, z^{-n}} = \frac{2n-1}{z}\,. \tag{6.7.18}$$

Substituting (6.7.18) into (6.7.10) and simplifying yields the small-La growth rate

$$s \sim \frac{(n+1)\big(2\sqrt{-sLa} + \sqrt{-sLa}(2n-1)\big)\Pi}{4\sqrt{-sLa}(\Lambda_2 - \Lambda_1)} = -\frac{(n-1)(n+1)(2n+1)}{2(2n^2+1)}\,. \tag{6.7.19}$$

Here, Π, Λ_1, and Λ_2 are defined in (6.7.7) and (6.7.8). Taking the limit $La \to 0$ in (6.1.1) yields the Stokes equations, and hence the limit $La \to 0$ of (6.7.10) should recover the Stokes-flow growth rate. Indeed, comparison of (6.7.19) with the growth rate obtained under the Stokes-flow approximation in Chapter 4 (4.6.12) shows exact agreement.

By the complex-conjugate relation, Case 3 yields the same magnitude of growth/decay rate, confirming that in the viscous-dominated regime, inertial effects introduce no additional instability.

Large-La limit ($La \to \infty$)

Next, we consider the inertia-dominated regime $La \to \infty$. We begin with Case 2, for which $z = \sqrt{-sLa}$ satisfies

$$z^2 = -\frac{La\,(n+1)\big(2z + z^2 R_n^{(1)}(z)\big)\Pi}{4z\left(\Lambda_2 + \frac{1}{2}z^2\right) - 4z^2\left(\Lambda_1 - \frac{1}{4}z^2\right) R_n^{(1)}(z)}\,, \tag{6.7.20}$$

where the ratio function is defined as

$$R_n^{(1)}(z) = \frac{h_n^{(1)}(z)}{h_{n-1}^{(1)}(z)}\,. \tag{6.7.21}$$

To evaluate the large-La limit, we require the asymptotic behaviour of the spherical Bessel functions for large argument. For $|z| \gg 1$, these are given by (6.3.15) as

$$j_n(z) \sim \frac{1}{z}\sin\left(z - \frac{n\pi}{2}\right) , \tag{6.7.22a}$$

$$y_n(z) \sim -\frac{1}{z}\cos\left(z - \frac{n\pi}{2}\right) . \tag{6.7.22b}$$

Since $z = \sqrt{-sLa}$, solutions with s algebraically small as $La \to \infty$ correspond to the large-$|z|$ regime.

Using (6.7.22), the spherical Hankel function of the first kind satisfies

$$h_n^{(1)}(z) = j_n(z) + \mathrm{i}y_n(z) \sim \frac{1}{z}\left[\sin\left(z - \frac{n\pi}{2}\right) - \mathrm{i}\cos\left(z - \frac{n\pi}{2}\right)\right] . \tag{6.7.23}$$

Applying Euler's formula,

$$e^{\mathrm{i}z} = \cos z + \mathrm{i}\sin z\,,$$

this expression can be written compactly as

$$h_n^{(1)}(z) \sim \frac{1}{z}(-\mathrm{i})^{n+1}e^{\mathrm{i}z} . \tag{6.7.24}$$

Therefore, for $|z| \gg 1$, the ratio function (6.7.21) has the asymptotic form

$$R_n^{(1)}(z) \sim \frac{\frac{1}{z}(-\mathrm{i})^{n+1}e^{\mathrm{i}z}}{\frac{1}{z}(-\mathrm{i})^{n}e^{\mathrm{i}z}} = -\mathrm{i}\,. \tag{6.7.25}$$

Substituting (6.7.25) into (6.7.20) yields

$$z^2 \sim -\frac{La(n+1)\left(2z - \mathrm{i}z^2\right)\Pi}{4\Lambda_2 z + 2z^3 + 4\mathrm{i}\Lambda_1 z^2 - \mathrm{i}z^4} .$$

Factoring z^2 from the numerator and z^4 from the denominator gives

$$z^2 \sim -\frac{La(n+1)\Pi}{z^2}\,\frac{\left(\frac{2}{z} - \mathrm{i}\right)}{\left(\frac{4\Lambda_2}{z^3} + \frac{2}{z} + \frac{4\mathrm{i}\Lambda_1}{z^2} - \mathrm{i}\right)} .$$

As $|z| \to \infty$,

$$\frac{2}{z} \to 0\,, \qquad \frac{4\Lambda_2}{z^3} \to 0\,, \qquad \frac{4\mathrm{i}\Lambda_1}{z^2} \to 0\,,$$

and therefore

$$\frac{\left(\frac{2}{z} - \mathrm{i}\right)}{\left(\frac{4\Lambda_2}{z^3} + \frac{2}{z} + \frac{4\mathrm{i}\Lambda_1}{z^2} - \mathrm{i}\right)} \to 1\,.$$

Hence,

$$z^2 \sim -\frac{La(n+1)\Pi}{z^2}\,,$$

so that

$$z^4 \sim -La(n+1)\Pi\,.$$

Recalling that $z^2 = -sLa$, we obtain

$$s^2 \sim -\frac{(n+1)\Pi}{La}\,,$$

and therefore

$$s \sim \pm\mathrm{i}\sqrt{\frac{(n+1)\Pi}{La}} \qquad \text{as} \qquad La \to \infty\,. \tag{6.7.26}$$

Thus, the growth rate vanishes like $La^{-1/2}$ in the inertia-dominated limit. Here, Π is defined as in (6.7.7) to be

$$\Pi = (n-1)(n+2) + \mathcal{B}\delta_{n,0}\,. \tag{6.7.27}$$

We now consider the isobaric limit, in which the gas pressure inside the bubble remains constant. In the adiabatic law (4.5.28),

$$p_G V^\gamma = \bar{k}\,, \tag{6.7.28}$$

this corresponds to taking the adiabatic index $\gamma = 0$, where $\bar{k}$ is constant. It then follows from (6.5.6) that

$$\mathcal{B} = \frac{3k\gamma}{\sigma_c \bar{a}^{3\gamma-1}} = 0\,. \tag{6.7.29}$$

Hence,

$$\Pi = (n-1)(n+2)\,,$$

and the large-La growth rate (6.7.26) reduces to

$$s \sim \pm \mathrm{i}\sqrt{\frac{(n-1)(n+1)(n+2)}{La}}\,, \qquad La \to \infty\,. \tag{6.7.30}$$

This agrees, subject to non-dimensionalisation, with the classical result of Lamb (1932) (p. 469) for shape oscillations of a bubble with constant equilibrium radius in an inviscid fluid with constant internal gas pressure.

By the complex-conjugate relation, Case 3 yields the conjugate branch of the growth rate obtained in Case 2, and therefore the same oscillation frequency and asymptotic decay behaviour. In both cases,

$$s = O(La^{-1/2})\,, \qquad La \to \infty\,,$$

so that the growth rate vanishes in the inertia-dominated limit. Thus, no additional instability arises in the inertia-dominated regime.

6.7.5 Growth rate as a polynomial in z

In this section we will show that the transcendental equations for the growth rate for Case 2 (6.7.10) and Case 3 (6.7.14) can be expressed as polynomial equations in z, where $z = \sqrt{-sLa}$.

To achieve this, we use Rayleigh's formulas to rewrite the spherical Hankel functions in a form for which the oscillatory exponential factors cancel in the ratio functions $R_n^{(1)}(z)$ and $R_n^{(2)}(z)$. The resulting growth-rate equations then reduce to algebraic polynomial equations in z.

Recall that, by Rayleigh's formulas (6.3.11), the spherical Bessel functions can be expressed as

$$j_n(z) = (-z)^n \left(\frac{1}{z}\frac{\mathrm{d}}{\mathrm{d}z}\right)^n \left(\frac{\sin z}{z}\right)\,, \tag{6.7.31a}$$

and

$$y_n(z) = -(-z)^n \left(\frac{1}{z}\frac{\mathrm{d}}{\mathrm{d}z}\right)^n \left(\frac{\cos z}{z}\right)\,. \tag{6.7.31b}$$

We begin by considering Case 2.

6.7.6 Growth rate polynomial for Case 2

For Case 2, we have the Hankel function of the first kind which is expressed as

$$\begin{aligned} h_n^{(1)}(z) &= j_n(z) + \mathrm{i} y_n(z) && (6.7.32)\\ &= (-z)^n \left(\frac{1}{z}\frac{\mathrm{d}}{\mathrm{d}z}\right)^n \frac{\sin z}{z} - \mathrm{i}(-z)^n \left(\frac{1}{z}\frac{\mathrm{d}}{\mathrm{d}z}\right)^n \frac{\cos z}{z} && (6.7.33)\\ &= -\mathrm{i}(-z)^n \left(\frac{1}{z}\frac{\mathrm{d}}{\mathrm{d}z}\right)^n \frac{e^{\mathrm{i}z}}{z}, && (6.7.34) \end{aligned}$$

using (6.7.31). We can simplify this further with the following proposition

Proposition 6.7.1.

$$\left(\frac{1}{z}\frac{\mathrm{d}}{\mathrm{d}z}\right)^n \frac{e^{\mathrm{i}z}}{z} = e^{\mathrm{i}z} \left(\frac{1}{z}\frac{\mathrm{d}}{\mathrm{d}z} + \frac{\mathrm{i}}{z}\right)^n \frac{1}{z}. \qquad (6.7.35)$$

Proof. By induction on n.

Base case: $n = 0$. Substituting $n = 0$ into (6.7.35) the left- and right-hand sides are equal to each other and so the base case holds.

Inductive step: assume (6.7.35) is true for $n = k$, for $k = 0, 1, 2, ...$ such that

$$\left(\frac{1}{z}\frac{\mathrm{d}}{\mathrm{d}z}\right)^k \frac{e^{\mathrm{i}z}}{z} = e^{\mathrm{i}z} \left(\frac{1}{z}\frac{\mathrm{d}}{\mathrm{d}z} + \frac{\mathrm{i}}{z}\right)^k \frac{1}{z}. \qquad (6.7.36)$$

Next we show (6.7.35) is true for $k + 1$. To do this we apply

$$\frac{1}{z}\frac{\mathrm{d}}{\mathrm{d}z}, \qquad (6.7.37)$$

to both sides of (6.7.36). This gives us

$$\left(\frac{1}{z}\frac{\mathrm{d}}{\mathrm{d}z}\right) \left[\left(\frac{1}{z}\frac{\mathrm{d}}{\mathrm{d}z}\right)^k \frac{e^{\mathrm{i}z}}{z}\right] = \left(\frac{1}{z}\frac{\mathrm{d}}{\mathrm{d}z}\right) \left[e^{\mathrm{i}z} \left(\frac{1}{z}\frac{\mathrm{d}}{\mathrm{d}z} + \frac{\mathrm{i}}{z}\right)^k \frac{1}{z}\right]. \qquad (6.7.38)$$

By applying the product rule to the right-hand side of (6.7.38) we get

$$\frac{1}{z}\frac{\mathrm{d}}{\mathrm{d}z}(e^{\mathrm{i}z}) = e^{\mathrm{i}z}\left(\frac{1}{z}\frac{\mathrm{d}}{\mathrm{d}z}+\frac{\mathrm{i}}{z}\right)\left(\frac{1}{z}\frac{\mathrm{d}}{\mathrm{d}z}+\frac{\mathrm{i}}{z}\right)^{k}\frac{1}{z}\,. \tag{6.7.39}$$

Thus we have

$$\left(\frac{1}{z}\frac{\mathrm{d}}{\mathrm{d}z}\right)^{k+1}\frac{e^{\mathrm{i}z}}{z} = e^{\mathrm{i}z}\left(\frac{1}{z}\frac{\mathrm{d}}{\mathrm{d}z}+\frac{\mathrm{i}}{z}\right)^{k+1}\frac{1}{z}\,, \tag{6.7.40}$$

where $k+1$ replaces k in (6.7.36). This completes the inductive step. As we know (6.7.35) is true for $n=0$, we now know it to be true for $n=k=0,1,2,\ldots$ □

The ratio function (6.7.9) can now be expressed as

$$R_n^{(1)}(z) = \frac{h_n^{(1)}(z)}{h_{n-1}^{(1)}(z)} = \frac{(-z)\left(\frac{1}{z}\frac{\mathrm{d}}{\mathrm{d}z}+\frac{\mathrm{i}}{z}\right)^{n}\frac{1}{z}}{\left(\frac{1}{z}\frac{\mathrm{d}}{\mathrm{d}z}+\frac{\mathrm{i}}{z}\right)^{n-1}\frac{1}{z}}\,. \tag{6.7.41}$$

Therefore, the z-equation for Case 2 (6.7.10) contains no explicit $\sin z$ or $\cos z$ terms, and may be written as

$$z^2 = -\frac{La(n+1)\left(2z+z^2R_n^{(1)}(z)\right)\Pi}{4z(\Lambda_2+\frac{1}{2}z^2)-4z^2(\Lambda_1-\frac{1}{4}z^2)R_n^{(1)}(z)}\,. \tag{6.7.42}$$

The corresponding equation for the growth rate s is thus given by

$$s = \frac{(n+1)(2\sqrt{-sLa}-sLaR_n^{(1)}(\sqrt{-sLa}))\Pi}{4\sqrt{-sLa}(\Lambda_2-\frac{1}{2}sLa)+4sLa(\Lambda_1+\frac{1}{4}sLa)R_n^{(1)}(\sqrt{-sLa})}\,. \tag{6.7.43}$$

Since $R_n^{(1)}(z)$ may be expressed as a rational function whose numerator is a polynomial of degree n, clearing denominators in (6.7.42) yields a polynomial equation in z. The highest-order contribution arises from the $z^4R_n^{(1)}(z)$ term in the denominator of (6.7.42), resulting in an overall polynomial degree of $n+4$.

For the case $n=2$, (6.7.42) becomes

$$z^6+5\mathrm{i}z^5-45z^4-72\mathrm{i}z^3+12(6+La)z^2+60\mathrm{i}Laz-60La=0\,, \tag{6.7.44}$$

which has six solutions, say $\{z_k : k = 1, 2, ..., 6\}$. The corresponding equation for the growth rate s is

$$\begin{aligned} s^3 La^2 - 5\mathrm{i}(-s)^{5/2} La^{3/2} + 45 s^2 La + 72\mathrm{i}(-s)^{3/2} La^{1/2} \\ + 12s(6 + La) - 60\mathrm{i}\sqrt{-sLa} + 60 = 0\,. \end{aligned} \tag{6.7.45}$$

As $s = -z^2/La$, it would be tempting to say that the solutions of (6.7.45) would be

$$s_k = -\frac{z_k^2}{La}\,. \tag{6.7.46}$$

However, we assume that we are working with the principal branch of $s^{1/2}$, that is to say

$$-\pi < \arg s \leq \pi\,. \tag{6.7.47}$$

A problem may arise if any of the complex numbers in (6.7.46) lie outside the principal branch and on another Riemann sheet. A Riemann sheet is one branch of a multi-valued complex function, defined so that the function is single-valued on that branch. For functions involving square roots, such as $\sqrt{-sLa}$, the associated Riemann surface consists of two sheets, which are connected at branch points and distinguished by the choice of sign of the square root. More information on this can be found in text books on analysis (see, for example, Ahlfors, 1979).

To see this, we consider the toy equation

$$z + z^{\frac{1}{2}} + 1 = 0\,, \tag{6.7.48}$$

where we assume that we work with the principal branch of $z^{1/2}$, viz.

$$-\pi < \arg z \leq \pi\,. \tag{6.7.49}$$

As before, it is tempting to say that (6.7.48) has two roots since we can put

$z = p^2$ so that

$$p^2 + p + 1 = 0 \qquad \Longrightarrow \qquad p = -\frac{1}{2} \pm \frac{\sqrt{3}}{2}\mathrm{i}\,. \tag{6.7.50}$$

Then

$$z = p^2 = -\frac{1}{2} \mp \frac{\sqrt{3}}{2}\mathrm{i}\,. \tag{6.7.51}$$

The problem is that both of the complex numbers in (6.7.51) lie outside of the principal branch and on another Riemann sheet. To see this we note that

$$p = -\frac{1}{2} \mp \frac{\sqrt{3}}{2}\mathrm{i} = e^{\mp 2\mathrm{i}\pi/3}\,, \qquad z = p^2 = e^{\mp 4\mathrm{i}\pi/3}\,. \tag{6.7.52}$$

Therefore, perhaps surprisingly, there are no solutions, with the square root interpreted according to (6.7.49), to (6.7.48). To confirm this we plot in Figure 6.7.1 the contours of the modulus of $F(z) = z + z^{1/2} + 1$. This plot was created using Matlab which uses the principal branch for the square root as in (6.7.49). It appears from the plots that $z = -1/2$ might be a solution but it is clear that it is not since

$$-\frac{1}{2} + \frac{1}{\sqrt{2}}\mathrm{i} + 1 \neq 0\,. \tag{6.7.53}$$

Returning to the study of (6.7.44), since we are working in Case 2, only the values of $z = z_r + \mathrm{i}z_i$ where $z_i > 0$ are valid. To calculate the numerical solutions to (6.7.44), we will now take $La = 1$. In Section 6.7.8, we will numerically calculate the solutions to (6.7.43) for a range of La from 10^{-3} to 10^5. The solutions to

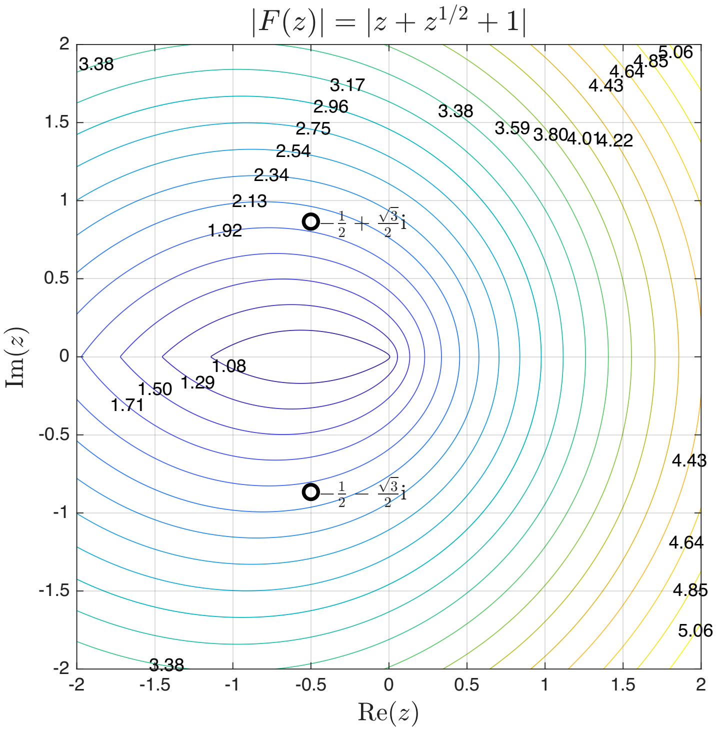

(a) The lines represent contours of $|F|$ with the numerical values shown.

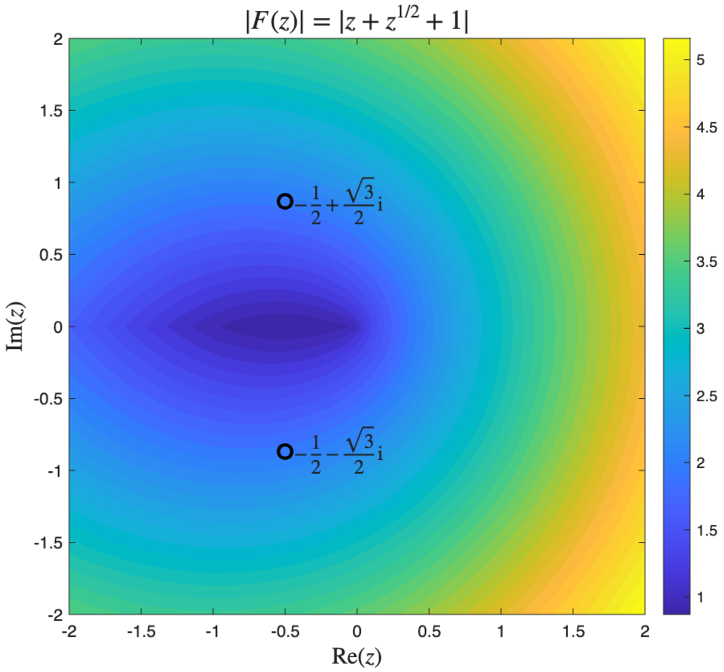

(b) The colour chart tells you what the values of $|F(z)|$ are in the complex plane.

Figure 6.7.1: Contours of $|F(z)|$. The black circle plots are the points (6.7.51).

(6.7.44) for $n = 2$, which were calculated using Matlab, are to six decimal places

$$z_1 = 0.975289 + 0.138279\mathrm{i}\,, \tag{6.7.54a}$$

$$z_2 = -0.975289 + 0.138279\mathrm{i}\,, \tag{6.7.54b}$$

$$z_3 = -0.820840 - 0.992012\mathrm{i}\,, \tag{6.7.54c}$$

$$z_4 = 0.820840 - 0.992012\mathrm{i}\,, \tag{6.7.54d}$$

$$z_5 = -5.881192 - 1.646260\mathrm{i}\,, \tag{6.7.54e}$$

$$z_6 = 5.881192 - 1.646260\mathrm{i}\,, \tag{6.7.54f}$$

and are plotted in the Argand diagram in Figure 6.7.2. Only the roots in the upper-half plane will be valid for Case 2.

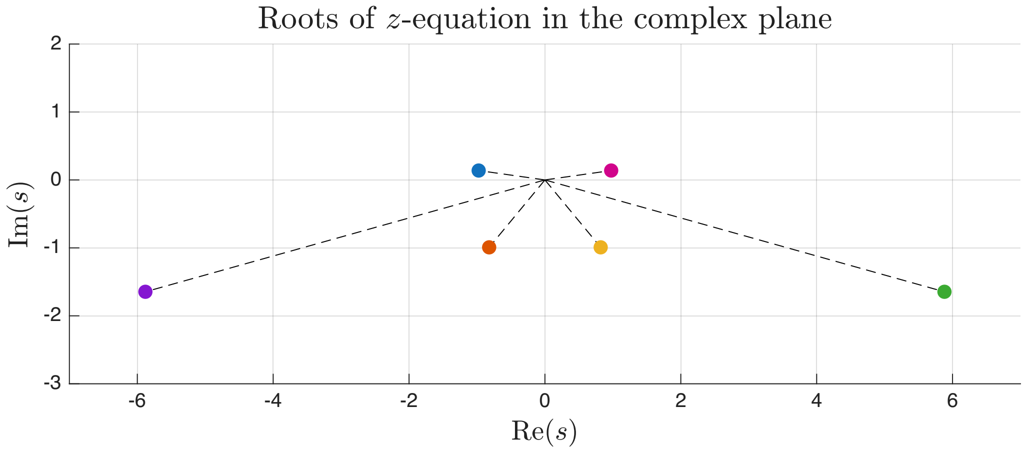

Figure 6.7.2: Plot of the solutions (6.7.54) to the equation (6.7.44).

As we can see from the solutions z_k and plot in Figure 6.7.2, the only two values are valid for Case 2, namely,

$$z_1 = 0.975289 + 0.138279\mathrm{i}\,, \tag{6.7.55a}$$

$$z_2 = -0.975289 + 0.138279\mathrm{i}\,. \tag{6.7.55b}$$

The corresponding values of s are

$$s_1 = -0.932068 - 0.269729\mathrm{i}\,, \tag{6.7.56a}$$

$$s_2 = -0.932068 + 0.269729\mathrm{i}\,. \tag{6.7.56b}$$

We now determine which of these values is consistent with the principal branch condition (6.7.47). Define

$$H(s) = -s^3 + 5\mathrm{i}(-s)^{5/2} - 45s^2 - 72\mathrm{i}(-s)^{3/2} - 84s + 60\mathrm{i}(-s)^{1/2} - 60\,. \tag{6.7.57}$$

Therefore, the only admissible solution of (6.7.45), and hence the only valid growth rate of (6.7.3), is

$$H(s_1) = 0.000000 + 0.000000\mathrm{i}\,, \tag{6.7.58a}$$

$$H(s_2) = 18.784260 + 17.445904\mathrm{i}\,. \tag{6.7.58b}$$

Therefore, the only valid solution of (6.7.45) and thus the only growth rate of (6.7.3) is

$$s_1 = -0.932068 - 0.269729\mathrm{i}\,, \tag{6.7.59}$$

where $\mathrm{Re}(s_1) < 0$, which means that the bubble is linearly stable for $n = 2$, $La = 1$.

6.7.7 Growth rate polynomial for Case 3

For Case 3, the analysis proceeds analogously using the spherical Hankel function of the second kind,

$$h_n^{(2)}(z) = j_n(z) - \mathrm{i}y_n(z)\,.$$

Following the same procedure as in Case 2, the growth-rate equation may be written in terms of $z = \sqrt{-sLa}$ as

$$z^2 = -\frac{La(n+1)\left(2z + z^2 R_n^{(2)}(z)\right)\Pi}{4z(\Lambda_2 + \frac{1}{2}z^2) - 4z^2(\Lambda_1 - \frac{1}{4}z^2)R_n^{(2)}(z)}\,, \tag{6.7.60}$$

which again reduces to a polynomial equation in z of degree $n+4$. The corresponding equation for the growth rate s is thus given by

$$s = \frac{(n+1)(2\sqrt{-sLa} - sLaR_n^{(2)}(\sqrt{-sLa}))\Pi}{4\sqrt{-sLa}(\Lambda_2 - \frac{1}{2}sLa) + 4sLa(\Lambda_1 + \frac{1}{4}sLa)R_n^{(2)}(\sqrt{-sLa})}\,, \tag{6.7.61}$$

For $n = 2$, the polynomial (6.7.60) is

$$z^6 - 5\mathrm{i}z^5 - 45z^4 + 72\mathrm{i}z^3 + 12(6+La)z^2 - 60\mathrm{i}Laz - 60La = 0\,. \tag{6.7.62}$$

As shown previously, the growth rates for Cases 2 and 3 form a complex-conjugate pair. Therefore, for $La = 1$, the admissible growth rate for Case 3 is

$$s = -0.932068 + 0.269729\mathrm{i}\,. \tag{6.7.63}$$

Since

$$\mathrm{Re}(s) < 0\,,$$

the bubble is linearly stable for $n = 2$ and $La = 1$.

6.7.8 Growth rate for Case 2 and 3 for varying Laplace number

In Section 6.7.3, we showed that the admissible growth rates for Cases 2 and 3 form a complex-conjugate pair. To determine whether growth rates with positive real part can arise, we repeated the calculation of admissible growth rates while varying the Laplace number, La. These computations were carried out numerically in Matlab over the range

$$10^{-3} \leq La \leq 10^{5}\,.$$

The corresponding admissible growth rates for $n = 2$ and $n = 3$ are shown in Figures 6.7.3 and 6.7.4, respectively. The figures show the trajectories of the admissible growth rates in the complex s-plane as La varies.

For $n = 2$ and $La = 1$, the admissible growth rates calculated in Sections 6.7.6

and 6.7.7 are

$$s_1 = -0.932068 - 0.269729\mathrm{i}\,, \tag{6.7.64}$$

and

$$s_2 = -0.932068 + 0.269729\mathrm{i}\,. \tag{6.7.65}$$

These values lie on the curves shown in Figure 6.7.3.

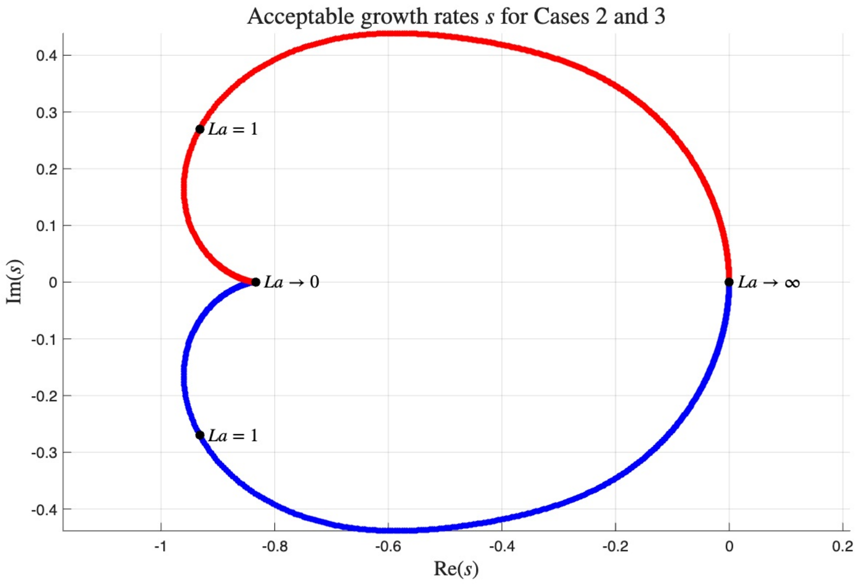

Figure 6.7.3: Admissible growth rates s in the complex plane for Cases 2 (blue) and 3 (red) with $n = 2$, obtained by varying the Laplace number over $10^{-3} \leq La \leq 10^5$. The two branches form a complex-conjugate pair and approach the origin as $La \to \infty$, consistent with the asymptotic result (6.7.26). The black markers indicate the points corresponding to $La \to 0$, $La = 1$, and $La \to \infty$. In particular, the $(La \to 0)$ marker corresponds to the limit $s = -5/6$ from (6.7.19), which forms the cusp of the cardioid-like curve.

For each pair (La, n), we find a unique admissible growth rate in each of Cases 2 and 3, related by complex conjugation. The admissible growth rates trace a cardioid-like curve in the complex s-plane.

As $La \to 0$, the growth rates approach the asymptotic limit derived in Section 6.7.4,

$$s = -\frac{(n-1)(n+1)(2n+1)}{2(2n^2+1)}\,. \tag{6.7.66}$$

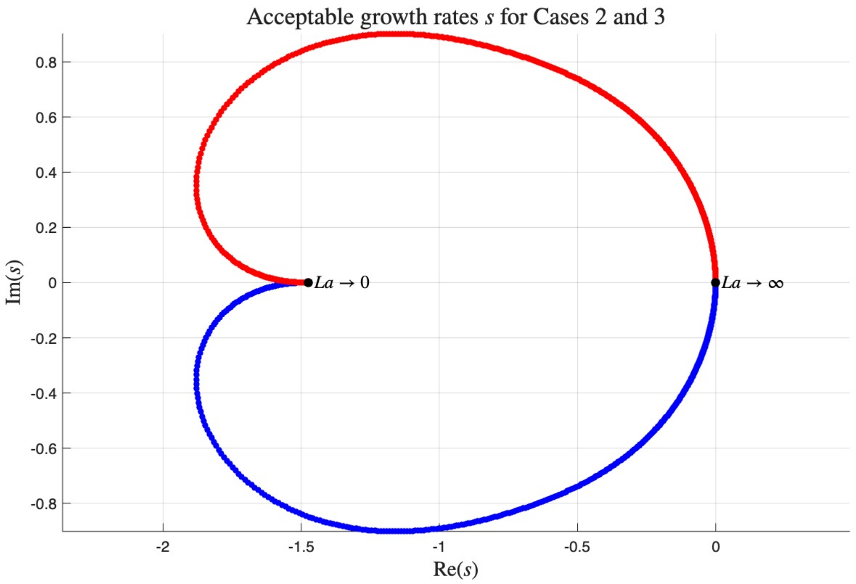

Figure 6.7.4: Admissible growth rates s in the complex plane for Cases 2 (blue) and 3 (red) with $n = 3$, obtained by varying the Laplace number over $10^{-3} \leq La \leq 10^5$. As in Figure 6.7.3, the two branches are complex conjugates and tend toward the origin as $La \to \infty$. The black markers indicate the points corresponding to $La \to 0$ and $La \to \infty$, with the left-most marker corresponding to the cusp of the cardioid-like curve.

For $n = 2$, this gives

$$s = -\frac{5}{6}\,, \tag{6.7.67}$$

which is indicated by the black circle in Figures 6.7.3 and 6.7.4. This point corresponds to the cusp of the cardioid-like curve.

Conversely, as $La \to \infty$, the growth rates tend toward the origin, consistent with the asymptotic result obtained in Section 6.7.4,

$$s \sim \pm \mathrm{i}\sqrt{\frac{(n-1)(n+1)(n+2)}{La}} \to 0\,. \tag{6.7.68}$$

Increasing the mode number n shifts the cusp further into the negative real half-plane, since

$$\lim_{n\to\infty} -\frac{(n-1)(n+1)(2n+1)}{2(2n^2+1)} = -\infty\,. \tag{6.7.69}$$

In particular, the cusp location scales linearly with n for large mode number.

For all computed values of La and n, the admissible growth rates satisfy

$$\mathrm{Re}(s) < 0\,.$$

While a fully rigorous analytical proof remains elusive, the numerical evidence suggests that no unstable growth rates arise in Cases 2 and 3.

In conclusion, for a steady base-state radius ($\dot{a} = 0$, $a = 1$) in the Navier–Stokes regime, the numerical computations provide compelling evidence that the bubble remains linearly stable.

6.8 Growth rate for time-dependent base-state bubble radius

In this section, we develop a theoretical framework for the numerical computation of growth rates when the base-state bubble radius is time dependent. In Section 6.2 of this chapter, we derived the general inertial perturbation equations governing the evolution of a disturbance to a radially oscillating bubble. Starting from the stream-function decomposition (6.2.1),

$$\psi(r, \xi, t) = -a^2\dot{a}\xi + \epsilon\psi_1(r, \xi, t)\,, \tag{6.8.1}$$

where ψ_1 is given by (6.2.7),

$$\psi_1(r, \xi, t) = \sum_{n=0}^{\infty} g_n(r, t)\mathscr{P}_n(\xi)\,, \tag{6.8.2}$$

where we recall that

$$\mathscr{P}_n(\xi) = \int_{-1}^{\xi} P_n(x)\,\mathrm{d}x\,. \tag{6.8.3}$$

We subsequently obtained the coupled equations (6.2.12) and (6.2.14) for the functions $g_n(r, t)$ and $w_n(r, t)$, together with the associated kinematic and dynamic boundary conditions at the bubble interface.

In section 6.3, analytical progress was obtained by restricting attention to the case of a steady base-state radius, corresponding to the simplification $\Delta = 0$ in (6.4.2). We now remove that assumption and consider the more general case of a time-dependent periodically oscillating base state. The resulting governing equations now contain coefficients that vary periodically in time, and closed-form analytical solutions are no longer available. Consequently, the stability problem must instead be formulated as a discretised Floquet eigenvalue problem.

Specifically, we consider a periodically oscillating base-state radius of the form

$$a(t) = 1 + \Delta \cos(Ca\, t)\,, \tag{6.8.4}$$

where Ca is the capillary number. As before, we neglect surfactant effects by setting $\beta_s = 0$ in (6.5.4), so that $\sigma_0 = \sigma_1 = 0$.

The perturbed bubble surface is written as in (6.4.1),

$$f(\theta, t) = a(t) + \epsilon A_n(t) P_n(\cos\theta)\,, \tag{6.8.5}$$

where $A_n(t)$ is the perturbation amplitude. Linear stability is determined by the temporal behaviour of $A_n(t)$: growth indicates instability, while decay implies stability.

The amplitude evolution equation in this regime is given by (6.4.14),

$$\frac{\mathrm{d}A_{1,n}}{\mathrm{d}t} + \frac{2\dot{a}}{a} A_{1,n}(t) = -\frac{1}{a^2} g_n(a, t)\,, \tag{6.8.6}$$

where the function $g_n(r, t)$ is related to the quantity $w_n(r, t)$ via (6.2.12)

$$w_n(r, t) = \frac{\partial^2 g_n}{\partial r^2} - \frac{n(n+1)}{r^2} g_n\,, \tag{6.8.7}$$

and w_n satisfies the linearised Navier–Stokes equation (6.2.14)

$$La \left[\frac{\partial w_n}{\partial t} + \frac{a^2 \dot{a}}{r^2} \left(\frac{\partial w_n}{\partial r} - \frac{2}{r} w_n \right) \right] = \frac{\partial^2 w_n}{\partial r^2} - \frac{n(n+1)}{r^2} w_n\,. \tag{6.8.8}$$

The solutions to (6.8.7) and (6.8.8) must satisfy the dynamic boundary conditions

$$-p_1(a,t) + 12\frac{\dot{a}}{a^2}A_{1,n}(t) + \frac{2}{a^2}\left(\frac{2g_n(a,t)}{a} - \frac{\partial g_n}{\partial r}\right) = \frac{1}{a^2}\left((n-1)(n+2)\sigma_0 + \mathcal{B}\delta_{n,0}\right)A_{1,n}(t)\,, \qquad (6.8.9a)$$

from (6.5.5a) and

$$3n(n+1)\frac{\dot{a}}{a}A_{1,n}(t) + \frac{1}{2a^2}\left(a^2\frac{\partial^2 g_n}{\partial r^2} - 2a\frac{\partial g_n}{\partial r} + n(n+1)g_n(a,t)\right) = 0\,, \qquad (6.8.9b)$$

from (6.5.5b), which are to be evaluated at $r = a(t)$.

The physical domain extends from the bubble surface $r = a(t)$ to infinity. For numerical purposes, this unbounded domain is truncated by introducing an artificial outer permeable boundary at $r = aR$, where $R > 1$. This boundary allows a flux of fluid at leading-order. At this boundary, we impose permeability and no-slip conditions, requiring

$$u_r = \frac{\dot{a}}{R^2} \qquad \text{and} \qquad u_\theta = 0 \qquad \text{at} \qquad r = aR\,.$$

The radial velocity is given by

$$u_r = -\frac{1}{r^2}\frac{\partial\psi}{\partial\xi} = -\frac{1}{r^2}\left(-a^2\dot{a} + \epsilon g_n P_n(\cos\theta)\right)\,. \qquad (6.8.10)$$

Evaluating this condition at $r = aR$ yields

$$\frac{\dot{a}}{R^2} - \epsilon\frac{1}{a^2R^2}g_n P_n(\cos\theta) = \frac{\dot{a}}{R^2}\,. \qquad (6.8.11)$$

At $O(1)$, (6.8.11) is automatically satisfied. At $O(\epsilon)$, the permeability condition (6.8.11) is satisfied provided that

$$g_n(R,t) = 0\,. \qquad (6.8.12)$$

The tangential velocity is

$$u_\theta = -\frac{1}{r\sin\theta}\frac{\partial\psi}{\partial r} = -\frac{\epsilon}{r\sin\theta}\frac{\partial g_n}{\partial r}\mathscr{P}_n(\cos\theta)\,, \tag{6.8.13}$$

and the no-slip condition therefore implies

$$\frac{\partial g_n}{\partial r} = 0 \qquad \text{at } r = aR\,. \tag{6.8.14}$$

To simplify the numerical treatment and fix the computational domain, we introduce the scaled radial coordinate

$$\eta = \frac{r}{a(t)}\,, \tag{6.8.15}$$

so that the domain becomes $1 \le \eta \le R$. Applying the chain rule yields

$$\frac{\partial}{\partial t} = -\frac{\dot a}{a}\eta\frac{\partial}{\partial\eta} + \frac{\partial}{\partial t}\,, \qquad \frac{\partial}{\partial r} = \frac{1}{a}\frac{\partial}{\partial\eta}\,. \tag{6.8.16}$$

Substituting (6.8.15) and (6.8.16) into the above differential equations and boundary conditions gives us the following problem to solve.

$$w_n(\eta,t) = \frac{1}{a^2}\frac{\partial^2 g_n}{\partial\eta^2} - \frac{n(n+1)}{a^2\eta^2}g_n\,, \tag{6.8.17}$$

$$La\left[-\frac{\dot a}{a}\eta\frac{\partial w_n}{\partial\eta} + \frac{\partial w_n}{\partial t} + \frac{\dot a}{\eta^2}\left(\frac{1}{a}\frac{\partial w_n}{\partial\eta} - \frac{2}{a\eta}w_n\right)\right] = \frac{1}{a^2}\frac{\partial^2 w_n}{\partial\eta^2} - \frac{n(n+1)}{a^2\eta^2}w_n\,, \tag{6.8.18}$$

with a kinematic boundary condition, at $\eta = 1$

$$a^2\frac{\mathrm{d}A_{1,n}}{\mathrm{d}t} + 2a\dot a A_{1,n}(t) = -g_n(1,t)\,, \tag{6.8.19}$$

and dynamic boundary conditions at $\eta = 1$ given by (6.8.9a)

$$-p_1a^3 + 12a\dot a A_{1,n} + 2\left(2g_n - \frac{\partial g_n}{\partial\eta}\right) = a\left((n-1)(n+2) + \frac{\mathcal{B}}{a^{3\gamma-1}}\delta_{n,0}\right)A_{1,n}\,, \tag{6.8.20}$$

and (6.8.9b)

$$3n(n+1)a\dot{a}A_{1,n}+\frac{1}{2}\left(\frac{\partial^2 g_n}{\partial\eta^2}-2\frac{\partial g_n}{\partial\eta}+n(n+1)g_n(1,t)\right)=0\,, \tag{6.8.21}$$

where, from (6.6.16) and changing variable $r \leftrightarrow \eta$ via (6.8.15),

$$p_1(1,t)=-\frac{1}{an(n+1)}\frac{\partial w_n}{\partial\eta}+\frac{La}{an(n+1)}\left(\frac{\partial^2 g_n}{\partial\eta\,\partial t}-\frac{\dot{a}}{a}\frac{\partial g_n}{\partial\eta}\right)\,. \tag{6.8.22}$$

We also have the permeability condition

$$g_n(R,t)=0\,, \tag{6.8.23}$$

and a no slip condition

$$\frac{\mathrm{d}g_n}{\mathrm{d}\eta}=0\,, \tag{6.8.24}$$

at $\eta = R$.

Since the base-state radius is periodic in time, the governing equations have periodic coefficients. We therefore seek solutions using a Floquet–Fourier decomposition.

$$A_{1,n}=e^{st}\sum_{m=-\infty}^{\infty}A_m e^{\mathrm{i}mCa\,t}\,,\qquad a=\sum_{k=-\infty}^{\infty}a_k e^{\mathrm{i}kCa\,t}\,, \tag{6.8.25}$$

$$a^2=\sum_{k=-\infty}^{\infty}\alpha_k e^{\mathrm{i}kCa\,t}\,,\qquad a\dot{a}=\sum_{k=-\infty}^{\infty}\beta_k e^{\mathrm{i}kCa\,t}\,, \tag{6.8.26}$$

and

$$g_n=e^{st}\sum_{m=-\infty}^{\infty}F_m(\eta)e^{\mathrm{i}mCa\,t}\,,\qquad w_n=e^{st}\sum_{m=-\infty}^{\infty}W_m(\eta)e^{\mathrm{i}mCa\,t}\,, \tag{6.8.27}$$

where s is a growth rate, A_m, a_k, α_k and β_k are constants and F_m and W_m are functions of η. The values of a_k, α_k and β_k are as follows:

$$a_k = \begin{cases} 1\,, & k=0 \\ \dfrac{\Delta}{2}\,, & k=\pm 1 \\ 0\,, & |k|\geq 2 \end{cases}\,, \qquad \alpha_k = \begin{cases} 1+\dfrac{\Delta^2}{2}\,, & k=0 \\ \Delta\,, & k=\pm 1 \\ \dfrac{\Delta^2}{4}\,, & k=\pm 2 \\ 0\,, & |k|\geq 3 \end{cases}\,, \tag{6.8.28}$$

$$\beta_k = \begin{cases} \dfrac{Ca\,\Delta}{2}\mathrm{i}\,, & k=1 \\ -\dfrac{Ca\,\Delta}{2}\mathrm{i}\,, & k=-1 \\ \dfrac{Ca\,\Delta^2}{4}\mathrm{i}\,, & k=2 \\ -\dfrac{Ca\,\Delta^2}{4}\mathrm{i}\,, & k=-2 \\ 0\,, & \text{else} \end{cases}\,. \tag{6.8.29}$$

Substituting these expansions into the governing equations and boundary conditions yields a coupled system of linear algebraic equations for the Fourier coefficients. Truncating the Fourier series at $|m| \leq M$ results in a finite-dimensional system. We now substitute these Fourier expressions into the above differential equations and boundary conditions truncated at M. As we are only interested in values of $n \geq 2$, $\delta_{n,0} = 0$ in (6.8.20).

6.8.1 Discretisation and formulation of the eigenvalue problem

To discretise the radial dependence, we introduce a uniform grid in the rescaled coordinate $\eta = r/a(t)$. For $j = 1, \ldots, N$, we define

$$\eta_j = 1 + (j-1)h\,, \tag{6.8.30}$$

where

$$h = \frac{R-1}{N-1}\,. \tag{6.8.31}$$

The quantities

$$F_{m,j} = F_m(\eta_j)\,, \qquad W_{m,j} = W_m(\eta_j)\,,$$

denote the values of the Fourier mode m evaluated at the grid point η_j. Here, the first index labels the Fourier mode and the second index labels the radial grid point. Thus, $F_{m,j}$ represents a scalar unknown associated with the pair (m, η_j), rather than a two-dimensional array.

To allow the use of centred finite-difference schemes at the boundaries $\eta = 1$ and $\eta = R$, we introduce two *ghost points* (or fictitious points) at

$$\eta_0 = 1 - h\,, \qquad \eta_{N+1} = R + h\,.$$

These points do not correspond to physical locations but are introduced so that centred finite-difference approximations may also be applied at the boundary grid points. The ghost-point values therefore appear as additional unknowns in the discretised system and are determined simultaneously with the interior values through the discretised boundary and interface conditions. This approach preserves second-order accuracy throughout the computational domain.

Using centred finite differences, the first and second derivatives are approximated as

$$F'_{m,j} \approx \frac{F_{m,j+1} - F_{m,j-1}}{2h}\,, \qquad F''_{m,j} \approx \frac{F_{m,j+1} - 2F_{m,j} + F_{m,j-1}}{h^2}\,, \tag{6.8.32}$$

with analogous expressions for $W_{m,j}$.

With these approximations, the equation defining W, given by (6.8.17), becomes

$$\sum_{k=-M}^{M} \alpha_{m-k} W_{k,j} - F''_{m,j} + \frac{n(n+1)}{\eta_j^2} F_{m,j} = 0\,. \tag{6.8.33}$$

Similarly, the governing equation (6.8.18) becomes

$$\begin{aligned} &La\left(\frac{1}{\eta_j^2}-\eta_j\right)\sum_{k=-M}^{M}\beta_{m-k}W'_{k,j}-La\frac{2}{\eta_j^3}\sum_{k=-M}^{M}\beta_{m-k}W_{k,j}-W''_{m,j} \\ &\quad+\frac{n(n+1)}{\eta_j^2}W_{m,j}+La\,\mathrm{i}m\,Ca\sum_{k=-M}^{M}\alpha_{m-k}W_{k,j}=-La\,s\sum_{k=-M}^{M}\alpha_{m-k}W_{k,j}\,. \end{aligned} \tag{6.8.34}$$

The kinematic condition (6.8.19) at $\eta = 1$ becomes

$$\mathrm{i}m\,Ca\sum_{k=-M}^{M}\alpha_{m-k}A_k+2\sum_{k=-M}^{M}\beta_{m-k}A_k+F_{m,1}=-s\sum_{k=-M}^{M}\alpha_{m-k}A_k\,. \tag{6.8.35}$$

The first dynamic condition (6.8.20) becomes

$$\begin{aligned} &\frac{1}{n(n+1)}\sum_{k=-M}^{M}\alpha_{m-k}W'_{k,1}+12\sum_{k=-M}^{M}\beta_{m-k}A_k+4F_{m,1}-2F'_{m,1} \\ &\quad-(n-1)(n+2)\sum_{k=-M}^{M}a_{m-k}A_k+\frac{La}{n(n+1)}\sum_{k=-M}^{M}\beta_{m-k}F'_{k,1} \\ &\quad-\frac{\mathrm{i}m\,Ca\,La}{n(n+1)}\sum_{k=-M}^{M}\alpha_{m-k}F'_{k,1}=\frac{La\,s}{n(n+1)}\sum_{k=-M}^{M}\alpha_{m-k}F'_{k,1}\,. \end{aligned} \tag{6.8.36}$$

The second dynamic condition (6.8.21) becomes

$$3n(n+1)\sum_{k=-M}^{M}\beta_{m-k}A_k+\frac{1}{2}F''_{m,1}-F'_{m,1}+\frac{n(n+1)}{2}F_{m,1}=0\,. \tag{6.8.37}$$

At the outer boundary $\eta = R$, the impermeability and no-slip conditions (6.8.12) and (6.8.14) become

$$F_{m,N}=0\,,\qquad F'_{m,N}=0\,. \tag{6.8.38}$$

Collecting the discretised governing equations, boundary conditions, and interface conditions yields a finite-dimensional linear system for the unknown Fourier–radial coefficients,

$$\boldsymbol{x}=(\boldsymbol{F}\,,\boldsymbol{W}\,,\boldsymbol{c})^{\mathsf{T}}\,, \tag{6.8.39}$$

where $\boldsymbol{F}$ and $\boldsymbol{W}$ denote vectors obtained by stacking the discrete Fourier–radial coefficients $F_{m,j}$ and $W_{m,j}$, respectively, over all Fourier modes $-M \leq m \leq M$ and radial grid points $0 \leq j \leq N+1$. Explicitly,

$$\boldsymbol{F} = \{F_{-M,0}, F_{-M,1}, \ldots, F_{-M,N+1}, \ldots, F_{M,0}, \ldots, F_{M,N+1}\}\,, \tag{6.8.40a}$$

$$\boldsymbol{W} = \{W_{-M,0}, W_{-M,1}, \ldots, W_{-M,N+1}, \ldots, W_{M,0}, \ldots, W_{M,N+1}\}\,, \tag{6.8.40b}$$

$$\boldsymbol{c} = \{A_{-M}, A_{-M+1}, \ldots, A_{M}\}\,. \tag{6.8.40c}$$

Here, the first index m labels the Fourier mode, while the second index j labels the radial grid point.

The discretised governing equations and boundary conditions define a coupled linear system for the unknown Fourier–radial coefficients contained in $\boldsymbol{x}$. Each discretised equation contributes a set of rows to the global matrices $\boldsymbol{A}$ and $\boldsymbol{B}$. Specifically,

- the discretised relation (6.8.33) between $F_{m,j}$ and $W_{m,j}$ contributes the block rows $\boldsymbol{A}_{FF}$ and $\boldsymbol{A}_{FW}$;

- the discretised evolution equation (6.8.34) for $W_{m,j}$ contributes the block $\boldsymbol{A}_{WW}$, while the terms proportional to the eigenvalue s contribute the corresponding block $\boldsymbol{B}_{WW}$;

- the kinematic condition (6.8.35) couples the interface amplitudes A_m to the interfacial values $F_{m,1}$, producing the blocks $\boldsymbol{A}_{AF}$ and $\boldsymbol{A}_{AA}$. The terms proportional to s contribute the block $\boldsymbol{B}_{AA}$;

- the first dynamic boundary condition (6.8.36) contributes the constraint blocks $\boldsymbol{A}_{C_1F}$, $\boldsymbol{A}_{C_1W}$, and $\boldsymbol{A}_{C_1A}$, while the terms proportional to s contribute the block $\boldsymbol{B}_{C_1F}$;

- the second dynamic boundary condition (6.8.37) contributes the blocks $\boldsymbol{A}_{C_2F}$ and $\boldsymbol{A}_{C_2A}$;

- the outer-boundary conditions (6.8.38) at $\eta = R$ generate the final constraint rows $\boldsymbol{A}_{C_3F}$ and $\boldsymbol{A}_{C_4F}$.

The subscripts indicate both the equation from which the block arises and the variables on which it acts. For example, $\boldsymbol{A}_{FF}$ contains the coefficients multiplying the unknowns $\boldsymbol{F}$ in the discretised $F_{m,j}$-equation (6.8.33), while $\boldsymbol{A}_{FW}$ contains the coefficients multiplying $\boldsymbol{W}$ in that same equation. Similarly, $\boldsymbol{A}_{AA}$ contains the coefficients multiplying $\boldsymbol{c}$ in the discretised A_m-equation (6.8.35).

The resulting system can be written compactly as the generalised eigenvalue problem

$$\boldsymbol{A}\boldsymbol{x} = s\,\boldsymbol{B}\boldsymbol{x}\,, \tag{6.8.41}$$

where $\boldsymbol{A}$ and $\boldsymbol{B}$ are block matrices encoding the spatial operators, time-periodic coupling, and boundary conditions. The block structure of this system is

$$\begin{pmatrix} \boldsymbol{A}_{FF} & \boldsymbol{A}_{FW} & \boldsymbol{0} \\ \boldsymbol{0} & \boldsymbol{A}_{WW} & \boldsymbol{0} \\ \boldsymbol{A}_{AF} & \boldsymbol{0} & \boldsymbol{A}_{AA} \\ \boldsymbol{A}_{C_1F} & \boldsymbol{A}_{C_1W} & \boldsymbol{A}_{C_1A} \\ \boldsymbol{A}_{C_2F} & \boldsymbol{0} & \boldsymbol{A}_{C_2A} \\ \boldsymbol{A}_{C_3F} & \boldsymbol{0} & \boldsymbol{0} \\ \boldsymbol{A}_{C_4F} & \boldsymbol{0} & \boldsymbol{0} \end{pmatrix} \boldsymbol{x} = s \begin{pmatrix} \boldsymbol{0} & \boldsymbol{0} & \boldsymbol{0} \\ \boldsymbol{0} & \boldsymbol{B}_{WW} & \boldsymbol{0} \\ \boldsymbol{0} & \boldsymbol{0} & \boldsymbol{B}_{AA} \\ \boldsymbol{B}_{C_1F} & \boldsymbol{0} & \boldsymbol{0} \\ \boldsymbol{0} & \boldsymbol{0} & \boldsymbol{0} \\ \boldsymbol{0} & \boldsymbol{0} & \boldsymbol{0} \\ \boldsymbol{0} & \boldsymbol{0} & \boldsymbol{0} \end{pmatrix} \boldsymbol{x}\,. \tag{6.8.42}$$

Each block of $\boldsymbol{A}$ and $\boldsymbol{B}$ is constructed using a standard *column-by-column matrix assembly* procedure. Concretely, to determine the column corresponding to a particular unknown, e.g., $F_{m,j}$, we set

$$F_{m,j} = 1\,, \qquad \text{all other components of } \boldsymbol{x} = 0\,,$$

and evaluate the left-hand side of all discretised equations. The resulting coefficients populate the corresponding rows of that column. Repeating this procedure for every degree of freedom constructs the full matrix.

This method is applied uniformly to all blocks, including those that couple different Fourier modes through the time-periodic base state. After assembly, the generalised eigenvalue problem can be solved numerically to obtain the Floquet growth rates s, which determine the stability of the bubble.

In this section, we have outlined an extension of the inertial stability analysis to the case of a time-dependent base-state bubble radius. While the formulation follows naturally from the steady-radius analysis developed earlier in this chapter, we have so far been unable to obtain reliable numerical results for the associated growth rates. The increased complexity of the governing equations, combined with the time dependence of the base state, presents significant analytical and computational challenges. Addressing these difficulties remains an important direction for future work and would allow a direct comparison with the Floquet-based stability results obtained in the Stokes flow regime.

7

Conclusions

7.1 Summary of research

The transport of water under negative pressure in plant xylem remains one of the most striking examples of metastable fluid behaviour in nature. Most detrimental to the plant in this phenomenon is the formation and evolution of gas bubbles within the xylem sap, which have traditionally been associated with cavitation and hydraulic failure. However, growing experimental evidence has revealed the widespread presence of long-lived, surfactant-coated nanobubbles that do not necessarily lead to embolism (Ingram et al., 2021). This thesis has aimed to address the fundamental mathematical question of whether such nanobubbles can be dynamically stable under physiologically relevant conditions.

In Chapter 2, the mathematical foundations required for modelling xylem bubble dynamics were established. Starting from the full Navier–Stokes equations, the Stokes flow regime appropriate for xylem conditions was derived using dimensional analysis. Classical bubble dynamics were reviewed through the Rayleigh–Plesset equation, and tools from linear stability theory and Floquet theory were introduced to analyse both steady and time-periodic systems. This chapter provided the analytical framework that underpins all subsequent modelling and analysis in the thesis.

Chapter 3 introduced numerical optimisation techniques designed to explore the high-dimensional parameter space associated with surfactant-covered bubble models. Global optimisation methods, including genetic algorithms and simulated annealing, were demonstrated to be effective tools for identifying parameter combinations that influence stability. These techniques were subsequently used to complement analytical results and to assess the sensitivity and robustness of stability outcomes across a broad range of physical parameters.

In Chapter 5, a detailed axisymmetric model of a surfactant-covered bubble immersed in a viscous fluid was developed. We considered both an infinite domain and the case where we introduce a wall. Governing equations were derived for both constant and time-dependent bubble radii, incorporating interfacial stress balances, gas compressibility, and surfactant transport along the bubble surface. Linear stability equations were obtained for spherical and weakly deformed bubbles. For a bubble with constant radius, exact expressions for the growth rate were derived both in the presence and absence of surfactants. These results showed that, regardless of the parameter values chosen, the bubble remains stable. In fact, in (4.9.32) we showed that the presence of surfactants further enhances stability in this regime.

For a bubble with a time-periodically varying radius, exact expressions for the growth rate were obtained in the absence of surfactants using Floquet theory. When surfactants were included, numerical methods were required to analyse the resulting stability equations. Numerical evaluation across a wide range of physically relevant parameters, using global optimisation techniques, consistently indicated that surfactants do not destabilise the bubble interface. No growing modes were observed in the parameter regimes explored, even under periodic forcing of the bubble radius.

The analysis was extended in Chapter 5 to non-axisymmetric perturbations, allowing fully three-dimensional surface deformations to be considered. Evolution equations were derived for the perturbation amplitudes, resulting in a coupled stability system that accounts for hydrodynamics, surfactant redistribution, and interfacial elasticity. The results demonstrated that the inclusion of three-dimensional perturbations does not alter the stability conclusions obtained in Chapter 4: the bubble remains stable across the parameter space considered, indicating that non-axisymmetric modes do not introduce new instability mechanisms in the presence of surfactants.

In Chapter 6, the assumption of negligible inertia was relaxed and inertial effects were incorporated through the full Navier–Stokes equations. Modified kinematic and dynamic boundary conditions were derived, and a simplified inertial regime was analysed. Although inertia introduces additional terms into the governing equations, the steady bubble case continued to exhibit a negative growth rate, indicating stability.

Taken together, the results of Chapters 4–6 provide a consistent and robust conclusion: within the modelling framework considered in this thesis, surfactant-covered nanobubbles are stable across a broad range of parameters relevant to plant xylem. This theoretical finding aligns naturally with experimental demonstrations that xylem sap can sustain significant negative pressures without widespread cavitation, and supports the view that nanobubbles, when stabilised by surfactants, need not inevitably lead to embolism. Moreover, no evidence was found to support the hypothesis that surfactants can destabilise and break down nanobubbles, in contrast to the results reported by Xiao et al. (2017).

7.2 Reflection

With the benefit of hindsight, there are several aspects of the project that provided valuable opportunities for learning. In particular, when I started this project, an earlier and deeper understanding of the work by Blyth & Pozrikidis (2005) would have provided a stronger foundation for the mathematical modelling and may have allowed additional avenues of research to be explored within the available time.

Similarly, prior to this project, I had not encountered the Lamb solution to Stokes flow in spherical geometry. Gaining familiarity with this solution over the course of the project has been instrumental in developing the non-axisymmetric analysis presented in Chapter 5 and has provided a useful toolset for future investigations of similar problems.

At the outset of the project, the research direction was strongly guided by my supervisors, with clear objectives focused on understanding and extending existing work. As the project progressed, I took increasing responsibility for shaping the direction of the research and making independent decisions regarding modelling approaches and analytical techniques. This transition represents a significant development in my ability to conduct independent research, but I recognise I still have more room to grow.

Also, the idea of giving presentations on my work scared me and I didn't think I would be able to do it. Giving talks can be challenging for many people, and this was particularly the case for me due to autism. Over the course of the PhD, however, I have delivered numerous presentations at UEA, the John Innes Centre, and conferences in Bristol, Newcastle, Harrogate, and Exeter. My confidence in presenting has improved substantially, and I regard this as an important personal and professional development arising from the PhD.

7.3 Future work

An immediate direction for future work is the continued development of the numerical Floquet framework introduced in Section 6.8 for the case of a time-dependent inertial base state. Although the governing equations and discretised eigenvalue problem have been formulated, obtaining reliable numerical growth rates has proved considerably more challenging than in the corresponding Stokes-flow analysis.

Ongoing work is focused on improving the numerical implementation and verifying convergence of the discretised system. We expect these difficulties to be resolved in the near future, allowing the resulting Floquet stability calculations to be published as a continuation of the present work.

Several natural extensions of this work remain. A key next step would be to incorporate surfactant effects into the inertial bubble model developed in Chapter 6. Doing so would help clarify whether the combination of inertia and surfactant dynamics could introduce destabilising mechanisms not captured in the present analysis.

As discussed in the Introduction, soluble surfactants are present in xylem sap. The surfactant transport model used in this thesis assumes insoluble surfactants and therefore neglects exchange between the bubble surface and the surrounding fluid. An important extension would be to adopt a transport model that allows for adsorption and desorption of surfactant molecules, enabling a more realistic representation of xylem chemistry. To account for this, we could extend the surfactant transport equation so that we have

$$\frac{\partial \Gamma}{\partial t} + \nabla_{\mathrm{s}} \cdot (\Gamma \boldsymbol{u}_{\mathrm{s}}) + 2\Gamma \kappa_m u_n = D_{\mathrm{s}} \nabla_{\mathrm{s}}^2 \Gamma + J_b \,, \tag{7.3.1}$$

where $u_n = \boldsymbol{u} \cdot \hat{\boldsymbol{n}}$ is the normal velocity, $\boldsymbol{u}_s = (\boldsymbol{I} - \hat{\boldsymbol{n}}\hat{\boldsymbol{n}}) \cdot \boldsymbol{u}$ is the surface velocity vector, $\nabla_{\mathrm{s}} = (\boldsymbol{I} - \hat{\boldsymbol{n}}\hat{\boldsymbol{n}}) \cdot \nabla$ is the surface gradient operator, D_{s} is the surfactant diffusivity and $\nabla_{\mathrm{s}}^2 = \nabla_{\mathrm{s}} \cdot \nabla_{\mathrm{s}}$ is the surface Laplacian operator and

$$J_b = k_a C \left(1 - \frac{\Gamma}{\Gamma_\infty}\right) - k_d \Gamma \Bigg|_{r=f} \,, \tag{7.3.2}$$

is the flux of surfactants onto and off the bubble surface where k_a is a measure of adsorption and k_d is a measure of desorption. $C(r, \theta, t)$ is the concentration of surfactants in the bulk fluid and satisfies the convection-diffusion equation

$$\frac{\partial C}{\partial t} + \boldsymbol{u} \cdot \nabla C = D_b \nabla^2 C \,, \tag{7.3.3}$$

where $\boldsymbol{u}$ is the velocity field given in an axisymmetric regime by $\boldsymbol{u} = u_r \hat{\boldsymbol{r}} + u_\theta \hat{\boldsymbol{\theta}}$ and D_b is the diffusivity constant in the bulk. We also have the boundary condition that

$$D_b(\hat{\boldsymbol{n}} \cdot \nabla C) = J_b \tag{7.3.4}$$

at $r = f$ where $\hat{\boldsymbol{n}}$ is the unit normal vector to the bubble surface.

As discussed in the introduction, water in the xylem is under tension. Under such conditions, the common assumption of incompressibility may no longer be strictly valid. While this assumption has been made here to simplify the mathematics, a more realistic treatment would account for density variations in the fluid. A natural extension of this work would be to consider the full compressible Navier–Stokes equations, where the fluid density is allowed to vary:

$$\rho\left(\frac{\partial \boldsymbol{u}}{\partial t} + \boldsymbol{u} \cdot \nabla \boldsymbol{u}\right) = -\nabla p + \nabla \cdot \boldsymbol{\tau} + \boldsymbol{f}\,, \tag{7.3.5a}$$

$$\frac{\partial \rho}{\partial t} + \nabla \cdot (\rho \boldsymbol{u}) = 0\,, \tag{7.3.5b}$$

$$\boldsymbol{\tau} = \mu\left(\nabla \boldsymbol{u} + \nabla \boldsymbol{u}^{\mathsf{T}}\right) + \left(\lambda - \frac{2}{3}\mu\right)(\nabla \cdot \boldsymbol{u})\,\boldsymbol{I}\,, \tag{7.3.5c}$$

where $\boldsymbol{\tau}$ is the viscous stress tensor, μ and λ are the shear and bulk viscosities, respectively, and $\boldsymbol{f}$ represents external body forces, such as gravity. Incorporating compressibility would allow for a more accurate description of bubble dynamics in xylem sap under tension and could provide insight into how density fluctuations interact with interfacial surfactants to affect bubble stability.

7

Bibliography

Abramowitz, M. & Stegun, I. A. (1964). *Handbook of mathematical functions with formulas, graphs, and mathematical tables*, volume 55. US Government printing office.

Adou, A.-h. E. & Tuckerman, L. S. (2016). Faraday instability on a sphere: Floquet analysis. *Journal of Fluid Mechanics*, 805, 591–610.

Ahlfors, L. V. (1979). *Complex Analysis: An Introduction to the Theory of Analytic Functions of One Complex Variable.* New York: McGraw–Hill, 3 edition.

Alqudah, A., Malkawi, A., & Alwadie, A. (2014). Adaptive control of dc-dc converter using simulated annealing optimization method. *Journal of Signal and Information Processing*, 5(4), 198–207.

Arbeille, P., Zuj, K. A., Macias, B. R., Ebert, D. J., Laurie, S. S., Sargsyan, A. E., Martin, D. S., Lee, S. M., Dulchavsky, S. A., Stenger, M. B., et al. (2021). Lower body negative pressure reduces jugular and portal vein volumes and counteracts the elevation of middle cerebral vein velocity during long-duration spaceflight. *Journal of Applied Physiology*, 131(3), 1080–1087.

Aris, R. (2012). *Vectors, tensors and the basic equations of fluid mechanics.* Courier Corporation.

Atchley, A. A. (1989). The blake threshold of a cavitation nucleus having a radius-dependent surface tension. *The Journal of the Acoustical Society of America*, 85(1), 152–157.

Batchelor, G. K. (1967). *An introduction to fluid dynamics*. Cambridge university press.

Bernoulli, D. (1738). Hydrodynamica. *Dulsecker*, 1738.

Blake, F. G. (1949). The onset of cavitation in liquids. *Tech. Memo.*, (12).

Blyth, M. G. & Morris, R. J. (2018). Fluid transport in plants. In *Mathematical Modelling in Plant Biology* (pp. 15–36). Springer.

Blyth, M. G. & Morris, R. J. (2019). Shear-enhanced dispersion of a wound substance as a candidate mechanism for variation potential transmission. *Frontiers in Plant Science*, 10, 1393.

Blyth, M. G. & Pozrikidis, C. (2004). Evolution equations for the surface concentration of an insoluble surfactant; applications to the stability of an elongating thread and a stretched interface. *Theoretical and Computational Fluid Dynamics*, 17(3), 147–164.

Blyth, M. G. & Pozrikidis, C. (2005). Effect of pulsations on the stability of a gas column. *Theoretical and Computational Fluid Dynamics*, 19(1), 23–37.

Brennen, C. E. (1995). *Cavitation and Bubble Dynamics*, volume 44 of *Oxford Engineering Science Series*. Oxford, UK: Oxford University Press.

Briggs, L. J. (1953). The limiting negative pressure of mercury in Pyrex glass. *Journal of Applied Physics*, 24(4), 488–490.

Brodersen, C. R. & McElrone, A. J. (2013). Maintenance of xylem network transport capacity: a review of embolism repair in vascular plants. *Frontiers in plant science*, 4, 108.

Carreras-Casanova, E. V. & Vanhille, C. (2025). A model for the dynamics of stable gas bubbles in viscoelastic fluids based on bubble volume variation. In *Acoustics*, volume 7 (pp.$\tilde{6}$7).: MDPI.

Cavanagh, A. P., South, P. F., Bernacchi, C. J., & Ort, D. R. (2022). Alternative pathway to photorespiration protects growth and productivity at elevated temperatures in a model crop. *Plant biotechnology journal*, 20(4), 711–721.

Chikasue, Y. & Furukawa, M. (2015). Adjustment of vorticity fields with specified values of casimir invariants as initial condition for simulated annealing of an incompressible, ideal neutral fluid and its mhd in two dimensions. *Journal of Fluid Mechanics*, 774, 443–459.

Ding, K. & Ye, L. (2006). *Laser shock peening performance and process simulation*. CRC press.

Dixon, H. H. & Joly, J. (1894). On the ascent of sap. *Proceedings of the Royal Society of London*, 57, 3–5.

Domec, J.-C., Lachenbruch, B., Meinzer, F. C., Woodruff, D. R., Warren, J. M., & McCulloh, K. A. (2008). Maximum height in a conifer is associated with conflicting requirements for xylem design. *Proceedings of the National Academy of Sciences*, 105(33), 12069–12074.

Duan, C., Karnik, R., Lu, M.-C., & Majumdar, A. (2012). Evaporation-induced cavitation in nanofluidic channels. *Proceedings of the National Academy of Sciences*, 109(10), 3688–3693.

Ellerby, D. & Ennos, A. (1998). Resistances to fluid flow of model xylem vessels with simple and scalariform perforation plates. *Journal of Experimental Botany*, 49(323), 979–985.

Esmaeilnezhad, E., Choi, H. J., Schaffie, M., Gholizadeh, M., & Ranjbar, M. (2017). Characteristics and applications of magnetized water as a green technology. *Journal of Cleaner Production*, 161, 908–921.

Floquet, G. (1883). Sur les équations différentielles linéaires à coefficients périodiques. *Annales scientifiques de l'École Normale Supérieure*, 12, 47–88.

Frenkel, A. L. & Halpern, D. (2002). Stokes-flow instability due to interfacial surfactant. *Physics of Fluids*, 14(7), L45–L48.

Gaiduk, A. P., Gygi, F., & Galli, G. (2015). Density and compressibility of liquid water and ice from first-principles simulations with hybrid functionals. *The journal of physical chemistry letters*, 6(15), 2902–2908.

Glendinning, P. (1994). *Linear differential equations*, (pp. 54–76). Cambridge Texts in Applied Mathematics. Cambridge University Press.

Guan, X., Schenk, H. J., Roth, M. R., Welti, R., Werner, J., Kaack, L., Trabi, C. L., & Jansen, S. (2022). Nanoparticles are linked to polar lipids in xylem sap of temperate angiosperm species. *Tree Physiology*, 42(10), 2003–2019.

Happel, J. & Brenner, H. (1983). *Low Reynolds Number Hydrodynamics: With Special Applications to Particulate Media*. Mechanics of Fluids and Transport Processes. Springer.

Holland, J. H. (1975). *Adaptation in natural and artificial systems: an introductory analysis with applications to biology, control, and artificial intelligence*. MIT press.

Huang, L.-B., Guan, X., Aritsara, A. N. A., Zhu, J.-J., Jansen, S., & Cao, K.-F. (2024). Lipid concentration and composition in xylem sap of woody angiosperms from a tropical savanna and a seasonal rainforest. *Plant Diversity*, 46(1), 126–133.

Ingram, S., Jansen, S., & Schenk, H. J. (2023). Lipid-coated nanobubbles in plants. *Nanomaterials*, 13(11), 1776.

Ingram, S., Salmon, Y., Lintunen, A., Hölttä, T., Vesala, T., & Vehkamäki, H. (2021). Dynamic surface tension enhances the stability of nanobubbles in xylem sap. *Frontiers in plant science*, 12.

Iooss, G. & Joseph, D. D. (1980). *Elementary Stability and Bifurcation Theory*. Berlin: Springer-Verlag.

Isasa, E., Link, R. M., Jansen, S., Tezeh, F. R., Kaack, L., Sarmento Cabral, J., & Schuldt, B. (2023). Addressing controversies in the xylem embolism resistance–vessel diameter relationship. *New Phytologist*.

Jackson, J. D. (1999). *Classical Electrodynamics*. New York: Wiley, 3rd edition.

Jensen, K. H., Berg-Sørensen, K., Bruus, H., Holbrook, N. M., Liesche, J., Schulz, A., Zwieniecki, M. A., & Bohr, T. (2016). Sap flow and sugar transport in plants. *Reviews of modern physics*, 88(3), 035007.

Kanduč, M., Schneck, E., Loche, P., Jansen, S., Schenk, H. J., & Netz, R. R. (2020). Cavitation in lipid bilayers poses strict negative pressure stability limit in biological liquids. *Proceedings of the National Academy of Sciences*, 117(20), 10733–10739.

Katoch, S., Chauhan, S. S., & Kumar, V. (2021). A review on genetic algorithm: past, present, and future. *Multimedia tools and applications*, 80(5), 8091–8126.

Khait, I., Lewin-Epstein, O., Sharon, R., Saban, K., Goldstein, R., Anikster, Y., Zeron, Y., Agassy, C., Nizan, S., Sharabi, G., et al. (2023). Sounds emitted by plants under stress are airborne and informative. *Cell*, 186(7), 1328–1336.

Kim, S. & Karrila, S. J. (2005). *Microhydrodynamics: Principles and Selected Applications*. Mineola, NY: Dover Publications, unabridged edition.

Kirkpatrick, S., Gelatt Jr, C. D., & Vecchi, M. P. (1983). Optimization by simulated annealing. *science*, 220(4598), 671–680.

Knoblauch, M. & Peters, W. S. (2010). Münch, morphology, microfluidics — our structural problem with the phloem. *Plant, cell & environment*, 33(9), 1439–1452.

Lamb, H. (1932). *Hydrodynamics*. Cambridge University Press, 6th edition.

Lens, F., Gleason, S. M., Bortolami, G., Brodersen, C., Delzon, S., & Jansen, S. (2022). Functional xylem characteristics associated with drought-induced embolism in angiosperms. *New Phytologist*, 236(6), 2019–2036.

Lens, F., Tixier, A., Cochard, H., Sperry, J. S., Jansen, S., & Herbette, S. (2013). Embolism resistance as a key mechanism to understand adaptive plant strategies. *Current opinion in plant biology*, 16(3), 287–292.

Li, F. & He, D. (2023). Dynamics of a surfactant-laden viscoelastic thread in the presence of surface viscosity. *Journal of Fluid Mechanics*, 966, A35.

Losso, A., Beikircher, B., Dämon, B., Kikuta, S., Schmid, P., & Mayr, S. (2017). Xylem sap surface tension may be crucial for hydraulic safety. *Plant Physiology*, 175(3), 1135–1143.

Lotka, A. J. (1925). *Elements of physical biology*. Williams & Wilkins.

Manikantan, H. & Squires, T. M. (2020). Surfactant dynamics: hidden variables controlling fluid flows. *Journal of fluid mechanics*, 892.

Martínez-Calvo, A., Rivero-Rodríguez, J., Scheid, B., & Sevilla, A. (2020). Natural break-up and satellite formation regimes of surfactant-laden liquid threads. *Journal of Fluid Mechanics*, 883, A35.

Metropolis, N., Rosenbluth, A. W., Rosenbluth, M. N., Teller, A. H., & Teller, E. (1953). Equation of state calculations by fast computing machines. *The journal of chemical physics*, 21(6), 1087–1092.

Morgan, F. (1994). Mathematicians, including undergraduates, look at soap bubbles. *The American Mathematical Monthly*, 101(4), 343–351.

Ohgaki, K., Khanh, N. Q., Joden, Y., Tsuji, A., & Nakagawa, T. (2010). Physicochemical approach to nanobubble solutions. *Chemical Engineering Science*, 65(3), 1296–1300.

Owoyele, O., Pal, P., & Vidal Torreira, A. (2021). An automated machine learning-genetic algorithm framework with active learning for design optimization. *Journal of Energy Resources Technology*, 143(8), 082305.

Palaparthi, R., Papageorgiou, D. T., & Maldarelli, C. (2006). Theory and experiments on the stagnant cap regime in the motion of spherical surfactant-laden bubbles. *Journal of Fluid Mechanics*, 559, 1–44.

Pallares, G., El Mekki Azouzi, M., González, M. A., Aragones, J. L., Abascal, J. L., Valeriani, C., & Caupin, F. (2014). Anomalies in bulk supercooled water at negative pressure. *Proceedings of the National Academy of Sciences*, 111(22), 7936–7941.

Peters, J. (2001). Total curvature of surfaces (via the divergence of the normal). *International Journal of Mathematical Education in Science and Technology*, 32(6), 795–810.

Plesset, M. S. & Prosperetti, A. (1977). Bubble dynamics and cavitation. *Annual review of fluid mechanics*, 9(1), 145–185.

Prendin, A. L., Mayr, S., Beikircher, B., von Arx, G., & Petit, G. (2018). Xylem anatomical adjustments prioritize hydraulic efficiency over safety as Norway spruce trees grow taller. *Tree Physiology*, 38(8), 1088–1097.

Pritzkow, C., Brown, M. J., Carins-Murphy, M. R., Bourbia, I., Mitchell, P. J., Brodersen, C., Choat, B., & Brodribb, T. J. (2022). Conduit position and connectivity affect the likelihood of xylem embolism during natural drought in evergreen woodland species. *Annals of Botany*, 130(3), 431–444.

Prosperetti, A. (1982). Bubble dynamics: a review and some recent results. *Applied Scientific Research*, 38(1), 145–164.

Rand, R. H. (1983). Fluid mechanics of green plants. *Annual Review of Fluid Mechanics*, 15(1), 29–45.

Rayleigh, L. (1917). Viii. on the pressure developed in a liquid during the collapse of a spherical cavity. *The London, Edinburgh, and Dublin Philosophical Magazine and Journal of Science*, 34(200), 94–98.

Riley, N. (1966). On a sphere oscillating in a viscous fluid. *The Quarterly Journal of Mechanics and Applied Mathematics*, 19(4), 461–472.

Rosen, M. J. & Kunjappu, J. T. (2012). *Surfactants and interfacial phenomena*. John Wiley & Sons.

Roth, A. (1996). Water transport in xylem conduits with ring thickenings. *Plant, Cell & Environment*, 19, 622–629.

Ryley, D. (1962). The thermodynamic and mechanical interaction of water globules and steam in the wet steam turbine. *International Journal of Mechanical Sciences*, 4(5), 447–462.

Schenk, H. J., Espino, S., Romo, D. M., Nima, N., Do, A. Y., Michaud, J. M., Papahadjopoulos-Sternberg, B., Yang, J., Zuo, Y. Y., Steppe, K., et al. (2017). Xylem surfactants introduce a new element to the cohesion-tension theory. *Plant Physiology*, 173(2), 1177–1196.

Schenk, H. J., Jansen, S., & Hölttä, T. (2021a). Positive pressure in xylem and its role in hydraulic function. *New Phytologist*, 230(1), 27–45.

Schenk, H. J., Michaud, J. M., Mocko, K., Espino, S., Melendres, T., Roth, M. R., Welti, R., Kaack, L., & Jansen, S. (2021b). Lipids in xylem sap of woody plants across the angiosperm phylogeny. *The Plant Journal*, 105(6), 1477–1494.

Schenk, H. J., Steppe, K., & Jansen, S. (2015). Nanobubbles: a new paradigm for air-seeding in xylem. *Trends in plant science*, 20(4), 199–205.

Shang, X., Liu, Z., Zhang, J., Lyu, T., & Zou, Y. (2023). Tailoring the mechanical properties of 3d microstructures: A deep learning and genetic algorithm inverse optimization framework. *Materials Today*, 70, 71–81.

Shi, Y., Ke, X., Yang, X., Liu, Y., & Hou, X. (2022). Plants response to light stress. *Journal of Genetics and Genomics*, 49(8), 735–747.

Stone, H. A. & Leal, L. G. (1990). The effects of surfactants on drop deformation and breakup. *Journal of Fluid Mechanics*, 220, 161–186.

Strang, G. (2014). *Differential equations and linear algebra*. Wellesley-Cambridge Press Wellesley.

Suman, B. & Kumar, P. (2006). A survey of simulated annealing as a tool for single and multiobjective optimization. *Journal of the operational research society*, 57(10), 1143–1160.

Van Der Leeden, P., Nio, L. D., & Suratman, P. (1955). The velocity of free falling droplets. *Applied Scientific Research, Section A*, 5(5), 338–348.

Vehmas, T. & Makkonen, L. (2021). Metastable nanobubbles. *ACS omega*, 6(12), 8021–8027.

Venturas, M. D., Sperry, J. S., & Hacke, U. G. (2017). Plant xylem hydraulics: what we understand, current research, and future challenges. *Journal of integrative plant biology*, 59(6), 356–389.

Volterra, V. (1926). Variazioni e fluttuazioni del numero d'individui in specie animali conviventi. *Memorie della Reale Accademia Nazionale dei Lincei, Serie 6*, 2, 31–113. Translated as "Variations and fluctuations of the number of individuals in coexisting animal species".

Wang, D., Heckathorn, S. A., Barua, D., Joshi, P., Hamilton, E. W., & LaCroix, J. J. (2008). Effects of elevated co2 on the tolerance of photosynthesis to acute heat stress in c3, c4, and cam species. *American Journal of Botany*, 95(2), 165–176.

Wang, X., Zhou, S., Shan, Z., & Yin, M. (2021). Investigation of cavitation bubble dynamics considering pressure fluctuation induced by slap forces. *Mathematics*, 9(17), 2064.

Wason, J., Bouda, M., Lee, E. F., McElrone, A. J., Phillips, R. J., Shackel, K. A., Matthews, M. A., & Brodersen, C. (2021). Xylem network connectivity and embolism spread in grapevine (vitis vinifera l.). *Plant Physiology*, 186(1), 373–387.

White, P. J. (2012). Long-distance transport in the xylem and phloem. In *Marschner's mineral nutrition of higher plants* (pp. 49–70). Elsevier, third edition.

Wilson, M. J., McGregor, S., Durney, C. H., Tomkins, M., Armand, J., Smith, R. S., Gray, J. E., Morris, R. J., & Fleming, A. J. (2025). Symplastic guard cell connections buffer pressure fluctuations to promote stomatal function in grasses. *New Phytologist*, 246(1), 192–203.

Wullschleger, S. D., Meinzer, F., & Vertessy, R. (1998). A review of whole-plant water use studies in tree. *Tree physiology*, 18(8-9), 499–512.

Xiao, Q., Liu, Y., Guo, Z., Liu, Z., & Zhang, X. (2017). How nanobubbles lose stability: Effects of surfactants. *Applied Physics Letters*, 111(13).

Yang, J., M Michaud, J., Jansen, S., Schenk, H. J., & Zuo, Y. Y. (2020). Dynamic surface tension of xylem sap lipids. *Tree physiology*, 40(4), 433–444.

Yang, K. & Cho, K. (2019). Simulated annealing algorithm for wind farm layout optimization: A benchmark study. *Energies*, 12(23), 4403.

Zheng, T., Haider, M. S., Zhang, K., Jia, H., & Fang, J. (2020). Biological and functional properties of xylem sap extracted from grapevine (cv. rosario bianco). *Scientia Horticulturae*, 272, 109563.

Zigunov, F., Sellappan, P., & Alvi, F. S. (2022). Reduction of noise in cold and hot supersonic jets using active flow control guided by a genetic algorithm. *Journal of Fluid Mechanics*, 952, A40.

Appendices

A1 Code for Genetic Algorithm

```
close all;
clear all;
clc

global  n  iPe  gamma B P Ca

format long

% Parameters

n      = 50;
iPe    = 0.0;
gamma  = 1.0; % adiabatic index
B      = 0.01;
Ca     = 1.0;

beta_min     = 0.1;
Delta_min    = 0.1;
Gamma_R_max = (1 - Delta_min)^2*(1 - exp(-1/beta_min));

if n==0
    P = 2;
else
    P = 0;
end
```

```


% Define Parameter Bounds
lb = [beta_min, 0.1, Delta_min]; % Lower bounds for parameters [beta_s, Gamma_R, Delta]
ub = [5, Gamma_R_max, 0.99];  % Upper bounds for parameters [beta_s, Gamma_R, Delta]


% Genetic Algorithm Optimization
options = optimoptions('ga', 'Display', 'iter', 'PopulationSize', 50, 'MaxGenerations', 200,'ConstraintTolerance', 1e-8);
optimal_params = ga(@(params) objective_function(params), 3, [],[], [], [],
lb, ub, @nonlinear_constraint, options);

% Display the Optimal Parameters
disp('Optimal Parameters Found:');
disp(['beta_s = ', num2str(optimal_params(1))]);
disp(['Gamma_R = ', num2str(optimal_params(2))]);
disp(['Delta = ', num2str(optimal_params(3))]);


% Display the Final Error
final_error = objective_function(optimal_params);
disp(['Maximum s1: ', num2str(-objective_function(optimal_params))]);
disp(['Minimum sig0: ', num2str(1 + optimal_params(1)*log(1 - optimal_params(2)/(1 - optimal_params(3))^2))]);


% Objective Function (Maximise s1)
function f = objective_function(params)
  global sig s1 Ca s2
```

```

beta_s  = params(1);
Gamma_R = params(2);
Delta   = params(3);


  Nt = 1000;
    T  = 2*pi/Ca;
    dt = T/Nt;

    yy1 = [1 0];
    t1  = 0;
    for it=1:Nt
        [t1,yy1] = runge4step(dt,t1,yy1,params);
        tk(it) = t1;
        yk(it) = yy1(1);
    end

    yy2 = [0 1];
    t2  = 0;
    for it=1:Nt
        [t2,yy2] = runge4step(dt,t2,yy2,params);
    end

        sol1 = [yy1(1),yy1(2)];
        sol2 = [yy2(1),yy2(2)];

        monod = [sol1',sol2'];
      % Eigenvalues of monod
        tt = trace(monod);
        dd = det(monod);
        e1 = 0.5*(tt + sqrt(tt^2-4*dd));
        e2 = 0.5*(tt - sqrt(tt^2-4*dd));
      % Growth rates
        s1 = log(e1)/T;
```

```
        s2 = log(e2)/T;


    f = min(-real(s1),-real(s2));  % Minus sign to maximise f
    end


% Nonlinear Constraint Function
function [c, ceq] = nonlinear_constraint(params)

    beta_s  = params(1);
    Gamma_R = params(2);
    Delta   = params(3);

    %The minimum value of sig0 must be greater than 0
    c = -(-Gamma_R+(1-exp(-1/beta_s))*(1-Delta)^2); % Must be <= 0

    ceq = []; % No equality constraints
end

% ODE system
function dydt = odefun(t,y,params)

global n iPe   gamma P L Pi sig B sig0 Gamma0 aa da Ca

beta_s  = params(1);
Gamma_R = params(2);
Delta   = params(3);


aa     = 1 + Delta*cos(Ca*t);
da     = -Delta*Ca*sin(Ca*t);
Gamma0 = Gamma_R./(aa.^2);
```

```
sig0    = 1 + beta_s*log(1-Gamma0);
L       = (n+1)/(2*(2*n^2+1));
Pi      = (n+2)*(n-1)*sig0 + B./aa.^(3*gamma-1)*P;

% Matrix entries

[mm] = matform(da,aa,Gamma0,Pi,params);


    dydt = [mm(1,1)*y(1) + mm(1,2)*y(2), mm(2,1)*y(1) + mm
        (2,2)*y(2)];


end

function [mm] = matform(da,aa,Gamma0,Pi,params)

global n iPe  L Ca

beta_s  = params(1);
Gamma_R = params(2);
Delta   = params(3);


mm(1,1) = -(n-1)*(4*n+1)./(2*n^2+1)*da/aa - (2*n+1)*Pi*L./(
    aa*(n+2));
mm(1,2) = (beta_s*L)/((1-Gamma0));
mm(2,1) = -(3*n*(n-1)*(2*n-1)/(2*n^2+1))*(da./aa.^2)*Gamma0
    + Gamma0*L*Pi./(aa.^2);
mm(2,2) = -beta_s*(2*n^2-n+2)*Gamma0*L./(aa.*(1-Gamma0)) -
    iPe*n*(n+1)/aa.^2 - 2*da./aa;


end

```

```
function [t,yy] = runge4step(h,t,yy,params)

 beta_s   = params(1);
 Gamma_R  = params(2);
 Delta    = params(3);

    [dydt]      = odefun(t,yy,params);
    yy_pred1    = yy + 0.5*h*dydt;
    [dy_pred1] = odefun(t+0.5*h,yy_pred1,params);
    yy_pred     = yy + 0.5*h*dy_pred1;
    [dy_pred2] = odefun(t+0.5*h,yy_pred2,params);
    yy_pred3    = yy + h*dy_pred2;
    [dy_pred3] = odefun(t+h,yy_pred3,params);

  dydt = (1/6)*( dydt + 2*dy_pred1 + 2*dy_pred2 + dy_pred3 )
     ;
  yy   = yy + h*dydt;
  t    = t + h;

end
```

A2 Code for Simulated Annealing

```
close all;
clear all
clc

global  n  iPe   sig gamma B P Ca

format long

% Parameters

n      = 3;
iPe    = 0.0;
```

```
gamma = 1.0; % adiabatic index
B     = 0.01;
Ca    = 1.0;

beta_min    = 0.1;
Delta_min   = 0.1;
Gamma_R_max = (1 - Delta_min)^2*(1 - exp(-1/beta_min));

if n==0
    P = 2;
else
    P = 0;
end


% Define Parameter Bounds
lb = [beta_min, 0.1, Delta_min];  % Lower bounds for parameters [Ma, Gamma_R, Delta]
ub = [5, Gamma_R_max, 0.99];        % Upper bounds for parameters [Ma, Gamma_R, Delta]
initial_guess = lb + rand(1, length(lb)).*(ub - lb);

% Simulated Annealing Optimization
options = optimoptions('simulannealbnd', 'Display', 'iter', 'MaxIterations', 3000, 'MaxFunctionEvaluations', 300000,'ReannealInterval', 50); %,'ReannealInterval', 30
% Run the optimization
[optimal_params, f] = simulannealbnd(@objective_function, initial_guess, lb, ub, options);

% Display the Optimal Parameters
disp('Optimal Parameters Found:');
disp(['beta_s = ', num2str(optimal_params(1))]);
disp(['Gamma_R = ', num2str(optimal_params(2))]);
disp(['Delta = ', num2str(optimal_params(3))]);
```

```



% Display the Final Error
final_error = objective_function(optimal_params);
disp(['Maximum s1: ', num2str(-objective_function(
    optimal_params))]);
disp(['Minimum sig0: ', num2str(1 + optimal_params(1)*log(1
    - optimal_params(2)/(1 - optimal_params(3))^2))]);


% Objective Function (Maximise s1)
function f = objective_function(params)
  global sig s1 s2 Ca

beta_s  = params(1);
Gamma_R = params(2);
Delta   = params(3);

if -Gamma_R + (1-exp(-1/beta_s))*(1-Delta)^2 < 0
    f = inf;
    return
end

   Nt = 6000;
    T  = 2*pi/Ca;
    dt = T/Nt;

    yy1 = [1 0];
    t1  = 0;
    for it=1:Nt
        [t1,yy1] = runge4step(dt,t1,yy1,params);
        tk(it) = t1;
        yk(it) = yy1(1);
    end
```

```

    yy2 = [0 1];
    t2  = 0;
    for it=1:Nt
        [t2,yy2] = runge4step(dt,t2,yy2,params);
    end

        sol1 = [yy1(1),yy1(2)];
        sol2 = [yy2(1),yy2(2)];

        monod = [sol1',sol2'];
      % Eigenvalues of monod
        tt = trace(monod);
        dd = det(monod);
        e1 = 0.5*(tt + sqrt(tt^2-4*dd));
        e2 = 0.5*(tt - sqrt(tt^2-4*dd));
      % Growth rates
        s1 = log(e1)/T;
        s2 = log(e2)/T;


    f = min(-real(s1),-real(s2));  %
    end


% ODE system
function dydt = odefun(t,y,params)

global n iPe   gamma P L Pi sig B sig0 Gamma0 Ca

beta_s  = params(1);
Gamma_R = params(2);
Delta   = params(3);


```

```
aa      = 1 + Delta*cos(Ca*t);
da      = -Delta*Ca*sin(Ca*t);
Gamma0  = Gamma_R./(aa.^2);
sig0    = 1 + beta_s*log(1-Gamma0);
L       = (n+1)/(2*(2*n^2+1));
Pi      = (n+2)*(n-1)*sig0 + B./aa.^(3*gamma-1)*P;

% Matrix entries

[mm] = matform(da,aa,Gamma0,Pi,params);

dydt = [mm(1,1)*y(1) + mm(1,2)*y(2), mm(2,1)*y(1) + mm(2,2)*
    y(2)];


end

function [mm] = matform(da,aa,Gamma0,Pi,params)

global n iPe  L Ca

beta_s  = params(1);
Gamma_R = params(2);
Delta   = params(3);


mm(1,1) = -(n-1)*(4*n+1)./(2*n^2+1)*da/aa - (2*n+1)*Pi*L./(
    aa*(n+2));
mm(1,2) = (beta_s*L)/((1-Gamma0));
mm(2,1) = -(3*n*(n-1)*(2*n-1)/(2*n^2+1))*(da./aa.^2)*Gamma0
    + Gamma0*L*Pi./(aa.^2);
mm(2,2) = -beta_s*(2*n^2-n+2)*Gamma0*L./(aa.*(1-Gamma0)) -
    iPe*n*(n+1)/aa.^2 - 2*da./aa;

end
```

```

function [t,yy] = runge4step(h,t,yy,params)

 beta_s  = params(1);
 Gamma_R = params(2);
 Delta   = params(3);

    [dydt]      = odefun(t,yy,params);
    yy_pred1    = yy + 0.5*h*dydt;
    [dy_pred1] = odefun(t+0.5*h,yy_pred1,params);
     yy_pred2   = yy + 0.5*h*dy_pred1;
    [dy_pred2] = odefun(t+0.5*h,yy_pred2,params);
    yy_pred3    = yy + h*dy_pred2;
    [dy_pred3] = odefun(t+h,yy_pred3,params);

  dydt = (1/6)*( dydt + 2*dy_pred1 + 2*dy_pred2 + dy_pred3 );
  yy   = yy + h*dydt;
  t    = t + h;

end
```